REFERENCE ONLY

UNIVERSITY OF LONDON THESIS

Degree PhD Year 2005 Name of Author HARPER, S.M.

COPYRIGHT

This is a thesis accepted for a Higher Degree of the University of London. It is an unpublished typescript and the copyright is held by the author. All persons consulting the thesis must read and abide by the Copyright Declaration below.

COPYRIGHT DECLARATION

I recognise that the copyright of the above-described thesis rests with the author and that no quotation from it or information derived from it may be published without the prior written consent of the author.

LOANS

Theses may not be lent to individuals, but the Senate House Library may lend a copy to approved libraries within the United Kingdom, for consultation solely on the premises of those libraries. Application should be made to: Inter-Library Loans, Senate House Library, Senate House, Malet Street, London WC1E 7HU.

REPRODUCTION

University of London theses may not be reproduced without explicit written permission from the Senate House Library. Enquiries should be addressed to the Theses Section of the Library. Regulations concerning reproduction vary according to the date of acceptance of the thesis and are listed below as guidelines.

A. Before 1962. Permission granted only upon the prior written consent of the author. (The Senate House Library will provide addresses where possible).

B. 1962 - 1974. In many cases the author has agreed to permit copying upon completion of a Copyright Declaration.

C. 1975 - 1988. Most theses may be copied upon completion of a Copyright Declaration.

D. 1989 onwards. Most theses may be copied.

This thesis comes within category D.

☑ This copy has been deposited in the Library of UCL

☐ This copy has been deposited in the Senate House Library, Senate House, Malet Street, London WC1E 7HU.

A study of the formation, dissociation and reactivity of molecular dications.

by

Sarah Margaret Harper

A thesis submitted for the degree of Doctor of Philosophy

University of London

2004

Gas Phase Ion Chemistry Group,
Department of Chemistry,
University College London

ProQuest LLC
789 East Eisenhower Parkway
P.O. Box 1346
Ann Arbor, MI 48106-1346

To my family

Abstract

This thesis describes the commissioning of a new position-sensitive coincidence (PSCO) time-of-flight (TOF) mass spectrometer, which has been designed and constructed for studying the dynamics and kinematics of dication-neutral reactions at low collision energies (4-25 eV). These reactions commonly form two singly charged ions that the PSCO experiment detects in coincidence on an event-by-event basis, allowing definitive partner ion associations to be made. Flight time and positional data are recorded for each ion allowing the calculation of their initial velocity vectors from which the complete dynamics and kinematics for each reactive event, including determination of reactant and product states, may be determined.

The "simple" Ar^{2+}-He collision system was investigated for the purposes of commissioning and quantifying the energy resolution of the new PSCO experiment, since it has been previously studied in the literature. Following the successful commissioning of the PSCO experiment, three more complex systems were studied: Ne^{2+}-Ar, Ne^{2+}-N_2, CF_2^{2+}-H_2O, in order to obtain an in-depth understanding of the dynamics and energetics of dication-neutral reactions. The PSCO investigation of the electron transfer reaction in the Ne^{2+}-Ar collision system revealed bimodal angular distributions of both products, Ne^+ and Ar^+, indicating the presence of two different electron transfer channels. The extraction of such detailed information for a simple "two-body" reaction (a reaction where two products are formed) shows that the PSCO experiment is a powerful tool for determining detailed dication-neutral reaction mechanisms. The Ne^{2+}-N_2 collision system indicated the presence of three reaction channels forming $Ne^+ + N^+ + N$ in coincidence. Two of these channels were investigated revealing distinctly different mechanistic pathways. One channel involves the formation of a transitory collision complex, and the other appears consistent with a sequential process involving the fast dissociation of N_2^{+*}. Five reaction channels were observed for the CF_2^{2+}-H_2O collision system: three electron transfer channels and two bond-forming channels including a previously unobserved hydride transfer reaction.

Acknowledgements

I would like to express my thanks to the following people:

Professor Steve Price for his care and unwavering assistance over nearly a decade!

All those in the Chemistry department who have been supportive, especially: Dr Gavin Boakes, Dr Wendy Brown, Paul Burnside, Deep Bolina, Dominic Clare, Susan Creighan, Sarah Dixon, Kate Gawler, Dr Sunny Hu, Dominic Kearney, Dr Robin Mukerji, Natalie Lambert, Natalie Love, Dr James Perry, Claire Ricketts, Dr Dave Rowley, Dan Stone, Nurun Tafadar, Emma Wilson, Angela Wolff, the Fielding group, and finally the Mass Spec, Electronics and Mechanical workshops.

My parents and two brothers for their constant encouragement and support.

Friends old and new but especially, Madeleine Lewington-Barnes, Neda Berardone, Rob Cockcroft, Ann David, Lin Yan Liu, Manisha Mistry, Matteo Morgandi, Dr Dinah Parker, Helen Pierce, Simon Reeve, Carolyn Saunders, Joan Sullivan and Emily Weekes.

Table of contents

Table of figures

Table of tables

Publications

The following publications are based on the work discussed in this thesis:

"A position-sensitive coincidence spectrometer to image the kinematics of the bimolecular reactions of molecular dications", Sunny W-P. Hu, Sarah M. Harper and Stephen D. Price, 2002, *Measurements in Science and Technology*, **13** (10) 1512-1522.

"Imaging the electron transfer reaction of Ne^{2+} with Ar using position-sensitive coincidence spectroscopy", Sarah M. Harper, Sunny W-P. Hu and Stephen D. Price, 2002, *Journal of Physics B: Atomic, Molecular and Optical Physics*, **35** (21) 4409-4423.

"Collision complexes in dissociative single electron transfer between Ne^{2+} and N_2", Sarah M. Harper, Sunny W-P. Hu and Stephen D. Price, 2004, *Journal of Chemical Physics*, 120 (16) 7245-7248.

"Experimental studies of the dynamics of the bond-forming reactions of CF_2^{2+} with H_2O using position-sensitive coincidence spectroscopy", Sarah M. Harper, Sunny W-P. Hu and Stephen D. Price, 2004, *Journal of Chemical Physics*, 121 (7) 3507-3514.

"Experimental studies of the dynamics of the electron transfer reactions of CF_2^{2+} with H_2O using position-sensitive coincidence spectroscopy", Sarah M. Harper, Sunny W-P. Hu and Stephen D. Price, 2004, *Journal of Chemical Physics*, In preparation.

Chapter 1

Introduction

1.1 Gas phase reactions of dications

This thesis describes the commissioning of a new experiment designed to study the reactions of dications with neutral collision species. Dications are doubly positive charged atomic or molecular ionic species that may be formed by a variety of methods, as will be discussed below, such as electron [1-12] or photon [13-19] ionisation. This chapter will examine why the study of dications is necessary by giving an overview of their properties and previous investigations of their gas phase ionic reactivity that will put into context the research described in this thesis.

Detailed experimental studies of monocations over the last 20 years have made it possible to accumulate a wealth of information on their structure, spectroscopy and dynamics. The important role of monocations, as a reactive species in a variety of environments such as the interstellar medium, has been recognised with extensive investigations of their chemical reactivity with neutral molecules in the gas phase [20-22]. In contrast, their doubly-charged relatives are often highly energised and unstable species, with markedly different properties to monocations, resulting in dicationic species being less well characterised. Therefore, the bimolecular chemical reactions of small doubly-charged ions (dications) in the gas phase have only recently received significant attention.

There are a number of reasons for the focus of experimental studies of gas-phase ion chemistry on monocation reactivity. Firstly, monocations are usually the major final product following molecular ionisation events [23-26], either as parent ions or

fragments. Hence, one would expect monocations to be the most influential positively charged species in the chemistry of energised media. Secondly, the presence of monocations in energised media is supported by a wealth of experimental evidence [27]. In contrast, the transient nature of the electronic states of many small molecular dications, as described below, means that clear signatures of their presence are elusive. In actual fact, the evidence for the presence of molecular dications in, for example, planetary atmospheres comes principally from modelling work [28, 29]. Lastly, there is a prevailing idea, particularly when considering electron-molecule collisions, that the cross-section for molecular double ionisation is only one or two percent of the single ionisation cross-section, even at significant ionising energies (>50 eV). Hence, the effects of multiple ionisation were considered insignificant when identifying ion-molecule reactions to study for the purpose of generating data for models of ionised media. However, recent experiments have shown that in many instances there has been a significant under-estimation of molecular double ionisation cross-sections, due to experimental shortcomings in detecting the energetic fragments from dissociative double ionisation [24-26, 30-33]. The efficient collection of such fragments reveals that in electron-molecule collisions, even at electron energies close to threshold, the ion yield contains a significant contribution from double ionisation. Furthermore, experimental and theoretical investigations have shown that many molecular dications can, in certain electronic states, survive for extended periods of time [34]. Accordingly, it became clear that the consequences of molecular double ionisation and the bimolecular chemistry of molecular dications were worthy of investigation.

The first detection of a gas phase molecular dication (CO^{2+}) was made in the 1930s [35]. Despite these early observations, molecular dications were generally considered a mass spectrometric curiosity due to their short life times and were rarely the targets of experimental investigations. However, over recent years, the properties of molecular dications have been the subject of a steadily increasing number of experimental studies [2-9]. This increase has occurred, in part, due to several new experimental techniques that have been developed to probe these short-lived species. With the development of these new experimental techniques, many groups are currently investigating the properties of molecular dications. As a result, a much clearer picture is now emerging

of the energetics and lifetimes of several diatomic and a small handful of triatomic dications in low-lying electronic states. Indeed, in some cases information is now available concerning the energies and dynamics of the vibrational levels supported in dicationic electronic states.

As with any poorly characterised species, the majority of experimental investigations have concentrated on probing the properties of molecular dications in an isolated environment. However, stimulated by the success of these experiments, research in this area has moved on to study the electron transfer and bond-forming reactivity of dications following 'collisions' with neutral species or photons.

At first glance, the study of molecular dications may be considered esoteric and of little relevance outside the specialised field of ion chemistry. However, the properties of dications may influence several areas of gas-phase physical chemistry. Therefore, an appreciation of the properties of such species is important if there is to be an enhancement of the understanding of a variety of environmental phenomena (e.g. atmospheric and ionospheric chemistry). For example, the double photoionisation of molecular species has been proposed as a source of energetic ions in planetary atmospheres including the Earth's ionosphere [28]. In addition, following the observation of IR emission, the existence of doubly-charged polycyclic aromatic hydrocarbons (PAH) in the interstellar medium has been proposed [39-41]. In addition to these practical applications, the modelling of molecular dications and their spectroscopic and energetic properties is also a theoretical challenge. Consequently, comparative experimental data is an essential requirement in assessing the applicability of new theoretical methodologies.

Since little is known of the interactions of dications with atomic and molecular neutral species at low collision energies, a number of experimental groups have embarked on programmes designed to study the dynamics and energetics of interactions of molecular dications with atoms, molecules and photons. It is such studies that are the objective of this thesis and other contributions to this field will be discussed where appropriate.

This thesis presents results from an investigation of the collision-induced reactivity of several gas-phase molecular dications using a new position-sensitive coincidence (PSCO) experiment designed for coincident detection of both singly charged ions formed in a dication-neutral reaction on an event-by-event basis. For each pair of detected ions formed by a reactive event, the positional and flight time data for each ion are extracted. Dynamics and energetics may then be calculated for each reactive event allowing the determination of mechanistic information and product and reactant states. Chapters Two, Three, Four and Five discuss the experimental and theoretical approach used together with commissioning results and the method of data analysis. Chapters Six, Seven, Eight and Nine present results for a variety of collision systems thereby demonstrating the capability of the PSCO instrument. The bulk of this thesis is a presentation of the results of the experimental work. Such results are displayed in graphical and tabular format, together with a discussion of the results and the appropriate conclusions drawn from the experimental data.

However, in order to place in context the experimental results and conclusions discussed in this thesis, it is first necessary to begin with an introduction to the properties of doubly-charged ions, together with a brief overview of ionisation, dissociation and the relevant experimental techniques used to investigate charged species and their reactivity. These topics are presented in this chapter.

1.2 Properties of dications

As mentioned above, the last decade, has seen an increasing amount of interest in molecular dications and a wide variety of different experimental techniques have been developed to study their properties. It is important to study these species, as knowledge of their behaviour is essential for explaining and predicting their contribution to the properties of energised media such as the interstellar medium and plasmas [22]. Molecular dications often have an open shell structure and a high density of electronic states, but they are particularly interesting due to the existence of long-lived metastable

electronic states that allow these species to interact with other atoms and molecules. The majority of small molecular doubly-charged ions are thermodynamically unstable with respect to a pair of singly charged ions [3, 36] (Figure 1.1):

$$AB^{2+} \rightarrow A^{+} + B^{+} \qquad (1.1)$$

$$AB_2^{2+} \rightarrow A^{+} + B^{+} + B \qquad (1.2)$$

This instability is due to the Coulomb repulsion present between the two positive charges in the molecule. In this respect, these species are very different to monocations [36, 37]. However, recent theoretical and experimental studies of rare gas clusters, halides and other species carried out by Schroder and Schwarz [38] have shown that diatomic dications such as $GeNe^{2+}$ and UF^{2+} are thermodynamically stable.

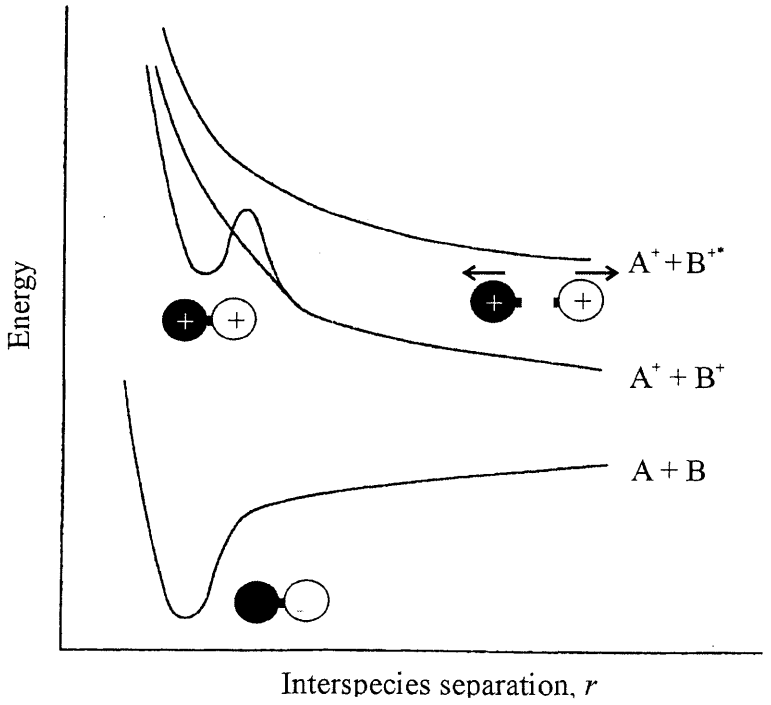

Figure 1.1 Schematic potential energy curves for a diatomic molecular dication

For many dications, at least one long-lived electronic state exists as a result of a barrier in the potential energy surface (Figure 1.1), caused by a combination of the molecular bonding and electronic repulsion, correlating with the charge separation asymptote (1.1). This state is termed 'metastable' as it usually lies at an energy above the charge separation asymptote. Metastable vibrational levels may be supported below the dissociation limit. The lower vibrational levels in the potential energy wells may often be extremely long lived, a matter of hours or even days, in contrast to higher vibrational levels which may dissociate within picoseconds. This behaviour has been observed experimentally, and recent experiments have determined that dications in low-lying vibrational states live for significantly longer than 1 second [34, 39, 40].

For some dications, such as O_2^{2+}, the potential well is relatively deep and supports many levels [41]. If the population is transferred to higher vibrational levels where the species can tunnel through the dissociation barrier, the dication dissociates and considerable kinetic energy is released; a typical value being 6 eV for the dissociation of a dication into an ion pair [42]. It is thought that the barrier in the metastable state is a result of competition between valence and Coulomb forces. It was initially surmised that the dications would dissociate by tunnelling through the barrier, which would cause *J*-dependent line-widths in predissociation spectra [42]. Dications close to the top of the barrier to dissociation have energies greater than the barrier to tunnelling, allowing dissociation to occur *via* tunnelling through discrete rotational levels. For N_2^{2+} however, predissociation spectroscopy shows that in the lower vibrational levels of the first excited electronic state, the dissociation is caused by electronic predissociation, with line-widths independent of the rotational constant [42]. Dications in these lower vibrational levels do not have sufficient energy to tunnel through the barrier, so instead coupling occurs with a nearby repulsive state [43]. In fact, tunnelling only seems to be a significant predissociation pathway for vibrational states that lie very close to the top of the barrier. The potential energy surface of the metastable state varies approximately with r^{-1} at large r, and the barrier to charge-separating decay becomes very broad as the vibrational excitation of the dication decreases [10]. Hence, tunnelling is rapidly disfavoured with interspecies separation.

The dissociation of some molecular dications may occur *via* deferred charge-separation (1.3), although such behaviour occurs predominantly in larger molecules [16, 44].

$$AB_2^{2+} \rightarrow AB^{2+} + B \qquad (1.3)$$

Following this process, the dication formed by the dissociation, AB^{2+}, may undergo further fragmentation (Figure 1.2) to form a pair of singly charged ions (1.4), or undergo a further dissociation (1.5).

$$AB^{2+} \rightarrow A^+ + B^+ \qquad (1.4)$$

$$AB^{2+} \rightarrow A^{2+} + B \qquad (1.5)$$

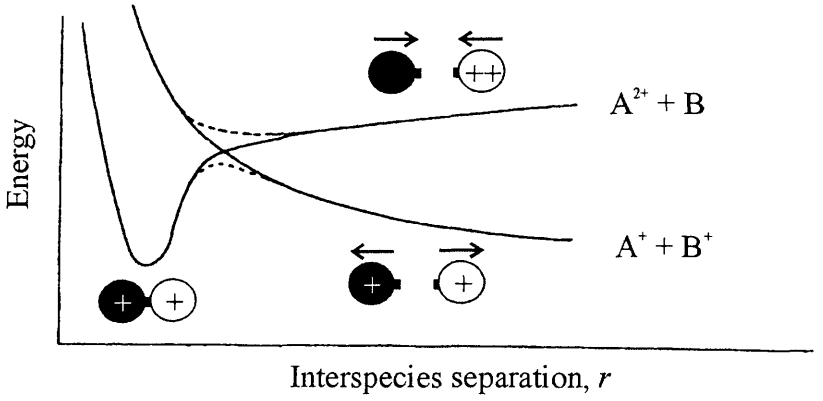

Figure 1.2 Schematic potential energy curves showing how metastable dication states can arise from the avoided crossing of potential energy curves which correlate with the charge-separated ($A^+ + B^+$) and neutral-loss ($A + B^{2+}$) asymptotes.

O'Neil and co-workers used computational methods to investigate the electronic structure of F_2^{2+} and put forward a different reason for the existence of these metastable species. They discovered that the potential-energy curves of F_2^{2+} could be well

reproduced by taking the previously established curves for the isoelectronic neutral species (O_2) and adding a Coulomb repulsion potential [45]. For this reason, it was proposed that dication states may be pictured as arising from the combination of an ordinary chemical binding potential and the Coulomb repulsion of the constituent ions; metastable states will exist when the strength of the chemical bond is sufficient to overcome the repulsion between the two positive charges. It has been shown, however, that in some heteronuclear diatomics, such as HCl^{2+}, the additive model put forward by O'Neil *et al*, is not appropriate. This is because, in these species, at small internuclear distances [42], both positive charges reside on one of the atoms.

For larger molecules, it is not yet possible to predict the observed structure and lifetimes of dications using *ab-initio* calculations, and it would seem that the region close to the top of the barrier (which is that probed by fast ion beam spectroscopy) is the hardest part of the potential energy curve to calculate accurately [42]. For light dications (small interspecies separation), the dissociation limit corresponds to two charged fragments repelling each other due to the Coulomb energy. The chemical bond lowers the Coulomb energy when the fragments are bought closer together and this leads to a potential energy well that supports vibration-rotation levels. Information about these levels can then be obtained, using a modified mass spectrometer with the beam from an infrared laser to give a vibration-rotation spectrum [41].

One of the first molecular dications to be identified was CO^{2+}, in 1930, by R. Conrad [35]. Other hetero-nuclear species have also been discovered: CF^{2+} [6], NO^{2+} [46], OCS^{2+} [4], $NeXe^{2+}$ [47], and $NeAr^{2+}$ [48]. Among the known first row homo-nuclear dication species are Be_2^{2+} [49-51], B_2^{2+} [52], C_2^{2+} [45], N_2^{2+} [53-55], and O_2^{2+} [53, 54].

1.3 Ion formation

The method of reactant ion formation used in the PSCO instrument is electron ionisation; "electron ionisation" being the IUPAC approved term for ionisation using an

electron, not "electron impact ionisation". A detailed description of the ion source is given in Chapter Three. Some alternative methods for ion beam production are alpha-particle bombardment or photoionisation (PI) using laser excitation [56, 57], a discharge lamp [14, 16] [13, 15] or a synchrotron radiation source [17, 18, 58, 59]. All these techniques require sophisticated equipment that can be very expensive, in contrast to the simplicity of the PSCO ion source.

1.3.1.1 Electron ionisation

Studies of the electron ionisation of N_2O_5 [46], O_3 [1], OClO [60], and HCl [26, 42] have recently been carried out. These experiments have shown that the dications are readily formed and the cross-sections for the double ionisation processes are quite large. The angle-integrated relative partial and total ionisation cross-sections observed are important for many areas of application, particularly in modelling plasma and discharge environments. This comes from the fact that these cross-sections govern the production rate of a variety of reactive species and secondary electrons used in these processes [61].

The study of electron ionisation of neutral gases has been combined with ion-ion coincidence spectroscopy studies [46, 60, 62-64]. Ion-ion coincidence spectroscopy is used to identify the products of the fragmentation of molecular dications. All coincidence experiments rely on the simultaneous detection of two or more species, such as singly charged fragment ions and electrons, formed in the same ionisation event:

$$AB + e^- \rightarrow \left[AB^{2+} + 3e^-\right] \rightarrow A^+ + B^+ + 3e^- \qquad (1.6)$$

The product fragments formed will be accelerated out of the reaction source region by an electric field. Since the ions originate from the same dissociation event, their times of flight will be related. From the two-dimensional data collected, ionisation cross-sections—the likelihood of a given ionisation event occurring—may be calculated.

Lindsay *et al* studied the electron ionisation of CH_4 to report the absolute ionisation cross-sections for the following ion pairs: (CH_2^+, H^+), (CH^+, H^+) and (C^+, H^+) [65]. A pulsed beam was passed through a static gas target. The ions were extracted, mass analysed and counted along a known path length. The counting electronics used are only able to process one event at a time; when two ions are produced from one ionising event, the first one arriving at the detector will be counted, precluding the detection of any following ions. This leads to the under-estimation of the cross-sections for the heavier ions formed. Therefore, for the true cross-section of, for instance, C^+ to be measured, a gate was applied to the timing signal to suppress the detection of the lighter H^+ ions. Data was collected in this way for each of the ions. The uncertainties in the cross-section measurements are large at ±15-20% because this detection system is not best suited to ion pair detection. In addition, it is assumed that relatively few ionisation events result in the formation of three positive ions. Sieglaff *et al* used a similar experimental set up to calculate the absolute partial cross-sections for the electron ionisation of CF_4 [66]. The uncertainties in the measurements were much improved on the experiment carried out by Lindsay *et al*, being in the region of ±5-8%.

Recent studies of the electron ionisation of Cl_2 have shown considerable evidence for the existence of long-lived doubly-charged and triply charged ions [25]. These experiments paid particular attention to the efficient collection of fragment ions with high translational energies. As a result, the first experimental estimate of the triple ionisation energy of molecular chlorine was obtained for the fragmentation of Cl_2^{3+} to Cl^{2+} and Cl^+ [25]. Investigations of this type have also been carried out for CS_2^{2+} [67, 68], HNO_3 [62], Cl_2O [63], CO_2^+ [69], *n*-octane [70] and $C_2H_2^{2+}$ [71].

1.3.1.2 Photoionisation

In contrast to electron ionisation, the widespread use of photoionisation as a means of generating ions is a comparatively recent phenomenon. However, with the increasing availability of synchrotron radiation sources and improved laser technology,

photoionisation is now a frequently used technique. The double ionisation of a neutral molecule using photon impact involves the interaction of a photon of known energy emitted by a discharge lamp [13-16], synchrotron radiation source [17, 18, 59] or laser [56, 57] with a neutral target molecule, thus resulting in ionisation (1.7).

$$AB + h\nu \rightarrow AB^{+} + e- \qquad (1.7)$$

Although photoionisation, as a means to double ionisation, requires equipment of significant complexity, the use of this method does offer two significant advantages over electron ionisation. Firstly, an investigation of the ionisation of various molecules by means of a He discharge revealed that photoionisation produces significantly greater numbers of doubly-charged species than the impact of electrons of corresponding energies [13]. The second advantage is that the energy of the incident photon is known and therefore, in contrast to electron ionisation, the energy deposition in the target molecule is known.

1.4 The bimolecular reactivity of dications

In a bimolecular reaction, a pair of atoms and/or molecules collide and exchange energy, atoms, or groups of atoms. This section will present previous research into different types of dication-neutral reactions. The prerequisite for a reaction is of course the encounter itself *i.e.* the collision of the two reactants. The result of a bimolecular reaction between a doubly-charged ion and a neutral collision partner are dependent upon the collision energy and the identity of the two reactants. However, the results of the experiments performed to investigate the reactivity of molecular dications with neutral collision partners at collision energies ranging from thermal to high (keV) energies [9, 11, 12, 72-76] have indicated that four main types of reactions are observed.

The first part of this section will describe the simplest type of observed dicationic bimolecular reactivity: electron transfer. This is followed by a description of collision

induced charge separation and collision induced neutral-loss reactions. This section is concluded with a discussion of the chemical reactions of dications.

A bimolecular dication-neutral chemical reaction involves an exchange or rearrangement of the atoms of the reactants and commonly forms two singly charged ions. The dynamics and energetics of the bond-forming reactions of dications have not been investigated as widely as electron transfer reactions. For this reason, the bond-forming reactions of dications are a particularly interesting reaction type for investigation using the PSCO instrument as will be shown in Chapters Seven and Nine.

1.4.1 Electron transfer

Electron transfer is usually the most abundant reaction that takes place in collisions of dications and neutrals. During the encounter, an electron is transferred from the neutral to the dication leaving the ionic products in stable electronic states [3-6, 73] (non-dissociative electron-transfer, Eq. 1.8).

$$AB_2^{2+} + M_2 \rightarrow AB_2^{+} + M_2^{+} \qquad (1.8)$$

Alternatively, the product ions may initially be formed in unstable excited electronic states, resulting in the fragmentation of the excited ion [3-6, 73, 76] (dissociative electron-transfer, Eq. 1.9).

$$AB_2^{2+} + M_2 \rightarrow AB_2^{+*} + M_2^{+} \rightarrow AB^{+} + B + M_2^{+} \qquad (1.9)$$

Examples of both types of electron transfer reactions will be described in this thesis (Chapters Five, Six and Eight). From the results presented in these chapters, it will become clear that the PSCO technique is able to extract detailed information about the dynamics of even these very 'simple' reactions, such as whether electron transfer occurs as the reactants approach each other or as they depart from each other (Chapter Six).

1.4.2 Collision induced charge separation (CICS) and collision induced neutral-loss (CINL)

In CICS and CINL reactions, the transfer of some kinetic energy of the collision to the dication leaves the dication in a predissociative state. This predissociative state then either fragments to form two singly charged ions (CICS) [3-6, 9, 73]

$$CO_2^{2+} + Ar \rightarrow CO^+ + O^+ + Ar \qquad (1.10)$$

or simply divides with the double charge intact on one of the fragments (CINL) [73, 77, 78].

$$CF_3^{2+} + Ar \rightarrow CF_2^{2+} + F + Ar \qquad (1.11)$$

Dynamical studies of the latter reaction using the PSCO technique are not possible. For a three-body reaction (1.11), it is necessary to detect at least two of the products formed so that, by conservation of momentum, the dynamics of the third undetected product may be determined. The PSCO instrument only detects ions, which leaves two undetected products in a CINL collision (1.11).

The first investigations of the reactions of dications with rare-gas atoms, such as Ar, Kr, and Xe, used CO^{2+} as the reactant dication [5, 12, 76, 79]. Many of these experiments were carried out at high collision energies [12, 76, 79]. Reactions between rare-gas atoms and CO_2^{2+}, CS_2^{2+}, CF_2^{2+} and CF^{2+}, have also been studied, in relation to product formation pathways [4-6, 78]. These experiments revealed that electron transfer dominated the product ion yield. Further experimental investigations have focused on the reactions of perfluorinated molecular ions such as CF_3^{2+} and SiF_2^{2+}. For these dications, neutral-loss reactions, in addition to electron transfer and collision-induced charge-separation, have been observed to occur following collisions with the rare gases (1.12) [77, 78].

$$SiF_3^{2+} + Rg \rightarrow SiF_2^{2+} + F + Rg \qquad (1.12)$$

1.4.2.1 Landau-Zener model and reaction window theory

The reaction window theory [5] is a simple theoretical model of the efficiency of dication-neutral electron transfer reactions, based on the Landau-Zener avoided crossing theory [80, 81] that is described in detail in Chapter Two. The models consider the reaction as taking place at a crossing, having an interspecies separation R_c (Figure 1.3), of two diabatic potential curves corresponding to an attractive reactant potential and a repulsive product potential.

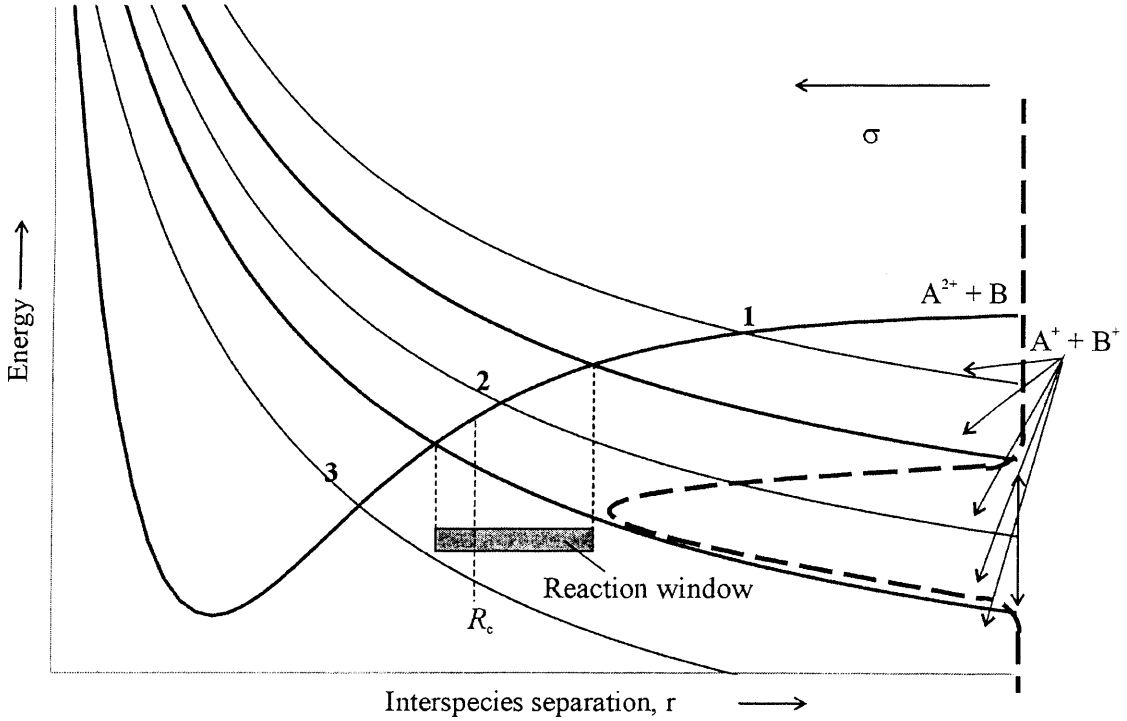

Figure 1.3 Schematics of potential energy curves for the reaction $A^{2+} + B \rightarrow A^+ + B^+$. Only case **2** leads to charge transfer of a sizeable cross-section; RW = reaction window.

Briefly, for an atomic ion-atom collision system, if the crossing between the reactant and product surfaces occurs at very large internuclear separations, where the interaction is very small, the single-passage transition probability, δ, is negligibly small and the colliding system remains on the incoming potential energy curve (Figure 1.3, case **1**). If, on the other hand, the crossing occurs at small internuclear separations and the

interaction is large, the reactant and product terms split adiabatically and δ is close to unity. The colliding system then approaches and departs on the reactant potential energy curve; though at small interparticle separations it moves on the section of the potential energy curve that belongs to the products (Figure 1.3, case **3**). Only if the crossing occurs within a certain range, where the single-passage transition probability is $0.1 < \delta < 0.9$, is there a finite chance that the system may approach on the reactant and depart on the product potential energy curve (Figure 1.3, case **2**). The cross-section of this charge transfer process is often large.

The overall transition probability includes the way in and the way out and is

$$P = 2\delta(1-\delta). \qquad (1.13)$$

The position of the reaction window is determined by the Landau-Zener formula and for collision energies in the eV range it lies at about 2.5-5.5 Å (Figure 1.3). The size of the total cross-section depends on the position of the crossing point. Consequently, the size of the cross-section is related to the exothermicity of the process in question [82, 83]. This is because the various repulsive product potential energy surfaces have the same form which is determined by simple electrostatics. The relation between the exothermicity, ΔE, and the position of the crossing point, R_c, may be roughly estimated (for a crossing of a flat and a Coulomb term) from

$$R_c = \frac{14.4}{\Delta E} \qquad (1.14)$$

where R_c is in Å, and ΔE in eV.

1.4.3 Bond-forming reactions

In reactions of dications with neutral molecules there exists the opportunity for chemical reactions, and this chemical reactivity has been investigated. The data gathered on this type of reactivity, to date, has been extremely limited. In this type of reaction, chemical rearrangement takes place following a collision, where Eq. 1.15 shows a common type of rearrangement observed in many dication-neutral collision systems [2, 3, 7, 73, 84, 85].

$$AB_2^{2+} + M_2 \rightarrow ABM^+ + M^+ \qquad (1.15)$$

The electronic structure of molecules causes them to be significantly more chemically reactive than the rare-gas atoms. Early observations of dication reactivity come from a series of dication-neutral collision experiments, performed by Price *et al* [7], using D_2 as the neutral species.

$$CF_2^{2+} + D_2 \rightarrow DCF_2^{2+} + D \qquad (1.16)$$

$$OCS^{2+} + D_2 \rightarrow DS^+ + [D + O + C]^+ \qquad (1.17)$$

The reactions with D_2 possess significant cross-sections [73]. These bond-forming reactions appear to involve effective D^- transfer from neutral molecule to the molecular dication (see Figure 1.4). Similar reactivity has been observed for atomic dications of the transition metals that are observed to extract H^- from organic molecules [86](1.18).

$$Nb^{2+} + C_2H_6 \rightarrow NbH^+ + C_2H_5 \qquad (1.18)$$

In the theoretical model used for these hydride transfer reactions, one similar to the Landau-Zener model [80, 81] that has been extensively used to model atomic electron transfer systems, the hydride ion is considered as a 'heavy electron', and its transfer is

pictured as occurring at a curve crossing between an attractive reactant potential and a repulsive product potential [86].

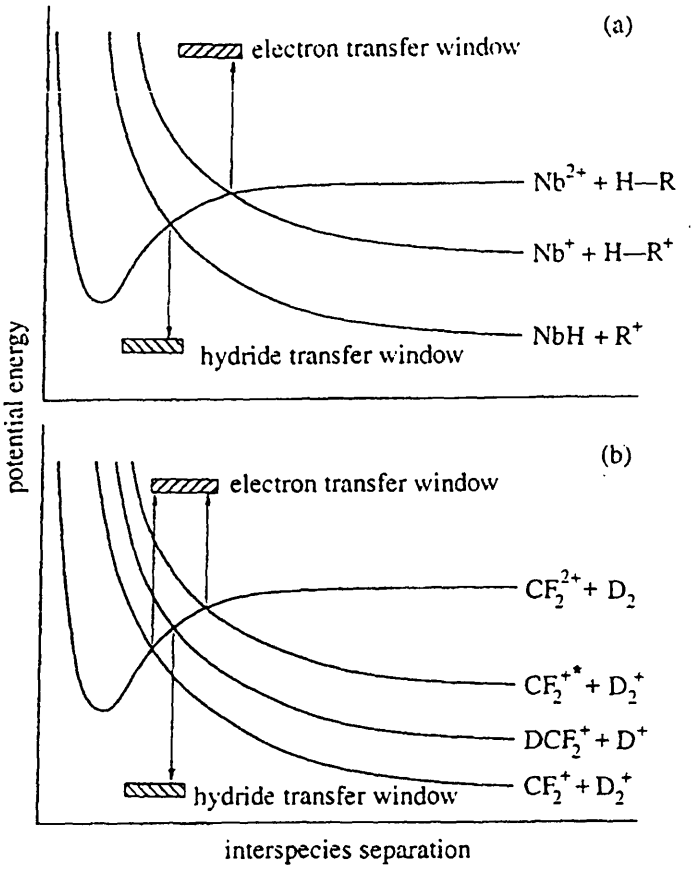

Figure 1.4 Schematic potential energy curves to illustrate the competition between electron and $H^-(D^-)$ transfer reactivity for (a) atomic and (b) molecular dications.

The reaction window theory can be used here to explain the competition between electron and H^- (D^-) transfer reactivity for atomic and molecular dications. It has been applied by many authors with good qualitative success [5, 86-89]. The key difference between the D^- (H^-) transfer reactions in the atomic and molecular dicationic systems can be accounted for by this curve-crossing model: the transition-metal dications frequently exhibit only hydride-transfer reactivity whereas, for the molecular dications, deuteride transfer always competes with electron transfer (Figure 1.4). This competition arises from the energetics of the molecular dication-D_2 collision system,

which always places the asymptote for electron transfer at a lower energy than the asymptote for D^- transfer.

Herman *et al* have also studied the reactions of CF_2^{2+} with D_2. Their experiments investigated the crossed beam scattering reactions of CF_2^{2+} with D_2 and H_2 [88], and CO_2^{2+} with D_2 [89].

$$CF_2^{2+} + D_2 \rightarrow CF_2^{+} + D_2^{+} \qquad (1.19)$$

$$CF_2^{2+} + D_2 \rightarrow DCF_2^{+} + D^{+} \qquad (1.20)$$

The reactions of D_2 with CF_2^{2+} showed that the ion products tended to be forward scattered with respect to the incoming dication, with little (15%) backward scattering. However, there is more backward scattering for (1.20) than for the reaction in (1.19), indicating the formation of an intermediate. The non-dissociative chemical reactions of CF_2^{2+} (1.19) with H_2 and D_2 showed a slow increase in the total cross-section with a decrease in the reactant relative velocity. On the other hand, the total cross-section for the charge transfer reaction showed a steep decrease to zero with decreasing relative velocity. The total cross-sections obtained showed an isotope effect favouring the reaction with H_2 by a factor of about 1.5-2 in comparison with D_2. The decrease seen in the total cross-section for the charge transfer reaction can be rationalised in terms of the Landau-Zener model as explained above. The charge transfer process is highly exothermic and the decrease in the relative velocity of the reactants causes the Coulomb repulsion between the two singly charged product ions to become more significant, decreasing the likelihood of charge transfer taking place.

In the last few years, Bassi *et al* have carried out one of the few studies of the reactions of doubly-charged rare gas ions with neutrals to form doubly-charged ions [90].

$$Ar^{2+} + N_2 \rightarrow ArN^{2+} + N \qquad (1.21)$$

The observed reactivity is unusual as dication-neutral collisions generally form two singly charged product ions. Argon is ionised by electrons to produce Ar^{2+}, extracted from the source region, mass selected and finally injected into a radio-frequency octopole ion guide that is surrounded by the scattering cell. The N_2 is introduced into the scattering cell at pressures below 10^{-4} Torr to avoid multiple collisions. The ions resulting from the collisions are collected using a quadropole mass spectrometer. The cross-sections are obtained by the ratio between the reactant and product ions. The cross-section for the reaction is roughly constant at low Ar^{2+} beam energies, while at about 2 eV the production of ArN^{2+} begins to rise. There is a rapid falloff of ArN^{2+} at energies higher than 10 eV. Very little is known about the coupling between the two nearly resonant charge transfer states $Ar^{2+} + N_2$ and $Ar + N_2^{2+}$ in the reactant channel. This resonance might influence the reaction dynamics. The only information on the product ArN^{2+} comes from a theoretical study by Wong and Radom who calculated that the reaction to form ArN^{2+} should be endothermic [91]. This discrepancy between theoretical and experimental results is thought to be due to the existence of metastable Ar^{2+} states in the experimental ion beam.

Bassi *et al* also carried out experiments [92] to measure the integral cross-sections for the bond-forming reaction

$$CO^{2+} + Ar \rightarrow ArC^{2+} + O \qquad (1.22)$$

using a similar experimental setup as mentioned earlier [90]. The production of ArC^{2+} peaks at approximately 3 eV and then drops off rapidly. This decline in the cross-section at high energy might be related to the vibrational predissociation of the metastable ArC^{2+}. The cross-section for formation of these products was shown to be a lot smaller than those observed for the other reaction channels such as the charge-transfer reaction producing $CO^+ + Ar^+$ [92, 93].

1.5 Probing the properties of dications

Numerous experimental methods are now available to probe the properties of doubly-charged molecular ions. However, the first experimental evidence for the existence of molecular dications came from mass spectrometric studies of carbon monoxide [35]. This work focused on the analysis of the ionic products of electron ionisation, and led to the determination of the single and double ionisation potentials of carbon monoxide. To investigate in more detail the properties of dications, such as the kinetic energy release upon dissociation, dicationic lifetime and fragmentation branching ratios, an advanced experimental technique is required. One suitable method for studying the dissociation of molecular dications involves coincidence techniques.

There are numerous types of coincidence experiments; however, they all rely on the same fundamental methodology, namely, the detection of two or more charged dissociation products, electrons and or fragment ions, which originate from the same ionisation event. The experimental procedure involves measuring the difference in the flight times of selected dissociation products formed upon dissociative double ionisation in a time-of-flight mass spectrometer. These experiments can reveal information on the electronic spectroscopy of the dications and on the dynamics of the double ionisation process. A brief summary of some of these experimental techniques is given below.

1.5.1 Coincidence experiments

1.5.1.1 The ion-ion and photoion-photoion coincidence (PIPICO) techniques

The ion-ion coincidence technique uses electron ionisation and a time-of-flight mass spectrometer to record the coincidences between a pair of fragment ions. This is done by measuring the differences in the flight times of the fragments A^+ and B^+ in a mass spectrometer for a dissociation process such as (1.23).

$$e^- + AB \rightarrow [AB^{2+} + 3e^-] \rightarrow A^+ + B^+ + 3e^- \qquad (1.23)$$

This technique has been used to investigate the dissociation of doubly-charged molecules such as O_3 [94], C_6H_6 [95, 96], $CXCl_3$ (X = H, D) [97], FC(O)SCl [98].

The PIPICO technique is a very similar coincidence technique that uses photoionisation instead of electron ionisation.

$$h\nu + AB \rightarrow [AB^{2+} + 2e^-] \rightarrow A^+ + B^+ + 2e^- \qquad (1.24)$$

The advantage of the PIPICO method over its electron ionisation rival is that the energy deposition to the molecule is precisely known. Some doubly-charged molecules studied by PIPICO are argon clusters [99], CF_4 [100], SO_2 [101] and C_6F_6 [102]. However, the ease of producing a usable beam of electrons of a suitable flux and energy makes electron ionisation a more reliable and inexpensive method of ionisation than PIPICO.

There are limitations associated with the two coincidence techniques discussed above. As mentioned, both these techniques measure the time-of-flight difference between pairs of fragment ions formed upon dissociative double ionisation. If these two techniques are applied to polyatomic dications, cases where ion pairs of equal mass are formed cannot be investigated, since the pair will be centred about a zero time-of-flight difference. For complex polyatomic dications, the above two techniques do not unambiguously identify the ions responsible for the coincidence signals, as there are a large number of available fragmentation channels which yield ion pairs with the same time-of-flight difference.

1.5.1.2 Photoelectron-photoion-photoion coincidences (PEPIPICO)

Photoelectron-photoion-photoion coincidence (PEPIPICO) spectrometry [59, 103-105] has similarities to the PIPICO coincidence method described above. The development of the PEPIPICO triple coincidence technique resolved the problems associated with the

two-particle coincidence techniques. In this technique, a single photoelectron and a pair of photoions are detected in coincidence. The time of ion formation is recorded by the detection of one or more of the ejected electrons. The actual flight times of the coincident photoions formed from the same dissociative event may then be calculated allowing the determination of their masses. Consequently, the major advantage of the PEPIPICO technique over the PIPICO technique is the ability to determine absolute masses of the coincident photoions. Hence, PEPIPICO is particularly well suited to studying larger organic dications such as the naphthalene dication $C_{10}H_8^{2+}$ [16], as the greater number of potential fragmentation channels in larger molecular dications complicates the analysis of the PIPICO spectra. The ability to determine absolute masses using the PEPIPICO technique makes it an ideal method for studying unimolecular three-body dissociations of dications. Examples of such work include investigations of the dissociation of ICN^{2+} by Eland [15] and the dissociation of OCS^{2+} by Masuoka [59].

1.5.2 Experimental techniques for studying ion-molecule reactions

As discussed earlier the majority of dications are very short-lived species and therefore mass spectrometric techniques are limited to the study of relatively long-lived metastable states. To study in detail properties of molecular dications, such as the dicationic lifetimes and fragmentation branching ratios and the kinetic energy release upon dissociation, new experimental techniques have been developed.

A brief description of these techniques is given below, including translational energy spectroscopy, guided beam techniques, crossed beam apparatus and velocity map imaging employed to study ion-neutral reactions at low (thermal) collision energies.

1.5.3 Translational energy spectroscopy

Translational energy spectroscopy (TES) [76, 106-108] plays an important role in the spectroscopy of ionic systems. Due to its extraordinarily high resolution, it allows characterisation of ionic systems whilst most other spectroscopic methods fail due to the extremely low concentration of the ion under investigation. In TES, the aim is to extract spectroscopic information on the energetics of the states of the participating species and in some cases to determine detailed information on the scattering process, such as the dynamics, the lifetimes of species, collision cross-sections and populations of states.

Typically TES involves the collision of a fast, monoenergetic (3000 eV ±0.1 eV), mass selected ion beam with a neutral gas, at thermal energy, under single collision conditions. An example of a translational energy spectroscopy experiment is one that uses a double focused translational energy spectrometer with two symmetrically arranged cylindrical electrostatic energy analysers [108]. The ions are generated using a high electron ionisation energy within an ionisation chamber, then extracted and accelerated to high translational energy. The ions are mass analysed and passed into a collision region with the neutral gas. Energy analysis of the collision products is carried out by scanning across the two electrostatic analysers.

Since collision systems in TES experiments are isolated, comparison of the reactant ion beam translational energy with the KER of the products makes it possible to establish a direct relationship between the total loss or gain of translational energy and internal energy states of the system. In this way, TES measurements provide information on electronic, vibrational and in some cases, the rotational states of the collision partners.

1.5.4 Guided ion beam experiments

In guided ion beam experiments (GIB) [92, 109-111], the ion beam is confined by a cylindrical effective potential created by an octopolar radio frequency field that guides the ions through the collision cell. The guiding field ensures complete collection of both scattered primary and secondary ions. Over the years, the GIB technique has become the method of choice for determining integral charge-transfer cross-sections at hyperthermal energies, including the difficult hyperthermal energy range from thermal energies, traditionally studied by flowing afterglow or ICR techniques to 10 eV below which traditional ion beam experiments have substantial sensitivity losses.

The GIB method allows the use of inhomogeneous electric fields to confine and transport ions, creating the possibility of quenching ionic reagent internal excitation, as well as resulting in very efficient product ion collection over broad collision energy ranges. The technique is best suited to quantitative measurements of total cross-sections as a function of collision energy as well as accurate branching ratio measurements in a multichannel reactive system.

In general, the ion of interest is prepared by either UV photoionisation or electron ionisation. An octopole structure guides the primary ions through a collision region and on to a detector. The instrument may use a number of interchangeable sources, including in-line and crossed beam ionisers, an electron-ionisation source followed by a drift region through a high-pressure gas cell to thermalise excited states in the beam, and a surface ionisation source. Following mass selection and deceleration, the ion beam enters an electrostatic octopole around which is wrapped a gas cell for the collision partner. The reaction products are trapped by the inhomogeneous electric field where they are transported to a quadropole mass filter followed by a detector. A computer-controlled data acquisition system allows the measurements of the total cross-sections and branching ratios.

1.5.5 Crossed beam experiments

Early investigations of the collisional reactivity of molecular dications were performed at high (keV) collision energies in conventional mass spectrometers, thus proving the feasibility of dication beam experiments. In order to investigate collisions at more realistic collision energies, specialist spectrometers must be used. Thus crossed beam experiments have been developed. The crossed beam method [2, 7, 88, 89, 112-115] is ideally suited to the study of detailed dynamics of reactive collisions.

Generally, in these experiments the dication is produced by electron or photoionisation in a low-pressure ion source. The reactant molecules are formed into a collimated beam with a narrow velocity distribution, which are then allowed to intersect at right angles in a small region, in which the reactive encounter takes place. The ambient pressure is kept low ($<10^{-6}$ Torr) to ensure single collision conditions, *i.e.* to eliminate secondary collisions, as described in Chapter Five. A detector is then used to mass analyse the product ions formed. The detection system can be designed such that it can be rotated at various angles with respect to the beam system and thus measure the angular distribution of the various scattered species (reactants as well as products) in the lab coordinate system.

The crossed beam apparatus used to collect the data presented in this thesis will be described in detail in Chapter Three.

1.5.6 Velocity map imaging (VMI) experiments

In contrast to conventional time-of-flight methods, where kinetic energy release information is contained in the temporal structure in the arrival period of electrons or ions of a specific mass, velocity ion imaging techniques [116, 117] extract all information (kinetic energy and angular distributions) from the spatial appearance of a

two dimensional image. From an image, the full three-dimensional information can be reconstructed by means of an Abel inversion or back projection method [118].

The mapping of 3D distributions of charged particles onto a 2D detector is particularly dependent on the electrode configuration used to form the extracting electric field. The ion lens used for this purpose can be operated such that particles with the same initial velocity vector are mapped on the same point on the detector, irrespective of their initial distance from the ion lens axis.

One type of apparatus that uses VMI is set up to allow the study of unimolecular dissociation or bimolecular crossed beam reactions [116, 117]. The apparatus involves two pulsed molecular beams and a plane-polarised laser mounted mutually perpendicular to the beams. One of the molecular beams is aligned along the TOF axis, the other is 'off-axis' and the angle to the on-axis beam may be varied. Each beam consists of the desired photolyte seeded in helium and is injected into a vacuum chamber through a 1 mm skimmer. The skimmer reduces the beam of particles to those with very similar velocities so effusion is minimised and molecular collisions are almost eliminated. The on-axis beam then passes through a narrow aperture in a repelling electrode, along the TOF axis and towards the point of intersection with the photodissociation laser, and, if applicable, the off-axis beam for a bimolecular reaction. The reaction products are then extracted by another electrode, the nature of which is the key feature of the VMI technique since it maps particles with the same initial velocity vector on to the same point on the detector. The particles hit an imaging detector consisting of chevron microchannel plate (MCP) assembly and phosphor screen.

One of the disadvantages of the VMI technique when used with a crossed beam apparatus is that it requires a very confined reaction region—a criterion that is not fulfilled in a typical crossed beam apparatus where the reaction source region is large—in order to produce well resolved images on the detector. However, one major advantage of VMI over some other imaging techniques, such as the PSCO technique described in this thesis, is that the quality of the resolution of the images at the detector does not depend on the z velocities of the detected ions.

1.6 Conclusion

The properties of singly charged ions have been rigorously investigated, as described above, however, their doubly-charged relatives, dications, remain far less well characterised. Nevertheless, advances in new experimental techniques have promoted a growing interest in the study of doubly-charged ions. Despite this interest, the majority of work to date has focused on these species in an isolated environment. However, stimulated by the success of these experiments, consideration is now being given to the reactivity of dications with neutral collision partners and this thesis aims to present advances in this field. Results from a newly designed position-sensitive coincidence spectrometer will be discussed in the chapters to follow.

1.7 References

[1] Newson, K. A., Luc, S. M., Price, S. D., and Mason, N. J., 1995, *Int. J. Mass Spectrom. Ion Proc.* **148** (3) 203-213.

[2] Dolejsek, Z., Farnik, M., and Herman, Z., 1995, *Chem. Phys. Lett.* **235** (1-2) 99-104.

[3] Newson, K. A. and Price, S. D., 1997, *Chem. Phys. Lett.* **269** (1-2) 93-98.

[4] Price, S. D., Rogers, S. A., and Leone, S. R., 1993, *J. Chem. Phys.* **98** (12) 9455-9465.

[5] Rogers, S. A., Price, S. D., and Leone, S. R., 1993, *J. Chem. Phys.* **98** (1) 280-289.

[6] Manning, M., Price, S. D., and Leone, S. R., 1993, *J. Chem. Phys.* **99** (11) 8695-8704.

[7] Price, S. D., Manning, M., and Leone, S. R., 1994, *J. Am. Chem. Soc.* **116** (19) 8673-8680.

[8] Koslowski, H. R., *et al.*, 1991, *J. Phys. B: At. Mol. Opt. Phys.* **24** (23) 5023-5034.

[9] Reid, C. J., Ballantine, J. A., and Harris, F. M., 1989, *Int. J. Mass Spectrom. Ion Process.* **93** (1) 23-47.

[10] Lundqvist, M., *et al.*, 1996, *J. Phys. B-At. Mol. Opt. Phys.* **29** (3) 499-514.

[11] Zhou, X. D., Shukla, A. K., Tosh, R. E., and Futrell, J. H., 1997, *Int. J. Mass Spectrom. Ion Process.* **160** (1-3) 49-62.

[12] Ehbrecht, A., Mustafa, N., Ottinger, C., and Herman, Z., 1996, *J. Chem. Phys.* **105** (22) 9833-9846.

[13] Tsai, B. P. and Eland, J. H. D., 1980, *Int. J. Mass Spectrom. Ion Proc.* **36** 143.

[14] Curtis, D. M. and Eland, J. H. D., 1985, *Int. J. Mass Spectrom. Ion Proc.* **63** (2-3) 241-264.

[15] Eland, J. H. D., 1993, *Chem. Phys. Lett.* **203** (4) 353-362.

[16] Leach, S., Eland, J. H. D., and Price, S. D., 1989, *J. Phys. Chem.* **93** (22) 7575-7583.

[17] Millie, P., *et al.*, 1986, *J. Chem. Phys.* **84** (3) 1259-1269.

[18] Ruhl, E., Price, S. D., and Leach, S., 1989, *J. Phys. Chem.* **93** (17) 6312-6321.

[19] Masuoka, T. and Koyano, I., 1991, *J. Chem. Phys.* **95** (2) 909-917.

[20] Smith, D. and Adams, N. G., 1989, *J. Chem. Soc.: Faraday Trans.* **85** 1613-1630.

[21] Herbst, E., 1995, *Annu. Rev. Phys. Chem.* **46** 27-53.

[22] Smith, D. and Spanel, P., 1995, *Mass Spectrom. Rev.* **14** (4-5) 255-278.

[23] Ma, C., Bruce, M. R., and Bonham, R. A., 1991, *Phys. Rev. A.* **44** (5) 2921-2934.

[24] Bruce, M. R. and Bonham, R. A., 1993, *Int. J. Mass Spectrom. Ion Process.* **123** (2) 97-100.

[25] Calandra, P., O'Connor, C. S. S., and Price, S. D., 2000, *J. Chem. Phys.* **112** (24) 10821-10830.

[26] Harper, S., Calandra, P., and Price, S. D., 2001, *Phys. Chem. Chem. Phys.* **3** (5) 741-749.

[27] Ohishi, M., *et al.*, 1996, *Astrophys. J.* **471** (1) L61-L64.

[28] Prasad, S. and Furman, F. R., 1975, *J. Geophys. Res.* **80** 1360.

[29] Witasse, O., *et al.*, 2002, *Geophys. Res. Letts.* **29** (8) 1263.

[30] Bruce, M. R., Ma, C., and Bonham, R. A., 1992, *Chem. Phys. Lett.* **190** (3-4) 285-290.

[31] Lindsay, B. G., Mangan, M. A., Straub, H. C., and Stebbings, R. F., 2000, *J. Chem. Phys.* **112** (21) 9404-9410.

[32] Straub, H. C., Lindsay, B. G., Smith, K. A., and Stebbings, R. F., 1998, *J. Chem. Phys.* **108** (1) 109-116.

[33] Straub, H. C., Lindsay, B. G., Smith, K. A., and Stebbings, R. F., 1996, *J. Chem. Phys.* **105** (10) 4015-4022.

[34] Andersen, L. H., *et al.*, 1993, *Phys. Rev. Lett.* **71** (12) 1812-1815.

[35] Conrad, R., 1930, *Physik Z.* **31** 888.

[36] Larsson, M., 1993, *Comments At. Mol. Phys.* **29** 29-51.

[37] Mathur, D., 1993, *Phys. Rep.-Rev. Sec. Phys. Lett.* **225** (4) 193-272.

[38] Schroder, D. and Schwarz, H., 1999, *J. Phys. Chem. A.* **103** (37) 7385-7394.

[39] Senekowitsch, J., O'Neil, S., Knowles, P., and Werner, H. J., 1991, *J. Phys. Chem.* **95** (6) 2125-2127.

[40] Mathur, D., *et al.*, 1995, *J. Phys. B-At. Mol. Opt. Phys.* **28** (15) 3415-3426.

[41] Larsson, M., *et al.*, 1990, *J. Phys. B-At. Mol. Opt. Phys.* **23** (7) 1175-1195.

[42] Bennet, F. R. and McNab, I. R., 1996, *Chem. Phys. Lett.* **251** 405-412.

[43] Mullin, A. S., *et al.*, 1992, *J. Chem. Phys.* **96** (5) 3636-3648.

[44] Leach, S., Eland, J. H. D., and Price, S. D., 1989, *J. Phys. Chem.* **93** (22) 7583-7593.

[45] Senekowitsch, J. and O'Neil, S., 1991, *J. Chem. Phys.* **95** (3) 1847-1851.

[46] O'Connor, C. S. S., Jones, N. C., O'Neale, K., and Price, S. D., 1996, *Int. J. Mass Spectrom. Ion Process.* **154** (3) 203-211.

[47] Johnsen, R. and Biondi, M. A., 1979, *Phys. Rev. A.* **20** 289.

[48] Ben-Itzhak, I., 1993, *Phys. Rev. A.* **47** 289-294.

[49] Nicolaides, C. A., Chrysos, M., and Valtazanos, P., 1990, *J. Phys. B-At. Mol. Opt. Phys.* **23** (5) 791-800.

[50] Bauschlicher, C. W. and Rosi, M., 1990, *Chem. Phys. Lett.* **165** (6) 501-502.

[51] Bauschlicher, C. W. and Rosi, M., 1989, *Chem. Phys. Lett.* **159** (5-6) 485-488.

[52] Bruna, P. J. and Wright, J. S., 1990, *J. Chem. Phys.* **93** (4) 2617-2630.

[53] Hurley, A. C., 1962, *J. Mol. Spectrosc.* **9** 18.

[54] Hurley, A. C. and Maslen, V. W., 1961, *J. Chem. Phys.* **34** 1919.

[55] Masters, T. E. and Sarre, P. J., 1990, *J. Chem. Soc.-Faraday Trans.* **86** (11) 2005-2008.

[56] Ernstberger, B., Krause, H., Kiermeier, A., and Neusser, H. J., 1990, *J. Chem. Phys.* **92** (9) 5285-5296.

[57] Fang, Z. and Kwong, V. H. S., 1997, *Phys. Rev. A.* **55** (1) 440-443.

[58] Lablanquie, P., *et al.*, 1985, *J. Chem. Phys.* **82** (7) 2951-2960.

[59] Masuoka, T., 1993, *J. Chem. Phys.* **98** (9) 6989-6994.

[60] O'Connor, C. S. S., Tafadar, N., and Price, S. D., 1998, *J. Chem. Soc.: Faraday Trans.* **94** (13) 1797-1803.

[61] Becker, K. H. and Tarnovsky, V., 1995, *Plasma Sources Sci. Technol.* **4** (2) 307-315.

[62] O'Connor, C. S. and Price, S. D., 1998, *Int. J. Mass Spectrom.* **177** (2-3) 119-129.

[63] O'Connor, C. S. and Price, S. D., 1999, *Int. J. Mass Spectrom.* **184** (1) 11-23.

[64] O'Connor, C. S. S., Jones, N. C., and Price, S. D., 1997, *Chem. Phys.* **214** (1) 131-141.

[65] Lindsay, B. G., Rejoub, R., and Stebbings, R. F., 2001, *J. Chem. Phys.* **114** (22) 10225-10226.

[66] Sieglaff, D. R., Rejoub, R., Lindsay, B. G., and Stebbings, R. F., 2001, *J. Phys. B-At. Mol. Opt. Phys.* **34** (5) 799-809.

[67] Field, T. A. and Eland, J. H. D., 1999, *Chem. Phys. Lett.* **303** (1-2) 144-150.

[68] Hochlaf, M., *et al.*, 1998, *Chem. Phys.* **234** (1-3) 249-254.

[69] Bahati, E. M., *et al.*, 2001, *J. Phys. B-At. Mol. Opt. Phys.* **34** (9) 1757-1767.

[70] Jiao, C. Q., DeJoseph, C. A., and Garscadden, A., 2001, *J. Chem. Phys.* **114** (5) 2166-2172.

[71] Thissen, R., *et al.*, 1993, *J. Chem. Phys.* **99** (9) 6590-6599.

[72] Jones, J. D. C., *et al.*, 1981, *Chem. Phys. Lett.* **78** (1) 75-77.

[73] Price, S. D., 1997, *J. Chem. Soc.: Faraday Trans.* **93** (15) 2451-2460.

[74] Kamber, E. Y., Akgungor, K., Safvan, C. P., and Mathur, D., 1996, *Chem. Phys. Lett.* **258** (3-4) 336-341.

[75] Price, S. D., Lee, Y. Y., Manning, M., and Leone, S. R., 1995, *Chem. Phys.* **190** (1) 123-130.

[76] Hamdan, M. and Brenton, A. G., 1989, *J. Phys. B-At. Mol. Opt. Phys.* **22** (2) L45-L50.

[77] Price, S. D., Manning, M., and Leone, S. R., 1993, *Chem. Phys. Lett.* **214** (6) 553-558.

[78] Lee, Y. Y., *et al.*, 1997, *J. Chem. Phys.* **106** (19) 7981-7994.

[79] Herman, Z., Jonathan, P., Brenton, A. G., and Beynon, J. H., 1987, *Chem. Phys. Lett.* **141** (5) 433-442.

[80] Landau, L., 1932, *Phys. Z. Sowjetunion.* **2** 26.

[81] Zener, C., 1932, *Proc. R. Soc. London, Ser. A.* **137** 696.

[82] Smith, D., Adams, N G, Alge E, and Lindinger W, 1980, *J. Phys. B: At. Mol. Phys.* **13** 2787-99.

[83] Spears, K. G., Fehsenfeld, F. C., McFarland, M., and Ferguson, E., 1972, *J. Chem. Phys.* **56** 2562.

[84] Jones, J. D. C., *et al.*, 1980, *Chem. Phys. Lett.* **78** 75.

[85] Newson, K. A. and Price, S. D., 1998, *Chem. Phys. Lett.* **294** (1-3) 223-228.

[86] Tonkyn, R. and Weisshaar, J. C., 1986, *J. Am. Chem. Soc.* **108** (22) 7128-7130.

[87] Champkin, P., Kaltsoyannis, N., and Price, S. D., 1998, *Int. J. Mass Spectrom.* **172** (1-2) 57-69.

[88] Herman, Z., Zabka, J., Dolejsek, Z., and Farnik, M., 1999, *Int. J. Mass Spectrom.* **192** 191-203.

[89] Mrazek, L., *et al.*, 2000, *J. Phys. Chem. A.* **104** (31) 7294-7303.

[90] Tosi, P., *et al.*, 1999, *Phys. Rev. Lett.* **82** (2) 450-452.

[91] Wong, M. W. and Radom, L., 1989, *J. Phys. Chem.* **93** (17) 6303-6308.

[92] Lu, W. Y., Tosi, P., and Bassi, D., 2000, *J. Chem. Phys.* **112** (10) 4648-4651.

[93] Tosi, P., Lu, W. Y., Correale, R., and Bassi, D., 1999, *Chem. Phys. Lett.* **310** (1-2) 180-182.

[94] Newson, K. A. and Price, S. D., 1996, *Int. J. Mass Spectrom. Ion Proc.* **153** (2-3) 151-159.

[95] McCulloh, K. E. and Rosenstock, H. M., 1968, *J. Chem. Phys.* **48** 2084.

[96] McCulloh, K. E., Sharp, T. E., and Rosenstock, H. M., 1965, *J. Chem. Phys.* **42** 3501.

[97] Lago, A. F., Santos, A. C. F., and de Souza, G. G. B., 2004, *J. Chem. Phys.* **120** (20) 9547-9555.

[98] Erben, M. F., Romano, R. M., and Della Vedova, C. O., 2004, *J. Phys. Chem. A.* **108** (18) 3938-3946.

[99] Ruhl, E., *et al.*, 1991, *J. Chem. Phys.* **95** (9) 6544-6550.

[100] Masuoka, T., Okaji, A., and Kobayashi, A., 2002, *Int. J. Mass Spectrom.* **218** (1) 11-18.

[101] Griffiths, I. W., Parry, D. E., and Harris, F. M., 1998, *Chem. Phys.* **238** (1) 21-32.

[102] Ibrahim, K., *et al.*, 1992, *J. Chem. Phys.* **96** (3) 1931-1941.

[103] Hsieh, S. and Eland, J. H. D., 1997, *J. Phys. B: At. Mol. Opt. Phys.* **30** (20) 4515-4534.

[104] Eland, J. H. D., 1987, *Mol. Phys.* **61** (3) 725-745.

[105] Ruhl, E., *et al.*, 1994, *Z. Phys. D-Atoms Mol. Clusters.* **31** (4) 245-251.

[106] Brenton, A. G., 1995, *J. Mass Spectrom.* **30** (5) 657-665.

[107] Curtis, J. M. and Boyd, R. K., 1984, *J. Chem. Phys.* **80** (3) 1150-1161.

[108] Brenton, A. G., 2000, *Int. J. Mass Spectrom.* **200** (1-3) 403-422.

[109] Bassi, D., Tosi, P., and Schlogl, R., 1998, *J. Vac. Sci. Tech. a-Vacuum Surfaces and Films*. **16** (1) 114-122.

[110] Tosi, P., Correale, R., Lu, W. Y., and Bassi, D., 1999, *J. Chem. Phys.* **110** (9) 4276-4279.

[111] Lu, W. Y., Tosi, P., and Bassi, D., 1999, *J. Chem. Phys.* **111** (19) 8852-8856.

[112] Zabka, J. and Herman, Z., 1999, *Czech. J. Phys.* **49** (3) 373-382.

[113] Roithova, J., Zabka, J., Thissen, R., and Herman, Z., 2003, *Phys. Chem. Chem. Phys.* **5** (14) 2988-2995.

[114] Roithova, J., *et al.*, 2003, *J. Phys. Chem. A.* **107** (38) 7347-7354.

[115] Kearney, D. and Price, S. D., 2003, *Phys. Chem. Chem. Phys.* **5** (8) 1575-1583.

[116] Eppink, A. T. J. B. and Parker, D. H., 1997, *Rev. Sci. Instrum.* **68** (9) 3477-3484.

[117] Parker, D. H. and Eppink, A. T. J. B., 1997, *J. Chem. Phys.* **107** (7) 2357-2362.

[118] Whitaker, B. J. American Chemical Society Symposium Series, ed. A.G. Suits and R.E. Continetti. Vol. 770. 2001.

Chapter 2

Theoretical aspects of bimolecular collisions

2.1 Introduction

This chapter examines various theoretical aspects of gas-phase ionic reactivity that are of primary importance in understanding the experimental work presented in this thesis and explaining the subsequent results. As has been discussed in Chapter One, the motivation behind the design of the PSCO spectrometer is to determine the dynamics and energetics of the products formed in dication-neutral reactions. Therefore, the first section of this chapter introduces topics such as reaction dynamics and mechanisms. It includes a discussion of the frames of reference that are used to describe the processed data, showing the movement of the reactants and products with respect to the centre-of-mass velocity of the system v^c, and of the products to each other.

The reactions of dications with neutrals are often dominated by electron transfer reactivity. However, as will be shown in Chapters Seven to Nine, product formation from dication-neutral interactions does not occur exclusively by electron transfer but also by bond-forming interactions. As will be demonstrated later in this thesis, the PSCO experiment is extremely capable of determining the mechanistic pathways associated with these reactive processes. Therefore, several different reaction mechanisms that characterise these dication-neutral interactions are described and accompanied by the expected product angular distributions for each type of mechanistic pathway.

Having described the theory behind the dynamics of dication-neutral interactions, consideration is given to the properties of electronic transitions that may occur as a

result of such interactions. A discussion of the Landau-Zener model of electron transfer probability and its derivative, the reaction window theory, is presented. The final section in this chapter gives a description of the spin selection rules that determine whether an electronic transition is allowed.

2.2 Reaction dynamics

The topic of reaction dynamics is a branch of chemical kinetics that is concerned with describing the motion of reactants and products during a reactive collision, and the relationship between the details of the quantum states of the reactant and products. An understanding of the dynamic behaviour of a system at the molecular microscopic level is the key to the interpretation of the "macroscopic" kinetics of the bulk system.

The following sections of this chapter describe the areas of reaction dynamics that are of particular significance in the study of ion-molecule reactions. However, in order to understand the dynamics, it is first necessary to understand the factors that determine the relative (intermolecular) motion of the reactants. The topics discussed include the reaction cross-section σ, as a measure of the reaction probability, and factors that affect σ such as the impact parameter b and therefore determine the angular distributions of products formed from reactive collisions. The three frames of reference that are used to represent the motion of the reactants and products, the centre-of-mass, laboratory and internal frames, are also described.

2.2.1 The reaction rate constant

For a bimolecular reaction between species A and B, such as those studied using the PSCO instrument,

$$A + B \rightarrow C \qquad (2.1)$$

the rate of reaction is proportional to the reactant concentrations, [A] and [B], where the proportionality constant is the temperature dependent rate coefficient, $k(T)$, as defined by the rate law,

$$-\frac{d[A]}{dt} = -\frac{d[B]}{dt} = \frac{d[C]}{dt} = k(T)[A]^n[B]^m \qquad (2.2)$$

where n and m are the orders of the reaction. This rate coefficient $k(T)$ is a measure of the rate of depletion of the reactants or the rate of appearance of the products at a given temperature.

Most chemists determine a value of k for a reaction. However, to best consider reaction dynamics of gas-phase reactions it is necessary to consider individual collision events. To allow this, a detailed knowledge of the energetics of the individual collision partners is required. Hence, the temperature dependent rate constant is replaced with a velocity dependent rate constant $k(v)$

$$k(v) = v\sigma_r \qquad (2.3)$$

where v is the centre-of-mass relative velocity and σ_r the reaction cross-section as described in section 2.2.2 below.

2.2.2 Collision theory: impact parameter and reaction cross-section

For a reaction to take place, the reactant species must come into close enough contact to allow either an electron to transfer from one species to the other, or the necessary chemical rearrangement of the collision partners to take place. As a first approximation, the reactants may be considered as hard spheres of radii r_A and r_B that must collide before a reaction can take place. Therefore, the collision diameter d is the sum of the

radii of the two reactants, $r_A + r_B$, and the collision cross-section, the area within which the two reactants must approach each other for a collision to take place, is

$$\sigma = \pi d^2 . \qquad (2.4)$$

The physical size of the two reactants therefore determines the collision cross-section, which may also be expressed in terms of the mean free path λ and number density of the collision partner n_b.

$$\sigma = \frac{1}{\lambda n_b} \qquad (2.5)$$

From this relationship it can be seen that increasing the cross-section increases the chance of a collision occurring. This is quantitatively observed as a reduction in the mean free path λ, the distance the reactant travels before a collision takes place. In reality, molecules cannot be regarded as hard spheres since reactive collisions may require reactant molecules to approach in preferred configurations or orientations to enable electrons to rearrange and thus allow bonds to be broken and/or new bonds formed. Therefore, a reactive collision needs to be considered in a little more detail.

Two reactants (Figure 2.1) approaching each other with relative velocity v_r may be oriented so that they collide head on (Figure 2.1(i)), or with a 'glancing blow' (Figure 2.1(ii)). The impact parameter b of the collision quantifies the difference between these two encounters and is defined as the distance of closest approach of the reactants in the absence of any interactions between them. So for the situation described in Figure 2.1(i), $b = 0$ and for Figure 2.1(ii) $b > 0$.

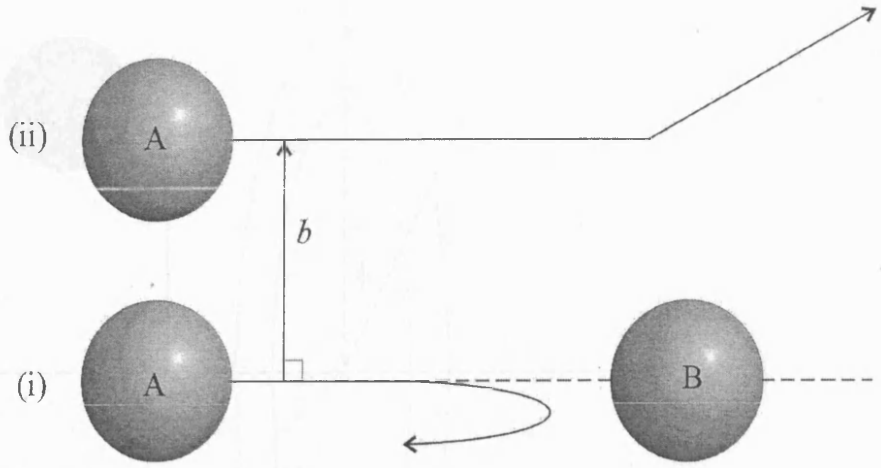

Figure 2.1 Definition of the impact parameter b. The reactants may approach each other and collide head on (i) or with a 'glancing blow'(ii).

Since it is not possible to control the magnitude of b in a reaction, the reaction cross-section must represent an average over collisions with a range of different impact parameters. Moreover, it is necessary to take into account that reactive collisions only make up a part of all collisions. Consequently, the collision cross-section σ_r must account for both the averaging over values of b (Figure 2.2) and the probability of reaction at a specified value of b, $P(b)$. This leads to the following expression for σ_r

$$\sigma_r = \int_0^{b_\infty} P(b) 2\pi b \, db \qquad (2.6)$$

For a collision where $P(b) = 1$, $b \leq b_{max}$ and $P(b) = 0$, $b > b_{max}$, the resulting cross-section is given by

$$\sigma_r = \pi b_{max}^2 . \qquad (2.7)$$

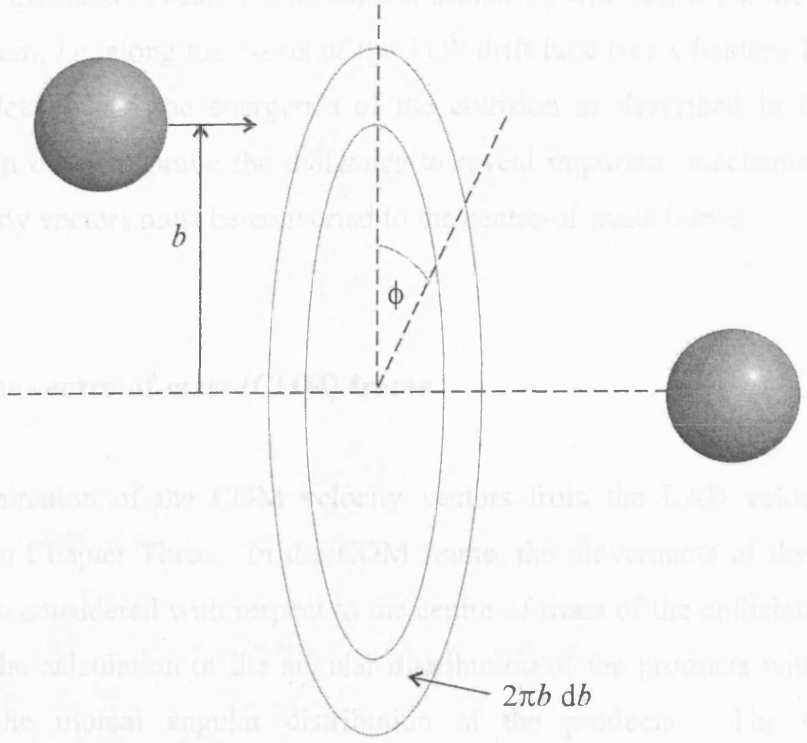

Figure 2.2 A schematic diagram of the average impact parameter where ϕ represents the azimuthal angle and ($2\pi b\ db$) the averaged impact parameter .

2.2.3 Frames of reference

In order to have a clear understanding of the data recorded from the PSCO experiment, both before and after its processing, three different frames of reference are used: the laboratory (LAB), centre-of-mass (COM) and internal (INT) frames. These are described below.

2.2.3.1 The laboratory frame

The LAB frame describes the movement of ions with respect to the axes of the PSCO instrument. The PSCO experiment records ionic flight times and positions from which

LAB frame velocity vectors for each ion may be calculated. From these data may be determined the mass of each ion, its angular scattering with respect to the velocity of the dication beam, *i.e.* along the *z*-axis of the TOF drift tube (see Chapters Three and Four for more detail), and the energetics of the collision as described in Chapter Three. However, in order to probe the dynamics to reveal important mechanistic details, the LAB velocity vectors must be converted to the centre-of-mass frame.

2.2.3.2 The centre-of-mass (COM) frame

The determination of the COM velocity vectors from the LAB velocity vectors is described in Chapter Three. In the COM frame, the movements of the reactants and products are considered with respect to the centre-of-mass of the collision system. This facilitates the calculation of the angular distribution of the products with respect to v^c and also the mutual angular distribution of the products. The COM angular distributions obtained using the positional and coincidence data gives a very clear and detailed insight into the mechanistic pathways of the studied reactions as will be demonstrated later in this thesis.

2.2.3.3 Converting the LAB frame to the COM frame

The experiment described in this thesis is a crossed beam apparatus that records product intensities resolved as a function of time and laboratory velocities and angles as described above. To obtain the desired angular distributions ϕ and mutual angles of scattering θ between the products, the lab velocities must be converted into the COM frame. The Newton diagram shown in Figure 2.3 illustrates the key features of this transformation, where 'v' is used to denote a lab velocity and 'w' to denote a velocity in the COM frame. The data analysis chapter (Chapter Four) gives a detailed description of the conversion algorithms.

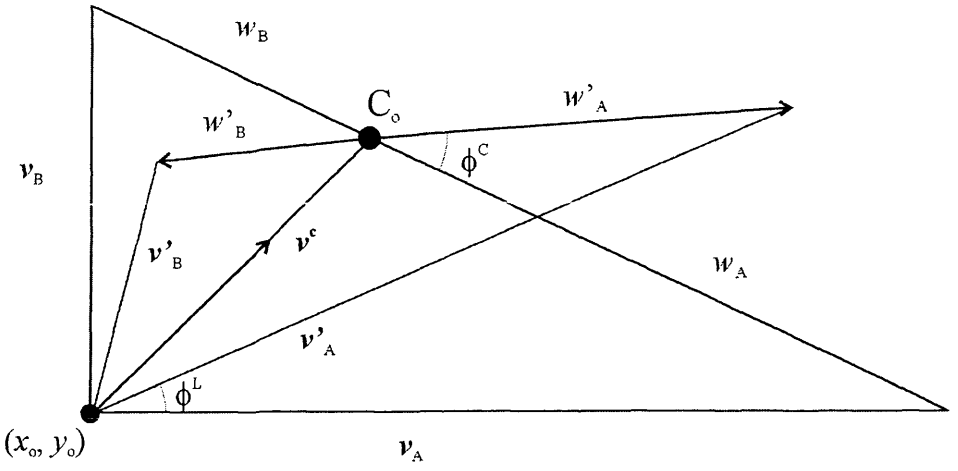

Figure 2.3 Velocity vector representation, 'Newton diagram', showing the relation between LAB and COM velocities. (x_o, y_o) corresponds to the collision point in the LAB frame. The LAB velocities of the reactants A and B are v_A (dication beam velocity) and v_B, respectively; the product LAB velocity vectors are v'_A and v'_B. The lab angle ϕ^L is measured relative to v_A. C_o corresponds to the centre-of-mass. The COM velocities of the reactants A and B are w_A (dication beam velocity) and w_B, respectively; the product COM velocity vectors are w'_A and w'_B. The COM angle ϕ^C is measured relative to v^c.

In the LAB frame, the centre-of-mass moves with a constant velocity v^c which is unchanged by the collision. In the COM frame the centre-of-mass is at rest and the angular scattering θ is the deflection of the relative velocity vector **v**'. The final velocity of a particle in the LAB frame is obtained by a vector addition of its final relative velocity with respect to v^c and the velocity of the COM itself. Chapter Four gives a full description of the derivation of v^c and the LAB and COM velocities.

2.2.3.4 COM frame vs. internal frame

As will be described in Chapter Four, the product velocity vectors in the centre-of-mass frame w provide dynamical information such as the COM scattering angles ϕ of the

products with respect to v^c (see Chapter Four for details). However, it is also very useful to describe the specific angular relationship between each of the products, the mutual angle θ. This can be done by plotting the scattering of two products with respect to the third: a scattering diagram in the 'internal frame' (Figure 2.4, Figure 2.5). Such a diagram shows how the velocity vectors of each of the products correlate with each other irrespective of their relation to the velocity of the centre-of-mass. As will be shown in Chapters Six to Nine, such internal frame scattering diagrams are a powerful probe of the dynamics of a reactive process providing very clear indications of the reaction mechanism.

2.3 Reaction mechanisms

A reaction mechanism describes the pathway by which product formation occurs. Product formation resulting from dication-neutral collisions may be characterised by one of two general mechanistic pathways, 'direct' (DI) or 'complex' (CX), which are described in more detail below. It is possible to discriminate between the two pathways by the studying the scattering of the products formed in each channel, as described below and in Chapters Five to Nine. Whether a given reaction favours DI or CX processes depends on the type of reaction considered and on the relative energies of the entrance and exit channels.

In general, a given collision system may include formation of a variety of products by both types of reaction mechanisms; however, one particular mechanistic pathway may dominate. For example, in a dication-neutral collision system, electron transfer reactions tend to be the more dominant pathway in comparison with bond-forming reactions. The ability of the PSCO instrument to image these dication-neutral interactions and hence reveal intricate dynamic and energetic details is demonstrated later in Chapters Six to Nine.

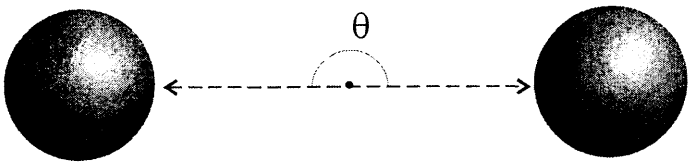

Figure 2.4 A schematic diagram of the angular relationship between two product species formed from the same event.

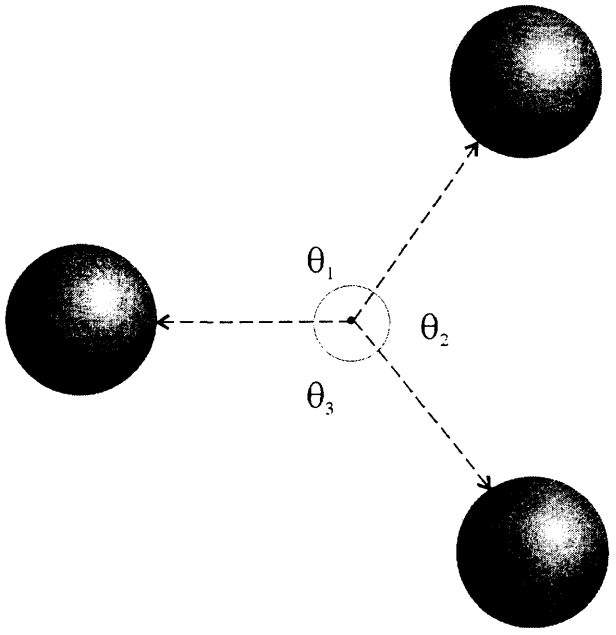

Figure 2.5 A schematic diagram of the angular relationship between three product species formed from the same event.

The collision systems studied and described in this thesis are two and three-body reactions. As explained in Chapter One, previous research in this area has only involved the detection of one of the two ionic products formed in a dication-neutral collision. This limits dynamical studies of dication-neutral collisions to events that form only two products, referred to here as a two-body reaction (Figure 2.4), where the dynamics of the undetected ion may be calculated by conservation of energy and momentum. The mutual angle between products formed in a two-body scenario would

be expected to be 180° as described in Figure 2.4. Detection of only one ion for collisions where three products are formed (Figure 2.5), termed a three-body event, leaves the full dynamics and energetics of a reaction inaccessible.

However, due to the capability of the PSCO instrument, where both ionic products from a reactive event are detected, it is possible to study three-body reactions (Figure 2.5). The dynamics of the third body, a neutral species, may be calculated by conservation of momentum from the dynamics of the two detected ions. In a three-body scenario, the magnitude of each of the mutual angles between each of the products in the internal frame, θ_1, θ_2 and θ_3, will be determined from the COM velocity vectors of the products w subsequent to their formation (see Chapter Four for more detail).

The following sections describe the DI and CX mechanisms in more detail and the angular scattering of the products that might be expected in each case.

2.3.1 Direct reaction mechanism

A direct reaction mechanism features a straightforward interaction (2.8) that forms the products C and D in a single step.

$$A + B \rightarrow C + D \qquad (2.8)$$

For dication-neutral interactions, this direct mechanism may characterise two types of interactions. The first is an electron transfer reaction forming two cations, termed a 'fly-by' interaction where no bonds are formed. The second is a chemical reaction where a bond is formed resulting in two singly charged ions, such as a reaction involving hydride transfer.

2.3.1.1 Angular scattering

Angular scattering data is plotted for each collision system and the method of plotting an angular scattering diagram (ASD) is described in detail in Chapter Four. Briefly, an ASD is a polar (r, ϕ) histogram where the radial co-ordinate r is the magnitude of the velocity of an ion in the COM frame $|w(i)|$, and the angular co-ordinate ϕ ($0^\circ \leq \phi \leq 180^\circ$) is the angle of $w(i)$ with respect to the velocity of the COM of the collision system v^c. Hence, the scattering of an ion may be described in one of three different ways: 'forward', 'sideways' or 'backward' scattered. An ion scattered in a direction close to the COM velocity v^c (*i.e.* in the same direction as the dication beam) is termed 'forward' scattered; an ion scattered in the opposite direction to the dication beam, *i.e.* with a scattering angle close to 180° with respect to v^c, is termed 'backward' scattered. Any ions scattered perpendicularly to the direction of v^c are 'sideways' scattered.

For a direct mechanism forming two products in a dication-neutral collision system, such as a non-dissociative electron transfer (NDET) reaction, strong forward and backward scattering of the two ionic products, C^+ and D^+, would be expected. From conservation of momentum, the angle between the products must be 180°. Such scattering has been frequently observed in NDET collision systems and will be discussed in Chapters Six and Eight. In some cases, an electron transfer reaction may then be followed by dissociation of one (or both) of the products, however, the initial separation of the products, C^+ and D^+, before any dissociation occurs, will have the same forward/backward scattering trend described above. The scattering of products D^+ and E^+, formed by dissociation of C^+, will be about the limiting velocity of product C^+ before it dissociated (Chapter Eight).

2.3.2 Complex formation

The angular scattering of products resulting from a chemical interaction, *i.e.* a bond-forming (BF) mechanism, usually differs markedly to the scattering observed for a

direct mechanism, since the BF mechanism generally involves the formation of a complex intermediate. However, as described in section 2.3.1 and also in Chapter Nine, bond-forming can also occur *via* a direct mechanism (*e.g.* hydride transfer). The timescale of interactions that result in product formation *via* an intermediate is usually of the order of $> 10^{-12}$ s, compared to a direct mechanism interaction time of $> 10^{-13}$ s. The prolonged interaction time involved in forming an intermediate allows the rearrangement of bonds and the formation of new bonds. Therefore, complex formation is often a feature of chemical reactions in the gas-phase. The relatively long lifetimes of these complex intermediates are of the same order as the rotation period ($\sim 10^{-12}$ s) of a typical complex and hence the complex may undergo several rotations before it dissociates.

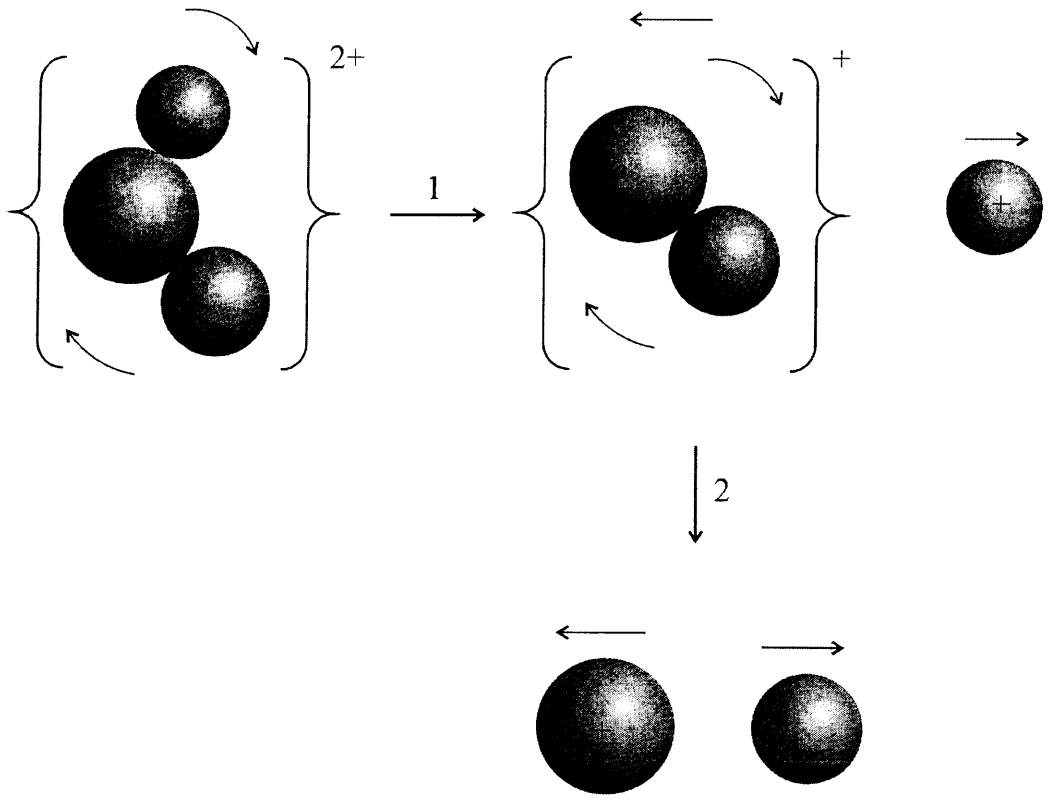

Figure 2.6 A schematic diagram showing the sequential dissociation of a rotating complex formed by a reactive dication-neutral collision.

A complex may dissociate *via* one of two pathways. The first pathway involves the primary loss of one species from the complex (Eq. 2.9)—in context of this thesis the complex will be doubly charged—followed by dissociation of the remaining singly charged complex (Eq. 2.10), termed a 'sequential' dissociation (Figure 2.6). In detail, the first leaving party C^+ will be scattered isotropically with respect to both $\boldsymbol{v}^c$ and to the other products D^+ and E due to the rotation of the doubly charged complex. The formation of the D^+ and E *via* dissociation of the singly charged complex will result in a fixed angle of scattering between D^+ and E.

$$[\text{Complex}]^{2+} \rightarrow C^+ + [\text{Complex}]^+ \qquad (2.9)$$

$$[\text{Complex}]^+ \rightarrow D^+ + E \qquad (2.10)$$

The alternative to a sequential dissociation of a complex is termed a 'concerted' dissociation, where C^+, D^+ and E are formed simultaneously (Eq. 2.11). The scattering of these products may be isotropic with respect to $\boldsymbol{v}^c$ but will be fixed with respect to each other in the internal frame.

$$[\text{Complex}]^{2+} \rightarrow C^+ + D^+ + E \qquad (2.11)$$

2.4 "Reaction Window" theory and the Landau-Zener model

2.4.1 The Landau-Zener model

The Landau-Zener (LZ) model [1, 2] is a semi-classical description of electron transfer reactivity for purely atomic collision systems. The model determines the probability of electron transfer between given reactant and product states and considers the reaction as taking place at a crossing, having an interspecies separation R_c (Figure 2.7), of two

diabatic potential curves corresponding to an attractive reactant potential and a repulsive product potential. As the interspecies separation R_c decreases, the coupling of the two surfaces increases.

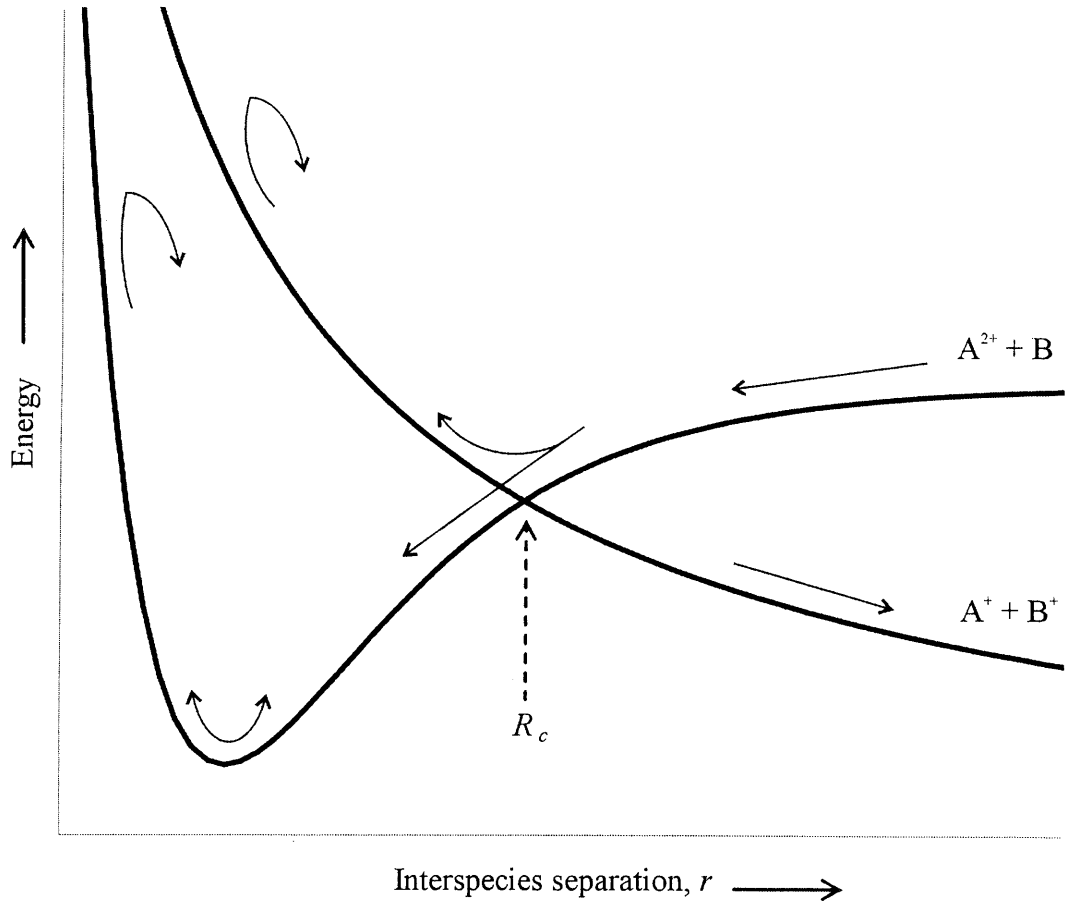

Figure 2.7 The attractive reactant and repulsive product potential surfaces in the Landau-Zener model giving R_c, the interspecies separation at which a reaction is most likely to take place.

2.4.2 'Reaction window' theory

The 'reaction window' (RW) theory [3] was formulated for dication-neutral reactions, based on the LZ model, taking into account the extent of the coupling between the reactant and product surfaces to give the window of interspecies separation at which electron transfer may take place, termed a 'reaction window'. In the RW theory an electron transfer occurs at the crossing of two simple electrostatic diabatic potential energy surfaces corresponding to the reactants (A^{2+} + B) and products (C^{+} + D^{+}).

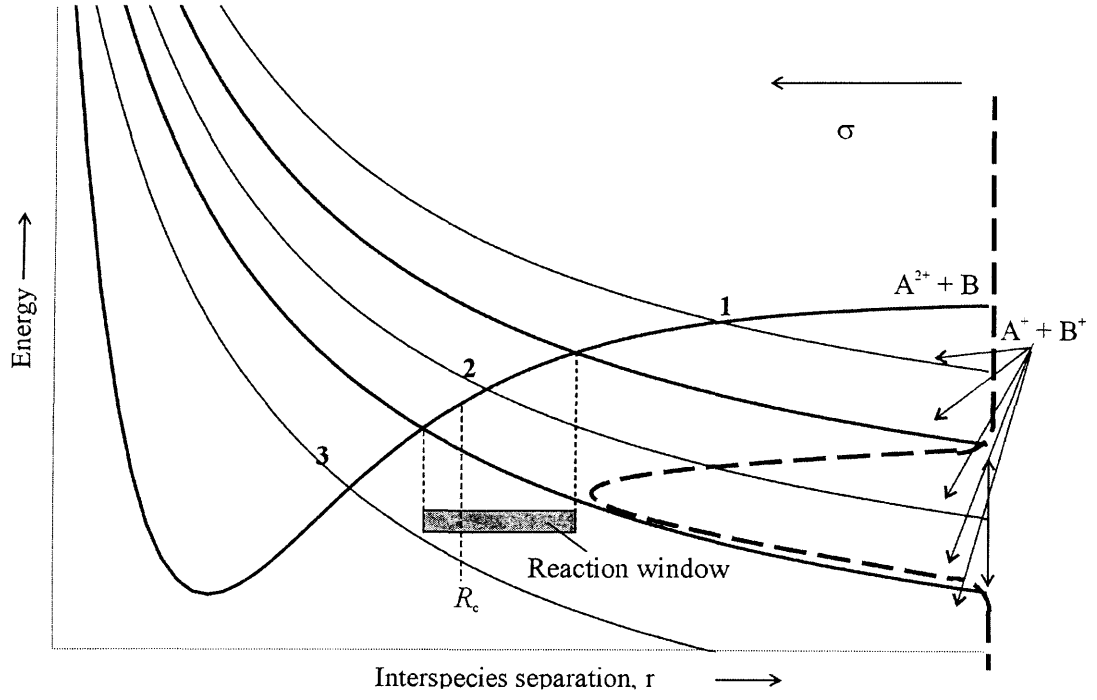

Figure 2.8 Schematics of potential energy curves for the reaction A^{2+} + B → A^{+} + B^{+}, indicating R_c and σ.

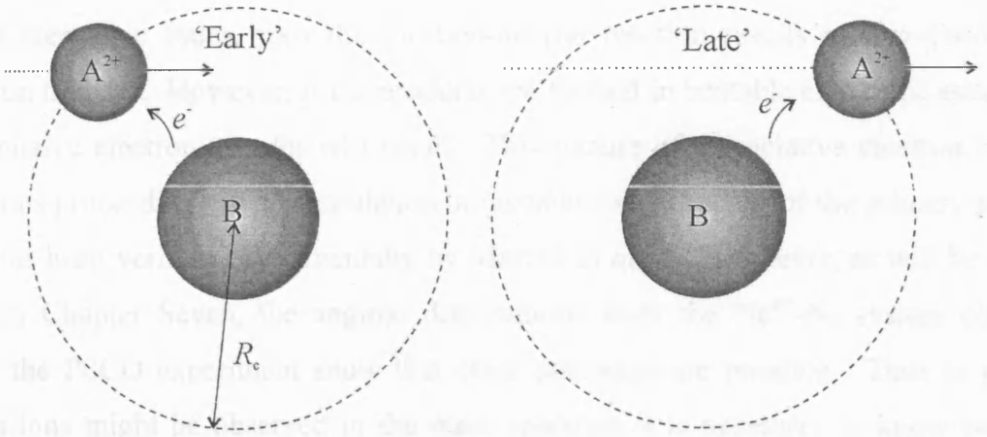

Figure 2.9 A schematic diagram indicating the two instances at which curve-crossing may take place, termed 'early' and 'late' electron transfer respectively.

The interaction between the reactants is modelled as a simple polarisation attraction potential and the product potential is represented as purely repulsive. The interspecies separation at the crossing of these two potential energy curves, the curve-crossing radius R_c, then determines the probability of electron transfer (Figure 2.8). If the curve-crossing is at a large interspecies separation, then there is little interaction between the reactant and product states and the probability for electron transfer is small. Conversely, if the curve-crossing is at small interspecies separation then the two states are strongly coupled and there is a high likelihood of electron transfer on one pass through the crossing. However, if a reaction is to take place the system must pass through the curve-crossing twice, once on approach and once on separation (Figure 2.9).

Hence, for small crossing radii the net probability of electron transfer is small even though the probability of electron transfer on one pass through the crossing is large. Between these two behavioural limits, there is a range of interspecies separations (the reaction window ~3-6 Å) where the coupling is neither too weak nor too strong and effective electron transfer can result.

The cross-sections (Figure 2.8) for the population of the different product electronic states can be calculated using this reaction window model. If the products are formed in stable electronic states, then the dication-neutral reaction results in non-dissociative electron transfer. However, if the products are formed in unstable electronic states then dissociative electron transfer will result. This picture of dissociative electron transfer reactions proceeding *via* the population of unstable excited states of the primary product ions has been verified experimentally by Mrazek *et al* [4]. However, as will be shown later in Chapter Seven, the angular distributions from the Ne^{2+}-N_2 system obtained using the PSCO experiment show that other pathways are possible. Thus to predict which ions might be observed in the mass spectrum it is necessary to know both the probability for populating the available A^+ and B^+ electronic states and also the stability of these electronic states.

The algorithm for the reaction window calculations [3] is now described. Briefly, if δ is the probability that there is no change in electronic state (*i.e.* remaining on the diabatic curve through the crossing), then the overall probability P that an electron transfer reaction will occur is given by

$$P = 2\delta(1-\delta) \qquad (2.12)$$

The value of δ can be evaluated using the magnitude of the difference in the gradients of the two potential curves at the crossing radius $|V_1' - V_2'|$, the relative radial velocity at the crossing v_b, which can be calculated for a given impact parameter from the collision energy, the interaction potential (described in detail in Chapter Four), and the electronic coupling matrix H_{12}. H_{12} is evaluated from the ionisation potentials of the reactants and the curve-crossing radius using the semi-empirical formula of Olson [5].

$$\delta = \exp\left[\frac{-\pi|H_{12}|^2}{2\hbar|V_1' - V_2'|v_b}\right] \qquad (2.13)$$

For reactions of atomic dications with neutral atoms, approximate potential energy surfaces and hence the curve-crossing radius R_c, may be calculated using the electrostatic equations

$$V_1 = \frac{-Z^2 e^2 \alpha}{2r^4} + \Delta E \qquad (2.14)$$

$$V_2 = \frac{e^2}{r} \qquad (2.15)$$

where V_2 is the potential of the reactant channel given by the sum of the reaction exoergicity (ΔE) and a polarization function where α is the polarisibility of the rare gas and Z is the charge on the ion, *i.e.* $Z = 2$. The quantity V_2 is the potential function for the product channel given by the Coulombic repulsion of the product ions, A^+ and B^+. Solving these equations for $V_1 = V_2$ gives the curve-crossing radius R_c and differentiating these functions at R_c gives the relative slopes of these two diabatic curves.

If the curve-crossing R_c is at large interspecies separation, δ will be effectively unity as $|H_{12}|$ is small. Whilst if the curve-crossing is at small interspecies separation δ will approach zero as $|H_{12}|$ is large. Between these two limits, in the reaction window, P can approach the Landau-Zener maximum of 0.5.

The probability of an electron transfer reaction P is a function of the radial collision velocity v_b, which is in turn a function of the collision energy and impact parameter b. At a given collision energy, it is possible to evaluate the electron transfer cross-section σ_{calc} by integrating P over b from $b = 0$ to b_{max} (the maximum value of b for which the collision system reaches the crossing radius):

$$\sigma_{calc} = \int_0^{b_{max}} 2\pi b P(b) \mathrm{d}b \,. \qquad (2.16)$$

2.4.3 Summary

The LZ model and 'reaction window' theory have been used successfully to model purely atomic collision systems. However, they do not encompass certain other subtleties of atom-molecule reactions. Atom-atom collisions have purely isotropic (spherically symmetric) potential energy surfaces entailing the incorporation of solely radially dependent terms when calculating the electron transfer probability. In contrast, anisotropic potentials lead to an angular dependence of both the crossing radii and the coupling matrix elements. Therefore, it might be expected that for atom-molecule systems the application of the LZ based reaction window theory would fail. Predictions obtained using the RW model will be compared with results recorded using the PSCO TOF experiment for both atom-atom and atom-molecule systems later on in this thesis.

2.5 Spin selection rules

The PSCO experiment [6] involves the detection of pairs of product ions formed in individual dication-neutral collisions and allows the extraction of the velocity vectors of each of these product ions for each reactive encounter detected. From these LAB frame velocity vectors, the exoergicity of the dication-neutral interaction can be calculated as explained in Chapter Four. Hence, the electronic states of the products and reactants may be assigned. To assign the electronic states correctly it is necessary to know which electronic transitions are allowed, *i.e.* can occur, between the two reactants and which are forbidden, *i.e.* are likely only to occur with low reaction cross-section.

2.5.1.1 Allowed or forbidden?

To assign exoergicity signals, recorded for a reactive collision, to the population of particular electronic states, it is first necessary to determine all the possible states of reactants and products accessible at a particular collision energy E^c, and, hence, the

expected exoergicities for electronic transitions that form the experimentally observed products. By comparing the experimental exoergicity signals with the expected exoergicities, some assignments of the exoergicity signals to population of particular product states may be made. Secondly, selection rules may be applied to determine whether a transition is allowed or forbidden. A selection rule is a statement that determines which transitions are allowed and is derived (for atoms) by identifying the transitions that conserve angular momentum when energy transfer occurs between reactants and products in a collision. Each atom or molecule has a 'term symbol' that describes the properties of its orbitals.

2.5.2 State-selectivity in electron transfer reactions

The PSCO experiment is not designed to actively state-select either the reactants or products. However, a certain amount of natural state selection does take place due to using a fixed electron ionisation energy that affects which states of a particular dication may be present in the ion beam. Instances of this unintended state-selection are evident for the Ne^{2+}-Ar collision system as described in Chapter Six.

2.5.2.1 Dominance of one electron transitions

During a single collision, the transition of one electron is much more likely than the transition of several electrons, since the Coulomb repulsion between two singly charged ions formed following electron transfer (in a dication-neutral reaction) will cause a rapid increase in the interspecies separation of the products, making a second electronic transition extremely unlikely. Although this statement does not hold true at very low impact energies, it does apply for impact velocities above 10^7 cm s^{-1}. At such velocities, the interaction time between the two reactants is short enough to inhibit effectively more electron transitions. This has been demonstrated for various cases:

double electron capture in C^{4+}-He [14], electron capture with rearrangement in Ne^{2+}-Xe [15] and transfer ionisation in He^{2+}-Ar [16].

2.5.2.1.1 Core conservation

A very significant effect of the dominance of one-electron transitions is the approximate conservation of the initial ion configuration during single electron transfer. Only for collisions at quite small impact parameters, which do not generally lead to a significant contribution to the cross-section for geometrical reasons, will a disturbance of the respective ion cores become likely [17]. Therefore, final states of the projectile particle are probably formed with the same core configuration as the primary reactant ion. This provides a very important selection rule for initial ion state-selective collision studies [18, 19].

2.5.2.1.2 Statistical population of multiplet states in secondary reaction products

If the energy splitting between various *l*-states of the same principal quantum number *n* is sufficiently small, they can be assumed as degenerate during collisions resulting in single electron transfer. In such cases spin-orbit recoupling after electron transfer into a certain (*n*, *l*) will lead to statistical population of various *l*-states within a multiplet [20]. This has been determined experimentally by Gaily *et al* [21]. If the energetics for population of different multiplet states from a common initial state are similar, this also results in a statistical distribution among all the final states.

2.5.2.1.3 Wigner's spin rule

If the quasimolecule being transiently formed by the collision of reactant molecules is well described by *LS* coupling, then according to Wigner's rule [22] its initial and final total spins should agree. Relevant experimental investigations have shown that this

holds for light collision partners only [23], and only if relatively large impact parameters (>1 Å) are involved [24]. In general, Wigner's spin rule is not particularly state-selective because a given total spin can be composed of different spin rules of the secondary collision products.

2.6 Conclusion

All the subjects discussed in this chapter are important in understanding the experimental studies of dication-neutral reactions. The PSCO spectrometer described in this thesis exploits the ability to detect two ions in coincidence from one dication-neutral reactive event, to allow the extraction of the dynamics and energetics of each reactive event. The dynamical information may then be used to predict the reaction mechanisms for each reactive channel observed, as will be described in the following chapters.

2.7 References

[1] Landau, L., 1932, *Phys. Z. Sowjetunion.* **2** 26.

[2] Zener, C., 1932, *Proc. R. Soc. London, Ser. A.* **137** 696.

[3] Rogers, S. A., Price, S. D., and Leone, S. R., 1993, *J. Chem. Phys.* **98** (1) 280-289.

[4] Mrazek, L., *et al.*, 2000, *J. Phys. Chem. A.* **104** (31) 7294-7303.

[5] Olson, R. E., Smith, F. T., and Bauer, E., 1971, *Appl. Opt.* **10** 1848.

[6] Hu, W. P., Harper, S. M., and Price, S. D., 2002, *Meas. Sci. Technol.* **13** (10) 1512-1522.

[7] Winter, H., 1983, *Phys. Scr.* **T3** 159-162.

[8] Sato, J. and Moore, J. H., 1979, *Phys. Rev. A.* **19** 495.

[9] Zwally, J. H. and Koopman, D. W., 1970, *Phys. Rev. A.* **2** 1851.

[10] Mann, R., Folkmann, F., and Beyer, H. F., 1981, *J. Phys. B-At. Mol. Opt. Phys.* **14** (7) 1161-1181.

[11] Knudsen, H., Haugen, H. K., and Hvelplund, P., 1981, *Phys. Rev. A.* **23** (2) 597-610.

[12] Ryufuku, H., Sasaki, K., and Watanabe, T., 1980, *Phys. Rev. A.* **21** 745.

[13] Grozdanov, T. P., 1980, *J. Phys. B: At. Mol. Phys.* **13** 3835.

[14] Crandall, D. H., Olson, R. E., Shipsey, E. J., and Browne, J. C., 1976, *Phys. Rev. Lett.* **36** 858.

[15] Rille, E. and Winter, H., 1980, *J. Phys. B: At. Mol. Phys.*, (13) L531.

[16] Groh, W., Schlachter, A. S., Muller, A., and Salzborn, E., 1982, *J. Phys. B: At. Mol. Phys.* **15** (6) L207-L212.

[17] Ice, G. E. and Olson, R. E., 1975, *Phys. Rev. A.* **11** 111.

[18] Matsumoto, A., Ohtani, S., and Iwai, T., 1982, *J. Phys. B-At. Mol. Opt. Phys.* **15** (12) 1871-1881.

[19] Brazuk, A. and Winter, H., 1982, *J. Phys. B: At. Mol. Opt. Phys.* **15** (14) 2233-2244.

[20] Matsumoto, A., *et al.*, 1980, *J. Phys. Soc. Japan.* **48** 575.

[21] Gaily, T. D., Coggiola, M. J., Peterson, R. J., and Gillen, K. T., 1980, *Rev. Sci. Instr.* **51** 1168.

[22] Wigner, E., 1927, *Nachr. Akad. Wiss. Gottingen, Math.-Physik.* **K1** (IIa) 375.

[23] Moore, J. H., 1974, *Phys. Rev. A.* **10** 724.

[24] Myers, G. D., Ambrose, J. G., James, P. B., and Leventhal, J. J., 1978, *Phys. Rev. A.* **18** 85.

[1] Landau, L., 1932, *Phys. Z. Sowjetunion.* **2** 26.

[2] Zener, C., 1932, *Proc. R. Soc. London, Ser. A.* **137** 696.

[3] Rogers, S. A., Price, S. D., and Leone, S. R., 1993, *J. Chem. Phys.* **98** (1) 280-289.

[4] Mrazek, L., *et al.*, 2000, *J. Phys. Chem. A.* **104** (31) 7294-7303.

[5] Olson, R. E., Smith, F. T., and Bauer, E., 1971, *Appl. Opt.* **10** 1848.

[6] Hu, W. P., Harper, S. M., and Price, S. D., 2002, *Meas. Sci. Technol.* **13** (10) 1512-1522.

[7] Winter, H., 1983, *Phys. Scr.* **T3** 159-162.

[8] Sato, J. and Moore, J. H., 1979, *Phys. Rev. A.* **19** 495.

[9] Zwally, J. H. and Koopman, D. W., 1970, *Phys. Rev. A.* **2** 1851.

[10] Mann, R., Folkmann, F., and Beyer, H. F., 1981, *J. Phys. B-At. Mol. Opt. Phys.* **14** (7) 1161-1181.

[11] Knudsen, H., Haugen, H. K., and Hvelplund, P., 1981, *Phys. Rev. A.* **23** (2) 597-610.

[12] Ryufuku, H., Sasaki, K., and Watanabe, T., 1980, *Phys. Rev. A.* **21** 745.

[13] Grozdanov, T. P., 1980, *J. Phys. B: At. Mol. Phys.* **13** 3835.

[14] Crandall, D. H., Olson, R. E., Shipsey, E. J., and Browne, J. C., 1976, *Phys. Rev. Lett.* **36** 858.

[15] Rille, E. and Winter, H., 1980, *J. Phys. B: At. Mol. Phys.*, (13) L531.

[16] Groh, W., Schlachter, A. S., Muller, A., and Salzborn, E., 1982, *J. Phys. B: At. Mol. Phys.* **15** (6) L207-L212.

[17] Ice, G. E. and Olson, R. E., 1975, *Phys. Rev. A.* **11** 111.

[18] Matsumoto, A., Ohtani, S., and Iwai, T., 1982, *J. Phys. B-At. Mol. Opt. Phys.* **15** (12) 1871-1881.

[19] Brazuk, A. and Winter, H., 1982, *J. Phys. B: At. Mol. Opt. Phys.* **15** (14) 2233-2244.

[20] Matsumoto, A., *et al.*, 1980, *J. Phys. Soc. Japan.* **48** 575.

[21] Gaily, T. D., Coggiola, M. J., Peterson, R. J., and Gillen, K. T., 1980, *Rev. Sci. Instr.* **51** 1168.

[22] Wigner, E., 1927, *Nachr. Akad. Wiss. Gottingen, Math.-Physik.* **K1** (IIa) 375.

[23] Moore, J. H., 1974, *Phys. Rev. A.* **10** 724.

[24] Myers, G. D., Ambrose, J. G., James, P. B., and Leventhal, J. J., 1978, *Phys. Rev. A.* **18** 85.

Chapter 3

Experimental techniques and apparatus

3.1 Introduction

As discussed in Chapter One, this thesis reports the results of experimental work to study the dynamics and kinematics of gas phase dication-neutral reactions. Over the last decade, experimental techniques designed to study the properties of dications have revealed information about their formation, reactivity and dissociation as described in Chapter One. The position-sensitive coincidence (PSCO) experiment described in this thesis provides a much more detailed insight into the motion of the products subsequent to the collisions of dications with neutral atoms or molecules, respectively, together with energetics for the reactants and products [1, 2].

This chapter will give a description of the development of the PSCO time-of-flight (TOF) mass spectrometer that has been designed to allow the coincident detection of pairs of ions from each dication-neutral reactive event. Each component of the apparatus is described in detail. The PSCO spectrometer records flight times and positions for each ion arrival; the processing and accumulation of these data are also described.

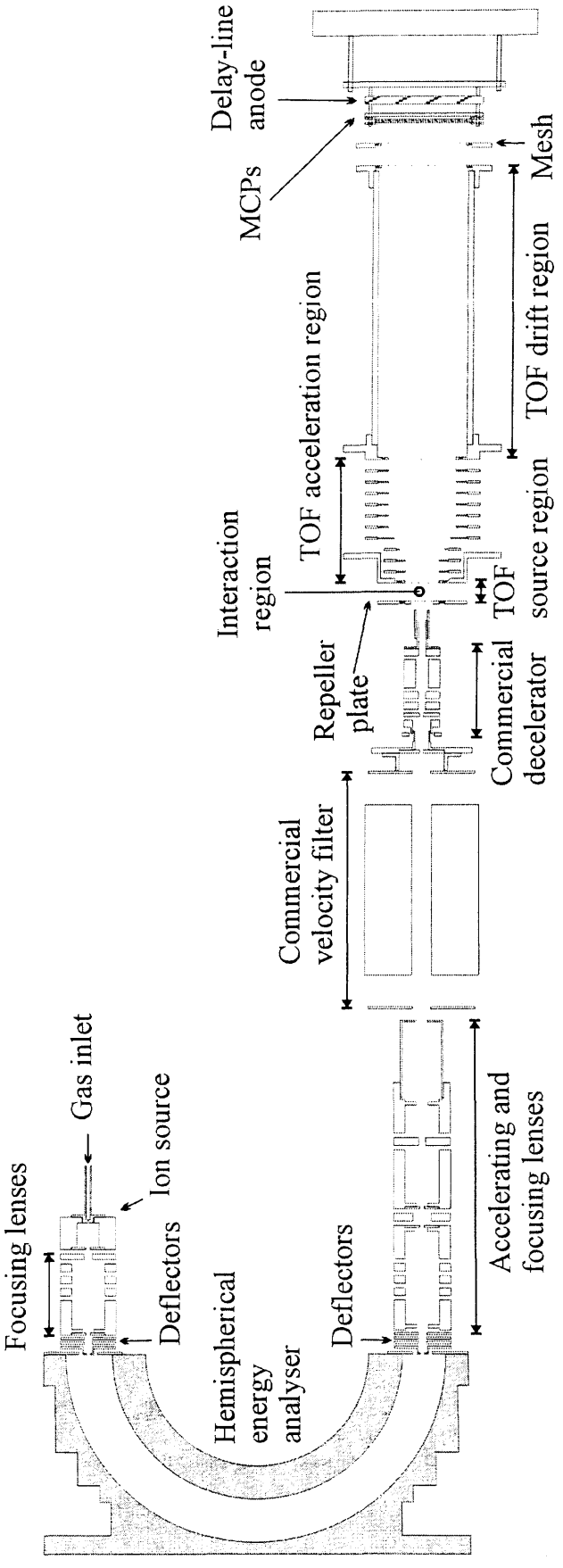

Figure 3.1 A schematic diagram of the experimental arrangement

3.2 Overview

The primary goal of the PSCO experiment is to detect both the singly charged ions formed in electron transfer and bond forming dication-neutral collisions, and then probe the dynamics and energetics of each collision using the position-sensitive data and flight times recorded for each ion.

Briefly, a beam of ions is formed by electron ionisation of a neutral precursor gas. These ions are then mass selected, by successive energy and velocity selection, to form a beam of dications (Figure 3.1). The dications are introduced into the source region of the TOF mass spectrometer where they interact with a neutral collision gas. Any ions in the reaction source region are then accelerated into the TOF drift tube and subsequently impact on the microchannel plate (MCP) of the detector. The flight times of all detected ions are recorded and a dual delay-line anode electronically encodes their positions. The recorded and encoded data is then amplified, discriminated and read by a fast time-to-digital converter (TDC) before being passed to a stand alone PC for storage, offline processing and data analysis.

3.3 Vacuum system

The vacuum system consists of three stainless steel chambers mounted on an aluminium frame (Figure 3.2), each pumped by a water-cooled Diffstak diffusion pump maintaining the background pressure below 2 x 10^{-7} Torr. A rotary pump with a fore-line trap backs each diffusion pump. The first diffusion pump is positioned beneath the largest of the three chambers, the ion source chamber, containing the ion source and the hemispherical energy analyser, the second pumps the reaction chamber and the third the detection chamber. Three ion gauges, controlled by an Edwards Active Ion Gauge Controller, monitor the pressures in each of the chambers. The backing pressure is monitored at each rotary pump by an (Edwards) Active Pirani gauge.

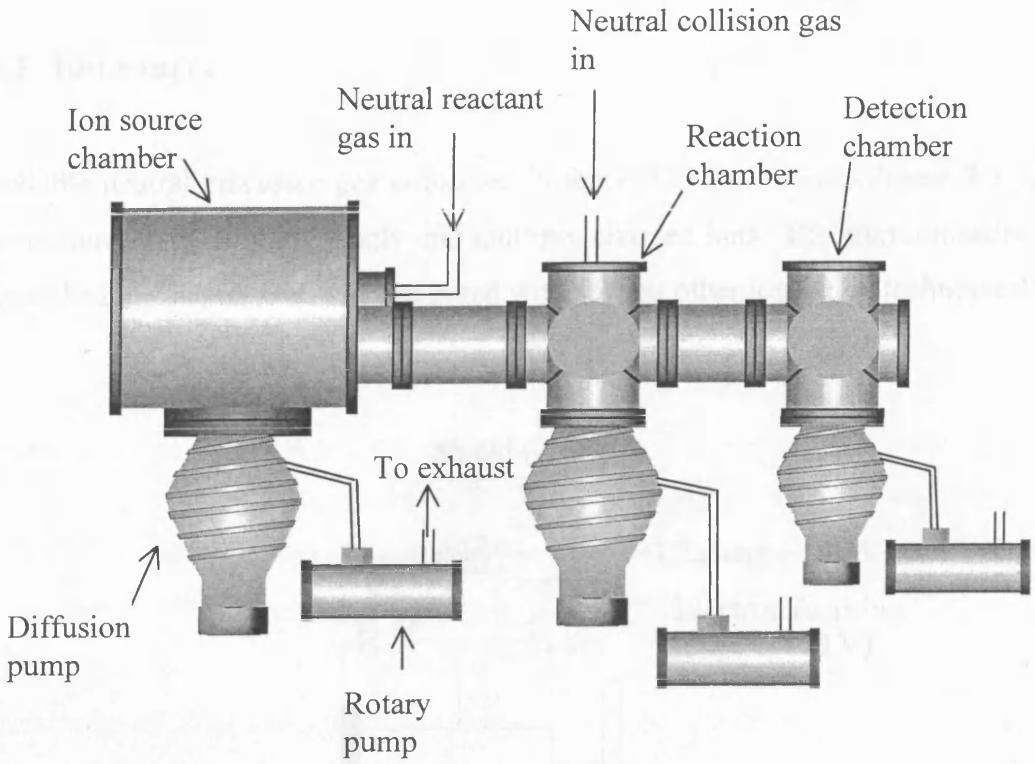

Figure 3.2 A schematic diagram of the three main chambers pumped by diffusion pumps that are backed by rotary pumps.

The vacuum system is protected by two relays. The first uses a relay switch on the ion gauge and turns off the ion gauge and voltages to the detector, repeller plate, Wein filter and electron gun if the pressure in the machine rises above 1×10^{-5} Torr. A second relay system is set to turn the diffusion pumps off if the backing pressure or the temperature of the diffusion pumps gets too high. When this second relay system is triggered, the first is automatically triggered.

3.4 Ion source chamber

3.4.1 Ion source

A suitable neutral precursor gas is ionised in the PSCO ion source (Figure 3.3)using electron ionisation, forming singly and multiply charged ions. Electron ionisation (EI) is described in Chapter One and compared with several other ionisation techniques.

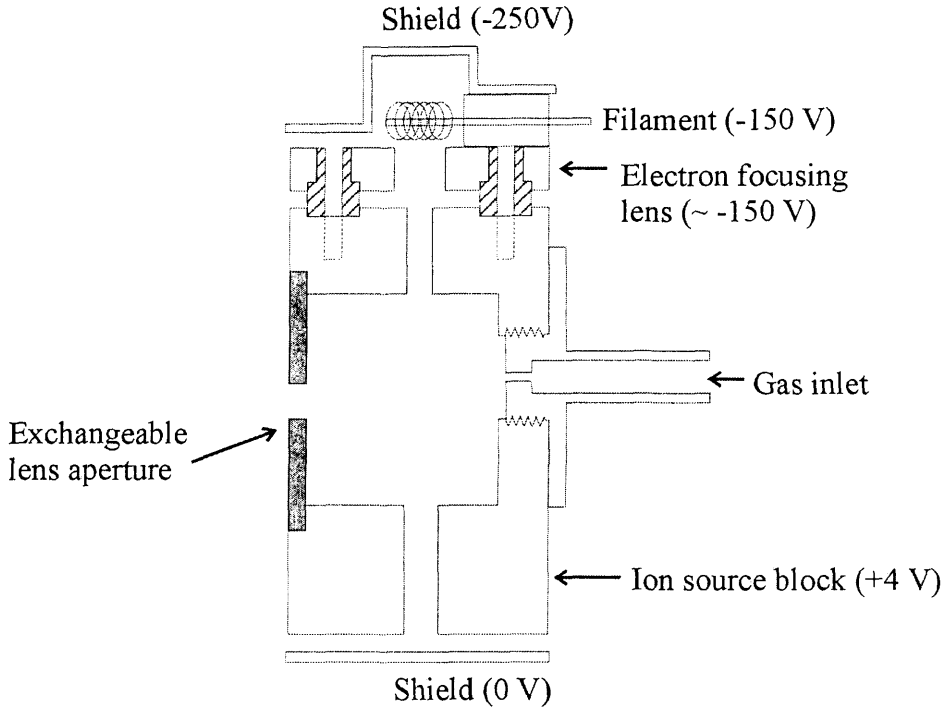

Figure 3.3 A schematic diagram showing the electron ionisation source (scale 1:1).

EI [3-6] is the most suitable method for ion formation in the PSCO experiment since it is a simple, robust and inexpensive technique despite not providing the highest yield of doubly-charged ions in comparison to some other techniques [7-15]. Whilst more sophisticated ionisation methods provide state and energy selection of the reactants, this is not a necessary feature for the PSCO apparatus, at the moment, since the position-sensitive data recorded allows the determination of the initial states of the reactants and

their corresponding product channels.

A future instrumental development would be to replace the EI ion source with a more state selective ionisation technique to improve the energy resolution. At present, translational energy selection of the reactants is achieved using a hemispherical energy analyser subsequent to ion formation, so that a small kinetic energy spread of the resulting beam can be realised.

Figure 3.3 shows the custom designed PSCO ion source with representative voltages for the formation of Ar^{2+}. The electron gun, consisting of a hot tungsten filament, produces electrons that are then accelerated to between 150-200 eV through a 4 mm aperture into the ionisation region of the source where a neutral precursor gas is introduced through a 2 mm aperture. The ions formed by the electron-neutral collisions are extracted through the 4 mm exit aperture of the ion source from the ionisation region using a negatively charged extraction lens (Figure 3.4). A stack of three electrostatic lenses then focuses the ion beam, with a fourth lens used to accelerate the ion beam to the appropriate potential before it enters the hemispherical energy analyser (Figure 3.4). Figure 3.4 also show representative voltages for the formation and transmission of Ar^{2+}.

The trajectory of the ion beam into the energy analyser can be adjusted, for alignment purposes, using two pairs of deflectors situated at the entrance to the analyser. The need for only very small voltages on these deflectors (*e.g.* ±0.2 V about the beam potential V_0) indicates the good mechanical alignment of the lens stack with the entrance to the hemisphere. Bad mechanical alignment of the lens stack with the hemisphere entrance slit would result in the *z*-axis of the beam prior to the analyser not being aligned with the entrance slit of the analyser. This would result in a very low ion beam count rate in the reaction region. To compensate for the bad alignment, voltages significantly larger than ±0.2 V would be needed on the analyser entrance and exit deflectors to redirect the beam through the analyser entrance slit and realign the beam at the exit slit of the analyser.

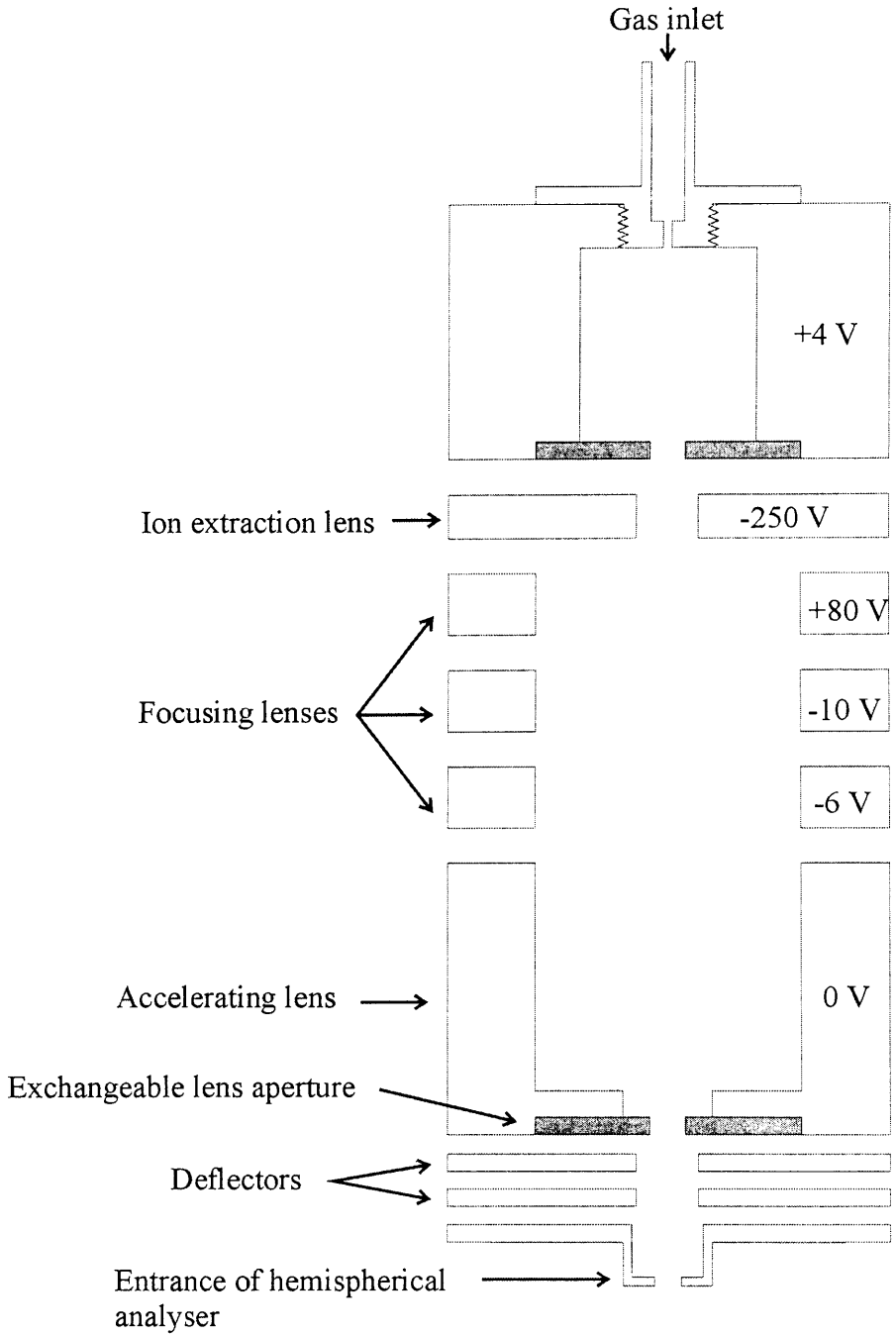

Figure 3.4 A schematic diagram showing the focusing and acceleration optics located at the exit of the ion source and prior to the entrance of the analyser with representative voltages. (Scale 1:1)

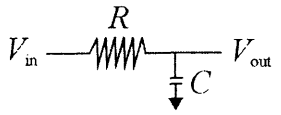

Figure 3.5 A schematic diagram of a low pass filter where R and C represent a resistor and capacitor respectively..

A 16-channel 16-bit DAC (Digital to Analogue Converter) card in a PC supplies the voltages (-10 up to +10 V) for the analyser, deflectors, and the associated focusing optics. Before the voltages are passed to the relevant lens elements, they are each filtered and smoothed by a low pass filter (Figure 3.5), consisting of a resistor and a capacitor. A low pass (LP) filter allows low frequency signals, *i.e.* the dc voltages supplied to the relevant lens elements as described above, to pass through the filter circuit unchanged. High frequency noise, such as radio frequency interference, is effectively blocked. The time constant t of a filter is given by

$$t = RC, \tag{3.1}$$

where R is the resistance (Ω) and C the capacitance (F).

Table 3.1 Location of the low pass filters and their properties.

Filters on voltages to...	R / Ω	C / μF	Capacitor voltage range	t / s
all lenses (excl. ion source elements)	100K	10	-100 V, ±250 V	1
vertical deflector plates at entrance to Wein filter	1M	1	-16 V, ±250 V	1
Wein filter voltages	1K	10	-100 V, ±250 V	0.01

Therefore, for the LP filters used in the PSCO experiment (Table 3.1), containing a 100 KΩ resistor and a 10 μF capacitor, t will be 1.0 seconds. A filter with a time constant of

this magnitude is perfectly adequate in the context of tuning up the PSCO ion beam. Low pass filters were implemented since the voltage supplies to some lenses were found to be noisy, one of the symptoms of this noise being poor energy resolution of the ion beam.

The next sections describe the principles behind the motion of ions in electrostatic and magnetic fields, putting these theories into the context of the instrumentation used to energy and mass select the ion beam. The use of an ion energy analyser is a very effective way of obtaining an ion beam with a narrow energy spread. Two different types of energy analysers are discussed below. Once the beam has passed through the hemispherical energy analyser, a Wein filter is used as a tool for mass (velocity) selection allowing the formation of a well-collimated beam of dications.

3.4.2 Electrostatic and magnetic analysers

3.4.2.1 Energy analysis

Several basic techniques have been used to achieve the energy analysis of charged particles, two of which are the basis of a great variety of analyser models. First is the use of a retarding potential in front of a collector, allowing collection of particles that have higher energies than the retarding potential, and the second is the deflection of ions in a magnetic or electrostatic field. The hemispherical energy analyser [16-21] used in the PSCO mass spectrometer is based on the latter design. The ion beam is guided around the hemisphere using the appropriate voltages. This process allows ions of a particular translational energy to be selected from the original ion cloud formed.

Collecting ions from a large solid angle imposes certain constraints on the design of a hemispherical analyser. These constraints are expressed in the Lagrange's Law, showing conservation of the Lagrange invariant along the ion beam, as described in the next section.

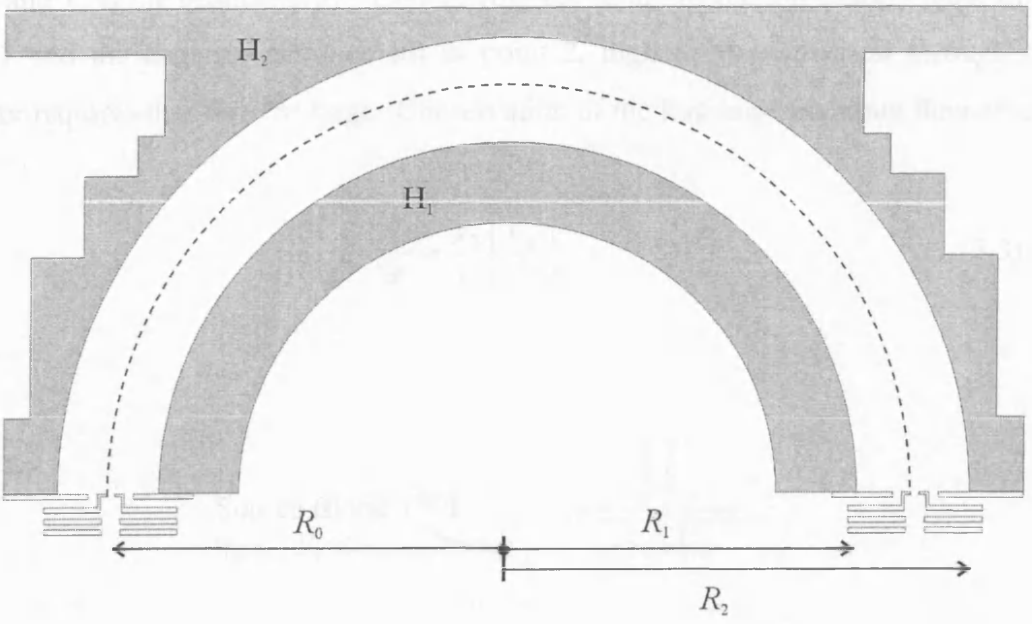

Figure 3.6 A schematic diagram of a hemispherical energy analyser, where R_1 and R_2 are the radii of the inner (H_1) and outer (H_2) hemispheres, respectively, as described in the text and V_1 and V_2 are the voltages applied to them. R_0 is their mean radius and V_0 is the equipotential created by the applied voltages V_1 and V_2.

3.4.2.1.1 Lagrange invariant

Large hemispheres, such as the one used in the PSCO experiment, are required to achieve good energy resolution, as described below, as well as good transmission of the ion beam through the analyser. The relationship between the angular divergence θ_1/θ_2 and the lateral divergence y_1/y_2 of the ion beam is described by the Lagrange's law [22] that governs ion optics indicating the conservation of the Lagrange invariant along the ion beam,

$$\theta_1 y_1 V_1^{1/2} = \theta_2 y_2 V_2^{1/2} \qquad (3.2)$$

where θ_i is the angular divergence of the beam at point i, y_i is the diameter of the ion beam, and V_i is the beam energy. Considering the centre of the ionisation region to be point 1 and the analyser entrance slit as point 2, high ion transmission through the analyser requires that θ_1/θ_2 be large. Conservation of the Lagrange invariant then gives

$$\frac{\theta_1}{\theta_2} = \frac{y_2}{y_1}\left[\frac{V_2}{V_1}\right]^{1/2}. \qquad (3.3)$$

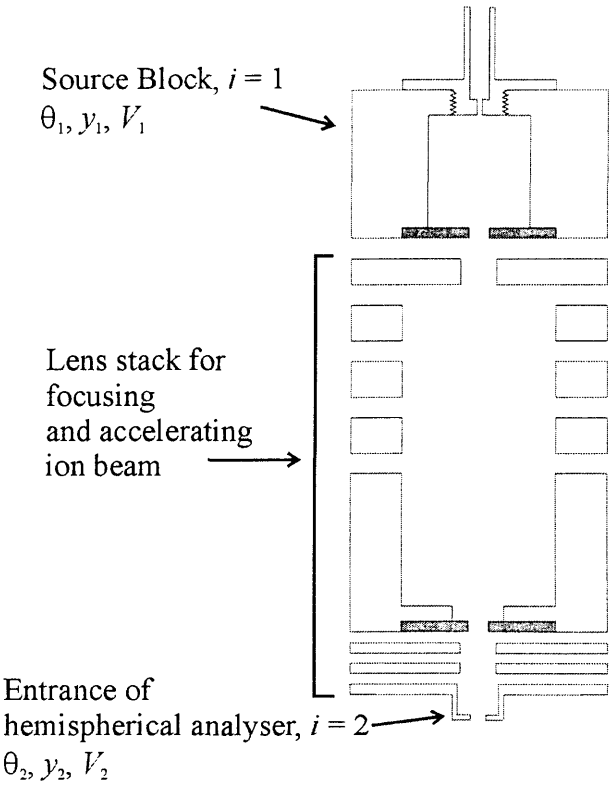

Figure 3.7 A schematic diagram indicating the parameters at the two points of reference in the PSCO apparatus used to describe the Lagrange in variant

For the low PSCO ion beam energies, the term $[V_2 / V_1]^{1/2}$ in Equation 2 will be close to unity, where $V_2 > V_1$, as the difference between V_1 and V_2 is limited in order to obtain the best possible energy resolution. Therefore, for large θ_1/θ_2 the relationship in equation 3.3 indicates that the lens system must have high linear magnification ($y_2 >> y_1$) *i.e.* the diameter of the beam is larger at point 2 than it is at point 1. In order to

achieve good ion transmission, the slits at the entrance to the hemisphere must then be large and hence the hemispherical analyser must also be large to have good resolution (Eqs. 3.2, 3.3), otherwise the transmission of ions through the system is impaired since the ion beam is constrained by the inter-hemisphere distance. The only constraints on the actual size of the analyser are the capabilities of the laboratory workshop.

3.4.2.1.2 The PSCO hemispherical analyser

As described in section 3.4.1, the ions formed in the ion source, are extracted to -250 eV. In an ideal situation, the ions in the source would all have the same initial velocity and always be extracted from the same position in the source; this should give the ion beam a well-defined energy range. However, in reality, the ions have a variety of positions and initial velocities in the ion source before they are extracted which results in a relatively less well-defined beam energy spread. Since a mono-energetic dication beam is very desirable in the PSCO experiment, a 180° hemispherical energy analyser (Figure 3.6) is used for further energy selection of the beam. It comprises of inner and outer hemispheres having radii R_1 = 130 mm and R_2 = 170 mm, respectively; hence the mean radius R_0 = 150 mm and the inter-hemisphere distance is 40 mm. Both the entrance and exit slits widths W_0 are 3 mm.

The following section describes the theoretical relationship between the hemispherical radii and the voltages that must be applied to them in order to create the equipotential that defines the energy selection of the ion beam. From this relationship, the theoretical energy resolution of the analyser can be obtained.

3.4.2.1.3 Hemispherical energy analysers—the theory

An ion enters the hemisphere at its mean radius R_0

$$R_0 = \frac{(R_1 + R_2)}{2}, \tag{3.4}$$

where R_1 and R_2 are the radii of the inner and outer hemispheres respectively. The ion is deflected through 180° as it travels along the arc through the hemisphere defined by R_0 and "pass voltage" V_0. In order for an ion, that has an initial kinetic energy T at potential V_0, to pass through the analyser, it must be retarded by a potential V_r

$$V_r = T - V_0. \tag{3.5}$$

Therefore, the potentials of the inner and outer hemisphere are

$$V_{\text{inner}} = -V_0\left[\left(\frac{2R_0}{R_1}\right) - 1\right] + V_r \tag{3.6}$$

and

$$V_{\text{outer}} = -V_0\left[\left(\frac{2R_0}{R_2} - 1\right)\right] + V_r, \tag{3.7}$$

respectively. If the kinetic energy of the ions deflected through an arc of 180° along R_0 is equal to the pass energy of the analyser then the potential difference between the hemispheres is

$$\Delta V = V_0\left(\frac{R_2}{R_1} - \frac{R_1}{R_2}\right). \tag{3.8}$$

Typically, the energy resolution of energy analysers is defined by

$$\frac{\Delta E_{1/2}}{E_0} \tag{3.9}$$

where $\Delta E_{1/2}$ is the full width at half maximum (FWHM) of the energy distribution of an ion beam, and E_0 is the pass energy at which the analyser is tuned. An alternative method for obtaining the energy resolution is from the base resolution ΔE_B. Generally, an analyser will have

$$\Delta E_{1/2} \sim \frac{\Delta E_B}{2} \tag{3.10}$$

Also, the resolution may be expressed as a function of R_0, the angular divergence of the beam α, and the equal slit widths W_0, at the entrance and exit of the hemisphere:

$$\frac{\Delta E_{1/2}}{E_0} = \left(\frac{W_0}{2R_0}\right) + (\text{terms in } \alpha_0^2). \tag{3.11}$$

The hemispherical energy analyser used in this experiment has a theoretical energy resolution of 1.1% of the equipotential energy E_0 [23]. The value for E_0, the pass energy, may be set manually for each experiment. Since the theoretical resolution is constant, the value of E_0 determines the magnitude of $\Delta E_{1/2}$ (the spread in beam energy). Therefore, the value of E_0 (usually 2-4 eV) is chosen to give the smallest possible value of $\Delta E_{1/2}$ whilst maintaining a sufficient ion beam count rate (> 1000 ions s^{-1}).

3.4.2.1.4 Experimental energy resolution

The actual experimental energy resolution achieved may be estimated from the temporal width of the signals of the unreacted dication in the TOF mass spectrum (6 ns at a source field of 30 V cm^{-1}), and has an upper limit of 4.5% at a hemisphere pass energy of 8 eV (4 V) for a dication beam with an energy of 4 eV in the interaction region. However, this experimental determination neglects other contributions to the width of the TOF mass spectrum signals such as the rise time of the repeller plate pulse and

imperfect space focusing in the reaction source region, but does allow for the electronic timing uncertainty, determined to be ±1.5 ns. The disparity between the theoretical resolution and the upper limit determined from the TOF mass spectrum signals is principally due to the significant angular spread of the ion beam injected into the analyser.

In order to realise a reasonable dication flux the ions need to be efficiently extracted and transported from the ion source, which results in an ion beam with a non-negligible angular spread (10^{o}) at the entrance slit of the analyser; the theoretical estimate of the energy resolution assumes a negligible angular spread. The energy resolution could be improved by reducing the angular spread of the beam by using a smaller exit aperture for the acceleration lens or smaller slits. Both these improvements would be at the expense of lower ion transmission. Data presented in Chapter Five will show that the current performance of the analyser is very satisfactory for the experiments performed.

3.4.2.1.5 Alternative instrumentation for energy analysis

The cylindrical analyser (Figure 3.8) is an alternative tool for energy analysis based on the ion deflection principle. This type of analyser is commonly used in surface analysis since it is possible to incorporate an electron gun into the design of the analyser providing an excitation source for surface techniques such as Auger electron spectroscopy, or electron energy loss spectroscopy. Ion deflection is caused by the potential difference, ΔV between two cylinders of radii, R_1 and R_2 as for a hemispherical analyser. The voltage ratio applied to the cylinders for an incident electron energy, eV_1, is connected with the ratio of the cylinder radii by

$$\frac{V_1}{(V_2 - V_1)} = 1.3 \ln \frac{r_1}{r_2} \qquad (3.12)$$

The beam trajectory passes through the axis at ΔS_1, is reflected by the electrostatic field and then passes through the axis again at ΔS_2. The focusing at most angles in this

analyser is first order, except for a special case at $\theta = 42.3^{\circ}$ and calibration constant K_0 = 1.31 where the focusing becomes second order and the analysing properties are improved. The disadvantage of the cylindrical analyser is that it has x-focusing properties but no y-focusing properties.

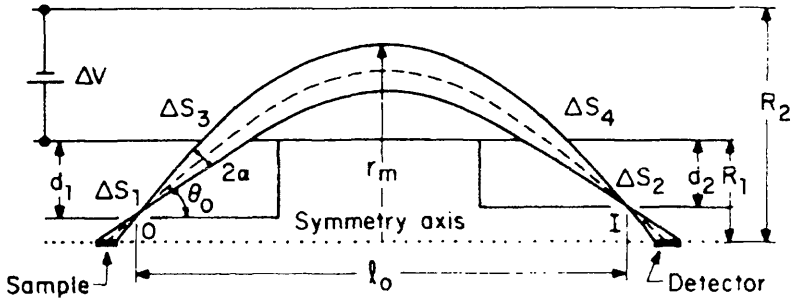

Figure 3.8 Schematic cross-section of a cylindrical mirror analyser; where d_1 and d_2 are the entrance and exit slit apertures, respectively [24].

A distinct advantage of the hemispherical analyser over the cylindrical analyser is the two plane focusing that prevents the loss of ions that have 'off-axis' trajectories. As a result, the beam current is not unnecessarily reduced.

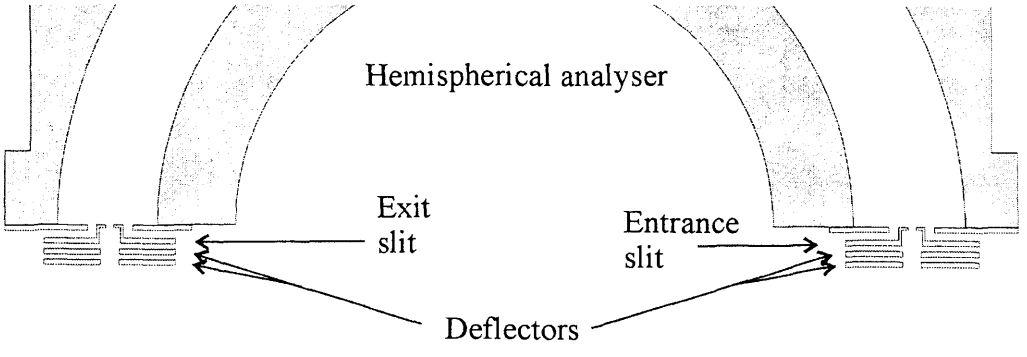

Figure 3.9 A schematic diagram showing the position of the deflector pairs at the entrance and exit of the energy analyser.

In order to ensure that the analysing field in the hemisphere is kept uniform up to the entrance and exit of the energy analyser, specialised entrance and exit slits (Figure 3.9),

called Jost plates [25], are employed. This prevents heavy disturbance of the ion beam as it passes through the energy analyser. Horizontal and vertical deflectors placed at the exit of the hemispherical energy analyser may be used to adjust the exit trajectory of the ion beam (Figure 3.9). The horizontal pair of deflectors is also used to pulse the ion beam as described in the section 3.5. The following section describes the instrumentation used for ion beam mass selection.

3.4.2.2 Mass analysis

The type of Wein filter used in the PSCO apparatus is a commercial velocity filter (Colutron Research Corp. Model 600-H) [26]. The filter selects ions of a particular velocity by applying crossed magnetic and electrostatic fields to the ion beam. In practice, a pair of magnets is mounted perpendicularly to a pair of electrostatic deflection (Figure 3.10 & Figure 3.11). When a beam of charged particles is passed through the filter at a velocity, v, the beam will be deflected by the magnetic field, B, in the x dimension, and by the electric field, E in the y dimension (Figure 3.11).

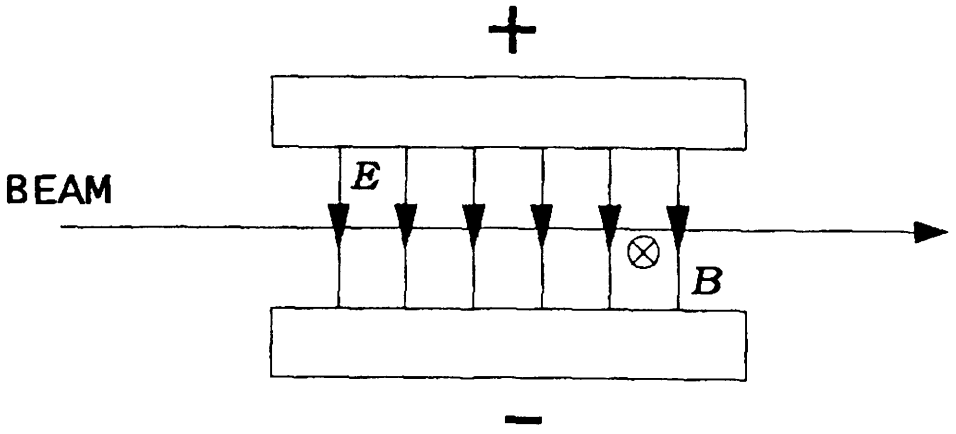

Figure 3.10 Top view of the velocity filter.

$$F_B = Bzv \tag{3.13}$$

$$F_E = Ez \tag{3.14}$$

where F_B is the magnetic force, B is the magnetic field strength, F_E is the electrostatic force, E is the electric field strength, z is the charge of the particle, and the velocity of the beam particles, v, is

$$v = \left(\frac{2zV_0}{m}\right)^{\frac{1}{2}} \tag{3.15}$$

with m being the particle mass and the V_0 is the beam potential (Figure 3.10).

When the two opposing forces F_B and F_E are equal,

$$Bzv_0 = Ez \tag{3.16}$$

implying

$$Bz\left(\frac{2zV_0}{m_0}\right)^{\frac{1}{2}} = Ez\,, \tag{3.17}$$

then ions with (v_0, V_0, m_0), will pass undeflected through the filter for the appropriate values of B and E. All other ions not having mass m_0, *i.e.* where $v < v_0$ or $v > v_0$ are deflected away from the z-axis of the Wein filter and are eliminated from the ion beam. Hence, the beam can be selected for an ion with a specific mass.

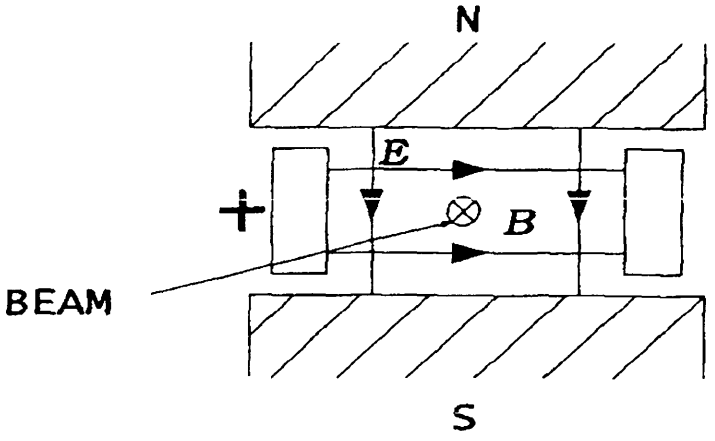

Figure 3.11 Filter viewed from beam entrance.

The velocity filter has a strong focal property, which limits the length of the drift path between the filter and the target and Figure 3.12 explains this effect. A positively charged ion beam is entering the filter with a velocity v (Eq. 17). It is assumed that the electrostatic plates are electrically balanced so that the zero-equipotential shown in the diagram passes through the centre of the filter. All ions passing through the centre of the filter or along the zero-equipotential will pass undeflected if $Bzv = Ez$. Ions on either side of the centre have to cross positive or negative forces in the equation $Bzv = Ez$. That is, the ions crossing below the zero-equipotential are accelerated slightly while crossing the negative equipotentials. The total velocity increases and the magnetic force Bzv exceeds the electric force Ez and bends the ions toward the centre. Ions above the zero-equipotential are slightly decelerated and the magnet force becomes weaker so that the electric force will bend the ions back toward the centre and a crossover point is formed at F.

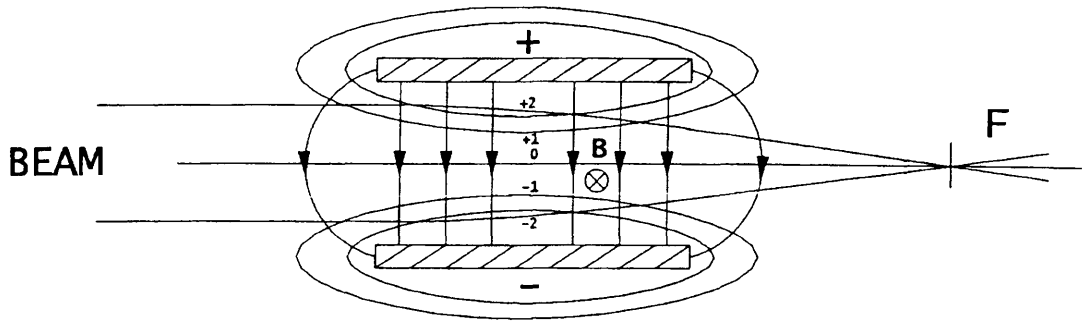

Figure 3.12 Focusing effect of the filter.

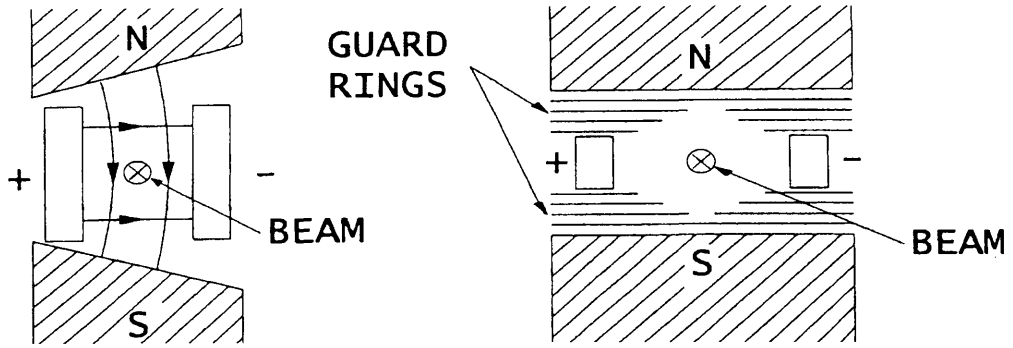

Figure 3.13 a) tapered pole plates; b) electrically biased guard-rings.

Problems relating to this focusing effect have been overcome by shaping the E field or B field or both in such a way that it will compensate for any increase or decrease in the magnetic force Bzv (Figure 3.13a). The magnetic field strength B is increasing toward the positive plate side and decreasing toward the negative plate side due to the tapered shape of the magnetic pole shapes. A gradient on the electrostatic field is also introduced by means of electrically biased guard rings (Figure 3.13b). The guard rings are made of stainless steel shims and each guard ring is individually connected to a potentiometer that provides the correct bias (±10 V relative to the Wein filter field ~2809 V m^{-1} for m/z = 20). When the guard-rings are properly biased they force the electric equipotentials between the deflection plates to produce the correct field shape. It is possible to compensate for the unwanted focusing effect by making the electrostatic

field weaker at the positive and stronger at the negative plate. By careful adjustment of the potentiometers while monitoring the beam count rate, position and shape at the detector, the best bias voltage settings can be determined. The Wein filter is operated here as a non-focusing device. However, by a small adjustment of one or two of the guard-ring potentiometers, the filter becomes cylindrical again.

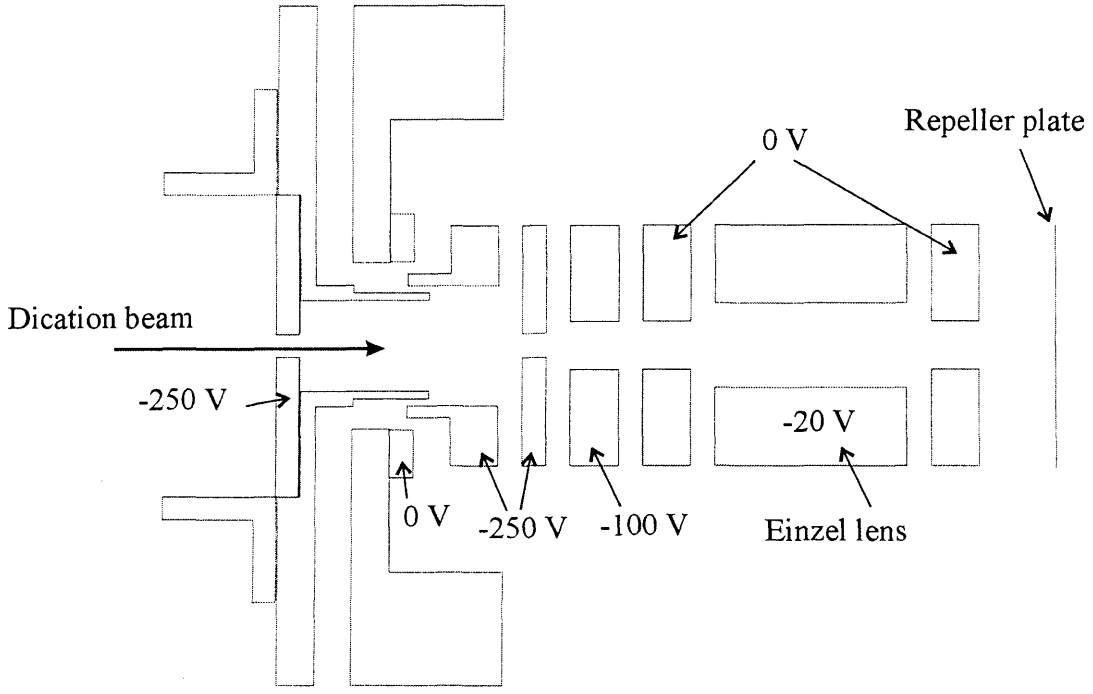

Figure 3.14 Schematic diagram of the decelerator with representative voltages for a beam of Ar^{2+}. (scale = 1:1)

On exiting the Wein filter, the dication beam is then decelerated to the required collision energy, usually between 4-22 eV in the LAB frame, using a commercial decelerator, before being focused into the reaction source region. The decelerator (Figure 3.14) consists of 8 lenses including an Einzel lens. The Einzel lens is specifically designed to correct any divergence of the beam as it is decelerated, ensuring that a well-collimated beam passes into the reaction source region where it may react with a neutral gas as will be explained in section 3.6. The quality of the generated ion beam is demonstrated in Chapter Five.

3.5 Pulsed beam

The above methodology describes the experimental set-up for formation of a continuous ion beam that can react with a neutral gas in the source region of the TOF mass spectrometer. Using a continuous ion beam often leads to a lot of background counts in both the mass spectrum (Figure 3.15) and the coincidence spectrum, at flight times less than that of the dication.

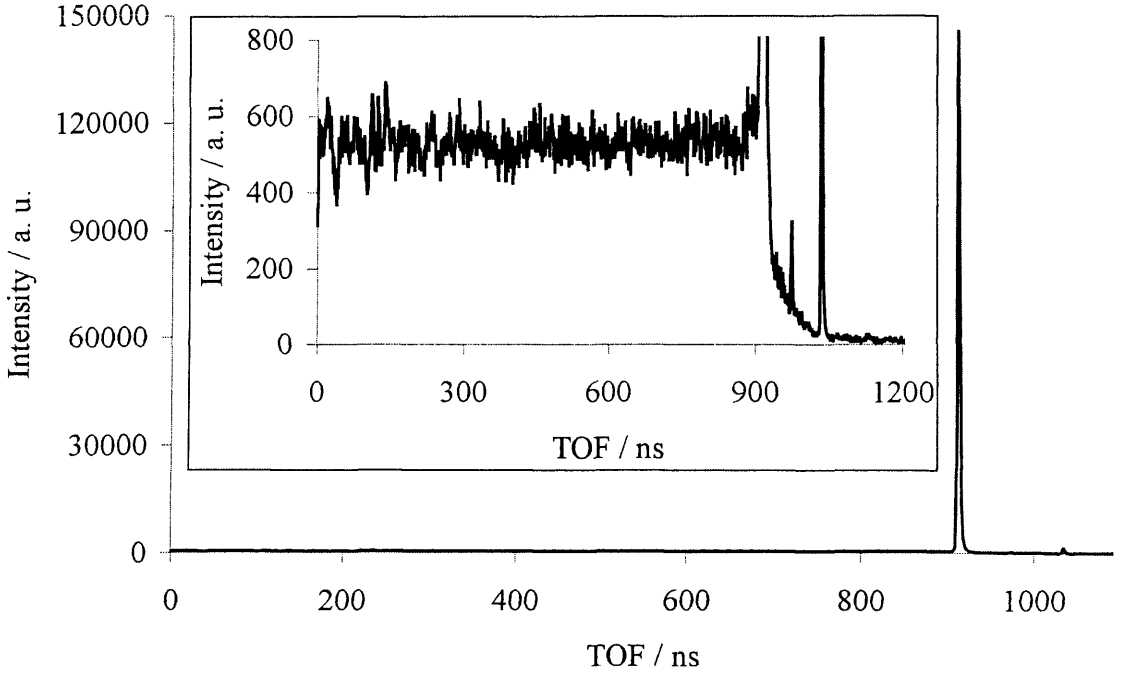

Figure 3.15 A TOF mass spectrum of a continuous beam of Ne^{2+}. The inset shows detail around the base of the dication peak. The much smaller secondary peaks at longer flight times than the main dication peak are the isotopes of Ne^{2+}.

Background counts arise from ions that are in the acceleration region or drift tube of the TOF mass spectrometer when the repeller plate is pulsed and, therefore, have shorter flight times due to the reduced flight distance to the detector compared to ions in the reaction source region at the time of the repeller pulse (see Chapter Five). In order to reduce the background counts it is preferable to pulse the dication beam.

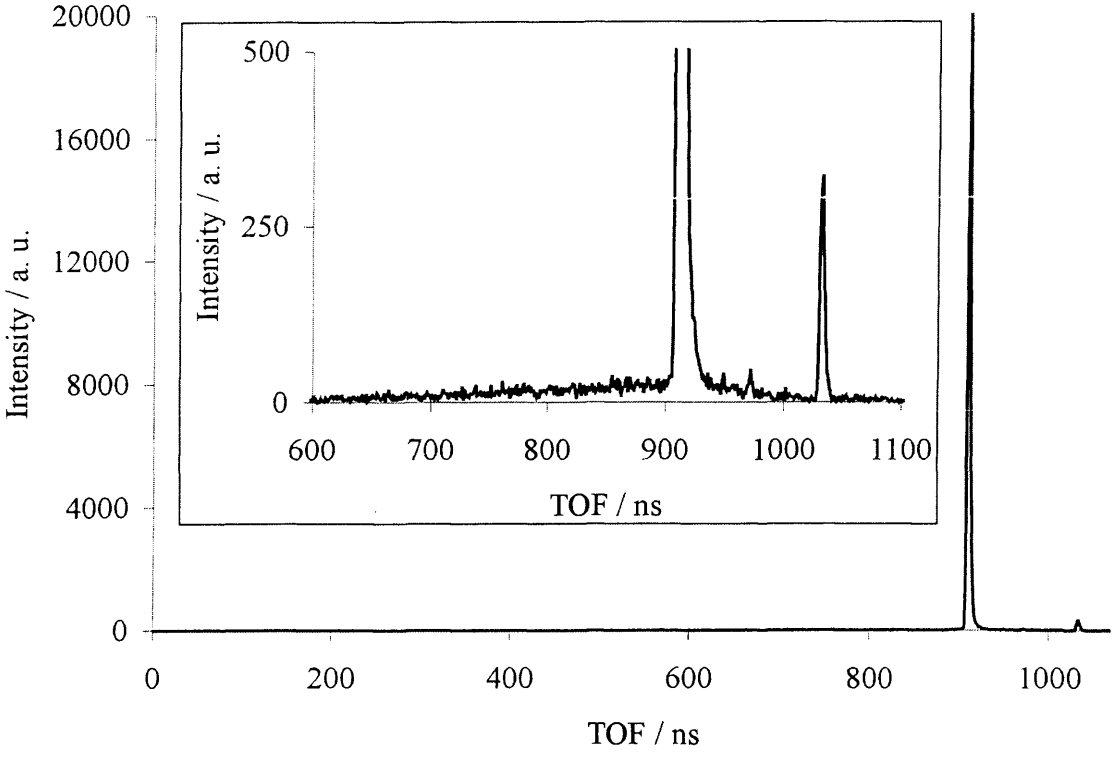

Figure 3.16 A TOF mass spectrum of a pulsed beam of Ne^{2+}. The inset shows detail around the base of the dication peak. The much smaller secondary peaks are the isotopes of Ne^{2+}. It is clear from a comparison of this spectrum with Figure 3.15 that the background before the dication peak is significantly reduced when pulsing is implemented.

Figure 3.16 shows a TOF mass spectrum of a pulsed beam. It is clear from the inset in this figure that, in comparison to Figure 3.15, the background counts at shorter flight times than the dication peak are significantly reduced. Another advantage of using a pulsed beam is that by creating small well-defined packets of ions, the point of interaction between the two reactants is more localised. A pulsed beam also results in a reduction in the number of reactions that occur outside of the source region of the TOF mass spectrometer, *i.e.* in the acceleration region or drift tube of the TOF mass spectrometer, and therefore yields a pairs spectrum with very little noise around each peak (see Chapter Five for commissioning details).

Experimentally, a pulsed beam is produced by applying appropriate voltage waveforms to the horizontal deflectors at the exit of the hemispherical analyser (Figure 3.18). Equal voltages with opposite polarity, relative to the ion beam potential, are applied to each element of the deflector pair. Hence, the ion beam can be deflected without perturbing the energy of the ions when they are transmitted through the exit of the hemisphere.

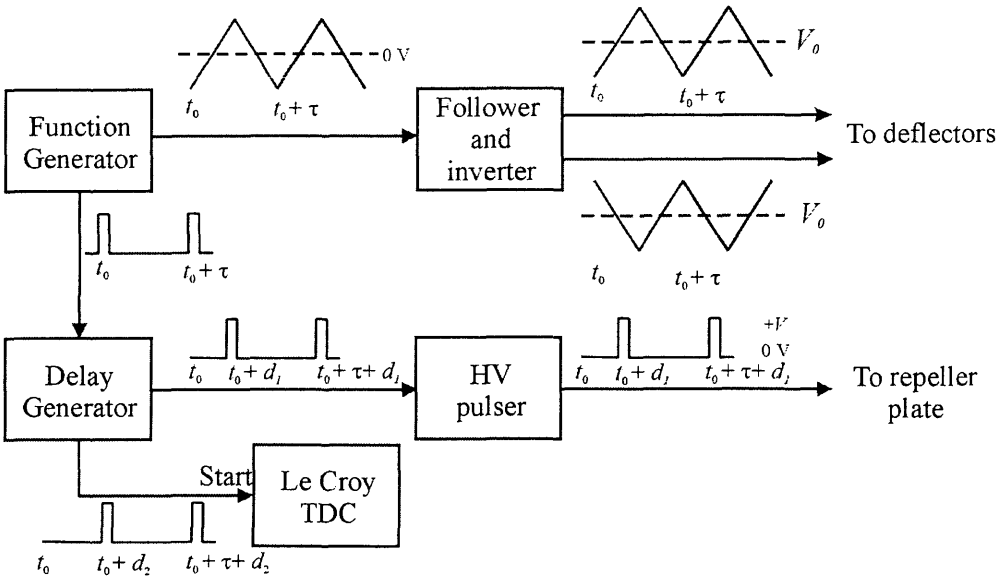

Figure 3.17 A schematic diagram of the timing chain. As described in the text, a function generator produces a triangular waveform. This waveform is used to generate the waveforms applied to the deflectors after the energy analyser to generate a pulsed ion beam. The function generator also triggers a delay generator, which controls the application of the voltage pulse to the repeller plate of the TOFMS and starts the TDC. The delay between the triggering of the delay generator and the repeller plate pulse (d_1) is adjusted so that a dication pulse is in the centre of the reaction region when the voltage is applied to the repeller plate. The signal to start the TDC is also delayed (d_2, $d_2 > d_1 + 200$ ns) so no RF noise from the repeller plate pulse reaches the TDC when it is live.

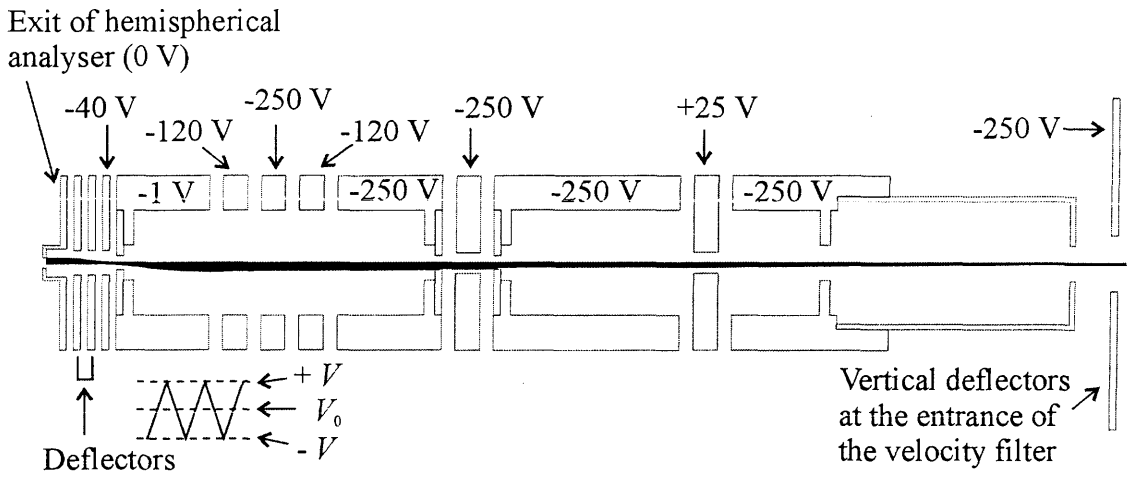

Figure 3.18 A schematic diagram of the accelerating lens system together with the trajectories of Ar^{2+} ions with a rest potential of 4 V. One of the voltage waveforms applied to one of the horizontal deflectors at the exit of the hemispherical analyser to generate a pulsed dication beam is shown. The waveform applied to the other horizontal deflector differs in phase by 180°.

The ion beam is deflected from one side of its central path through the electrostatic lenses to the other side and back again, by sweeping the magnitude of the offset voltages on the deflectors relative to the ion beam potential. The only conditions under which ions can pass through the deflectors are when the deflector offset voltages are at or near the beam voltage V_0, and when the ion beam angle to the axis is at zero or is small enough to be focused by the ion lenses following the deflectors.

The ion beam is therefore pulsed and the ion pulse duration depends on how fast the deflector voltages are changing with respect to the ion beam velocity. The ion pulses become shorter the faster the deflector voltages change, since ions are only able to pass through the deflectors when both the horizontal deflector voltages are near or at the beam potential V_0. However, if the rate of change of the deflector voltages is fast enough to be of the same order of magnitude as the ion transit time across the deflector region, then the rest potential of the ions will be shifted. This situation needs to be avoided (see Chapter Five for more detail).

In order to make certain that there is no perturbation of the ion energy in the shortest ion pulses, the TOF mass spectrum of the pulsed dication beam is compared with that of a continuous dication beam of the same nominal energy. If the pulsed and continuous beam dication signals in the mass spectrum show the same TOF then the pulsing is not perturbing the transmitted ion energy, since the flight time of an ion in the TOF mass spectrum is a function of the initial velocity of an ion in the source region.

A commercial function generator, with variable frequency and amplitude controls, is used to generate a triangular master waveform to apply to the deflectors. The timing chain is represented in Figure 3.17. This master waveform is passed into a custom designed waveform follower and inverter unit. This unit uses operational amplifiers to create two waveforms with identical frequency and magnitude, centred about the beam potential, but with their phase offset by 180°. The commercial function generator also provides the master trigger for the repeller plate pulse and the data acquisition electronics, as described in more detail below.

The quality of the ion pulses formed by the above method can be monitored by allowing them to fly freely through the source region of the TOF mass spectrometer all the way to the PSD without pulsing the repeller plate located behind the reaction source region (Figure 3.19). This procedure shows it is possible to generate dication pulses, between 0.5 to 1.5 μs in duration, at beam energies in the reaction source region of 2-10 eV.

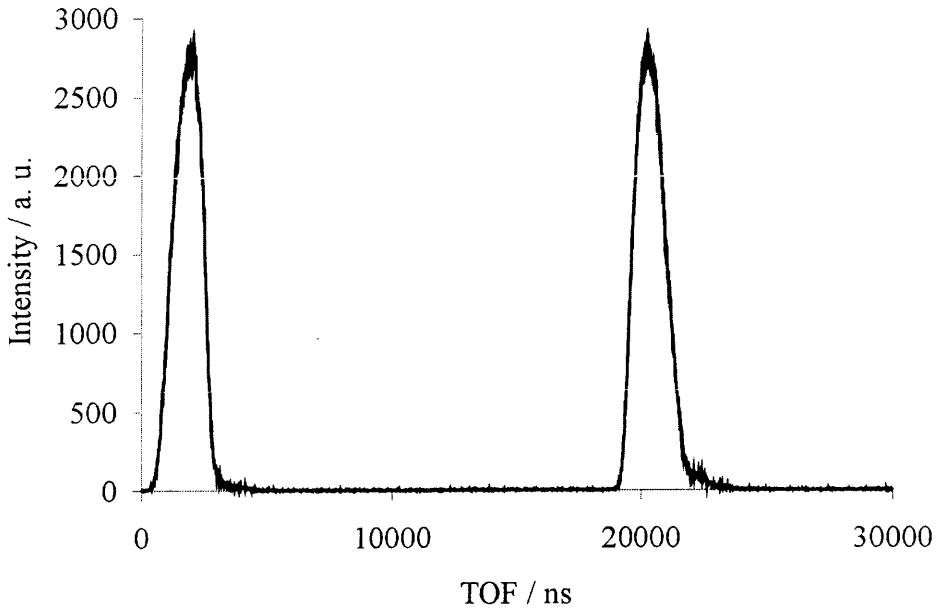

Figure 3.19 A mass spectrum showing the temporal width (1.4 μs) of the dication pulses.

The above sections describe the formation of a dication beam with a narrow energy spread for both continuous and pulsed beam operation in preparation for the subsequent dication-neutral interactions. To recap: after the ion beam has been pulsed using the horizontal deflectors at the exit slit of the energy analyser, it is focused and accelerated (Figure 3.18) into a commercial Wein (velocity) filter as described in section 3.4.2.2. The packets of dications are then decelerated into the reaction source region. The following section describes the reaction source region where the dication-neutral interactions take place, and the TOF mass spectrometer into which the products and any unreacted dications are accelerated and there by identified.

3.6 Reaction chamber

3.6.1 Reaction source region

Following deceleration of the beam to the desired collision energy, typically between 4-22 eV, the dication beam is focused into the reaction region *via* a mesh-covered aperture in the repeller plate. The reaction region also serves as the source region for the TOF mass spectrometer. In the reaction region, the dications interact with an effusive jet of neutral molecules that are introduced *via* a hypodermic needle.

To record a mass spectrum, a pulsed positive voltage is applied to the repeller plate, located behind the reaction region, to accelerate the resulting cloud of reactant and product ions into the TOF drift tube and towards the detector. A multi-channel digital delay generator (DDG) running at a chosen frequency, typically 30 kHz, controls the trigger for the repeller plate as indicated in Figure 3.17 and is itself externally triggered by the commercial waveform generator controlling the deflector pulses. The DDG is used to introduce an appropriate delay before triggering the repeller plate, in order that the packets of dications exiting the decelerator arrive at the centre of the reaction region as the repeller plate is pulsed. Since the events being studied (dication-neutral electron transfer and bond-forming reactions) have very low reaction cross-sections it is necessary to optimise the triggering delay to maximise the count rate and hence the likelihood of a reactive event occurring.

3.6.1.1 Optimising the repeller plate triggering delay

The specific timings for repeller plate triggering are set up by monitoring the dication beam count rate in tandem with the dication peak shape in the mass spectrum. If the repeller plate is pulsed too early or late, then the count rate may drop below the maximum achievable count rate and the peak shape will be asymmetrical with a tail either to longer or shorter flight times, respectively (Figure 3.20).

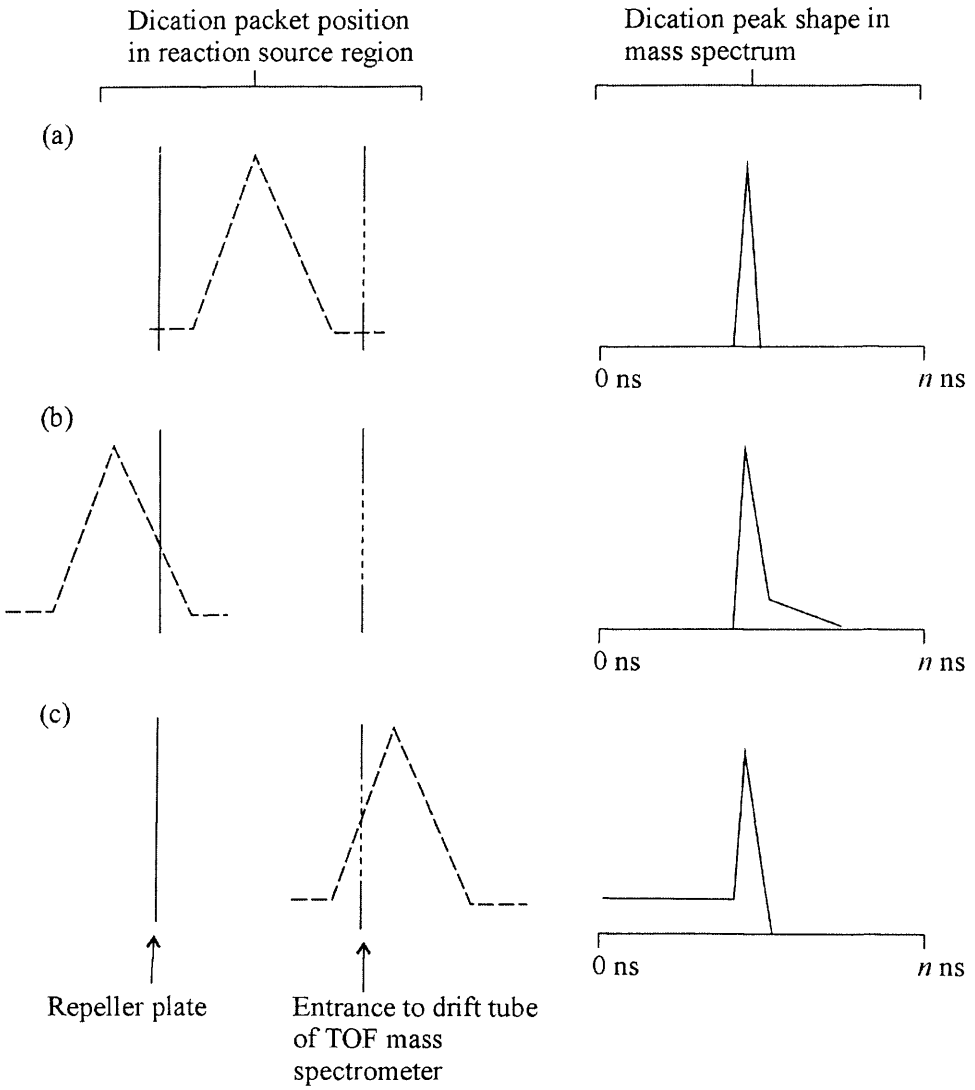

Figure 3.20 A diagram showing the effect of the repeller plate timing on the shape of the dication peak in the mass spectrum; (a) is the optimal timing (the ion packet is in the centre of the source region), (b) the repeller plate is pulsed early and (c) the repeller plate is pulsed late. Cases (a) and (b) lead to a much reduced dication peak intensity.

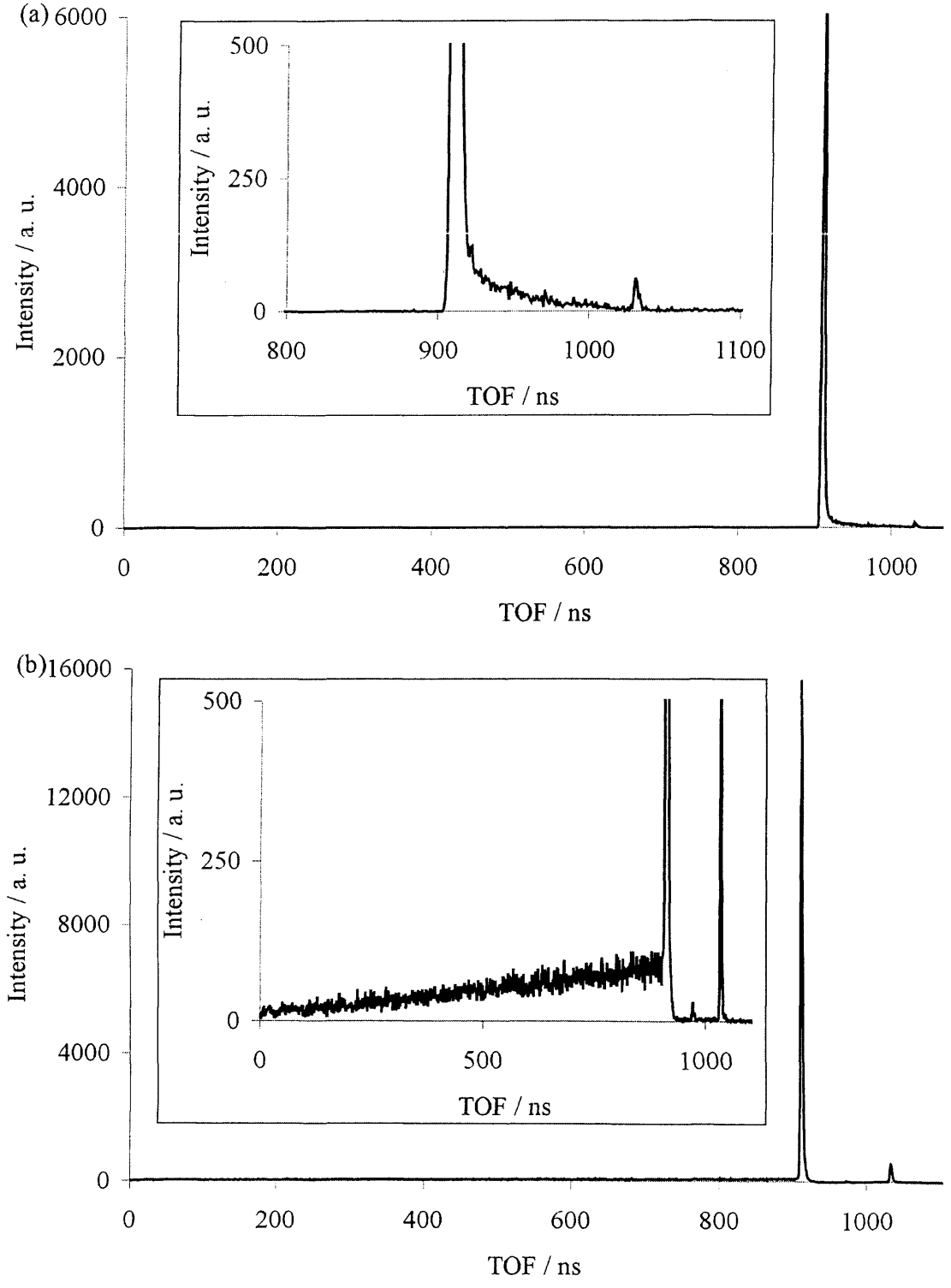

Figure 3.21 TOF mass spectra for a pulsed Ne^{2+} beam showing the effect of pulsing the repeller plate (a) too early or (b) too late. The insets show detail around the base of the dication peak. The much smaller secondary peaks are the isotopes of Ne^{2+}.

In Figure 3.16, the repeller is pulsed when the packet of dications is in the centre of the source region. This is the ideal scenario. From the recorded spectrum, it can be seen that the dication signal is very symmetrical with few background counts in the rest of the spectrum. In the spectra in Figure 3.21, there are a small number of background counts after the dication peak. As described earlier in section 3.5, background counts arise from ions that are in the acceleration region or drift tube of the TOF mass spectrometer when the repeller plate is pulsed. Therefore, these ions experience different field strengths from the repeller plate pulse resulting in a variety of flight times that are not encompassed by the dication signal in the mass spectrum (see Chapter Five). When the repeller plate is pulsed too early or too late (Figure 3.20 (a), (b)) the intensity of the dication peak will be lower than when the dications are in the centre of the reaction source region.

In Figure 3.20 (b), where the repeller plate is pulsed too late, most of the dication packet has passed into the entrance of the drift tube resulting in significant background counts before the dication signal in the mass spectrum—a similar scenario to a continuous beam (see Chapter Five). These ions in the drift tube still experience the repeller plate field, and, due to being closer to the detector than ions that are still in the reaction source region, have shorter flight times than the main dication signal.

3.6.1.2 Repeller plate pulse duration

The duration of the repeller plate pulse is also controlled by the DDG and is set for a duration that allows all of the ions of interest to leave the source before the repeller plate returns to ground potential. There is an upper limit on the repeller plate pulse frequency of approximately 50 kHz due to the perturbation of the beam that occurs at if the repeller plate is pulsed at frequencies higher than this.

3.6.2 Time-of-flight mass spectrometry

Time-of-flight (TOF) mass spectrometry works on the basis that ions of different mass, when accelerated to the same kinetic energy possess different velocities. Hence, ions of different mass will have different flight times over a given path length. So, the flight time of an ion in a field free drift region may be derived using a combination of Newtonian mechanics and electrostatics, and it is found that the time-of-flight, t_{exp}, is dependent on the square root of its mass, m

$$t_{exp} = k\sqrt{m} \tag{3.18}$$

where k is a constant for a given set of electric fields and apparatus geometry. Hence, if the times of flight for the various ions are known, their masses can be determined. It is expected that all ions of the same mass would have uniform flight times in the TOF mass spectrometer. However, when a field is applied to the source region, the ions present have some spatial distribution. This causes ions of the same mass and charge to have a range of flight times. To reduce this effect, the ions can be 'focused' by appropriate choice of electric fields ensuring that ions of a given mass arrive at the ion detector at the same time, despite any spatial distribution in the reaction region. One type of focusing is first order [27] (Figure 3.22 (a)) and can be described mathematically as:

$$\left(\frac{dt_{exp}}{ds}\right)_{s=s_0,u_0=0} = 0 \tag{3.19}$$

where t_{exp} is the flight time of the ion, u_0 is the initial energy of the ion and s is the initial displacement of an ion in the source region from the entrance to the acceleration region; at $s = s_0$ an ion is in the centre of the reaction source region (Figure 3.22).

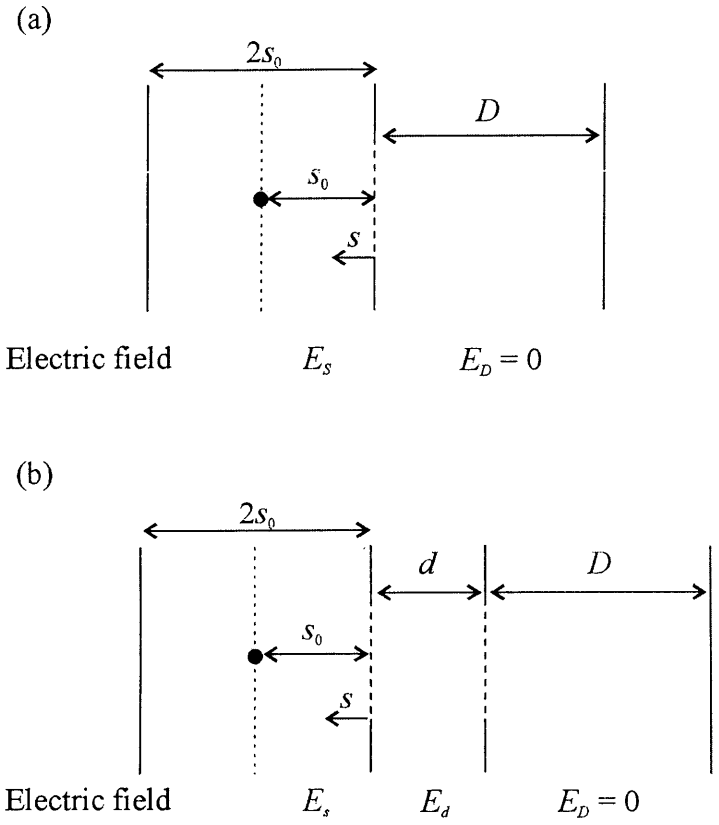

Figure 3.22 Schematic diagrams of the (a) one and (b) two electric field TOF configurations along with the basic definitions of the lengths and electric fields used in the mathematical derivations.

The TOF mass spectrometer used in the PSCO experiment is a two-field device (Figure 3.22 (b)) constructed to achieve second order focusing [10, 28] (Appendix C). Where the first order focusing mass spectrometer satisfies the relationship in Eq. 20, the second order device uses a more sophisticated arrangement of fields to create a field in the reaction region that satisfies

$$\left(\frac{\mathrm{d}^2 t_{\exp}}{\mathrm{d}s^2}\right)_{s=s_0,u_0=0} = 0 \qquad (3.20)$$

and Eq. 21.

In practice, the ion peaks in the mass spectrum have finite half widths corresponding to a range of ion flight times. However, for a pulsed dication beam of 4 eV energy (in the LAB frame) and a repeller plate voltage of 300 V, where the dication energy spread contributes minimally to the TOF peak width, the peak width of the unreacted dication in the TOF mass spectrum has a satisfying small half-width of 3 ns. This width can be ascribed principally to timing jitter in the timing electronics, showing the excellent quality of space focusing that is achieved using this two-field device.

As described above, the reaction region (1.6 cm long) doubles as the source region of the TOF mass spectrometer. When the repeller plate is pulsed, ions are accelerated out of the source region and into the 11 cm long acceleration region. Field uniformity is maintained over this long acceleration distance using eleven equally spaced guard rings, held at the appropriate potentials. The excellent agreement between calculated and experimental flight times and the lack of any curvature in the ion pair signals in the coincidence spectra indicate that a high degree of field uniformity and linearity is achieved. Subsequent to acceleration region, the ions pass into a 27.5 cm long field-free drift tube, before accelerated finally to 2.2 keV to hit the MCP.

The following section describes the instrumentation that detects the ion arrivals at the MCP recording flight times and positions for each ion detected.

3.7 Detection chamber

3.7.1 Delay-line detector

The detector consists of a pair of selected rimless MCPs in chevron configuration having a linear active diameter of 80 mm, supported by a pair of partially metallised ceramic rings 2 mm thick, 105 mm outer diameter and a 2D position-sensitive delay-line anode (Figure 3.23). The Nickel metallisation of the ceramic rings provides a good contact between the voltage supply and the MCP plates.

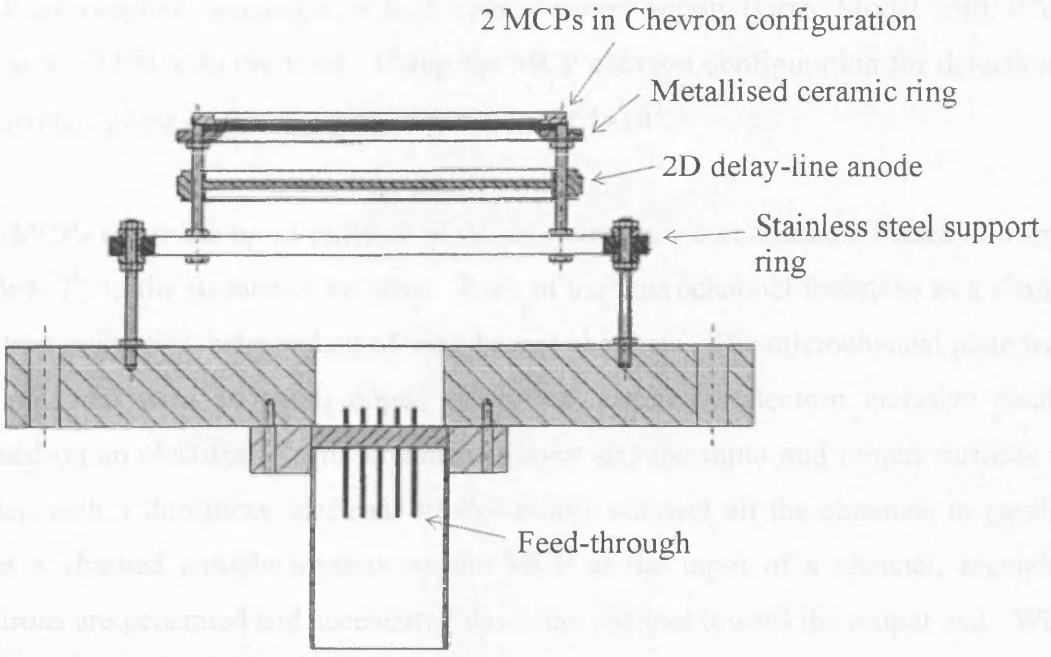

Figure 3.23 A schematic diagram showing how the MCP detector and dual wire-wound delay line anode are mounted.

The position-sensitive detector used in this experiment used to record the position and flight times of ions at the end of the TOF drift tube is a commercial RoentDek MCP (DLD80) device with delay-line anode [29-31]. This detector is a high-resolution 2D-imaging and timing device for charged particle or photon detection at high rates with multi-hit capability. This multi-hit capability, allowing the detection of two ion arrivals at the detector within tens of nanoseconds of each other, is of paramount importance in this PSCO experiment where it is necessary to detect both ions formed for each dication-neutral reactive event, whose flight times may be very close together.

3.7.1.1 Microchannel Plates

The MCP stack is mounted independently from the anode so that different anode types may be implemented. The MCP-holder system itself measures 105×7 mm. There are

two DC voltages for MCP front and back contacts and three voltages for the support plate and the anode reference and signal wires. Voltages to the back and front of the MCP are supplied by a negative high voltage power supply (Ortec Model 556): 0 V to the back, -2200 V to the front. Using the MCP chevron configuration for detection of ion arrivals gives an electron gain of the order of 1×10^7.

The MCPs are made up of millions of 25 μm pores or microchannels biased at a small angle (~7°) to the surface of the plate. Each of the microchannel functions as a channel electron multiplier, independent of the adjacent channels. The microchannel plate walls are prepared with an alkali doped silica-rich secondary electron emissive coating formed on an electrically semi-conductive layer and the input and output surfaces are coated with a thin metal electrode to electrically connect all the channels in parallel. After a charged particle impacts on the MCP at the input of a channel, secondary electrons are generated and accelerated down the channel toward the output end. When these electrons hit the channel wall, additional secondary electrons are generated. The bias across the semi-conductive layer supplies the electrons necessary to continue the electron multiplication process. This process is repeated continually yielding up to 10^4 electrons at the output for a single plate.

3.7.1.2 Position encoding

The anode that provides the position encoded data for each ion consists of a wire-wound array. Each array comprises two double wire-wound propagation delay-lines (Lecher-line). For each dimension, a collection (signal) wire and a reference wire form a wire pair. To ensure that the electron cloud emerging from the MCP is mainly collected on the signal wires, a potential difference of about +70 V of the signal wire with respect to the reference wire is applied. The anode holder is supplied with an intermediate potential with respect to the anode wire and the MCP back potential, to ensure proper charge cloud propagation and spatial broadening in the drift zone between the MCP and anode wires. The reference wire (+480 V), signal wire (+550 V) and anode holder (+150 V) voltages are supplied by a parallel resistor chain. As electrical fringing fields

can result in image distortions, the penetration of strong external electrical and magnetic fields into the electron cloud drift region are avoided.

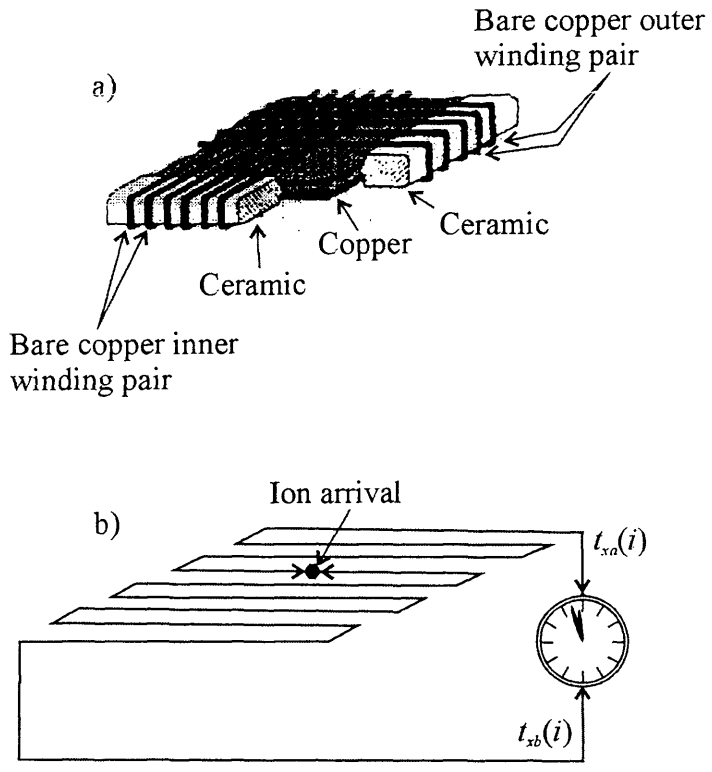

Figure 3.24 The delay-line anode where a) shows the anode and b) a delay-line for the x dimension.

The position of the detected ion fragment is encoded by the signal arrival time difference at both ends for each parallel pair delay-line, for each dimension independently. The corresponding ends of the delay-line for each dimension are located on the opposite corners of the array (Figure 3.24). Each wire has an electrical resistance of approximately 12 Ω. The four signals from both delay-line ends of each dimension are connected from the corner contacts of the anode to vacuum feed-throughs by a twisted-pair wire configuration. After DC decoupling, the signals from the feed-throughs are transmitted to a differential amplifier *via* coaxial cables.

The difference between the arrival time signals at either ends of each delay-line ($t_{xa}(i) - t_{xb}(i)$) (Figure 3.24) is proportional to the position on the MCP in the respective

dimension. The sum of these arrival times is constant for each ion arrival event, within the time resolution of about a nanosecond. The single-path signal propagation time on the delay line is approximately 0.98 ns mm^{-1} for DLD80. Thus, the correspondence between position and time in the 2D image is approximately 1.96 ns mm^{-1}. These values are only accurate to within 3% and vary slightly for each dimension. A time-to-digital converter (TDC) is used to measure the time sequence of the signals. The signal generated at the back of the MCP following an ion impact is used as time reference.

The digital encoding to receive a digital image (x_i, y_i) is

$$x_i = \frac{[t_{xa}(i) - t_{xb}(i)]}{1.96} \tag{3.21}$$

and

$$y_i = \frac{[t_{ya}(i) - t_{yb}(i)]}{1.96} \tag{3.22}$$

where $t_{xa}(i)$, $t_{xb}(i)$ $t_{ya}(i)$ and $t_{yb}(i)$ are the TDC channel numbers for each ion (i) arrival event (section 3.8.2).

Having described how the ion arrivals are detected, the following section details how the data for each ion is recorded and processed.

3.8 Signal processing

3.8.1 Differential amplifier

A 6-fold differential amplifier, the DLATR6-module, is used in signal processing. Each amplifier channel has integrated constant fraction discriminator (CFD) circuits. The amplification stage is optimised for differential signal input and amplification. In the

present configuration of the DLATR6, channel 1 processes the timing signal from the front of the MCP, channel 2 processes the timing signal from the back of the MCP providing the timing reference for the positional signals, and channels 3-6 amplify the signals from the four ends of the x and y delay-line wires. The CFD thresholds that are set to discriminate the signals from electronic noise are 500 mV for channel 2 and 170 mV for channels 3-6.

Differential amplifiers are important in applications where weak signals are contaminated by 'pick up' and other miscellaneous noise caused, for example, by transfer of a signal over long twisted pairs of wires. The detector used in the PSCO experiment has a dual delay-line anode, described in section 3.7.1, that uses long twisted wire pairs for signal transfer. The primary difference between a conventional (single-ended) output amplifier and a differential (bridged) output amplifier is that the negative terminal of the differential amplifier is active, supplying a voltage equal in amplitude and opposite in phase to the positive terminal, in contrast to the conventional amplifier where the negative terminal is grounded. The differential amplifier effectively doubles the input voltage and quadruples the output power capability P since

$$P = \frac{V_{input}{}^2}{R}, \tag{3.23}$$

where V_{input} is the input voltage and R is the resistance.

3.8.2 Data processing

The timing of the ion signals from the differential amplifiers, relative to the repeller plate pulse, are recorded using a Le Croy 3377, a 32-channel CAMAC (computer aided measurement and control) based time-to-digital converter (TDC) with multi-hit capability. The TDC is started by the same delay generator (DG) that controls the repeller plate pulse. This DG introduces a short delay between triggering the repeller

plate pulse and activating the TDC to avoid detecting the RF noise from the repeller plate pulse. The TDC is set to ignore events where it receives no ion signals following the start signal from the pulse generator. Hence, events involving multiple ion arrivals at the detector can be identified and recorded.

In order to allow a high data collection rate, the encoded ion arrival times $t_{exp}(i)$ and positional times $t_{xa}(i)$, $t_{xb}(i)$ $t_{ya}(i)$ and $t_{yb}(i)$ from the 3377 are read out directly *via* a fast FERA interface to a memory module (Le Croy 2367). The memory unit can accumulate 512 kB worth of data at a rate of 100 ns per cycle. Once full, data acquisition is paused and the contents of the memory unit are rapidly transferred to a 400 MHz PC *via* a SCSI interface incorporated in a DDC3000/PCI minicrate, for offline processing. The use of FERA (Fast Encoding and Readout Analogue to digital converter) interfacing coupled with data transfer using a SCSI bus allows this system to gather data at over 50 kHz. Under appropriate reaction source region conditions, *i.e.* high source field, all the ions formed in the dication-neutral reactions may be detected, as explained in Chapter Two. The low energy beams (2-20 eV) used in the PSCO experiment facilitate the occurrence of chemical reactions by allowing a long enough interaction time between the reactants for bonds to be formed and broken.

3.8.3 Data gathering

A computer program written in Visual Basic is used to set all the voltages (-10 to +10 V) after the ion source extraction lens, up to and including the hemisphere voltages. It also collects and pre-processes the data from the Le Croy unit. Once the 512 kB of data has been read from the memory unit to the PC, as described above, the memory unit is cleared and data collection restarted. The PC then performs some preliminary processing of the data whilst the memory is refilling, to ensure only events of interest are stored. The data the PC receives from the memory unit comprises of up to ten 'times' for each repeller plate pulse. These ten times correspond to a 'pair' event, being the arrival of two ions, with each arrival generating five times. In a case where ten

times are not present, the flight time of the ion or ions making up the event are simply histogrammed to form a mass spectrum.

3.9 Summary

This chapter has described the experimental arrangement of the position-sensitive coincidence time-of-flight mass spectrometer. The data processing and gathering procedures, from which a flight time and a position at the detector for each ion arrival are obtained, are also explained.

3.10 References

[1] Hu, W. P., Harper, S. M., and Price, S. D., 2002, *Meas. Sci. Technol.* **13** (10) 1512-1522.

[2] Harper, S. M., Hu, W. P., and Price, S. D., 2002, *J. Phys. B: At. Mol. Opt. Phys.* **35** (21) 4409-4423.

[3] Dolejsek, Z., Farnik, M., and Herman, Z., 1995, *Chem. Phys. Lett.* **235** (1-2) 99-104.

[4] Ehbrecht, A., Mustafa, N., Ottinger, C., and Herman, Z., 1996, *J. Chem. Phys.* **105** (22) 9833-9846.

[5] Koslowski, H. R., *et al.*, 1991, *J. Phys. B: At. Mol. Opt. Phys.* **24** (23) 5023-5034.

[6] Lundqvist, M., *et al.*, 1996, *J. Phys. B-At. Mol. Opt. Phys.* **29** (3) 499-514.

[7] Fang, Z. and Kwong, V. H. S., 1997, *Phys. Rev. A.* **55** (1) 440-443.

[8] Ernstberger, B., Krause, H., Kiermeier, A., and Neusser, H. J., 1990, *J. Chem. Phys.* **92** (9) 5285-5296.

[9] Curtis, D. M. and Eland, J. H. D., 1985, *Int. J. Mass Spectrom. Ion Proc.* **63** (2-3) 241-264.

[10] Eland, J. H. D., 1993, *Meas. Sci. Technol.* **4** (12) 1522-1524.

[11] Leach, S., Eland, J. H. D., and Price, S. D., 1989, *J. Phys. Chem.* **93** (22) 7575-7583.

[12] Ruhl, E., Price, S. D., and Leach, S., 1989, *J. Phys. Chem.* **93** (17) 6312-6321.

[13] Masuoka, T., 1993, *J. Chem. Phys.* **98** (9) 6989-6994.

[14] Millie, P., *et al.*, 1986, *J. Chem. Phys.* **84** (3) 1259-1269.

[15] Lablanquie, P., *et al.*, 1985, *J. Chem. Phys.* **82** (7) 2951-2960.

[16] Parr, A. C., Southworth, S. H., Dehmer, J. L., and Holland, D. M. P., 1983, *Nucl. Instrum. Methods Phys. Res.* **208** (1-3) 767-770.

[17] Parr, A. C., Southworth, S. H., Dehmer, J. L., and Holland, D. M. P., 1984, *Nucl. Instrum. Methods Phys. Res. Sect. A-Accel. Spectrom. Dect. Assoc. Equip.* **222** (1-2) 221-229.

[18] Baraldi, A. and Dhanak, V. R., 1994, *J. Electron Spectrosc. Relat. Phenom.* **67** (1) 211-220.

[19] Martensson, N., *et al.*, 1994, *J. Electron Spectrosc. Relat. Phenom.* **70** (2) 117-128.

[20] Gelius, U., *et al.*, 1990, *J. Electron Spectrosc. Relat. Phenom.* **52** 747-785.

[21] Harkoma, M. and Akseia, S., 2002, *J. Electron Spectrosc. Relat. Phenom.* **122** 209-219.

[22] Klemperer, O., *Electron Optics*. Cambridge University Press ed. 1971.

[23] Ovrebo, G. K. and Erskine, J. L., 1981, *J. Electron Spectrosc. Relat. Phenom.* **24** (2) 189-204.

[24] Ibach, H., *Electron Spectroscopy for surface analysis*. 1977.

[25] Jost, K., 1979, *J. Phys. E: Sci. Instrum.* **12** 1001-1005.

[26] Wahlin, L., 1964, *Nucl. Instrum. Methods Phys. Res. Sect. A-Accel. Spectrom. Dect. Assoc. Equip.* **27** 55.

[27] Wiley, W. C. and McLaren, I. H., 1955, *Rev. Sci. Instrum.* **26** 1150-1157.

[28] Seccombe, D. P. and Reddish, T. J., 2001, *Rev. Sci. Instrum.* **72** (2) 1330-1338.

[29] Ali, I., *et al.*, 1999, *Nucl. Instrum. Methods Phys. Res. Section B: Beam Interactions with Materials and Atoms*. **149** (4) 490-500.

[30] Jagutzki, O., *et al.*, 2002, *Nucl. Instrum. Methods Phys. Res. Sect. A-Accel. Spectrom. Dect. Assoc. Equip.* **477** (1-3) 256-261.

[31] Oelsner, A., *et al.*, 2001, *Rev. Sci. Instrum.* **72** (10) 3968-3974.

[1] Hu, W. P., Harper, S. M., and Price, S. D., 2002, *Meas. Sci. Technol.* **13** (10) 1512-1522.

[2] Harper, S. M., Hu, W. P., and Price, S. D., 2002, *J. Phys. B: At. Mol. Opt. Phys.* **35** (21) 4409-4423.

[3] Dolejsek, Z., Farnik, M., and Herman, Z., 1995, *Chem. Phys. Lett.* **235** (1-2) 99-104.

[4] Ehbrecht, A., Mustafa, N., Ottinger, C., and Herman, Z., 1996, *J. Chem. Phys.* **105** (22) 9833-9846.

[5] Koslowski, H. R., *et al.*, 1991, *J. Phys. B: At. Mol. Opt. Phys.* **24** (23) 5023-5034.

[6] Lundqvist, M., *et al.*, 1996, *J. Phys. B-At. Mol. Opt. Phys.* **29** (3) 499-514.

[7] Fang, Z. and Kwong, V. H. S., 1997, *Phys. Rev. A.* **55** (1) 440-443.

[8] Ernstberger, B., Krause, H., Kiermeier, A., and Neusser, H. J., 1990, *J. Chem. Phys.* **92** (9) 5285-5296.

[9] Curtis, D. M. and Eland, J. H. D., 1985, *Int. J. Mass Spectrom. Ion Proc.* **63** (2-3) 241-264.

[10] Eland, J. H. D., 1993, *Meas. Sci. Technol.* **4** (12) 1522-1524.

[11] Leach, S., Eland, J. H. D., and Price, S. D., 1989, *J. Phys. Chem.* **93** (22) 7575-7583.

[12] Ruhl, E., Price, S. D., and Leach, S., 1989, *J. Phys. Chem.* **93** (17) 6312-6321.

[13] Masuoka, T., 1993, *J. Chem. Phys.* **98** (9) 6989-6994.

[14] Millie, P., *et al.*, 1986, *J. Chem. Phys.* **84** (3) 1259-1269.

[15] Lablanquie, P., *et al.*, 1985, *J. Chem. Phys.* **82** (7) 2951-2960.

[16] Parr, A. C., Southworth, S. H., Dehmer, J. L., and Holland, D. M. P., 1983, *Nucl. Instrum. Methods Phys. Res.* **208** (1-3) 767-770.

[17] Parr, A. C., Southworth, S. H., Dehmer, J. L., and Holland, D. M. P., 1984, *Nucl. Instrum. Methods Phys. Res. Sect. A-Accel. Spectrom. Dect. Assoc. Equip.* **222** (1-2) 221-229.

[18] Baraldi, A. and Dhanak, V. R., 1994, *J. Electron Spectrosc. Relat. Phenom.* **67** (1) 211-220.

[19] Martensson, N., *et al.*, 1994, *J. Electron Spectrosc. Relat. Phenom.* **70** (2) 117-128.

[20] Gelius, U., *et al.*, 1990, *J. Electron Spectrosc. Relat. Phenom.* **52** 747-785.

[21] Harkoma, M. and Aksela, S., 2002, *J. Electron Spectrosc. Relat. Phenom.* **122** 209-219.

[22] Klemperer, O., *Electron Optics*. Cambridge University Press ed. 1971.

[23] Ovrebo, G. K. and Erskine, J. L., 1981, *J. Electron Spectrosc. Relat. Phenom.* **24** (2) 189-204.

[24] Ibach, H., *Electron Spectroscopy for surface analysis*. 1977.

[25] Jost, K., 1979, *J. Phys. E: Sci. Instrum.* **12** 1001-1005.

[26] Wahlin, L., 1964, *Nucl. Instrum. Methods Phys. Res. Sect. A-Accel. Spectrom. Dect. Assoc. Equip.* **27** 55.

[27] Wiley, W. C. and McLaren, I. H., 1955, *Rev. Sci. Instrum.* **26** 1150-1157.

[28] Seccombe, D. P. and Reddish, T. J., 2001, *Rev. Sci. Instrum.* **72** (2) 1330-1338.

[29] Ali, I., *et al.*, 1999, *Nucl. Instrum. Methods Phys. Res. Section B: Beam Interactions with Materials and Atoms*. **149** (4) 490-500.

[30] Jagutzki, O., *et al.*, 2002, *Nucl. Instrum. Methods Phys. Res. Sect. A-Accel. Spectrom. Dect. Assoc. Equip.* **477** (1-3) 256-261.

[31] Oelsner, A., *et al.*, 2001, *Rev. Sci. Instrum.* **72** (10) 3968-3974.

Chapter 4

Data processing and presentation

4.1 Introduction

This chapter describes how the raw data, from the PSCO spectrometer, are processed to allow the determination of the dynamics and kinematics of two and three-body dication-neutral reactions [1, 2]. After plotting a coincidence spectrum [3] to reveal the reactive channels, the initial x, y and z velocity components in the laboratory (LAB) frame may be calculated from the flight time and positional data of each ion in an ion pair for each reactive channel. These velocities are then converted to the centre-of-mass (COM) frame to facilitate the understanding of the reaction dynamics.

4.2 Coincidence spectrum

The two flight times recorded for a pair of ions, detected from the same reactive event, are plotted in a two dimensional histogram, called a coincidence spectrum (Figure 4.1). The flight time of the heavier ion in the pair is plotted on the x-axis and the lighter ion on the y-axis. In an A^{2+}-B collision system, a peak will be observed in the coincidence spectrum each reactive channel forming two monocations. Plotting a coincidence spectrum in this way makes it possible to select the data pertaining to a particular reactive channel in the collision system and, therefore, determine the dynamics and energetics of that individual channel. The following sections describe how these details are extracted from the data in the coincidence spectrum.

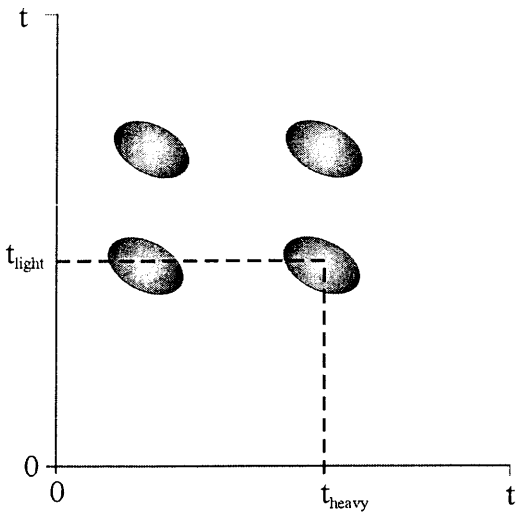

Figure 4.1 A schematic representation of a coincidence spectrum.

4.3 Determination of *x*, *y* and *z* velocity components

As mentioned in Chapter Three, the data collection program receives five times for each ion arrival, a total of ten times for the pair events of interest. The position of arrival of each ion at the detector is determined from the difference between t_{x1} and t_{x2}, t_{y1} and t_{y2}, which is proportional to the position on the MCP in the respective dimension. The correspondence between position and time in the 2D image is ~1.96 ns mm^{-1}, hence the position of an ion *i* (Figure 4.2) may be determined from

$$x(i) = \frac{[t_{x1}(i) - t_{x2}(i)]}{1.96} \tag{4.1}$$

$$y(i) = \frac{[t_{y1}(i) - t_{y2}(i)]}{1.96} \tag{4.2}$$

From the position of each ion at the detector, the x and y lab velocity vectors $v_x(i)$ and $v_y(i)$ for each of the product ions can be calculated relative to the experimentally determined point of dication-neutral interaction (x_0, y_0):

$$v_x(i) = \frac{(x(i) - x_0)}{t_T(i)} \tag{4.3}$$

$$v_y(i) = \frac{(y(i) - y_0)}{t_T(i)} \tag{4.4}$$

where $t_T(i)$ is the total flight time of the ion. The point of interaction (x_0, y_0) is determined from the (x, y) position of the unreacted dication beam at the detector.

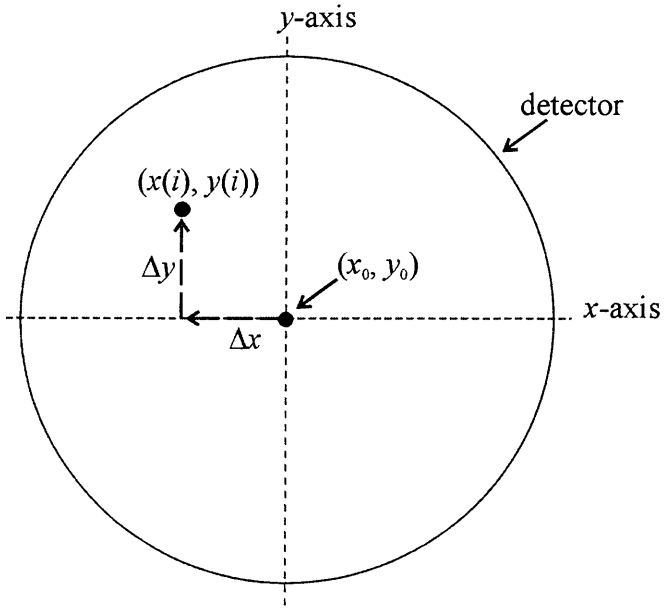

Figure 4.2 A schematic diagram of the detector indicating the point of dication-neutral interaction (x_0, y_0) and the position of an ion arrival $(x(i), y(i))$.

The experimental TOF $t_{exp}(i)$ recorded for the arrival of an ion at the detector is not equal to the total flight time, $t_T(i)$, of the ion. This difference is due to the delay inserted between the repeller plate pulse and the start of data collection, to avoid detecting any

noise from the repeller plate pulse, along with other electronic timing delays. If the sum of these delays is denoted c then

$$t_T(i) = t_{exp}(i) + c. \tag{4.5}$$

So to determine $t_T(i)$ from the $t_{exp}(i)$ values recorded by the TDC a value for c is required, which in turn requires a calibration of the mass spectrometer. The measured flight time $t_0(i)$ of an ion i of mass $m(i)$ and charge $z(i)$ which has no initial velocity along the principle z-axis of the TOF mass spectrometer is given by the fundamental mass spectrometric equation for a TOF mass spectrometer [4]:

$$t_0(i) = k\sqrt{\left(\frac{(m(i)}{z(i)}\right)} + c \tag{4.6}$$

where k is a constant depending on the geometry of the TOF mass spectrometer and the electric fields it employs. The value $t_0(i)$ is often termed the 'thermal' or 'zero kinetic energy' flight time. In order to determine c it is necessary to know $t_0(i)$ for two ions of different mass but, since the PSCO TOF mass spectrometer samples the ions from ion beams which always have a velocity component along the z-axis, it is not possible to measure thermal flight times directly. However, since the PSCO ion beams that are generated have a known velocity towards the detector, values of $t_0(i)$ can be determined from measured values of $t_{exp}(i)$ using the braking time relationship of Wiley and McLaren [4]:

$$t_{exp}(i) = t_0(i) - \frac{(2m(i)E)^{\frac{1}{2}}}{qz(i)F} \tag{4.7}$$

where F is the electric field across the source region of the TOF mass spectrometer and E is the ion's energy along the z-axis towards the detector. So, to determine $t_0(i)$ and F, $t_{exp}(i)$ is plotted against E for two ions of different mass and $t_0(i)$ and F are determined from the intercept and the gradient respectively. The values of F determined are in excellent agreement with those derived from the magnitude of the voltage applied to the

repeller plate and the length of the source region (Chapter Five). With $t_0(i)$ determined for two different ions of different mass, c can be calculated by solving Eq. 4.3 simultaneously. With c determined, $v_x(i)$ and $v_y(i)$ can be determined using Equations 4.3-4.5. As described earlier, x_0 and y_0, the x and y co-ordinates of the ion beam as it crosses the interaction region, are determined from the central position of the unreacted dication beam on the detector.

The z component of an ion's velocity v_z is determined from the deviation between its flight time $t_{exp}(i)$ and its the thermal flight time $t_0(i)$ by rearranging equation 4.7 and expressing E in terms of $v_z(i)$

$$v_z(i) = -\left[t_{exp}(i) - t_0(i)\right]\frac{Fqz(i)}{m(i)} \qquad (4.8)$$

where a positive value of $v_z(i)$ indicates motion towards the detector.

From Equation 4.8, it is apparent that any variations in $t_{exp}(i)$ that are not due to differences in ionic velocity will translate into an uncertainty in the magnitude of $v_z(i)$ and degrade the energy resolution of the PSCO experiment. Thus, any other factors which cause variation in $t_{exp}(i)$ must be minimised to achieve as high an energy resolution as possible. To this end, a high-quality space focus is required in the TOF mass spectrometer and a pulsed dication beam, which restricts where reactions can occur in the source region. The PSCO TOF mass spectrometer is a second-order focusing instrument [5-7] and is described in detail in Chapter Three. Briefly, the second-order focusing spectrometer (Figure 4.3) is a two-field device where the ratio of the field strengths, applied using a sophisticated lens arrangement, are adjusted to improve space focusing resulting in narrower ionic peaks in the time-of-flight mass spectrum, as described in Chapter Three and Appendix C, to satisfy the following relationship:

$$\left(\frac{d^2 t_{exp}}{ds^2}\right)_{s=s_0,u=u_0} = 0. \qquad (4.9)$$

This is in contrast to a first-order space focusing TOF spectrometer [4] where the quality of space focusing may be limited by the apparatus geometry or the magnitude of the applied fields.

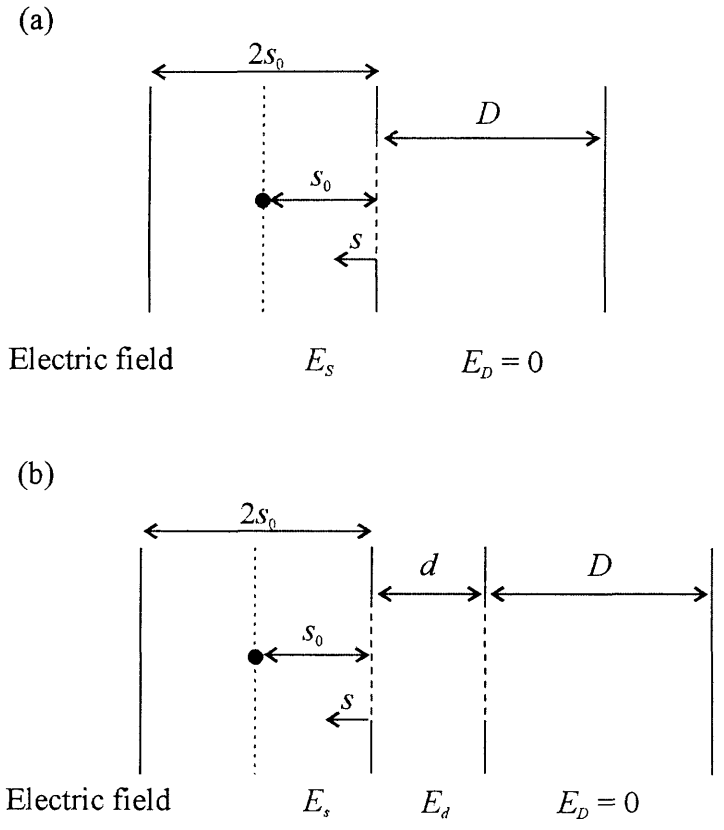

Figure 4.3 Schematic diagrams of (a) one and (b) two electric field TOF configurations, along with the basic definitions of the lengths and electric fields used in the mathematical derivations, as explained in Chapter Three and Appendix C.

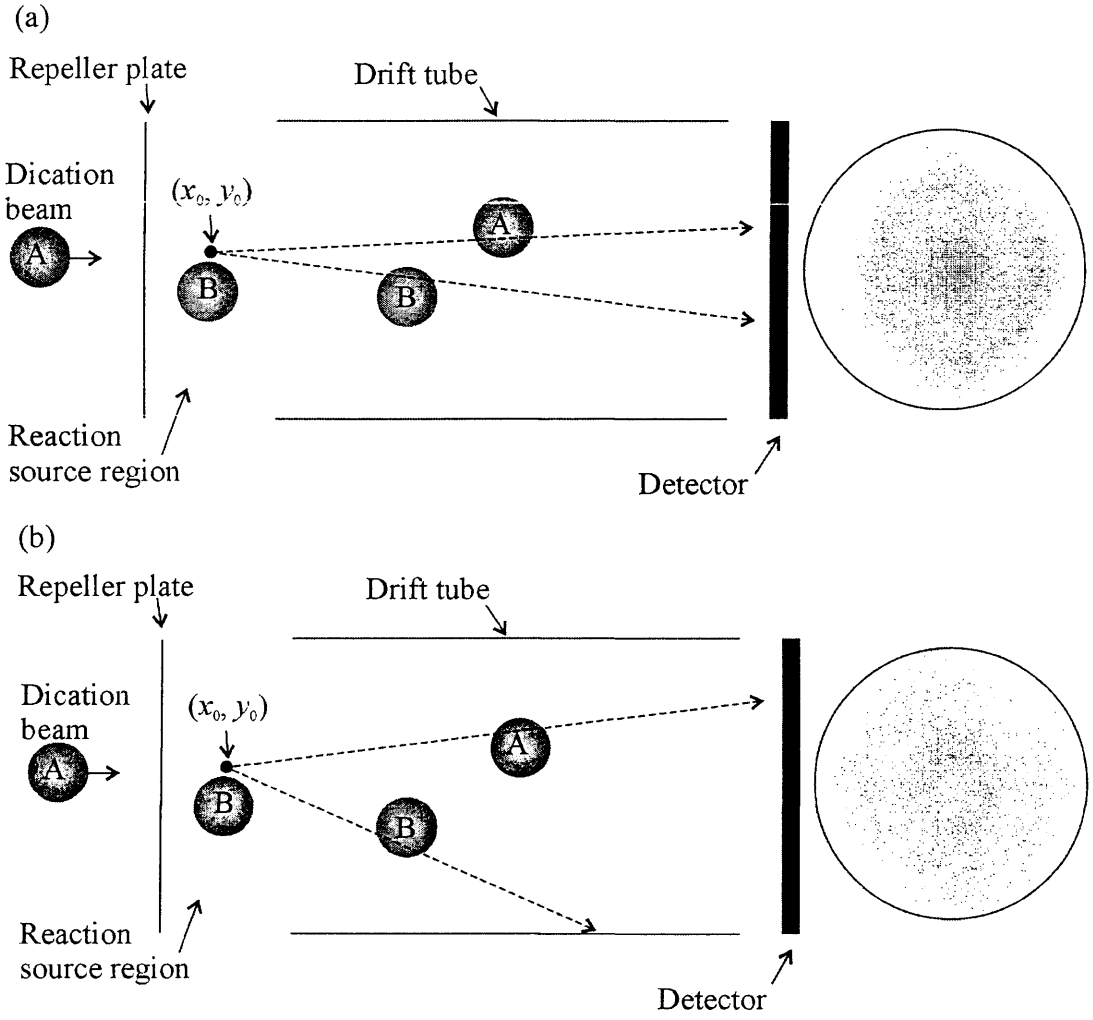

Figure 4.4 Schematic diagrams representing the effect of the magnitude of the applied source field on the detection and scattering of product ions at the detector; where (a) is at high source field, and (b) at low source field.

Equation 4.8 also shows that for a given initial velocity along the z-axis, $v_z(i)$, the time deviation of $t_{exp}(i)$ from $t_0(i)$ is inversely proportional to the source field of the TOF mass spectrometer F. Hence, to achieve maximum energy resolution it is necessary to operate at low values of F. In more detail, for an ion (i) at a low value of F there will be a greater deviation between $t_{exp}(i)$ and $t_0(i)$. Therefore, there will be a greater difference between the velocities (*i.e.* the flight times) of two ions of different mass at low F, compared with a high value of F; the positions of ion arrivals at the detector will also be

more widely distributed at low F (Figure 4.4). The uncertainties in the x and y velocity components arise largely from the fact that x_0 and y_0 are average positions and not precisely correct for each reactive event, as the dication beam has a finite size (< 3 mm) in the xy plane. However, such uncertainty is relatively insignificant because, as will be seen in the results chapters of this thesis, the product velocity vectors are primarily directed along the z-axis of the TOF mass spectrometer.

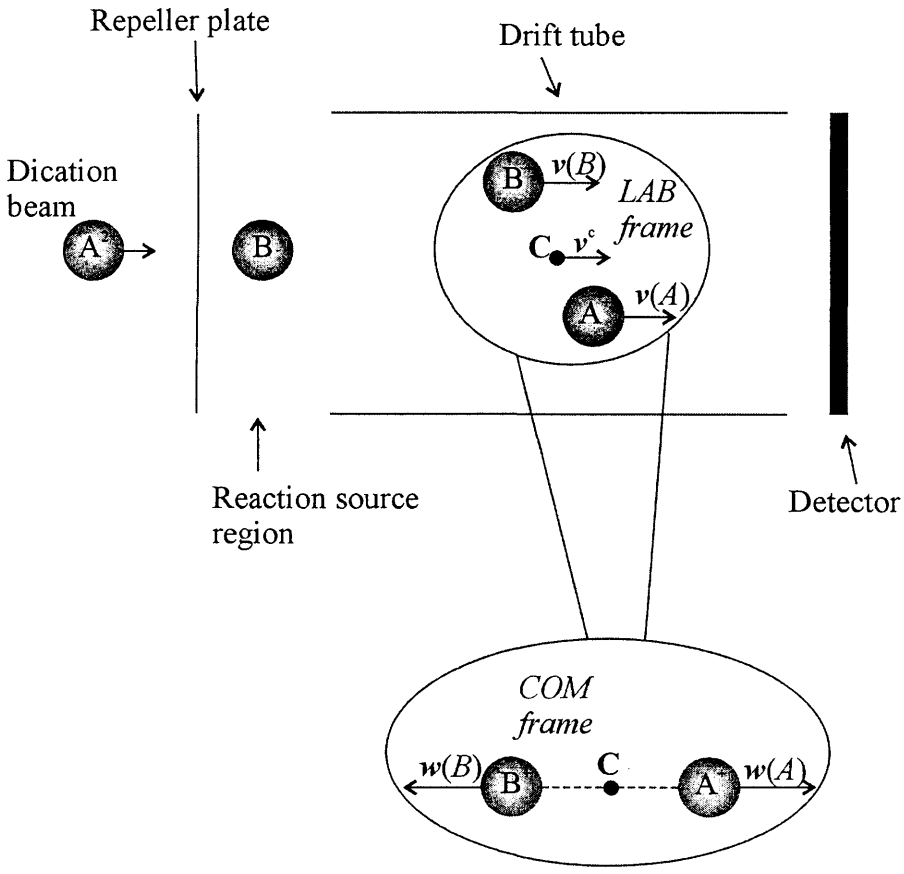

Figure 4.5 Schematic representation of the LAB frame and COM frame.

The x, y and z velocities of the product ions determined by the algorithms above are referenced to the laboratory (LAB) frame. To represent the dynamics of the reaction in a convenient way, these LAB velocities need to be converted into the COM frame

(Figure 4.5). This requires a determination of $\boldsymbol{v}^{c}$, the COM velocity of the collision system, in the LAB frame.

4.4 The centre-of-mass velocity

There are two methods by which the velocity $\boldsymbol{v}^{c}$ of the COM of the collision system in the LAB frame may be calculated. Both of these methods produce very similar values of $\boldsymbol{v}^{c}$ (Appendix B). The first method involves recognising that the speed of the reactant dication s_d is known, which is determined by the energy of the dication beam which is in turn determined by the voltage on the source block with respect to the voltage (0 V) of the source region of the TOF mass spectrometer when the reactions occur. However, since some charging occurs in the ion source a more accurate ion beam energy may be determined from the hemispherical energy analyser. The value of this energy can be confirmed by the voltages required to allow the hemispherical energy analyser to transmit the ion beam. Assuming that the dication velocity is directed along the z-axis of the TOF mass spectrometer, a good assumption given the quality of the PSCO ion beams, and that the velocity of the neutral collision partner (Appendix A), of mass m_n, is negligible in comparison to the ions velocity then $v_x^{c} = 0$ and $v_y^{c} = 0$ and

$$v_z^{c} = \frac{m_d s_d}{(m_d + m_n)}. \tag{4.10}$$

Using this method, one distinct value of $\boldsymbol{v}^{c}$ is determined for an individual experiment and this value is used for transforming every reactive event from the LAB to the COM frame.

Alternatively, for a two-body reaction, $\boldsymbol{v}^{c}$ can be derived from the velocities $v(i)$ of both product ions for each reactive event and the data converted to the COM frame on an event-by-event basis:

$$\boldsymbol{v}^{c} = \frac{m(1)v(1) + m(2)v(2)}{m(1) + m(2)}. \tag{4.11}$$

The range of values of v^c generated by this procedure agrees well with both the dication beam energy spread, deduced from the dication peak width in the TOF mass spectrum, and the average v^c value derived (Eq. 4.10) from the average dication velocity.
Once v^c has been determined, it is possible to calculate the velocity in the COM frame $w(i)$ for both product ions for each event of interest using

$$w(i) = v(i) - v^c . \tag{4.12}$$

Having determined $w(1)$ and $w(2)$ for each product ion pair, the angular relationships between these vectors may then be calculated and the motion of the COM to reveal the angular scattering in the collision system.

4.5 Angular scattering

The mutual angle θ (Figure 4.6) between the two ionic products as they separate can be calculated from the scalar product of their velocities

$$\cos\theta = \frac{w(1)\cdot w(2)}{|w(1)||w(2)|}, \tag{4.13}$$

and the angular distribution of the ionic products in the COM frame ϕ (Figure 4.7) can be determined using

$$\cos\phi = \frac{w(i)\cdot v^c}{|w(i)||v^c|}. \tag{4.14}$$

A histogram of the values of θ will reveal both the average angle of separation and its distribution. For a two-body reaction, the angle of separation would be expected to be 180°, due to conservation of momentum. In later chapters, experimental data will be presented that shows excellent agreement with this expectation.

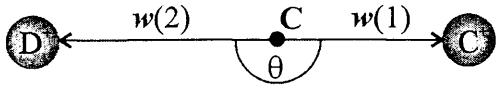

Figure 4.6 A schematic diagram of the mutual angle θ between two products in the COM frame with respect to **C** the COM of the collision system.

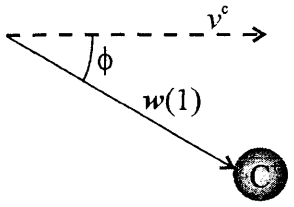

Figure 4.7 A schematic diagram of the scattering angle ϕ of an ionic product C^+ in the COM frame with respect to v^c.

The common way of representing the angular scattering in a collision system is *via* an angular scattering diagram (Figure 4.8). This is a radial histogram of each ion's speed in the COM frame (one above the horizontal line and one below) as the radial co-ordinate and the angle ϕ ($0 \leq \phi \leq 180^\circ$) of the ion's velocity with respect to the velocity of the COM as the angular co-ordinate. From the PSCO data set the velocities of the fragments are readily derived from the $w(i)$ values and the angle ϕ determined from the dot product between the individual values of $w(i)$ and v^c.

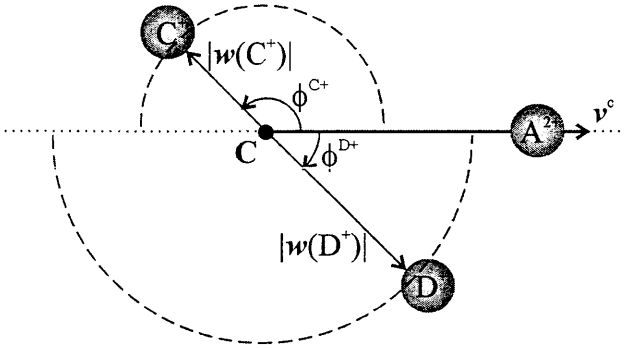

Figure 4.8 A schematic scattering diagram of the product ion velocities with respect to the COM velocity v^c. The radius of the typically semicircular shaped ionic scattering, between 0-180°, is the ionic velocity in the COM frame $w(i)$.

Having described the derivation of the ionic COM velocities and angular distributions from the experimental data, the following section will show how the KER can also be characterised along with the COM collision energy of the system E^c, leading to a determination of which product and reactant states are populated in the system.

4.6 Reaction exoergicity

The COM kinetic energy release T can be determined directly from the x, y and z velocity components in the LAB frame for a two-body reaction:

$$T = \frac{1}{2}\mu_p[(v_x(1) - v_x(2))^2 + (v_y(1) - v_y(2))^2 + (v_z(1) - v_z(2))^2] \qquad (4.15)$$

where

$$\mu_p = \frac{m(1) \cdot m(2)}{m(1) + m(2)} \tag{4.16}$$

is the reduced mass of the product ion pair.

In any reaction, energy must be conserved. So, considering the energy balance in the COM, the following expression for the exothermicity of the reaction ΔE in terms of T and E^c, the COM collision energy of the system, can be derived:

$$\Delta E = E_{products} - E_{reactants} = T - E^c. \tag{4.17}$$

An average value of the COM collision energy can be determined from the speed of the dication s_d, which is known from the settings of the hemispherical analyser. If the direction of the dication beam velocity is assumed to be along the z-axis of the TOF mass spectrometer, from the small diameter and central position of the dication beam image at the detector, and the dication velocity is significantly larger than the neutral velocity, which for the 4-25 eV dication beams employed in this experiment is a good assumption, then

$$E^c = \frac{1}{2} \mu_r s_d^2 \tag{4.18}$$

where μ_r is the reduced mass of the reactants. Alternatively, for a two-body reaction, a value of E^c can be derived individually for every reactive event from the value of $\boldsymbol{v}^c$ (Eq. 4.11) again assuming the neutral velocity is negligible:

$$E^c = \frac{\left(m_n \boldsymbol{v}^c\right)^2}{2\mu_r}. \tag{4.19}$$

Since the PSCO technique is not limited by detecting only one product ion, as described earlier, it is possible to probe the dynamics of three-body reactions. The dynamics of the third undetected body can be derived from the initial velocities of the two detected ions due to conservation of momentum:

$$-m(3)w(3) = m(1)w(1) + m(2)w(2)\,. \qquad (4.20)$$

Using this methodology, the three-body reaction dynamics can then be determined as shown below.

4.7 Three-body dynamics and energetics

In order to derive the full dynamics and energetics for dication-neutral reactions where three products are formed (Eq. 4.21), it is necessary to detect and record experimental data for two out of three of the products formed (Figure 4.9).

$$A^{2+} + B \rightarrow C^{+} + D^{+} + E \qquad (4.21)$$

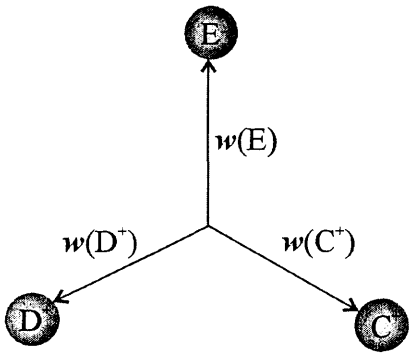

Figure 4.9 Formation of three products in a dication- neutral reaction.

Conventional experiments detect one ionic product at a time over all angles for a particular reaction in order to determine the angular distribution for each ion. The PSCO technique has a significant advantage over conventional mass spectrometric experiments because the two ionic products are detected in coincidence on an event-by-event basis allowing definitive ion pair associations to be made. Since the dynamics and energetics for two out of three of the products may be determined directly from

their flight times and positions, conservation of momentum allows the dynamics of the third undetected body to be calculated Eq. 4.20.

By rearrangement of Eq. 4.20, the following expression for $w(3)$ may be derived

$$w(3) = -\frac{(m(1)w(1) + m(2)w(2))}{m(3)}. \tag{4.22}$$

4.7.1.1 Angular distribution

Using this determination of $w(3)$, the mutual angle between $m(3)$ and either $m(1)$ or $m(2)$ may then be expressed as

$$\cos\theta = \frac{w(3).w(i)}{|w(3)||w(i)|}. \tag{4.23}$$

Determination of the angular distribution ϕ of $m(3)$ is same as for $m(1)$ and $m(2)$ as described in Eq. 4.14.

4.7.1.2 Three-body energetics

The COM energy of the neutral body is calculated from its COM velocity vector

$$E(3) = \frac{1}{2}m(3)w(3)^2 \tag{4.24}$$

and the KER for the reaction is then

$$T = \frac{1}{2}\sum_{i=1}^{3} m(i)w(i)^2 \tag{4.25}$$

allowing the exoergicity to be determined.

4.7.2 Summary

This section has described how the dynamics and energetics of a third undetected neutral body, formed in association with two detected ionic products from a dication-neutral reactive event, may be calculated from the velocity vectors of the two detected partner ions.

4.8 Conclusion

The analysis procedure that is performed on the PSCO positional and flight time data for each ion, initially plots a coincidence spectrum using the flight times for each detected pair of coincident ions. From the coincidence spectrum, the pairs data for each reactive channel, pertaining to two or three-body events, may be selected and then analysed to reveal the dynamics and energetics for each channel as described above.

4.9 References

[1] Harper, S. M., Hu, W. P., and Price, S. D., 2002, *J. Phys. B: At. Mol. Opt. Phys.* **35** (21) 4409-4423.

[2] Hu, W. P., Harper, S. M., and Price, S. D., 2002, *Meas. Sci. Technol.* **13** (10) 1512-1522.

[3] Curtis, D. M. and Eland, J. H. D., 1985, *Int. J. Mass Spectrom. Ion Proc.* **63** (2-3) 241-264.

[4] Wiley, W. C. and McLaren, I. H., 1955, *Rev. Sci. Instrum.* **26** 1150-1157.

[5] Eland, J. H. D., 1993, *Meas. Sci. Technol.* **4** (12) 1522-1524.

[6] Seccombe, D. P. and Reddish, T. J., 2001, *Rev. Sci. Instrum.* **72** (2) 1330-1338.

[7] Price, D. and Milnes, G. J., 1990, *Int. J. Mass Spectrom. Ion Process.* **99** (1-2) 1-39.

[1] Harper, S. M., Hu, W. P., and Price, S. D., 2002, *J. Phys. B: At. Mol. Opt. Phys.* **35** (21) 4409-4423.

[2] Hu, W. P., Harper, S. M., and Price, S. D., 2002, *Meas. Sci. Technol.* **13** (10) 1512-1522.

[3] Curtis, D. M. and Eland, J. H. D., 1985, *Int. J. Mass Spectrom. Ion Proc.* **63** (2-3) 241-264.

[4] Wiley, W. C. and McLaren, I. H., 1955, *Rev. Sci. Instrum.* **26** 1150-1157.

[5] Eland, J. H. D., 1993, *Meas. Sci. Technol.* **4** (12) 1522-1524.

[6] Seccombe, D. P. and Reddish, T. J., 2001, *Rev. Sci. Instrum.* **72** (2) 1330-1338.

[7] Price, D. and Milnes, G. J., 1990, *Int. J. Mass Spectrom. Ion Process.* **99** (1-2) 1-39.

Chapter 5

Commissioning the PSCO TOF spectrometer

5.1 Introduction

This chapter describes the commissioning tests used to demonstrate the performance of the PSCO TOF spectrometer. The first section demonstrates that the dication-neutral collisions in the spectrometer are occurring under single collision conditions. These conditions are a crucial aspect of the PSCO arrangement since the entire principle of the experiment relies on the fact that the two detected products ions from a dication-neutral collision are formed by the same reactive event.

In the second section, the energy resolution of the PSCO ion beam and the factors that affect the experimental resolution are discussed. This section begins with a comparison of the experimental performance of the hemispherical energy analyser with its theoretical capability. Following this, some results are presented for the Ar^{2+}-He collision system to demonstrate the quality of energy resolution that the PSCO instrument is capable of achieving.

The third section in this chapter describes the calibration of the source field in the reaction source region of the TOF mass spectrometer. Some of the preliminary results for the collisions of Ne^{2+} with Ar, presented in detail in Chapter Six, are then used to demonstrate how the magnitude of the source field affects the quality of the energy resolution in the PSCO experiments.

5.2 Single collision conditions

As described earlier in Chapter Three, the design of the PSCO experiment enables detailed dynamical and energetic information to be derived from the position and flight time data recorded for each reactive event that forms a pair of cations (Chapters Three & Four). In order to make a definitive association between the detection of an ion pair and a specific dication-neutral event, it is essential to implement 'single collision' conditions [1] in the reaction source region of the PSCO spectrometer. Under such conditions, the products formed from a dication-neutral reaction do not undergo further collisions before being detected. To implement single collision conditions, several factors need to be considered: the cross-section of the dication-neutral reaction, the ion beam flux and the pressure of the neutral collision gas, as will be discussed below.

5.2.1 Ion beam count rate

Dication-neutral reaction cross-sections are small, therefore to ensure a reasonable product ion data collection rate it is necessary to maximise the ion beam count rate. However, the double ionisation cross-sections for forming dications are usually low as will be seen from the PSCO ion count rate below [2]. This section will describe the typical magnitude of the PSCO ion beam count rate.

5.2.1.1 Calculation of the ion beam count rate

The PSCO instrument, described in detail in Chapter Three, monitors the ion beam count rate in the following way. Flight time data (*i.e.* a mass spectrum collected for each pulse of the repeller plate pulse) is accumulated in the memory module for 5-10 seconds. When the data is downloaded to the computer, the ion beam count rate is calculated by averaging the count rate, per second, from the accumulated data.

5.2.1.2 Magnitude of the ion beam count rate

Using this method for determining the count rate, the continuous ion beam count rate is typically of the order of 5000 ions s^{-1} at 30 kHz for an Ar^{2+} ion beam at 4 V (8 eV) energy. If the beam is pulsed using the vertical deflectors at the exit of the hemisphere, as described in Chapter Three, the ion beam count rate is ~2000-2500 ions s^{-1}. From the repeller plate frequency (30 kHz ≡ 1 pulse of the repeller plate every 3×10^{-5} seconds) and the count rate of a continuous ion beam (~5000 ions s^{-1}) it is possible to determine the average number of dications present in the reaction source region for each repeller plate pulse: 0.15 ions. This equates to approximately 1 ion per 10 pulses of the repeller plate. At the appropriate neutral collision gas pressure, to ensure single collision conditions, no more than one reactive event will occur for each repeller plate pulse.

5.2.2 Neutral collision gas pressure

As described above, the ion beam flux and cross-section are fixed factors in the PSCO experiment, therefore to verify single collision conditions, it is necessary to vary a factor that is easy to change: the neutral collision gas pressure. If the neutral collision gas pressure is too high, then, following the initial formation of products,

$$Ar^{2+} + CF_4 \rightarrow Ar^+ + CF_2^+ + 2F \qquad (5.1)$$

side reactions may occur; for example

$$Ar^+ + CF_4 \rightarrow CF_2^+ (+Ar + 2F) \qquad (5.2)$$

or

$$CF_2^+ + CF_4 \rightarrow CF^+ (+CF_4 + 3F). \qquad (5.3)$$

The PSCO experiment relies on the assumption that two ions detected in coincidence have been formed directly by the same primary reactive collision. If side reactions were to occur, the PSCO technique may falsely identify a coincidence event as the net effect (5.4) of reactions 5.1 and 5.3. Formation of products in this way is indistinguishable from the coincident formation of CF_2^+ with Ar^+ from the same reactive event (5.1), except that dynamics calculated for a reactive coincidence channel containing this data would be inaccurate.

$$Ar^{2+} + 2CF_4 \rightarrow Ar^+ + CF_2^+ (+2F + CF_4) \qquad (5.4)$$

Under single collision conditions, a reaction such as Eq. 5.1 forms two ionic products at a ratio of 1:1 for each reactive event. Hence, it is simple enough to monitor the intensity of the two ions formed over a range of neutral collision gas pressures in order to verify the single collision conditions. When the intensity of each of the ions (formed under SCC) is normalised to the dication intensity *i.e.* $I(X^+ / Ar^{2+})$, the plot of intensity vs. pressure should be linear.

If single collision conditions were not present in the reaction source region due to the pressure of the neutral collision gas being too high, then the relationship between CF_2^+ and Ar^{2+} would become second order, *i.e.* the graphical plot of $I(CF_2^+ / Ar^{2+})$ would no longer be linear.

As an aside, the PSCO experiment would not be used to investigate the dynamics of this particular reaction (5.1) since four product bodies are formed. As described earlier in Chapter Four, reactions forming up to three products may be studied since the dynamics and energetics of the third undetected body may be calculated by conservation of momentum from the dynamics of the two detected ionic products. Hence, the dynamics and energetics of four body reactions such as Eq. 5.1 are inaccessible.

5.2.2.1 Verifying single collision conditions

A series of experiments were carried out to monitor the intensities of the products, Ar^+ and CF_2^+ formed in Eq. 5.1, with increasing pressures of CF_4 in order to demonstrate that the PSCO dication-neutral interactions are occurring under single collision conditions. The pressure of the neutral collision gas was increased with each experiment starting at 2×10^{-6} Torr. The intensities of both Ar^+ and CF_2^+ were normalised to Ar^{2+} and plotted against pressure (Figure 5.1). The linear relationship between the pressure and $I(X^+ / Ar^{2+})$ in the high vacuum range sampled, clearly indicates that the reactions are taking place under single collision conditions.

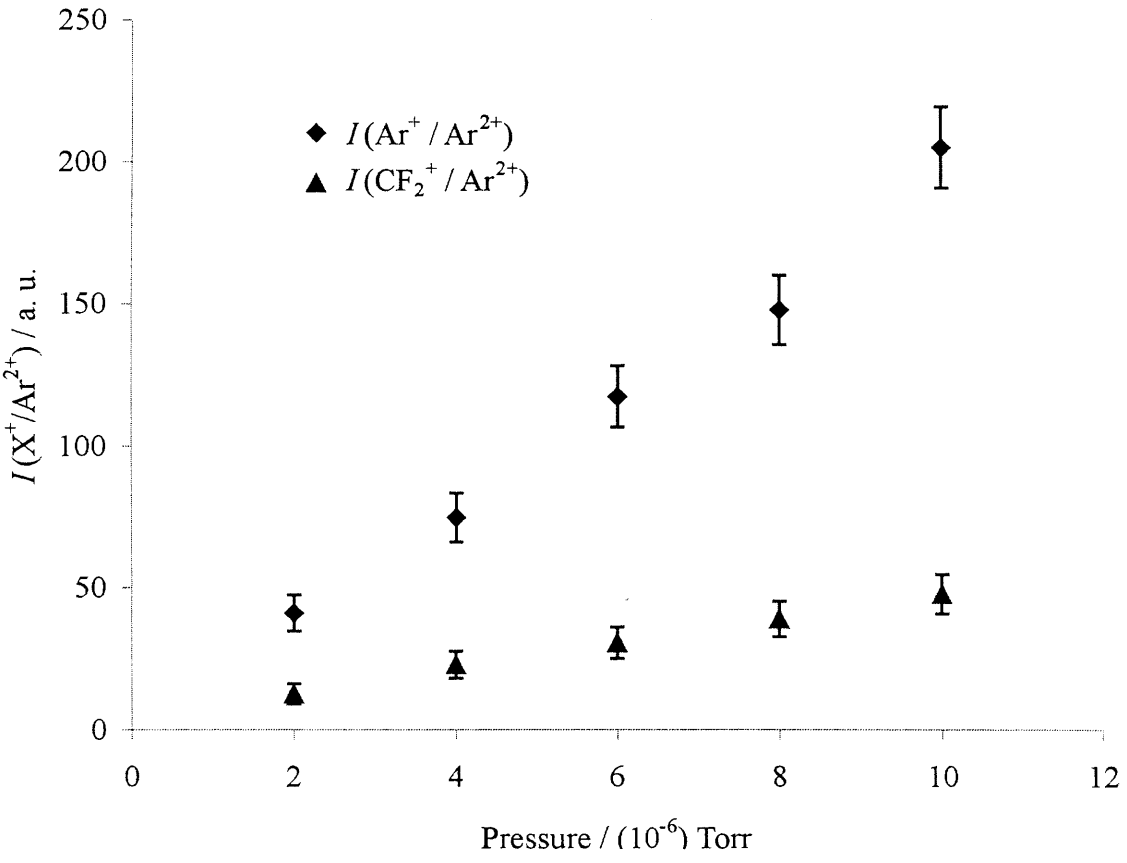

Figure 5.1 Plot of $I(X^+ / Ar^{2+})$ vs Pressure. The linearity of the plots for both ions indicates that the collisions are occurring under single collision conditions.

5.3 Energy resolution

The quality of energy resolution in the PSCO experiment described in this thesis is determined primarily by the energy resolution of the hemispherical energy analyser but also by electronic timing jitter related to the data acquisition process and the angular divergence of the beam. The first part of this section presents a comparison of the experimental performance of the hemispherical energy analyser with its theoretical capability, and the second part presents some results for the Ar^{2+}-He collision system to demonstrate the quality of energy resolution that the PSCO instrument is capable of attaining.

5.3.1 Experimental resolution of the hemispherical energy analyser

The theoretical energy resolution of the analyser E_{theo} is 1.1% of the analyser pass energy E_0 [3], and is defined by

$$E_{\text{theo}} = \frac{\Delta E_{1/2}}{E_0}, \tag{5.5}$$

where $\Delta E_{1/2}$ is the full width at half maximum (FWHM) of the energy distribution of an analysed ion beam, and E_0 is the pass energy at which the analyser is tuned, as described in Chapter Three. Ideally, the experimental energy resolution E_{exp} of the ion beam is only determined by the performance of the energy analyser (*i.e.* $E_{\text{theo}} = E_{\text{exp}}$) although, as will be shown later, other factors such as electronic timing effects also play a part in an experiment where t_{exp} is related to E_{exp}.

A retarding field (RF) experiment was carried out to investigate the performance of the energy analyser. In such an experiment, a field is applied to a mesh-covered aperture in the path of the ion beam. Ions will only be able to pass through the aperture if the beam potential V_0 is greater than or equal to the retarding field. The retarding field may then

be stepped through a range of fields that encompasses $RF_{min} < V_0 < RF_{max}$ as indicated in Figure 5.2, where RF_{min} and RF_{max} define the retarding field on the repeller plate at which the beam is not retarded and fully retarded, respectively. The larger the energy spread of the ion beam, the greater the voltage difference needed between the RF_{min} and RF_{max} to retard the beam fully (Figure 5.2).

Therefore, to retard an ion beam with a very narrow energy spread only a small difference between RF_{min} and RF_{max} is required. Hence, the energy resolution of the beam is defined by

$$\frac{RF_{max} - RF_{min}}{2}. \tag{5.6}$$

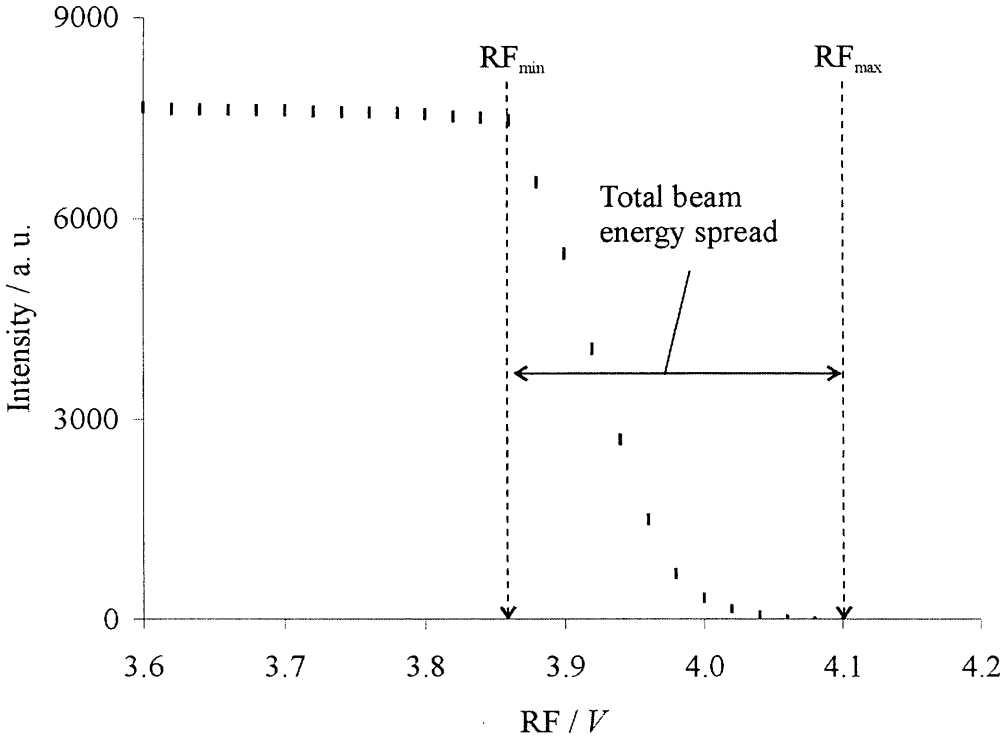

Figure 5.2 Raw data from a retarding field analysis experiment for a pass energy of 4 eV and a beam energy of 8 eV (4V).

In the PSCO experiment, a convenient mesh-covered aperture is the repeller plate

behind the reaction source region. For this retarding field experiment, the beam count rate was recorded with respect to the retarding field applied to the repeller plate (with the repeller plate not pulsed) for a range of analyser pass energies at two different beam energies. For example, with an analyser pass energy of 4 eV and an ion beam energy of 4 eV, the voltage applied to the repeller plate would be stepped at intervals of 0.005 V between 3.6 V and 4.2 V.

The voltage applied to the repeller plate is plotted against the count rate recorded at that voltage as shown in Figure 5.2. By plotting the change in the count rate between each voltage point applied to the repeller plate dC with respect to the change in the voltage dV, *i.e.* dC/dV, against the voltage applied to the repeller plate V, the energy resolution of the beam can be obtained from the FWHM (Figure 5.3).

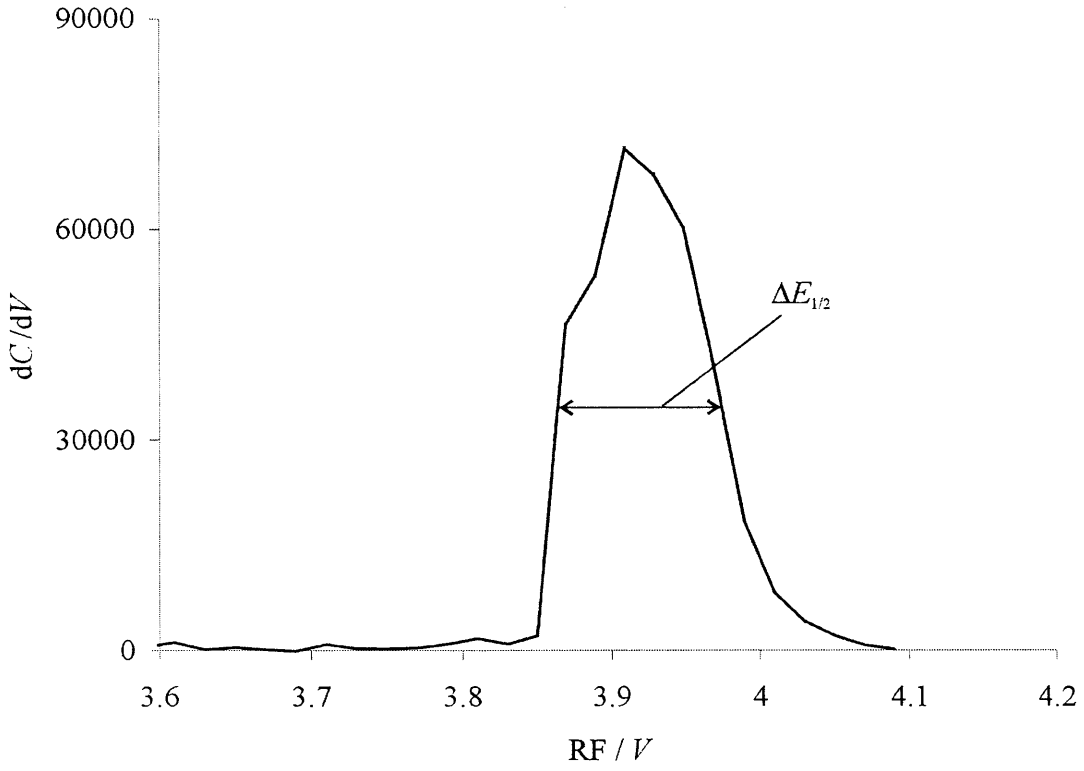

Figure 5.3 Plot of the change in count rate dC with respect to change in the voltage dV versus the potential applied to the repeller plate, RF. The error bars for each of the points are very small so a line has been drawn to represent the data trend.

Data from experiments recorded at beam energies in the LAB frame of 8 and 12 eV, respectively, are shown in Table 5.1 and Table 5.2 below. The energy resolution of the beam at each PE should be close to the theoretical resolution of the analyser (1.1%), as discussed earlier. From Table 5.1 and Table 5.2, it can be seen that the experimental energy resolution E_{exp} seems to improve from low E_0 through to high E_0 at both beam energies, and approaches the theoretical energy resolution (E_{theo}) of 1.1%. Hence, this trend indicates that the energy resolution varies depending on the pass energy, in contrast to the theoretically expected resolution which should be 1.1% of E_0.

Table 5.1 Energy resolution of an 8 eV (LAB) dication beam at different pass energies.

E_0 / eV	$\Delta E_{1/2}$ / eV	$\Delta E_{1/2}$ / E_0	*Resolution / (%)*
3	0.14	0.047	4.7
4	0.1	0.025	2.5
6	0.13	0.022	2.2

Table 5.2 Energy resolution of a 12 eV (LAB) dication beam at different pass energies.

E_0 / eV	$\Delta E_{1/2}$ / eV	$\Delta E_{1/2}$ / E_0	*Resolution / (%)*
3	0.15	0.05	5
4	0.07	0.018	1.8
6	0.1	0.017	1.7

In fact, it can be seen that the values for $\Delta E_{1/2}$ vary very little from one value of E_0 to another at both beam energies. Since the resolution approaches 1.1% at higher values of E_0, it is clear that at lower values of E_0 a factor other than the resolving capability of the analyser is determining the FWHM width of the beam.

5.3.1.1 The effect of angular divergence on the energy resolution

In order to diagnose the cause of the larger than theoretically predicted values of the FWHM observed above (Table 5.1 and Table 5.2), it is necessary to consider the relevant aspects of the PSCO arrangement. As discussed in Chapter Three, the energy resolution of the hemispherical analyser is defined by the apparatus geometry, the slit widths W_0, the radius of the equipotential R_0, and the angular divergence of the beam α (Eq. 5.7). Since W_0 and R_0 are fixed dimensions within the apparatus and E_0 is kept constant for any particular experiment, it can be seen from Eq. 5.7, that the only factor that may affect the energy resolution, *i.e.* the FWHM of the beam $\Delta E_{1/2}$, is the angular divergence of the beam, α.

$$\frac{\Delta E_{1/2}}{E_0} = \left(\frac{W_0}{2R_0}\right) + (\text{terms in } \alpha_0^2) \qquad (5.7)$$

In order to obtain the theoretical resolution of 1.1% of E_0 terms in α must be negligible. Hence, the slightly elevated FWHM cited in Table 5.1 and Table 5.2 may indicate some significant angular divergence of ions in the ion beam.

The angular divergence α arises in the ion source. In an ideal situation, the ions extracted from the source would all be formed in the same central source position, thus eliminating any angular divergence in the ion beam (Figure 5.4) (Chapter Three). However, in reality the position in the ion source at which each atom/molecule undergoes ionisation varies over all ionisation events. The effect of extracting these ions from their various positions in the ion source will result in a range of ion trajectories in the beam (Figure 5.4) *i.e.* some ions have off-axis trajectories. In these cases, the *z*-component of energy of each ionic trajectory will determine whether an ion passes through, or is deflected by, the hemispherical energy analyser. Of course, the *z*-component of an on-axis ion will be equal to its total energy. However, the total energy of an off-axis ion will be greater than its *z*-component of energy resulting in the passage of such an ion through the hemisphere, where an on-axis ion with the same energy would have been deflected. As a result, the ion beam will not have the theoretical

energy resolution (1.1%) that the hemispherical energy analyser is capable of attaining which is evident in the resolution values in Table 5.1 and Table 5.2.

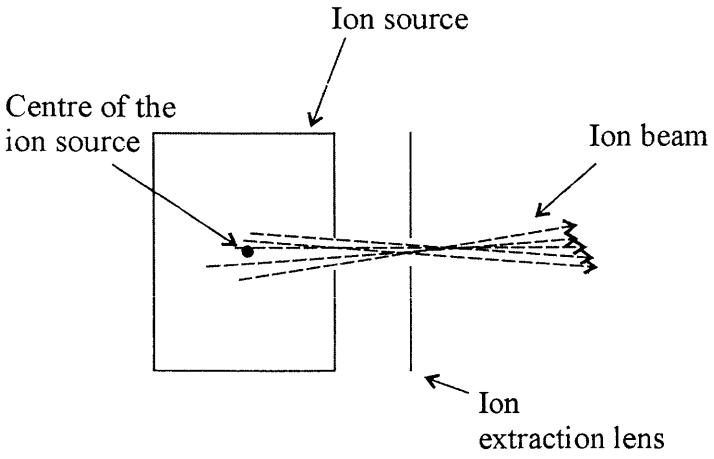

Figure 5.4 A schematic diagram of the ion source indicating the variation in ionic position in the ion source that results in angular divergence in the beam.

In summary, it is only possible to achieve the theoretical energy resolution of the ion beam if angular divergence within the beam is minimised. The retarding field experiments described above demonstrate that there is some angular divergence in the ion beam leading to a greater energy spread of the beam. However, from Table 5.2 (data at LAB ion beam energy of 12 eV), it is clear that the experimental energy resolution is in fact very close to the theoretical value of 1.1% of E_0, where E_0 = 4 and 6 eV. The improved energy resolution at the higher beam energy of 12 eV, compared to 8 eV, is not surprising since the higher velocity of the ions will lead to an improvement in the co-linearity of the beam. This section has discussed the quality of energy resolution of the ion beam at the repeller plate. However, as will be described in section 5.4, the dication peak width in the mass spectrum is actually mainly determined by timing jitters. Hence, the energy resolution of the beam is in fact of a satisfactory standard for the PSCO experiment, and the following section describes experimental data that demonstrates the excellent resolving power.

5.3.2 Energy resolution of the beam at the detector

As described in Chapters One to Four, the PSCO instrument uses coincident detection of both product cations from a dication-neutral collision to calculate the dynamics and energetics of all the species involved in that reactive event. From the energetics of the reaction, it is possible, in principle, to determine the electronic states of the reactants and products involved.

$$Ar^{2+} + He \rightarrow Ar^{+} + He^{+} \qquad (5.8)$$

In order to demonstrate the quality of energy resolution that the PSCO instrument is capable of attaining, a commissioning experiment was carried out for the reaction of Ar^{2+} with Helium (Eq. 5.8). This reactive system was chosen since it is one of the few atomic dication-neutral reactions that has been previously studied at an angularly resolved level [4-7], allowing a comparison with the results from the literature and the dynamics derived from the PSCO experiments.

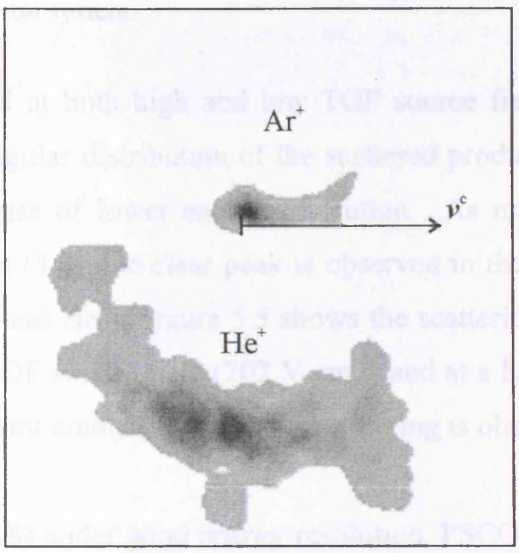

Figure 5.5 The scattering diagram for Ar^{+} and He^{+}, formed by Ar^{2+}-He collisions, with respect to the COM velocity of the collision system (E^{c} = 1.2 eV, F = 202 V cm^{-1}). The scale is represented by the horizontal arrow that is equivalent to 1.5 cm μs^{-1}.

At typical PSCO collision energies (4-25 eV), Ar^+ and He^+ (5.8) may only be formed in their ground states. There are only two states of the dication present in the PSCO ion beam, $Ar^{2+}(^3P, ^1D)$, and therefore two distinct product forming channels are present in the Ar^{2+}-He collision system (Figure 5.6). Such a small number of distinguishable product forming channels makes this collision system an ideal choice for demonstrating the resolving power of the PSCO instrument, since two distinct exoergicity signals pertaining to these asymptotes should be observed in the exoergicity spectrum.

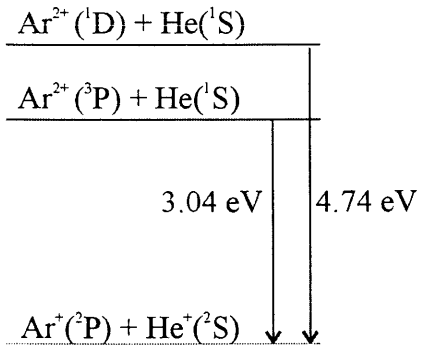

Figure 5.6 A schematic diagram of the energetics for product formation in the Ar^{2+}-He collision system.

PSCO data was recorded at both high and low TOF source fields. As mentioned in Chapter Four, the full angular distribution of the scattered products is collected at high source field at the expense of lower energy resolution. As might be expected for a simple two-body reaction (5.8) one clear peak is observed in the coincidence spectrum for the formation of Ar^+ and He^+. Figure 5.5 shows the scattering diagram for reaction (5.8) measured at high TOF source field (202 V cm^{-1}) and at a LAB collision energy of 13.4 eV, where a significant amount of sideways scattering is observed.

To study this reaction (5.8) under good energy resolution, PSCO data was recorded at a collision energy of 4.44 eV, 0.40 eV in the COM frame, with a source field of 30.4 V cm^{-1}. As shown in Chapter Four, the mutual angle θ between the velocities of the ionic products of a two-body reaction should be 180°. From Figure 5.7, it is clear that the distribution of the mutual angle θ for the reaction products (5.8) is centred at 180°. The

half-width of this distribution arises due to the finite size of the dication beam that results in a small variation in the point of dication-neutral interaction (x_0, y_0).

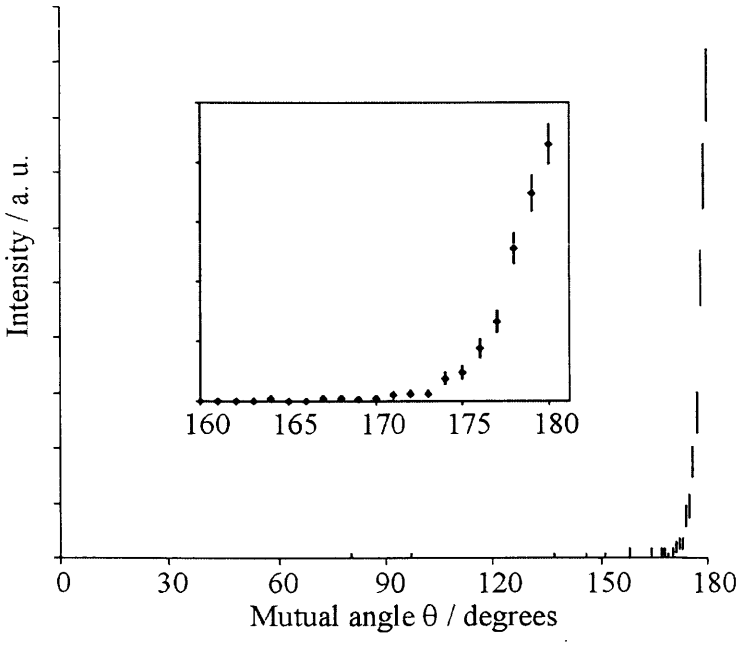

Figure 5.7 The mutual angle θ between Ar^+ and He^+ recorded at COM collision energy of 0.4 eV, $F = 30.4$ V cm^{-1}.

Figure 5.8 shows the exoergicity spectrum for formation of Ar^+ and He^+ derived from the reactive events recorded at low source field, as well as scattering diagrams for the reactive events associated with the different exoergicity signals. It is clear from Figure 5.8 that two reactive channels are present in reaction (5.8) with exoergicities of approximately 3.0 and 4.8 eV. Earlier work by Friedrich and Herman [6] has shown that reaction (5.8) forms Ar^+ and He^+ exclusively in their ground electronic states, under comparable experimental conditions to the PSCO experiment.

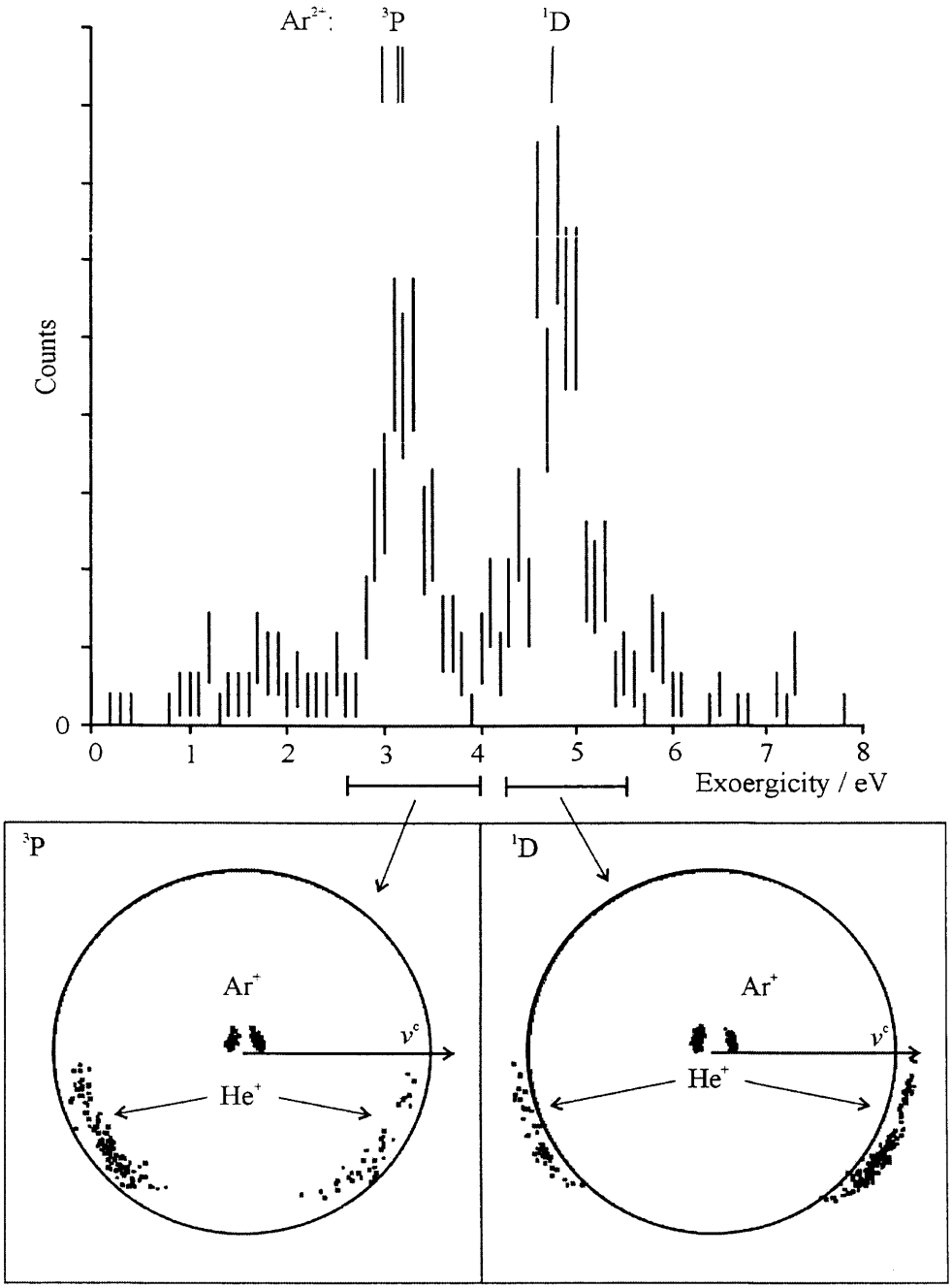

Figure 5.8 The exoergicity spectrum for the reaction of Ar^{2+} with He (E^c = 0.4 eV). The predicted exoergicities for the reaction of the $^3P_{2,1,0}$ and $^1D_2$ states of Ar^{2+} to form $Ar^+(^2P_{3/2})$ and $He^+(^2S_{1/2})$ are indicated by the vertical arrows. The inserts are the scattering diagrams obtained from the reactive events with the indicated ranges of exoergicity, corresponding to the reaction of the ^3P and ^1D states of Ar^{2+}. The circles on the scattering diagrams have a radius of 1.4 cm μs^{-1}.

The two reactive channels observed in the exoergicity spectrum may then be readily identified, in agreement with the conclusions of Friedrich and Herman [4, 6], with the reaction of the ground (^{3}P) and lowest lying excited states (^{1}D) of Ar^{2+}. The energetics of the respective processes, calculated for the lowest spin-orbit states, are:

$$Ar^{2+}(^3P) + He(^1S) \rightarrow Ar^{+}(^2P) + He(^2S) - \Delta E = 3.04\ eV \qquad (5.9)$$

$$Ar^{2+}(^1D) + He(^1S) \rightarrow Ar^{+}(^2P) + He(^2S) - \Delta E = 4.74\ eV \qquad (5.10)$$

These exoergicities (Eqs 5.9 and 5.10) are in excellent agreement with the exoergicity signals for the two peaks observed in the exoergicity spectrum (Figure 5.8). The spread of the lowest exoergicity signal above 3.0 eV in the spectrum is readily attributed to the contribution of the higher spin-orbit states of the ^{3}P manifold. There is little or no evidence of reactions of the $Ar^{2+}(^1S)$ state in the PSCO data. This observation is in accord with previous investigations of this collision system at comparable collision energies [4, 5, 7] and is explained by the fact that the curve crossing for this more exothermic reaction lies outside of the favoured window for efficient electron transfer [8].

For the Ar^{2+}-He collision system where there are very few product asymptotes, it is possible to determine the quality of energy resolution of the PSCO instrument from the spread of the exoergicity signals in the spectrum. The FWHM of the lower exoergicity signal in Figure 5.8 is 0.6 eV. Whilst it is clear that the PSCO instrument is not able to resolve the three individual electronic transitions that give rise to this signal, the resolution is adequate for the purposes of the dynamical and energetic studies undertaken in this thesis.

The scattering diagrams shown in Figure 5.8 for each of the two reactive channels, $Ar^{2+}(^3P)$ and $Ar^{2+}(^1D)$ respectively, are plotted by separate selection of the associated events for each channel. It is apparent in Figure 5.8, that the scattering of Ar^+ in the $Ar^{2+}(^3P)$-He channel is principally forward, whilst the reaction of the ^{1}D state of Ar

results in the predominant backward scattering of Ar^+. Friedrich and Herman's angularly resolved study at a slightly higher collision energy also showed that forward scattering dominates the reaction of $Ar^{2+}(^3P)$, whilst the angular distribution for the products of the reaction of $Ar^{2+}(^1D)$ seems to vary sharply with collision energy, being distinctly forward at a collision energy of 1.62 eV and sideways at 0.53 eV. At the PSCO collision energy of 0.40 eV the products of the reaction of $Ar^{2+}(^1D)$ seem to be strongly back-scattered, in accord with the trend in Friedrich and Herman's data [4].

The difference in ionic scattering between the $Ar^{2+}(^3P)$ and (^1D) channels may be rationalised in the following way. The forward scattering of Ar^+ arises from the fact that the electron transfer to the $Ar^{2+}(^3P)$ state typically occurs as the Ar^{2+} and He are departing from each other, *i.e.* a 'late' electron transfer as the collision system crosses the favoured radius for electron transfer for the second time (Chapter Two) [6, 9]. Conversely, in the $Ar^{2+}(^1D)$ channel, the electron transfer occurs when the collision system first reaches the electron transfer radius, which results in sideways scattering through an angle which is very sensitive to the collision energy. This model agrees very well with the PSCO data and similar effects are observed in the Ne^{2+}-Ar collision system (Chapter Six).

The experimentally observed difference in ionic scattering between the $Ar^{2+}(^3P)$ and (^1D) channels may also be rationalised in terms of the interspecies separation at which curve-crossing of the potential energy surfaces of the reactants and products occurs in each channel. It is clear from Figure 5.9 that the curve-crossing in the ^3P channel occurs at a larger interspecies separation than for $Ar^{2+}(^1D)$. For a curve-crossing at small interspecies separation, the two reactants are strongly coupled and hence there is a high likelihood of 'early' electron transfer on one pass through the crossing which would result in the backward scattering of Ar^+ as observed in the ^1D channel. Conversely, the coupling between the reactants in the ^3P channel is much weaker due to the larger interspecies separation and, hence, the reactants are much more likely to pass through the curve crossing twice before the electron transfer occurs.

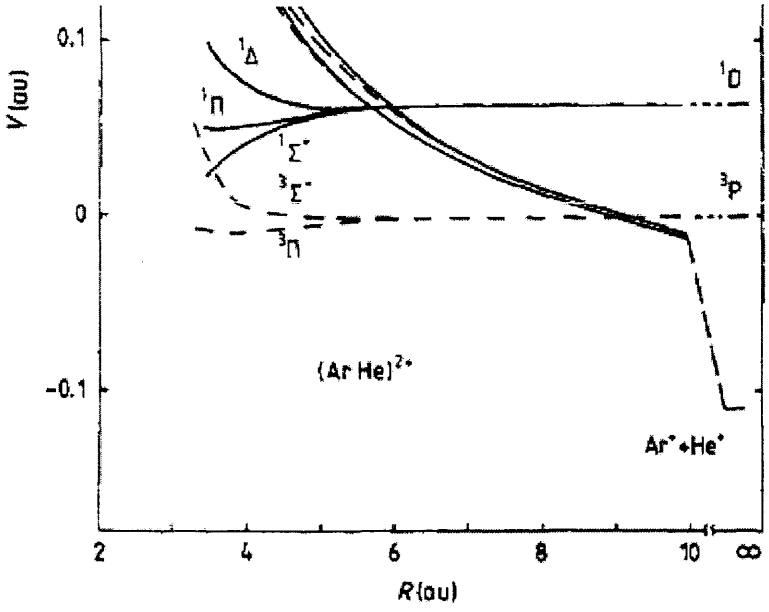

Figure 5.9 Molecular potential energy curves for $Ar^{2+}(^3P, ^1D)$-$He(1s^2)$ and $Ar^+(^2P)$-$He^+(1s)$ [6]

In summary, it is clear from Figure 5.8 that the experimental exoergicity signals for formation of the products Ar^+ and He^+, *via* the two separate reactive channels associated with the Ar^{2+} (^3P) and (^1D) dication states, are very well resolved. They are in excellent agreement with the expected exoergicities demonstrating the resolution that the instrument is able to attain.

5.4 PSCO ion beam

Chapter Three describes the formation of the continuous beam together with the current pulsed beam arrangement. This section comprises two parts. The first part shows SIMION simulations of the ion beam and the second part describes the development of the experimental pulsing arrangement.

5.4.1 Ion beam simulations

5.4.1.1 SIMION

The ion beam simulations in this section were carried out using a program called SIMION 3D. SIMION 3D version 7.0 is a Windows PC based ion optics simulation program designed to study and analyse ion optics in both two and three dimensional modes or views. Electrostatic and magnetic potential arrays may be studied with this software to determine their effect on ion trajectories. SIMION calculates the electric field of a lens by the finite difference relaxation method [10, 11]. Hypothetically, the area to be modelled may be considered covered with a Cartesian grid of points. Laplace's equation for the appropriate geometry, together with a Taylor series expansion of the potential at adjacent points is used to express the potential at an arbitrary point in the array in terms of the potential at the surrounding points. The grid points corresponding to electrodes are held fixed at the desired voltages, and the potential at each free point is calculated in terms of the surrounding points. Repeated iterations are performed, and monitoring the change in potential at a point after each cycle shows when a satisfactory degree of convergence has been achieved. Once the potential array has been calculated to a satisfactory degree of accuracy the trajectories of ions in that field can be calculated by numerical integration of their equations of motion for a given initial position and velocity. The field at a given ion position is calculated by the potential difference between the surrounding grid points.

5.4.1.2 Simulations

The simulations were carried out for the ion lenses between the source block and the entrance of the hemispherical energy analyser at source block voltages of 4 V and 6 V. These source block voltages were chosen to mimic the low ion beam energies used in PSCO experiment. The voltage on the ion extraction lens at the exit of the source block was set to -250 V (as in the PSCO machine experiment). It was clear from the SIMION

program that even raising the voltage to -150 V resulted in less efficient extraction of the ions from the source block and much more divergent beam as can be seen from Figure 5.10 and Figure 5.11 that show deliberately detuned beams with extraction voltages of -100 V and -150 V, respectively.

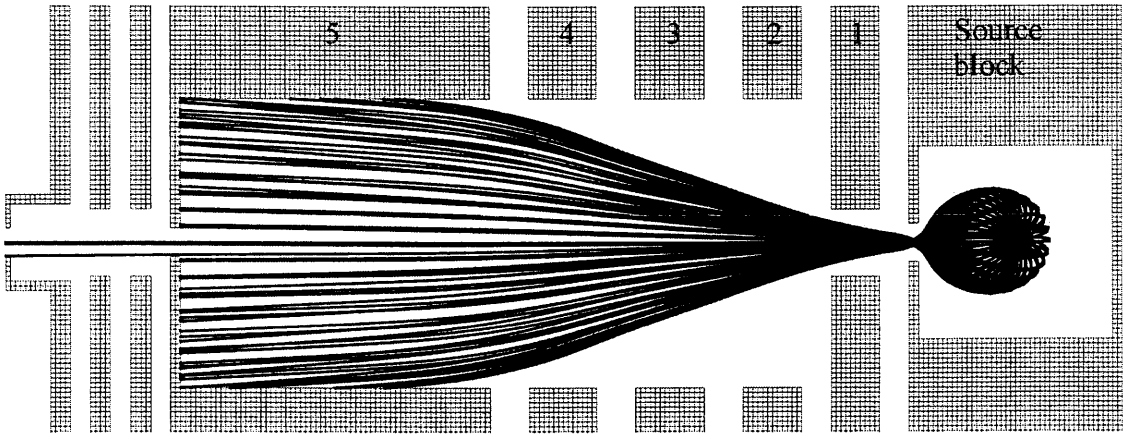

Figure 5.10 A SIMION simulation for a 'detuned' beam with theoretical voltages: source block at 6V, extraction lens at -100 V, focusing lenses 2-4 were -7 V , -17 V, and -1.3 V; the remaining lenses were set to 0 V.

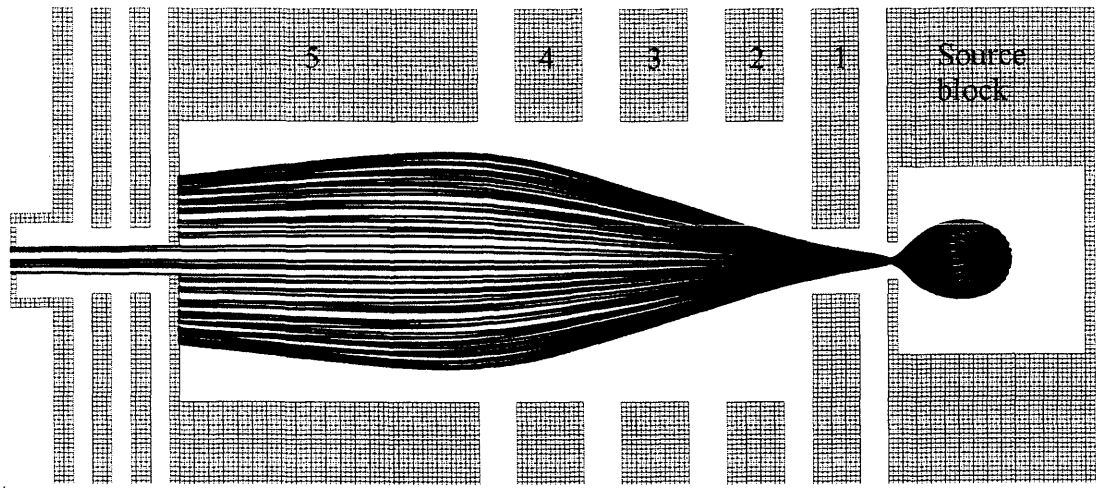

Figure 5.11 A SIMION simulation for a 'detuned' beam with theoretical voltages: source block at 4V, extraction lens at -150 V, focusing lenses 2-4 were -7 V , -17 V, and -1.3 V; the remaining lenses were set to 0 V.

The voltages on the lenses after the source block were optimised by trial and error with the aim of directing as many ions as possible into the entrance slit of the energy analyser (Figure 5.12 and Figure 5.13). These simulations were then compared with simulations using experimentally determined voltages (Figure 5.14 and Figure 5.15). The experimentally determined voltages were optimised in the PSCO machine using trial and error whilst monitoring the ion beam count rate (described in section 5.2.1).

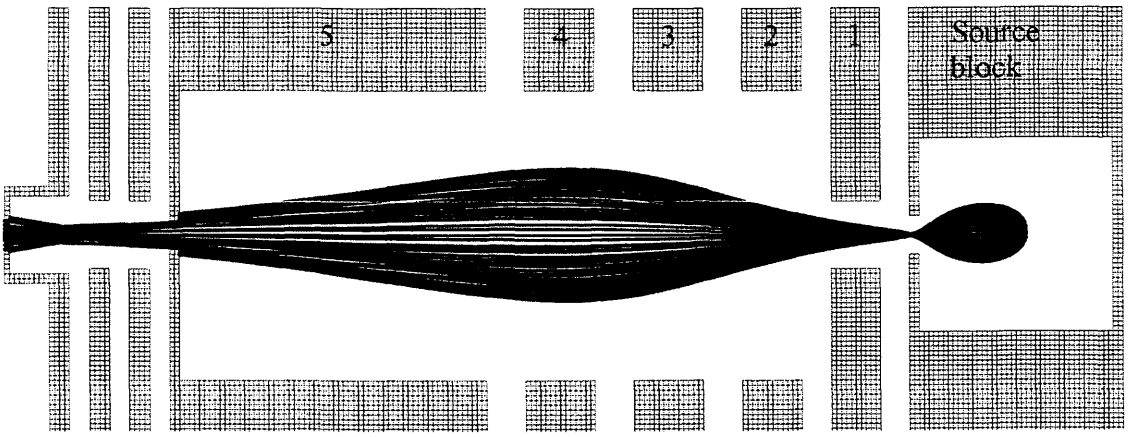

Figure 5.12 A SIMION simulation for a tuned beam with theoretical voltages: source block at 6V, extraction lens at -250 V, focusing lenses 2-4 were +10.7 V , +2 V, and +0.1 V; the remaining lenses were set to 0 V.

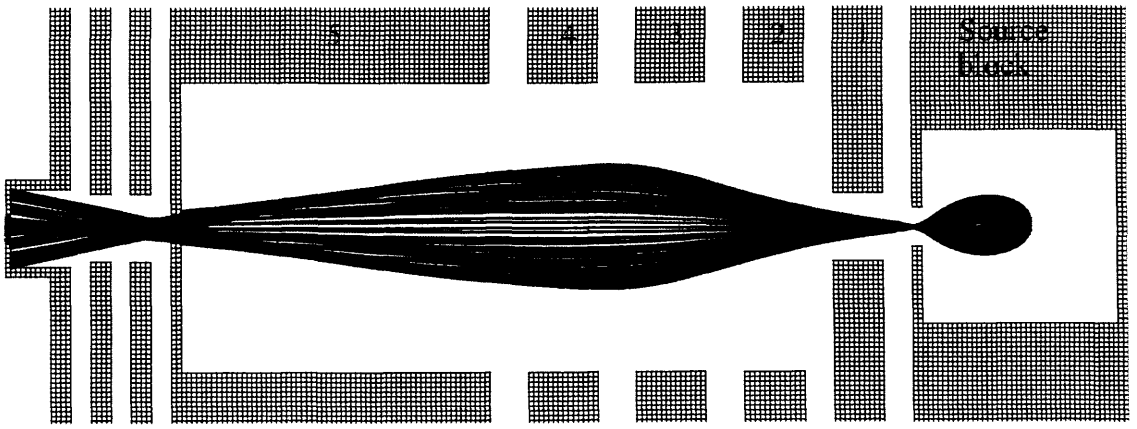

Figure 5.13 A SIMION simulation for a tuned beam with theoretical voltages: source block at 4V, extraction lens at -250 V, focusing lenses 2-4 were +1.7 V , +13 V, and -12.3 V; the remaining lenses were set to 0 V.

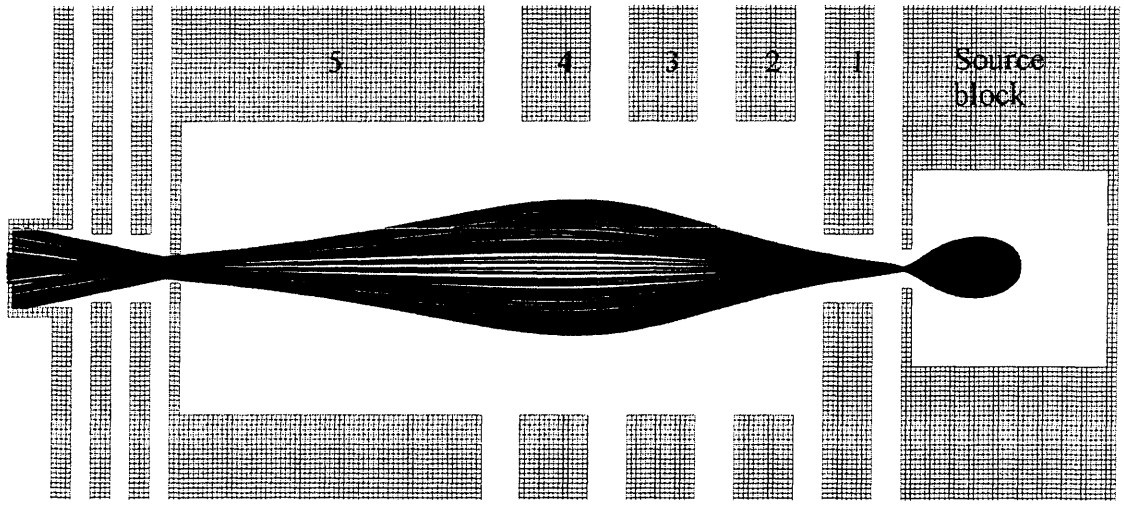

Figure 5.14 A SIMION simulation using voltages from the PSCO experiment with the source block at 6V, extraction lens at -250 V, focusing lenses 2-4 were +1 V, +5 V, and +1 V; the remaining lenses were set to 0 V.

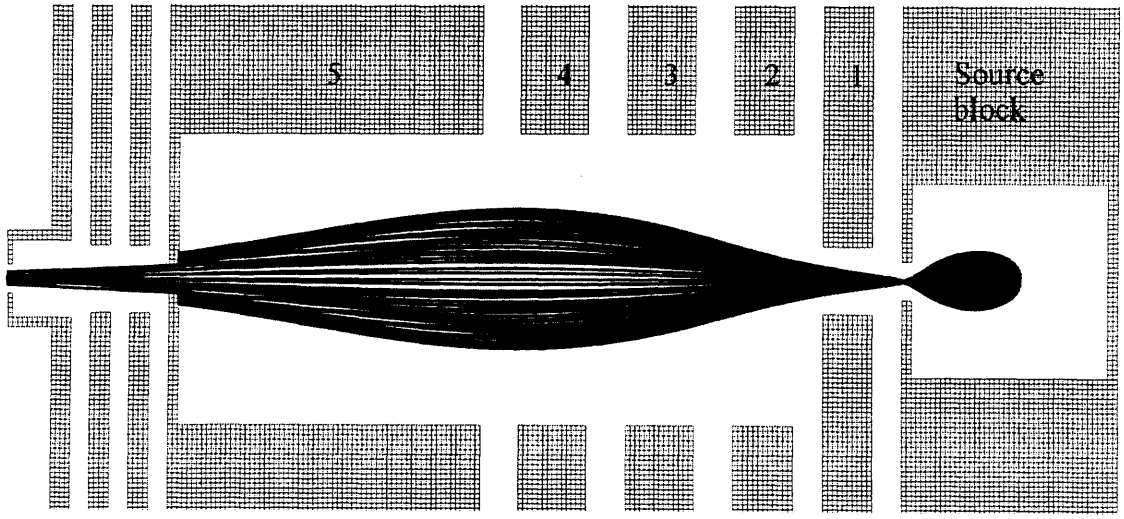

Figure 5.15 A SIMION simulation using voltages from the PSCO experiment with the source block at 4V, extraction lens at -250 V, focusing lenses 2-4 were +30.6 V, -9 V, and -2 V; the remaining lenses were set to 0 V.

5.4.1.2.1 Results

The simulations above indicate that the method used to optimise the experimental PSCO voltages (monitoring the ion beam count rate) is quite effective, giving beam shapes very similar to the ones obtained by trial and error in SIMION. However, the magnitudes of the voltages in the experimental vs. theoretical voltage situations are not exactly the same. This can be explained by considering the many different possible combinations of lens voltages that may give rise to a tuned beam due to the large number of electrostatic lenses used and the possible voltage range on each. However, it should be noted that the SIMION model assumes perfect lens shapes and does not take into account any effect of charging that may occur. Hence, the voltages that work theoretically may not actually be the most effective in experiment.

From the above simulations that used the experimental voltages, it is possible to extract angular values for the divergence of the ion beam and, hence, calculate the energy resolution of the beam, $\Delta E_{1/2} / E_0$. The resolution is determined by the slit widths W_0, the radius of the equipotential R_0, and the angular divergence of the beam α as expressed in the following equation:

$$\frac{\Delta E_{1/2}}{E_0} = \left(\frac{W_0}{2R_0}\right) + (\text{terms in } \alpha_0^2) \qquad (5.11)$$

Using equation 5.11 it can be confirmed that the angular divergence in the beam has a significant influence on the energy resolution as suggested in section 5.3.1 resulting in poorer resolution than the theoretical value of 1.1% of the pass energy. However, the simulations described above indicate that the ion beam has maximum values for the angular divergence of 6 degrees for 6 V on the source block (Table 5.3). Using equation 5.11, this magnitude of divergence gives the energy resolution of the ion beam to be 2.1% of the pass energy (4 eV) which is of the same order of magnitude as the experimentally calculated energy resolution values cited in section 5.3.1. In fact, using the values for the energy resolution determined in section 5.3.1 it seems that the

maximum value for the angular divergence must be $\alpha < 9^{o}$ for the determined energy resolution of the ion beam (Tables 5.1 and 5.2).

Table 5.3 Angular divergence of the ion beam at 4 eV pass energy and the equivalent energy resolution of the beam.

Source block / V	*Maximum* α / degrees	$\Delta E_{1/2}$ / eV	$\Delta E_{1/2} / E_0$	*Resolution* / (%)
4V	4.6	0.066	0.016	1.64
6V	6	0.084	0.021	2.1

5.4.2 Beam pulsing

This section describes the development of beam pulsing; the beam pulsing method currently employed in the PSCO arrangement is described in detail in Chapter Three. Pulsing a continuous ion beam to form packets of ions is desirable since it reduces the number of background counts in the coincidence spectrum by localising the site of dication-neutral interactions to the reaction source region alone. Background counts arise from reactions that take place outside the reaction source region *i.e.* in the acceleration region or drift tube of the time-of-flight mass spectrometer.

5.4.2.1 The coincidence spectrum

Two types of 'tails' are observed in the coincidence spectrum as indicated in Figure 5.16. The following section will describe how these tails arise and how tail (a) can be eliminated and tail (b) can be reduced by pulsing the reactant ion beam.

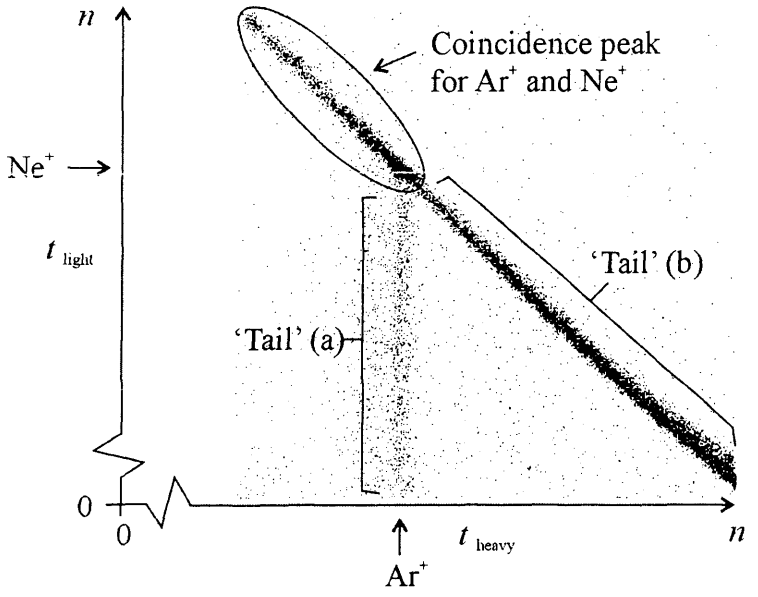

Figure 5.16 A coincidence spectrum recorded at high source field for collisions of a continuous beam of Ne^{2+} with Ar. For the reader's information, the (Ne^+ + Ar^+) coincidence peak is the most intense part of the spectrum.

5.4.2.1.1 Reactions taking place before the repeller plate pulse

The 'tail' (a), indicated in Figure 5.16, arises due to reactions using the continuous beam that take place markedly before the repeller plate pulse in the source region, which at the time is field free. Since the reactant dication already has significant translational energy in the LAB frame, the daughter monocation will have some velocity towards the detector and therefore enters the drift tube of the TOF mass spectrometer before the repeller plate pulse.

Here, in the specific example of the Ne^{2+}-Ar collision system, Ne^+ will have a range of flight times decreasing from the expected values of $t_{exp}(Ne^+)$ (*i.e.* ions encompassed by the coincidence peak). The flight time of Ne^+ decreases, since it enters the drift tube before the start time of the data acquisition cycle, triggered by the repeller plate pulse,

resulting in a shorter recorded flight time. In contrast, the daughter monocation of the neutral reactant gas Ar, having low initial translational energy, remains in the reaction source region of the TOF mass spectrometer until the repeller plate pulse is triggered. The resulting value of $t_{exp}(Ar^+)$ will vary very little in comparison to the flight times of Ar^+ in the 'true' coincidence peak. Thus, using a continuous beam results in a tail at fixed $t_{exp}(Ar^+)$ but decreasing $t_{exp}(Ne^+)$. Pulsing the dication beam should eliminate these tails as dications will not cross the source apart from in the reactant ion pulse. A comparison of Figure 5.16 and Figure 5.17 indeed demonstrates that pulsing the dication beam eliminates the presence of reactant ions in the reaction source region between pulses of the repeller plate since tail type (a) is clearly not present in Figure 5.17.

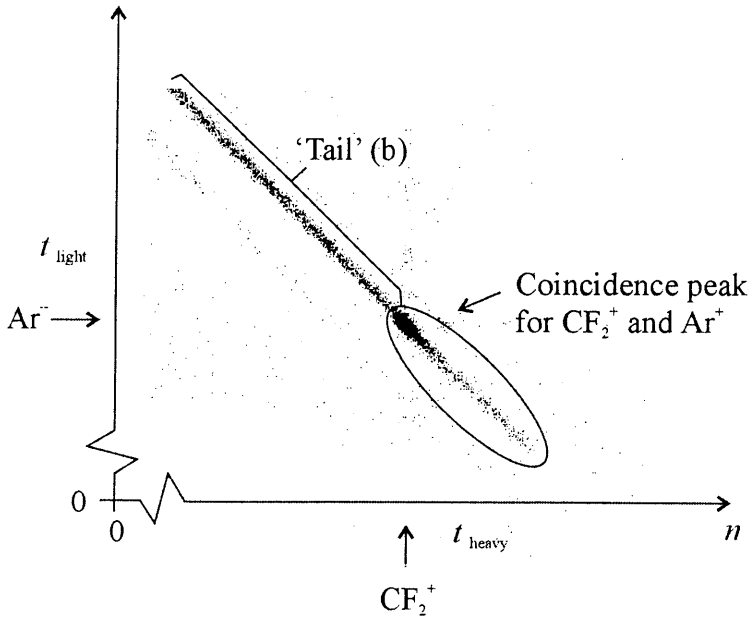

Figure 5.17 A coincidence spectrum recorded at high source field for the collisions of a pulsed beam of CF_2^{2+} with Ar, where tail (b) refers to the description in the text relating to ions formed outside the source region. It is clear, by comparison with the continuous beam coincidence spectrum in Figure 5.16 where an (a) type tail is clearly observed, that pulsing has eliminated tail type (a) in the pulsed coincidence spectrum shown in this figure.

5.4.2.1.2 Reactions taking place outside the source region

Dication-neutral collisions that take place outside the reaction source region, *i.e.* in the acceleration region or drift tube of the TOF mass spectrometer, will not experience the repeller plate pulse. Without the influence of the repeller extraction field, the flight times of the product ions are mainly determined by the initial energy of the parent reactant species A^{2+} and B and not by the extraction field.

In the PSCO experiment, the reactants have very different initial energies. The ion beam typically has a translational energy between 4-22 eV in the LAB frame and the energy of the neutral collision gas is considered negligible (Appendix A). For a collision taking place in the acceleration region or drift tube such as

$$A^{2+} + B \rightarrow A^{+} + B^{+}, \qquad (5.12)$$

A^+ has a shortened flight time compared to a typical product ion formed in the reaction source region since the species A spends a much longer time as A^{2+} before the electron transfer occurs to form A^+ and hence arrives at the detector very 'early' ($v_A{}^{2+} >> v_A{}^{+}$). In contrast, B^+ has a much longer flight time when formed outside the reaction source region, compared to its formation in the reaction source region, since it is the daughter of the neutral reactant B, which has no initial velocity.

For a continuous ion beam, reactions taking place outside the source region will therefore result in 'tails' in the coincidence spectrum (Figure 5.16 (b) and Figure 5.17 (b)), for the reasons described above, which can often obscure other reaction channels of interest. Pulsing the dication beam should reduce tail (b) as fewer dications are present in the drift tube, but tail (b) will not be eliminated as the reactant dication pulse still passes through the drift tube. A comparison of Figure 5.16 and Figure 5.17 shows that tail (b) is less intense in Figure 5.17. This indicates that pulsing the ion beam reduces the number of dications present in the acceleration region, and, hence, the tails in the coincidence spectrum, but does not eliminate them.

5.4.2.1.3 Summary

The section above describes two types of 'tails', that are observed in the coincidence spectrum when using a continuous ion beam, as indicated by (a) and (b) in Figure 5.16, and how using a pulsed ion beam can reduce or eliminate these tails. Tail (a) is caused by dication-neutral reactions occurring in the reaction source region between repeller plate pulses, and tail (b) by reactions taking place outside the reaction source region. A comparison of Figure 5.16 with Figure 5.17 clearly illustrates that pulsing the ion beam results in the elimination of tail type (a) and a reduction in tail type (b).

5.4.2.2 Developing the pulsing technique

The first factor considered in the formation of a pulsed ion beam was the importance of forming the ion pulses as close to the reaction source region as possible without perturbing the field in the source region. Since the decelerator was deemed to be too close to the source region, (one of) the vertical deflector plates at the entrance to the Wein filter was chosen as the first site at which to implement beam pulsing with a square waveform generator.

5.4.2.2.1 Pulsing at the Wein filter

At the vertical deflector in the Wein filter, the ion beam is travelling at a velocity of approximately 5 cm μs^{-1} (for an Ar^{2+} ion beam, source block voltage of 4 V and analyser pass energy of 4 eV). When the beam was pulsed at this Wein filter site, the temporal spectrum, *i.e.* a TOF spectrum recorded without pulsing the repeller plate, showed, with respect to the ion packet, a high ratio of background counts (in this case: ions not contained within the ion packet peak). It is clear from the background counts that the ions between ion pulses were not being deflected. In addition, it was only possible to form ion packets of ~10 μs in duration. Both these experimental features indicate that it was not possible to deflect the beam completely at the Wein filter.

Furthermore, since the vertical deflector is unshielded, there may have been some penetration of the pulsed electric field into the regions before and after the vertical deflectors causing undesired perturbation of the beam before and after the pulsing region. So, a more shielded region needed to be chosen as a beam pulsing site.

The second important factor for forming well defined ion packets is total deflection of the beam. This serves to eliminate the presence of background counts between ion packet signals and, consequently, reactions that occur outside of the source region or between repeller plate pulses in the reaction source region. Hence, total deflection of the beam should remove some of the 'tails' in the coincidence spectrum, described above in section 5.4.2.1. A square waveform pulser controls the bias and pulse voltages which were applied to the vertical deflector of the Wein filter, with a restriction of 400 V between the "on" and "off" voltages.

MOSFET pulsers are used since the voltage pulse rise time is very fast together with a reasonable pulse to bias voltage range. If necessary, a pulse generator could be built with a bigger pulse to bias voltage capability. At the Wein filter site, it was found that a voltage difference greater than 400 V was required to deflect the beam effectively off axis.

Since the vertical deflector at the entrance to the Wein filter proved to be an inappropriate region for beam pulsing, due to it being an unshielded region resulting in significant and undesirable perturbation of the ion beam outside of the pulsing region, using a shielded element to pulse the beam was thought to be more likely to succeed. Taking this factor in to consideration along with the initial aim of forming ion pulses as close as possible to the reaction source region, lens 4c (Figure 5.18, Figure 5.19) was chosen as the next element to be investigated in the quest for a suitable element to pulse.

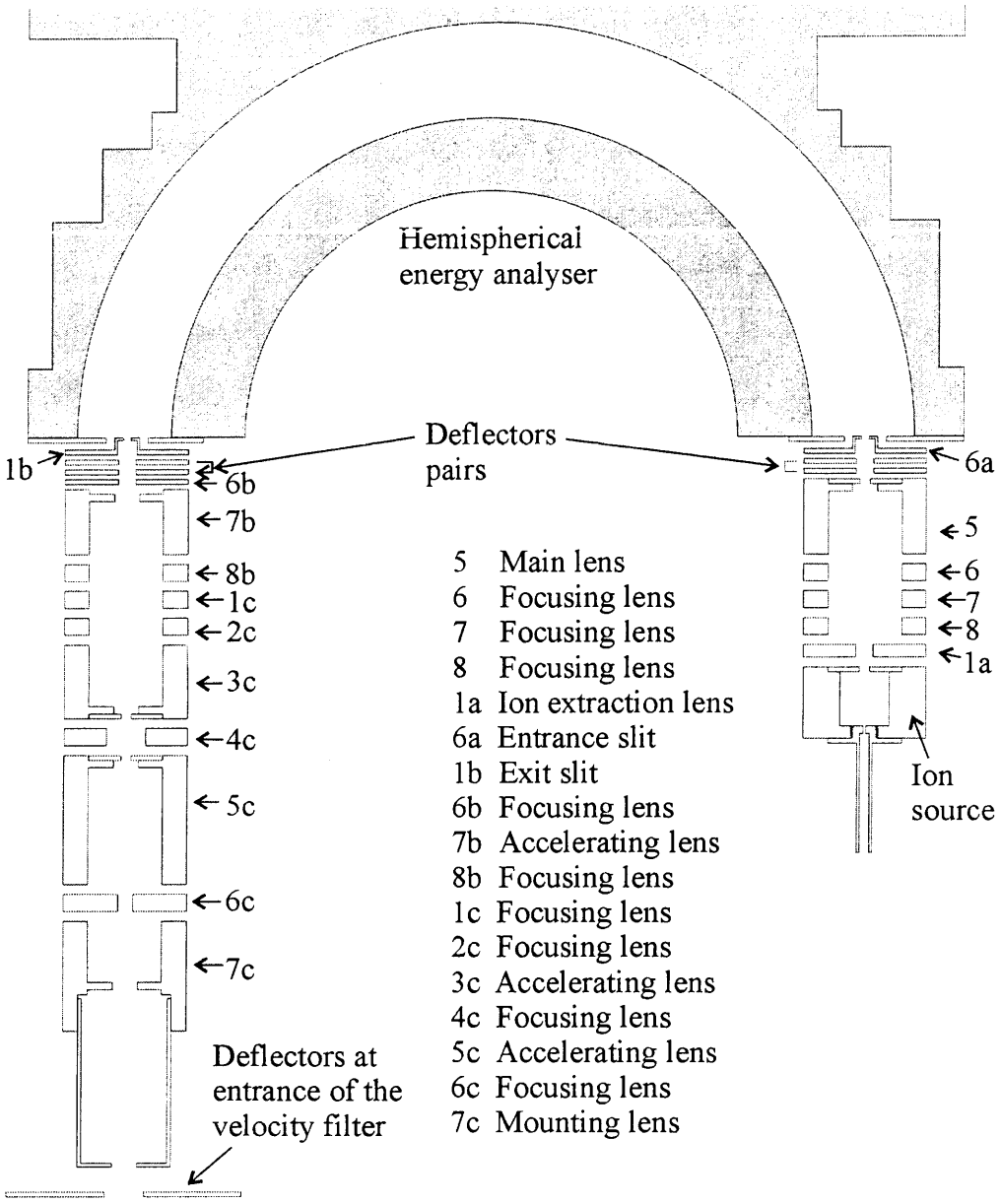

Figure 5.18 Schematic diagram of the lens stack (not to scale). Apertures of the lenses after the hemisphere are 6b: 8 mm; 7b-3c, 5c and 7c: 30 mm; exit of 3c and entrance of 5c: 4 mm; original aperture of 4c: 16 mm; 6c: 6mm.

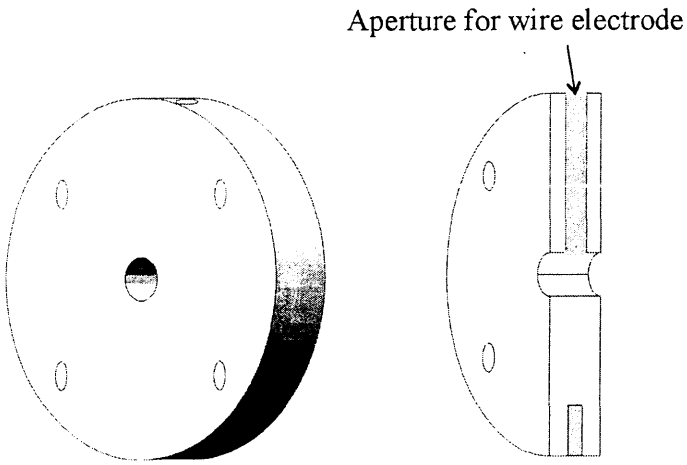

Figure 5.19 Lens 4c and cross-section.

5.4.2.3 Lens 4c

The velocity of the ion beam at lens 4c is approximately 3 cm μs^{-1}, a very similar speed compared to its velocity through the Wein filter. However, the apertures on the lenses either side of 4c (3c and 5c) are both small (4 mm), creating a shielded region around lens 4c. To implement beam pulsing using lens 4c, an electrode would need to be inserted into the lens as shown in Figure 5.19.

5.4.2.3.1 SIMION simulations of lens 4c

Firstly, the simulation program SIMION [12], described in section 5.4.1, was used to model lens 4c with an integrated electrode (Figure 5.20) to approximate what voltage would need to be applied to the electrode to deflect the beam most effectively. The simulations indicated that the original lens 4c with a 16 mm aperture resulted in the integrated electrode being too far from the ion beam to deflect it.

Therefore, the simulation was modified to investigate beam deflection with smaller apertures of 4 and 5 mm with varying voltages being applied to the electrode as shown in Figure 5.20 (a), (b) and (c). Figure 5.20 shows that with the smaller aperture lenses the electrode causes near total deflection of the beam.

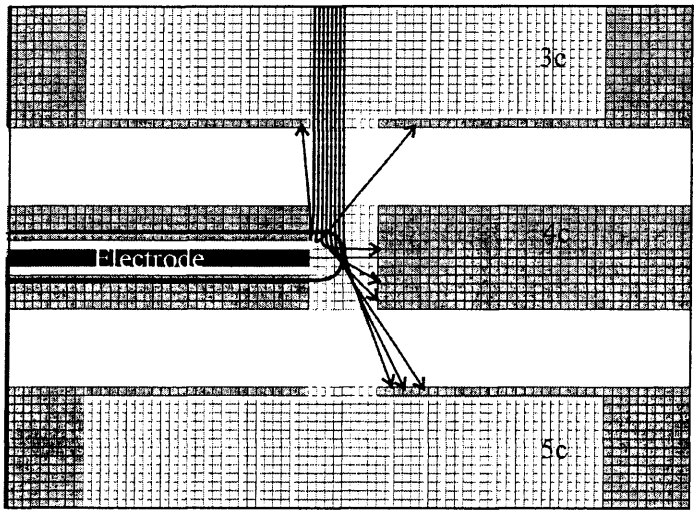

Figure 5.20 (a) A SIMION simulation indicating how the ion beam, after flying though lens 3c, is totally deflected by applying 150 V to the integrated electrode (2 mm diameter) in lens 4c (4mm aperture). Therefore, the beam cannot pass through lens 5c.

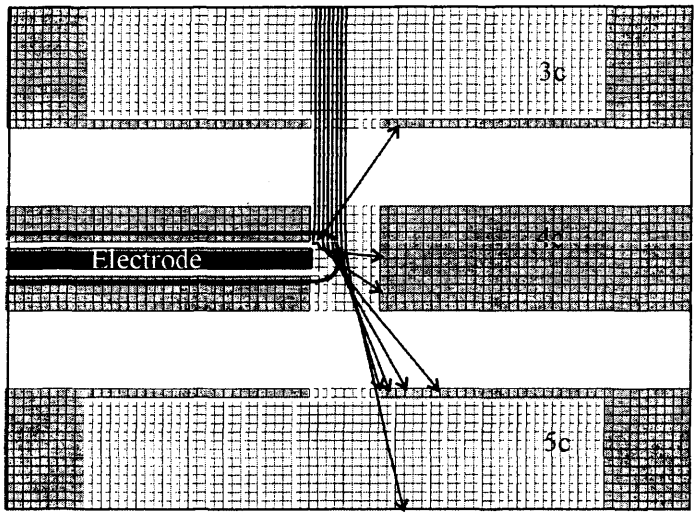

Figure 5.20 (b) A SIMION simulation indicating how the ion beam, after passing through lens 3c, is not totally deflected by applying 0 V to the integrated electrode (2 mm diameter) in lens 4c (4mm aperture), allowing some of ions to pass through lens 5c.

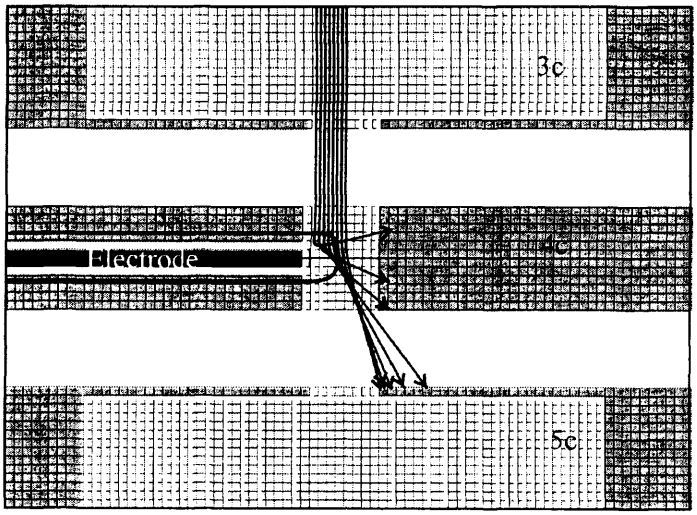

Figure 5.20 (c) A SIMION simulation indicating how the ion beam, after passing through lens 3c, is totally deflected by applying 150 V to the integrated electrode (2 mm diameter) in lens 4c (5 mm aperture).

5.4.2.3.2 Experimental tests of lens 4c

The 4c lens with 5 mm aperture was mounted in the apparatus and it was possible to create ion pulses of 1.5 μs duration. In reality, it proved impossible to cause total deflection of the beam by pulsing lens 4c with the restriction of a maximum of 400 V between the bias and pulse voltages, despite the prediction of total beam deflection by the SIMION simulations described above. The discrepancy between the simulation and experiment probably arises since the simulation does not take into account the angular divergence of the beam or the spread in the beam energy.

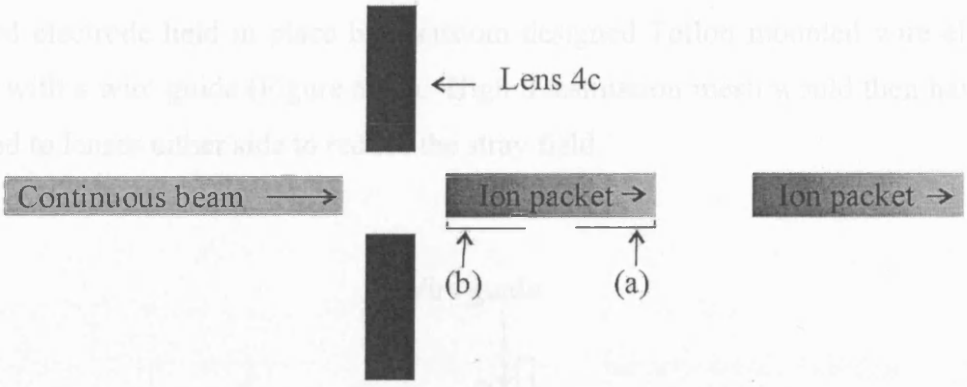

Figure 5.21 A schematic diagram of the ion beam before and after pulsing lens 4c. The greyscale gradient of the ion packets represents the pulsed beam potential in comparison to the continuous ion beam potential, where the darker grey is equivalent to higher energy. (a) and (b) indicate, approximately, the ions in the pulse that give rise to the two dication signals in the mass spectrum, as described in the text.

The TOF mass spectrum recorded with the pulsed lens 4c showed two peaks close to the expected dicationic flight time. One of the peaks was centred about the expected experimental flight time of the dication $t_{exp}(a)$ and the second peak $t_{exp}(b)$ appeared at a shorter flight time than $t_{exp}(a)$. These peaks were attributed to the dication beam now having two distinctly different energies. Figure 5.21 indicates the approximate positions of ions in the ion packet associated with each of these peaks (a) and (b) that are observe in the TOF mass spectrum. The peak at $t_{exp}(b)$ is thought to arise from the

disruption of ions that have already passed through the aperture of lens 4c which is caused by the deflection voltage as it is once more applied to the electrode in lens 4c to complete the formation of the ion packet. These ions in front of lens 4c are accelerated forward and therefore have slightly shorter flight times than ions in the packet that are at the desired beam potential (Figure 5.21). It is possible to conclude from these results that implementation of beam pulsing at lens 4c is not working as initially expected since it is evident that the ion beam is being perturbed by the pulsed field.

It was thought that the inductance of the integrated electrode might be hindering the rise time of the pulse, so a further modification of lens 4c was proposed. The position of the electrode was to be moved from inside the lens to a position in front of it creating an exposed electrode held in place by a custom designed Teflon mounted wire electrode holder with a wire guide (Figure 5.22). High transmission mesh would then have been attached to lenses either side to reduce the stray field.

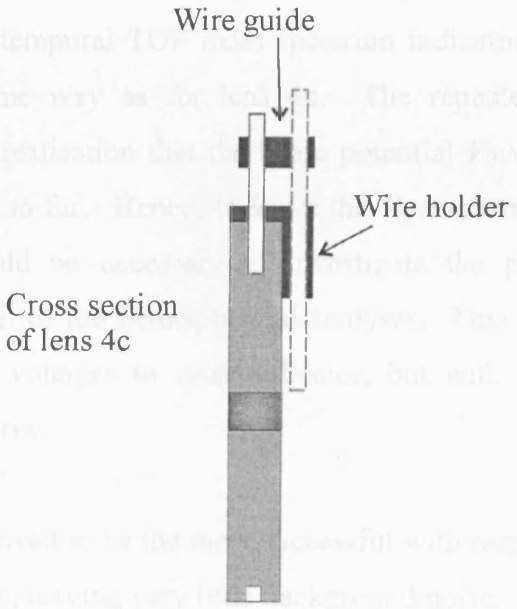

Figure 5.22 Cross-section of lens 4c with wire holder and wire guide attached. The dotted outline represents where the electrode would sit.

However, since this new design (Figure 5.22) would require yet another intrusion into the carefully aligned acceleration lens stack, it was put to one side whilst other less

intrusive methods for effective beam pulsing were first investigated. Since the pulsing at lens 4c also led to significant beam disruption, a triangular waveform was experimented with, creating a sweeping effect of the beam rather than an on / off pulse. The triangular waveform generator that was used had a maximum potential difference between the pulse and bias voltages of ±20 V centred about a chosen potential, in this case the beam potential V_0. A region in the apparatus was chosen where the ion beam was travelling more slowly than at elements considered previously, since a lower beam velocity means that the beam would be easier to deflect with a small voltage range: one of the vertical deflector pairs at the exit slit of the hemisphere was thus the obvious site to implement pulsing (Figure 5.18).

5.4.2.4 Vertical deflector on exit slit of hemispherical analyser

Initial pulsing tests involving the application of a bias and pulse voltage to one of the vertical deflectors at the exit of the hemispherical analyser led to the observation of two dication signals in the temporal TOF mass spectrum indicating some undesired beam perturbation in the same way as for lens 4c. The repeated observation of beam perturbation led to the realisation that the beam potential V_0 was being altered by the pulsing methods tested so far. Hence, to leave the V_0 unchanged before and after the pulsing region, it would be necessary to investigate the pulsing of both vertical deflectors at the exit slit of the hemispherical analyser. This is achieved by applying identical pulse to bias voltages to each deflector, but with a 180° phase offset, as described in Chapter Three.

This method and site proved to be the most successful with respect to total deflection of the beam between pulses, leaving very little background noise. The ability to deflect the beam at the vertical deflector site, as opposed to the other sites described, must arise from the relationship between the deflection voltage and the beam velocity. In detail, the deflection voltages used at the other tested sites, *i.e.* Wein filter and lens 4c, were not large enough to fully deflect a beam with such a high velocity ~5 cm μs^{-1}.

However, the velocity of the beam at the exit of the hemispherical analyser is closer to 0.9 cm μs^{-1} and therefore is more easily deflected by a small voltage.

5.4.2.5 Conclusion: criteria for pulsing the ion beam

The currently employed arrangement for pulsing the PSCO ion beam is described in Chapter Three and the above section. During the development process described above, certain criteria were determined to be important when forming packets of ions from a continuous ion beam and are summarised below.

The first factor to consider when implementing the formation of packets of ions in the ion beam is the position of the lens to which a pulsed field is to be applied. The position is important since the ion beam is travelling at different velocities through different parts of the PSCO apparatus. Therefore, a location in the apparatus at which the ion beam is travelling at a high velocity (~5 cm μs^{-1}) is most advantageous since perturbation of the ion beam energy or an excessive disruption of the ion beam either side of the element, due to the pulsed electric field, is minimised. A closely shielded region is therefore also desirable. It is essential for the beam to be entirely deflected away from its initial axis so that background counts between the pulses are effectively eliminated, hence avoiding the occurrence of some of the 'tails' in the coincidence spectrum as described in section 5.4.2.1. Finally, the pulsing must take place on an element that is not too close to the reaction source region so that stray fields do not penetrate the dication-neutral interaction site. Any field penetration of this sort may degrade the second order space focusing [13] in the reaction source region and, consequently, the quality of data recorded.

5.5 Source field calibration

It is essential to carry out a calibration of the pulsed extraction field in the reaction source region, referred to as the source field F in this thesis, in order that accurate data analysis may take place (Chapter Four). The magnitude of the source field F may be calculated by two methods.

5.5.1 Method one

The length of the reaction source region l (1.6 cm), and the voltage applied to the repeller plate V_{rp} (300 V for a high source field) determine the magnitude of F, where

$$F = \frac{V_{rp}}{l}. \qquad (5.13)$$

Therefore, the first method simply involves measuring l and V_{rp}. At V_{rp} = 300 V, F = 187.5 V cm^{-1} and for V_{rp} = 50 V, F = 31.25 V cm^{-1}. An alternative method for determining F is described next.

5.5.2 Method two

As described in Chapter Four there is a relationship between t_{exp} and F of the form:

$$-t_{exp} = \frac{1}{F}\left(\frac{2mV_0}{Lqz}\right)^{\frac{1}{2}} + t_0, \qquad (5.14)$$

where m is the ion's mass, V_0 is the beam potential (*i.e.* the LAB beam energy $E = zV_0$), L is Avogadro's number, q is the charge of an electron, z is the ionic charge and t_0 is the thermal flight time of an ion. Since the relationship in Eq. 5.14 is of the form

$$y = mx + c, \tag{5.15}$$

the second method of determining F uses a linear regression. A linear regression attempts to model a relationship between two variables by fitting a linear equation to observed data. In the context of Eq. 5.14, values of t_{exp} for an ion may be recorded at a range of values of V_0, and a linear regression may be performed to extract values of F and t_0. In order to check the consistency of values for F determined in this way, a linear regression may be carried out for a second ion of different mass under the same conditions and energies.

Spectra were recorded for beams of Ne^{2+} and Ne^{+} at beam potentials of 1-5 V (LAB energies of 1-10 eV) at low and high source fields in the reaction source region. An example of the data, values of t_{exp} for each ion as a function of V_0, recorded at high source field, are displayed in Table 5.4 along with determinations of F. Figure 5.23 shows a plot of t_{exp} as a function of x where

$$x = \left(\frac{2mV_0}{Lqz} \right)^{\frac{1}{2}}. \tag{5.16}$$

Table 5.4 Values of t_{exp} recorded as a function of energy, together with determinations of F for each ion.

V_0 / eV	Ne^{2+} ($z = 2$)		Ne^{+} ($z = 1$)	
	(LAB energy) / eV	t_{exp} / ns	(LAB energy) / eV	t_{exp} / ns
1	2	276	1	1327
2	4	281	2	1334
3	6	289	3	1344
4	8	296	4	1355
5	10	305	5	1367
F / V cm^{-1}	200.86		204.06	

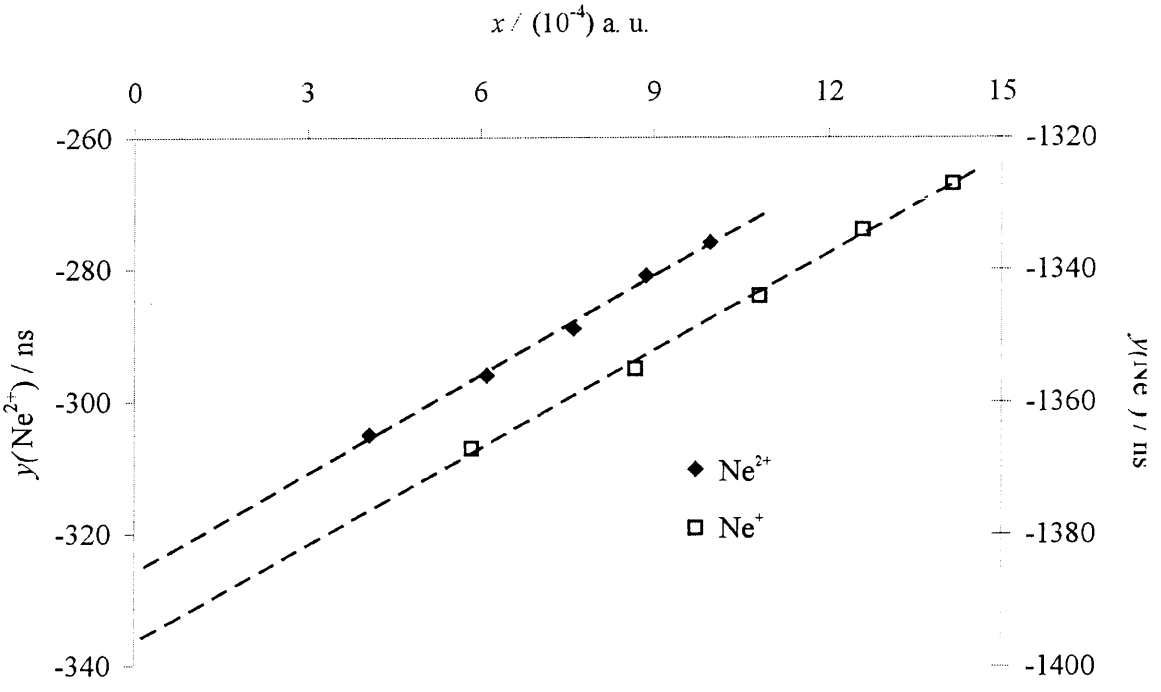

Figure 5.23 Linear regression for Ne^{2+} and Ne^{+} at high source field (see Table 5.4 for data) with trend-lines.

From Figure 5.23 it is instantly clear that the gradients (*i.e.* $1/F$ from Eq. 5.14) of the two trend-lines are very similar, indicating that the values of F determined for each ion are very similar, as would be expected.

From the source field calibrations determined by Method Two, values of 30.4 V cm^{-1} and 202 V cm^{-1} were obtained for repeller plate voltages of 50 (low F) and 300 V (high F), respectively. Each of these final values for F was determined by taking an average from several sets of experiments at each repeller plate voltage.

5.5.3 A comparison of method one and method two

Values of F determined by method one at low and high repeller voltages, are in very good agreement with those values determined using method two (Table 5.5). The deviation between the values determined by each method is most likely to be due to field penetration into the source region from the acceleration region. At the high repeller voltage, the difference between the two values of F is greater than at the low repeller voltage (Table 5.5). This is because the acceleration field is larger at the high repeller voltage and therefore the field penetration is more significant.

Table 5.5 A comparison of values of F determined by (a) method one and (b) method two.

Repeller voltage	(a) F / V cm^{-1}	(b) F / V cm^{-1}
300	187.5	202
50	31.25	30.4

5.5.4 Source field magnitude vs. energy resolution

This section will discuss the effect of the source field magnitude on the energy resolution of the dication-neutral collision experiments. PSCO experiments, as described in the following chapters, are usually carried out at two different source field settings, 'high' (202 V cm^{-1}) and 'low' (30.4 V cm^{-1}).

When using a high source field in the reaction region, with an appropriate voltage on the drift tube (-1983 V), the ionic flight times are short enough that even highly energetic product ions, with considerable energies perpendicular to the axis of the TOF mass spectrometer, do not fly beyond the edges of the detector. Hence, data recorded at a high source field reveal the full angular distributions of the product ions Figure 5.24, at the expense of reduced energy resolution, as shown in Figure 5.25.

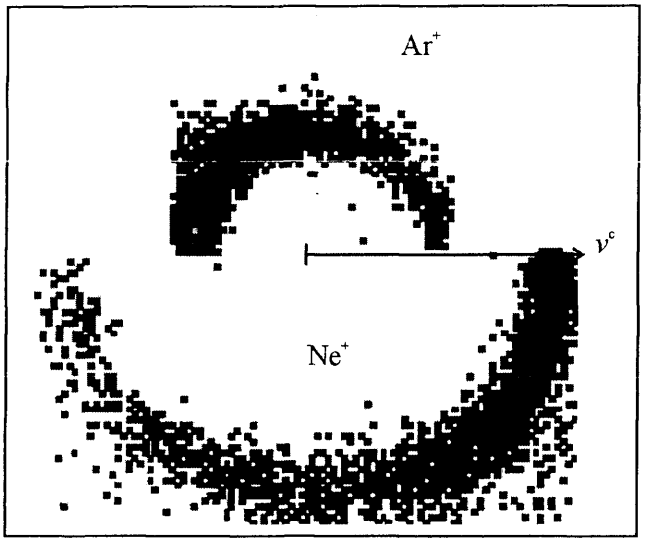

Figure 5.24 Angular scattering of Ne^+ and Ar^+ at high source field, 202 V cm^{-1}. The horizontal arrow is equivalent to 1 cm μs^{-1}.

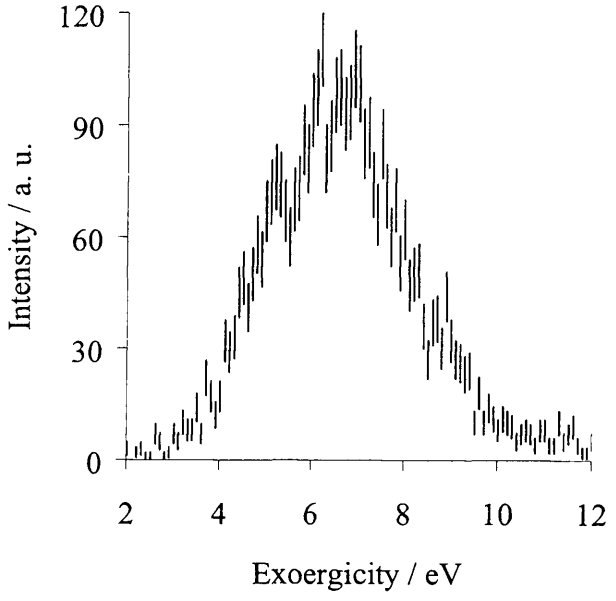

Figure 5.25 Exoergicity spectrum for the formation of Ne^+ and Ar^+ from the collisions of Ne^{2+} with Ar at high source field; E^c = 8.89 eV.

Conversely, with a low source field in the reaction region and a voltage of -329 V on the drift tube, product ions that have considerable x and y velocity components miss the detector as shown in Figure 5.26, but the energy resolution achievable from the TOF mass spectrum is greatly enhanced as shown in Figure 5.27.

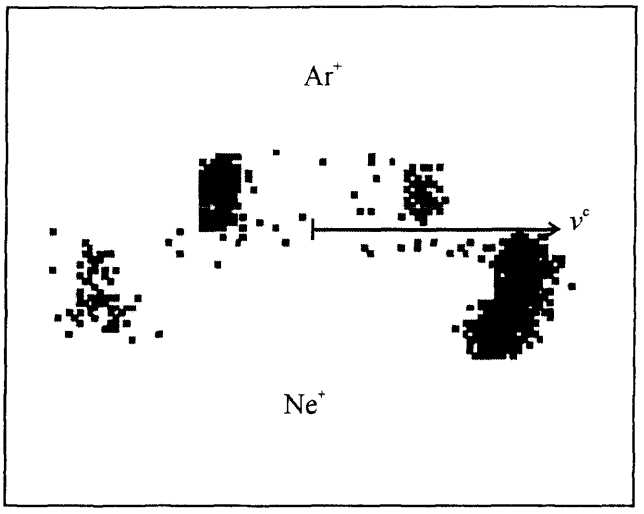

Figure 5.26 Angular scattering of Ne^+ and Ar^+ at low source field.

The change in energy resolution between the high and low source field occurs due to the relationship between the thermal flight time, the experimental flight time and the source field F as described by

$$v_z(i) = -\left[t_{\exp}(i) - t_0(i)\right]\frac{Fqz(i)}{m(i)} \qquad (5.17)$$

Equation 5.17 shows that for a given initial velocity along the z-axis, $v_z(i)$, the time deviation of $t_{\exp}(i)$ from $t_0(i)$ is inversely proportional to the source field F of the TOF mass spectrometer. Hence, to achieve maximum energy resolution it is necessary to operate at low values of F. In more detail, for an ion (i) at a low value of F there will be a greater deviation between $t_{\exp}(i)$ and $t_0(i)$. Therefore, there will be a greater difference between the velocities (*i.e.* the flight times) of two ions of different mass at low F, compared with a high value of F; the positions of ion arrivals at the detector will also be more widely distributed at low F. For these reasons, the energy resolution of the

experiment is improved at low F since the energetics of the reaction are derived from the velocity vectors, *i.e.* flight times and positions, of the detected ions.

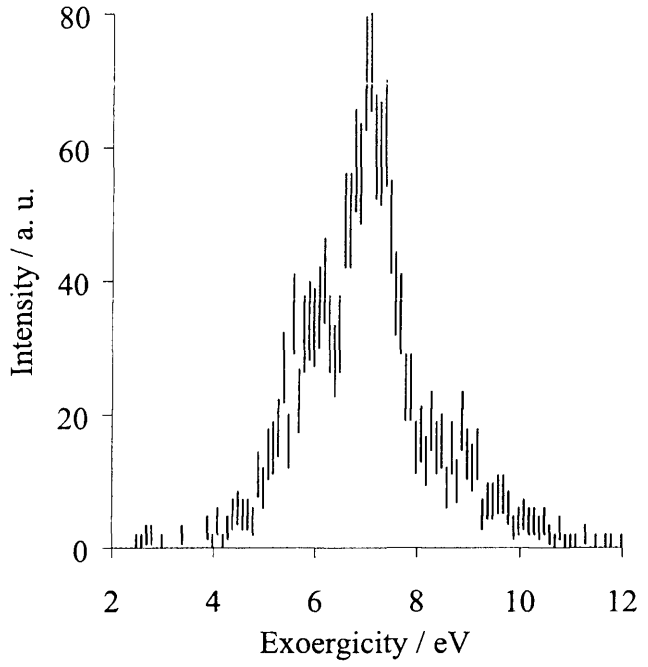

Figure 5.27 Exoergicity spectrum for the formation of Ne^+ and Ar^+ from the collisions of Ne^{2+} with Ar at low source field; E^c = 5.52 eV.

5.6 Summary

The results presented in this chapter demonstrate that all parts of the PSCO experiment are functioning correctly, amounting to a successful commissioning and calibration of the PSCO TOF experiment. The power of the new technique has been demonstrated by a study of the electron transfer reaction between Ar^{2+} and He (5.18) which shows that the ^3P and ^1D states of Ar^{2+} react with He, *via* electron transfer, to form pairs of singly charged ions with markedly different angular distributions [14].

$$Ar^{2+} + He \rightarrow Ar^+ + He^+ \qquad (5.18)$$

Commissioning results for the collisions of Ne^{2+} with Ar [15], used in this chapter to represent the differences in energy resolution at low and high source field, are presented in detail in Chapter Six and will reveal the detailed dynamical and mechanistic information that the experiment is able to resolve even for very simple two-body reactions (Eq. 5.19).

$$Ne^{2+} + Ar \rightarrow Ne^{+} + Ar^{+} \qquad (5.19)$$

5.7 References

[1] Yamasaki, K. and Leone, S. R., 1989, *J. Chem. Phys.* **90** (2) 964-976.

[2] Mark, T. D., *Electron Impact Ionization*, ed. T.D. Mark and G.H. Dunn. 1985, New York: Springer-Verlag.

[3] Ovrebo, G. K. and Erskine, J. L., 1981, *J. Electron Spectrosc. Relat. Phenom.* **24** (2) 189-204.

[4] Friedrich, B. and Herman, Z., 1984, *Chem. Phys. Lett.* **107** (4-5) 375-380.

[5] Jellenwutte, U., Schweinzer, J., Vanek, W., and Winter, H., 1985, *J. Phys. B: At. Mol. Opt. Phys.* **18** (22) L779-L785.

[6] Friedrich, B., *et al.*, 1986, *J. Chem. Phys.* **84** (2) 807-812.

[7] Koslowski, H. R., Huber, B. A., and Staemmler, V., 1988, *J. Phys. B: At. Mol. Opt. Phys.* **21** (17) 2923-2937.

[8] Price, S. D., 1997, *J. Chem. Soc.: Faraday Trans.* **93** (15) 2451-2460.

[9] Herman, Z., 1996, *Int. Rev. Phys. Chem.* **15** (1) 299-324.

[10] Klemperer, O., *Electron Optics*. Cambridge University Press ed. 1971.

[11] Szilagyi, M., *Electron Optics*. 1988, New York: Plenum.

[12] Dahl, D. A., *Simion 3D*. 1999, Idaho National Engineering and Environmental Laboratory: Bechtel BWXT.

[13] Eland, J. H. D., 1993, *Meas. Sci. Technol.* **4** (12) 1522-1524.

[14] Hu, W. P., Harper, S. M., and Price, S. D., 2002, *Meas. Sci. Technol.* **13** (10) 1512-1522.

[15] Harper, S. M., Hu, W. P., and Price, S. D., 2002, *J. Phys. B: At. Mol. Opt. Phys.* **35** (21) 4409-4423.

Chapter 6

The Ne^{2+}-Ar collision system: an electron transfer reaction

6.1 Introduction

In recent years, there has been increasing interest in the bimolecular reactivity of small doubly-charged ions with neutrals [1-6], as discussed in Chapter One. This chapter will describe in detail some experimental results probing the dynamics and kinetics of the Ne^{2+}-Ar collision system using position-sensitive coincidence (PSCO) time-of-flight (TOF) mass spectrometry [7-11].

Having completed the commissioning of the PSCO TOF instrument with an experimental study of the previously investigated Ar^{2+}-He collision system, described in Chapter Five, the Ne^{2+}-Ar collision system was chosen as the first post-commissioning study since it is a simple two-body system. Whilst this electron transfer reaction (6.1) has been previously studied at high collision energies, this chapter describes the first experiments for the electron transfer reaction of Ne^{2+} with Ar recorded at low collision energies (4-14 eV):

$$Ne^{2+} + Ar \rightarrow Ne^{+} + Ar^{+} \qquad (6.1)$$

As shown in Chapter Four, the PSCO experiment [10] involves the detection of the pairs of product ions (Eq. 6.1) formed on an event-by-event basis in dication-neutral collisions and allows the extraction of the velocity vectors of each of these product ions for each reactive encounter detected. The magnitudes of these vectors and their mutual

orientation can be processed, as will be demonstrated in this chapter, to give a detailed insight into the dynamics and energetics of the reactive process.

Electron transfer reactions are often the dominant reactive channel following the interaction of molecular and atomic dications with neutral species [2, 3]. The likelihood of electron transfer occurring in these collision systems has been rationalised using the "Reaction Window" approach based on an extension of Landau-Zener theory as explained in Chapter Two. Briefly, the electron transfer is modelled as occurring at the intersection of a reactant potential, which is dominated by the polarisation attraction between the dication and the neutral, and a product potential, which is dominated by the Coulomb repulsion between the pair of singly charged products [12, 13]. The collision system passes through this intersection twice, on approach and separation.

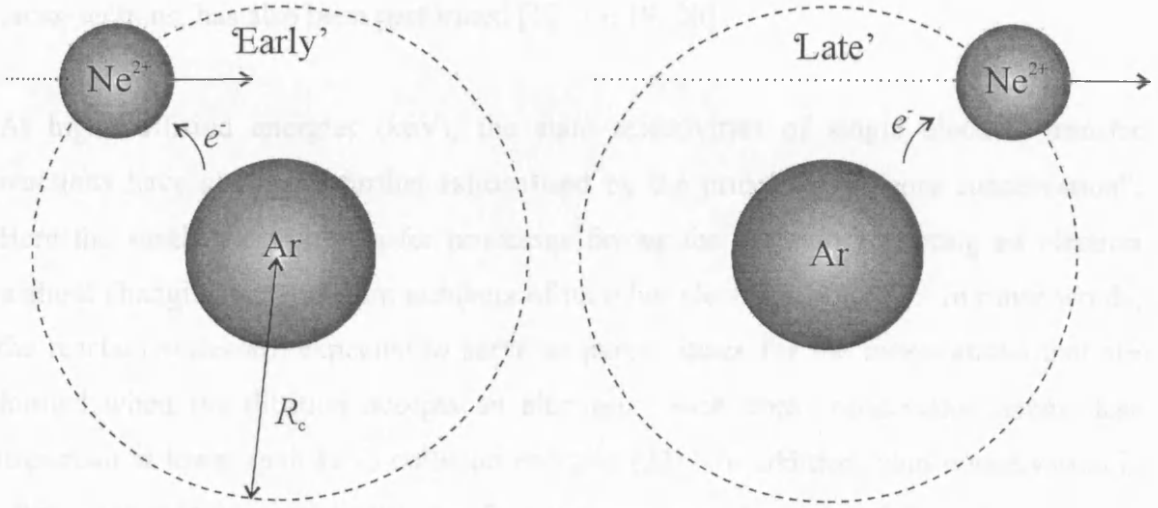

Figure 6.1 A schematic diagram showing the two possible scenarios for electron transfer. The dashed line indicates the diameter of the centre-centre separation R_c at which electron transfer may occur.

As explained in Chapter Two, in order that efficient electron transfer may occur, intermediate coupling between the reactant and product potential surfaces is required, since if the coupling is too weak there is little probability of the electron transferring.

Conversely, if the coupling is too strong, then the electron can transfer from the neutral to the dication on the first pass through the crossing but will hop back on the second pass through the crossing as the monocations separate from each other.

If the intersection between the reactant and product potentials lies at an interspecies separation of 3-6 Å, in the so-called "reaction window", then the coupling is usually appropriate for electron transfer to be efficient. Since the radius of the curve crossing is determined by the form of the potentials, which are in turn dominated by simple electrostatics, the extent of the reaction window is reasonably constant between different collision systems.

Qualitative rationalisation of the state-selectivity and rates of the electron transfer reactions of atomic and molecular dications using this methodology has proved to be extremely successful [14-18]. In addition, quantitative analysis of dicationic electron transfer probabilities, by using the Landau-Zener equation to calculate electron transfer cross-sections, has also been performed [12, 13, 19, 20].

At high collision energies (keV), the state selectivities of single electron transfer reactions have also been further rationalised by the principle of "core conservation". Here the single electron transfer processes favour the dication accepting an electron without changing the quantum numbers of its other electrons [14, 21]. In other words, the reactant states are expected to serve as parent states for the monocations that are formed when the dication accepts an electron. Such core conservation seems less important at lower (sub keV) collision energies [22]. In addition, spin conservation is often important in determining the favoured reaction channels of those interactions, which possess favourable curve crossing radii [14, 21].

The detailed angular distributions of the products of dication-neutral electron transfer reactions have been investigated [2, 10, 23, 24]. In general, these reactions appear to exhibit strong forward scattering, although some exceptions are known [25]. The preference for strong forward scattering is rationalised by realising that the reaction window occurs at a significant interspecies separation and, thus, the two reactants do

not have to come very close together to transfer an electron. In such large impact parameter collisions (see Chapter Two), the dication effectively just "flies by" the neutral, picking up an electron as it passes.

6.2 Experimental details

A detailed account of the experimental arrangement is given in Chapter Two. For the Ne^{2+}-Ar collision system, PSCO spectra were recorded at three different settings: a laboratory frame collision energy of 14 eV (E^c = 9.3 eV) with a repeller plate voltage of 300 V, and at laboratory frame collision energies of 8.3 eV (E^c = 5.5 eV) and 4.3 eV (E^c = 2.9 eV) with a repeller plate voltage of 50 V. The resulting data sets were processed as described in Chapter Four to extract the relevant energetic and angular information. At a high (+300 V) repeller plate voltage the experiment gives full angular scattering data for the reaction, but with lower angular and energy resolution than is available using the lower (+50 V) repeller plate voltages as described in Chapter Five.

6.3 Results and discussion

6.3.1 Angular distributions

An angular scattering diagram (ASD) (Figure 6.2) is an informative way of representing the angular scattering in a collision system. The manner in which it is constructed is described in detail in Chapter Three. Briefly, an ASD is a polar (r, ϕ) histogram where the radial co-ordinate r is the magnitude of the velocity of an ion in the COM frame $|w(i)|$, and the angular co-ordinate ϕ ($0^\circ \leq \phi \leq 180^\circ$) is the angle of $w(i)$ with respect to the velocity of the COM of the collision system v^c. Hence, the scattering of an ion may be described in one of three different ways: "forward", "sideways" or "backward" scattered. An ion scattered in a direction close to the COM velocity v^c (*i.e.* in the same

direction as the dication beam) is termed "forward" scattered; an ion scattered in the opposite direction to the dication beam, *i.e.* with a scattering angle close to 180° with respect to v^c, is termed "backward" scattered. Any ions scattered perpendicularly to the direction of v^c are "sideways" scattered.

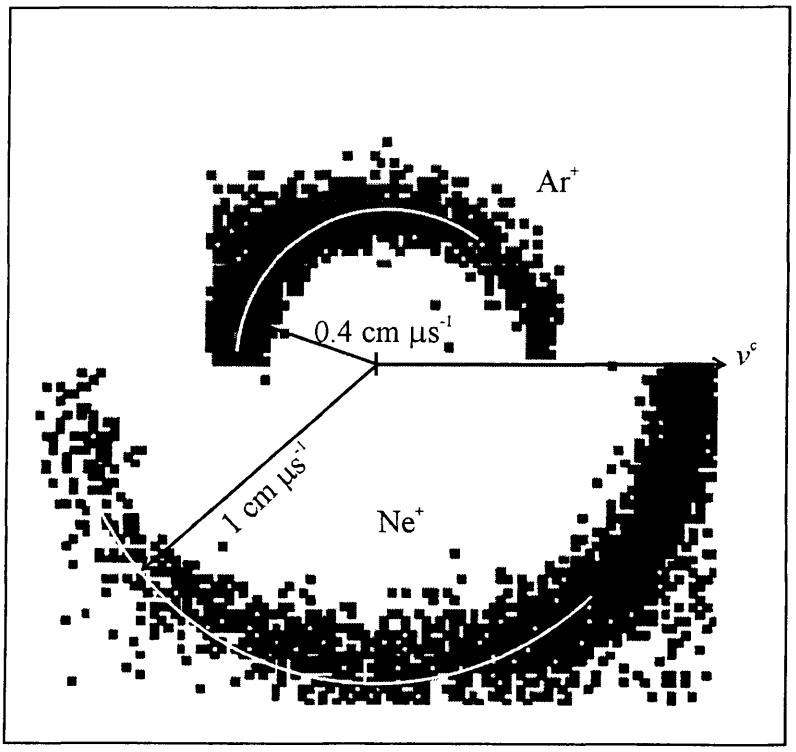

Figure 6.2 Scattering diagram showing the velocities of the product ions, Ar^+ and Ne^+, relative to the velocity of the Ne^{2+} beam at 9.3 eV in the COM frame, recorded with a repeller plate voltage of 300 V. Note that the scattering angle for each ion ϕ lies between 0 and 180°, where ϕ = 0 corresponds to a velocity along the direction of the reactant Ne^{2+} beam. For ease of interpretation, the data for the Ar^+ product ions are displayed in the upper semicircle of the figure and the data for the Ne^+ ions are displayed in the lower semicircle of the figure.

6.3.1.1 Results

The scattering diagram derived from the data recorded with a repeller plate voltage of 300 V is illustrated as a polar histogram in Figure 6.2. This scattering diagram clearly shows that forward scattering dominates at this collision energy as is often, but not exclusively, found in the electron-transfer reactions of atomic dications [2].

In principle, the data presented in Figure 6.2 could have been collected with a conventional apparatus where a rotatable mass spectrometer is moved about the scattering centre to measure the Ne^+ and Ar^+ intensities in the LAB frame. In practice, a whole scattering diagram (Figure 6.2) is hard to record with such a conventional apparatus due to geometric and time constraints. The PSCO experiment provides the complete angular distribution data for scattering diagram in one single experiment, as well as the coincident detection of a pair of ions from a single reactive event that allows dynamical and kinematic calculations on an event-by-event basis.

When the angular distribution of the products is displayed graphically (Figure 6.3 Angular distributions of Ne+ and Ar+ relative to the direction of the reactant beam (z-axis) at 9.3 eV in the COM frame recorded with a repeller plate voltage of +300 V.
) there is certainly a clear indication of two peaks in the angular distribution of the forward scattered events. The spectra recorded with the repeller plate at 50 V confirm this observation (Figure 6.4), clearly showing a bimodal angular distribution in the forward scattered events. It is important to recall that at such low repeller plate voltages only events where both ions have ϕ values less than approximately 40° will be collected.

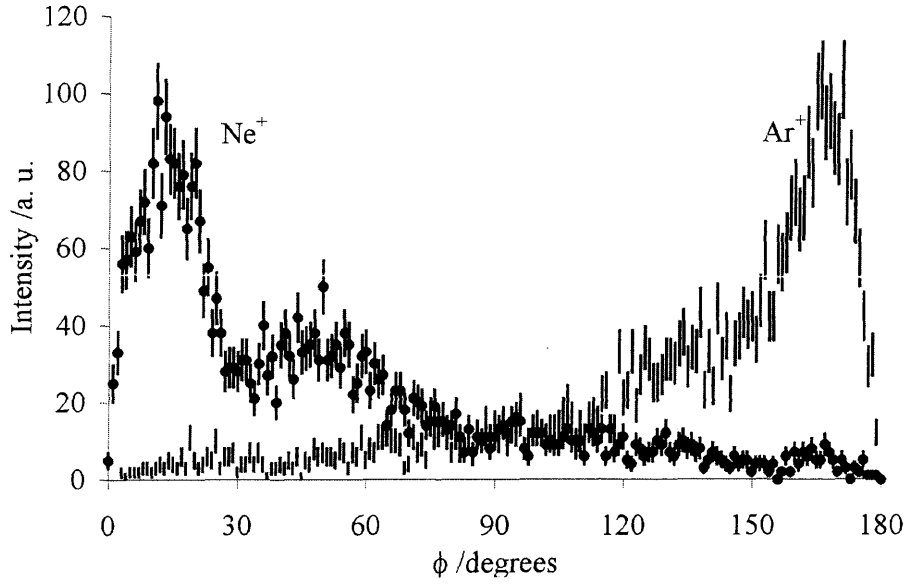

Figure 6.3 Angular distributions of Ne^+ and Ar^+ relative to the direction of the reactant beam (z-axis) at 9.3 eV in the COM frame recorded with a repeller plate voltage of +300 V.

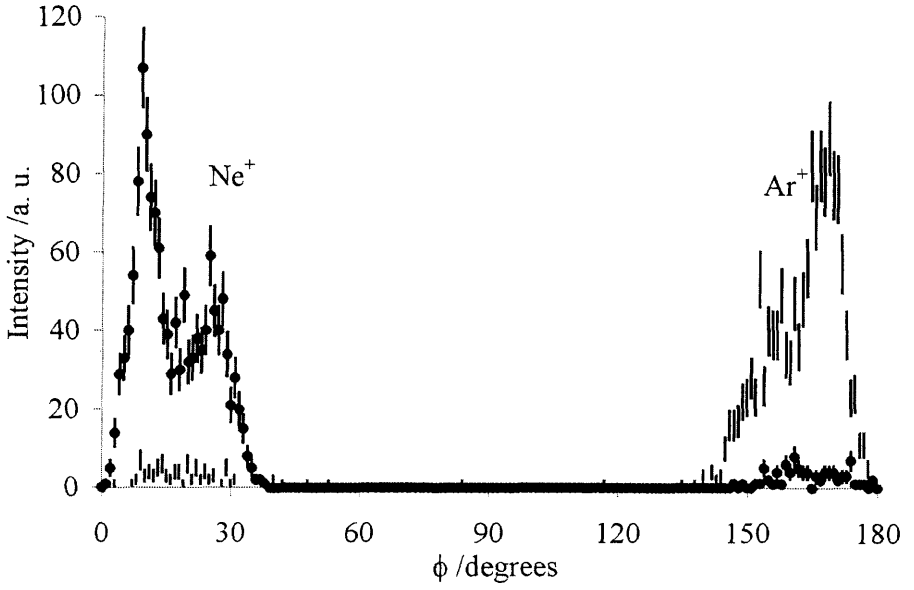

Figure 6.4 Angular distributions of Ne^+ and Ar^+ relative to the direction of the beam (z-axis) at 5.5 eV in the COM frame recorded with a repeller plate voltage of 50 V.

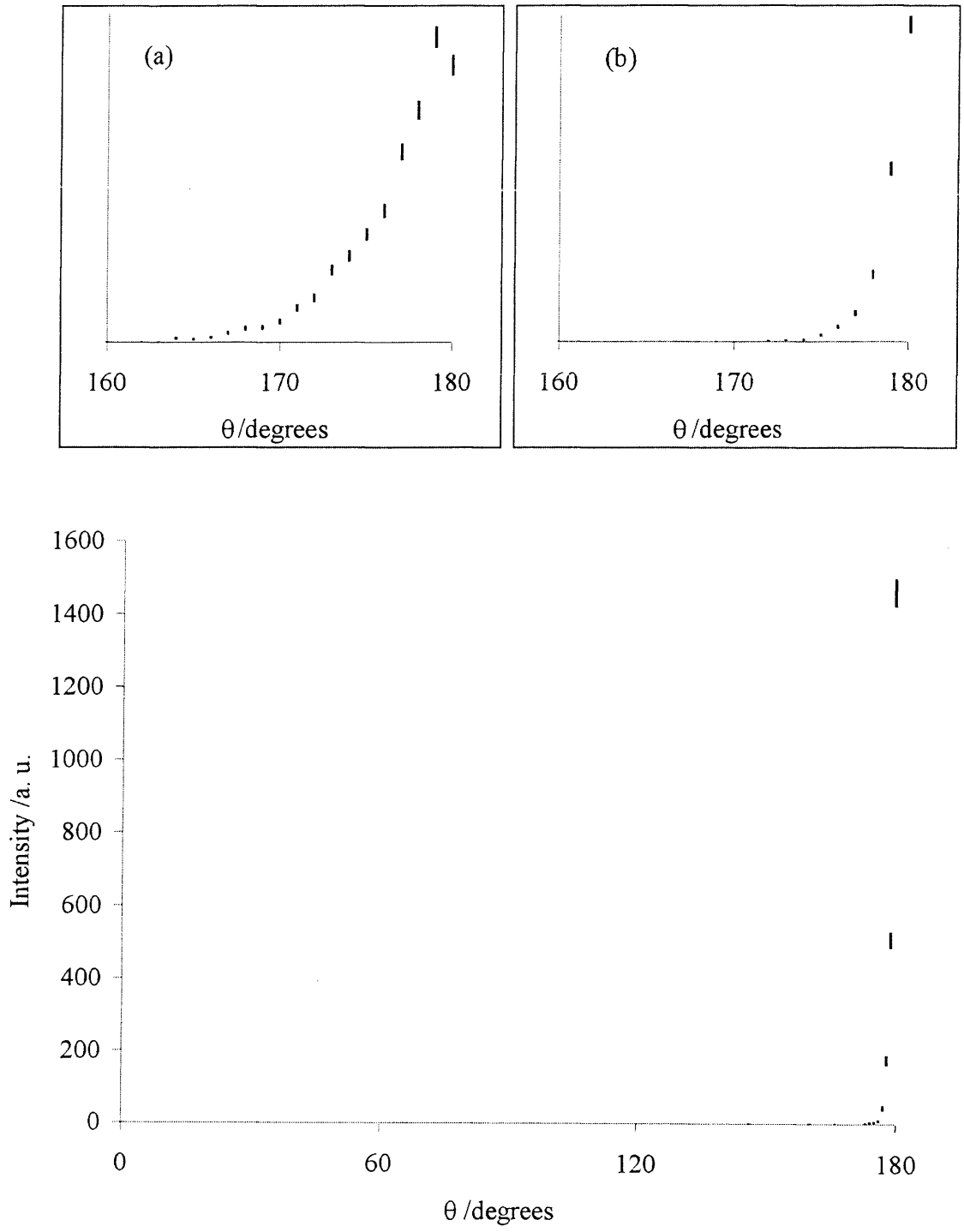

Figure 6.5 Mutual scattering angle θ between the product ions following the reaction of Ne^{2+} with Ar at E^c = 5.5 eV and a 50 V repeller plate pulse. The insets show (a) similar data recorded with a 300 V repeller plate pulse at a COM collision energy of 9.3 eV and (b) an expanded region of the data in the main figure.

Figure 6.5 shows a plot of the mutual scattering angle θ between the Ne^+ and Ar^+ products, which, from conservation of momentum for this two-body reaction, should equal 180°. The experimentally determined angle is clearly centred at 180° with a small angular spread. The two insets on the figure, (a) and (b), show that the mutual scattering angle is reproducible at both high and low resolution respectively. Such good agreement between the expected mutual angle and the experimentally determined angle is a satisfying indication of the accuracy of the data obtained from the PSCO experiment.

6.3.1.2 Discussion

Recently, there have been several investigations of the angular distributions following electron transfer between diatomic and neutral rare gas atoms [2]. As described above, forward scattering dominates these systems. However, in certain cases bimodal angular distributions are observed [25, 26].

These double-peaked distributions are commonly thought to arise from the fact that the collision system, under the Landau-Zener model, crosses the critical electron transfer radius twice: once as the reactants approach each other and once as the species separate as described in section 6.1. One pathway corresponds to the electron being transferred on the first pass through the crossing as the reactants approach each other, termed "early" electron transfer. The other pathway involves electron transfer on the second pass through the crossing, as the reactants separate, termed "late" electron transfer. These two different pathways possess different potential energy surfaces and may give rise to different angular scattering.

As shown below, many accessible states of Ar^+, formed together with Ne^+ in its ground state, are available for the Ne^{2+}-Ar collision system and the data are a sum of the contributions from several reactive channels. Thus, it is highly probable that channels involving both "early" and "late" electron transfer will be occurring in the system resulting in the bimodal angular distribution observed.

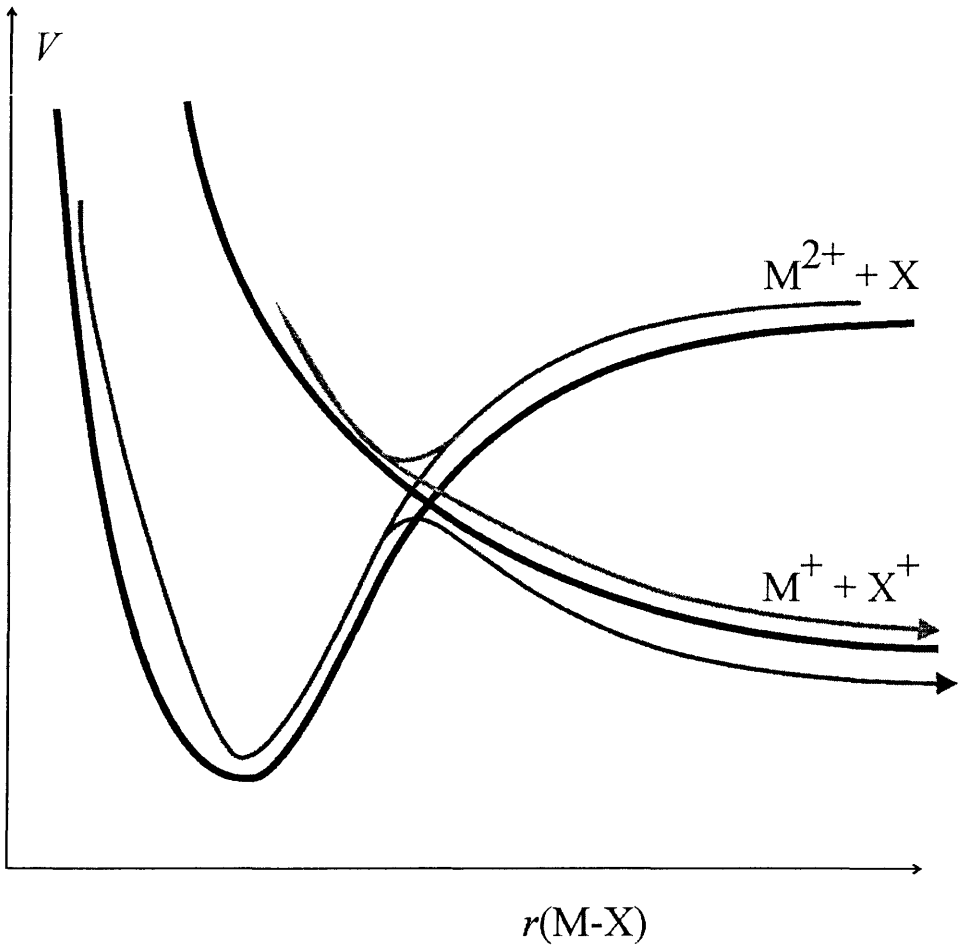

Figure 6.6 A schematic potential energy diagram of "early" and "late" electron transfer pathways, showing the crossing of an attractive reactant potential (red) and a repulsive product potential (blue), respectively.

6.3.2 Exoergicity spectra

6.3.2.1 Results

The exoergicity spectrum derived from the data set recorded at a repeller plate potential of 300 V is (Figure 6.7) unresolved but indicates a distribution of exoergicities between 3 and 11 eV with a maximum at approximately 6 eV. Such a range of exoergicities is predicted from the reaction window model [3, 13].

From the data recorded with low repeller plate potential (E^c = 2.9 and 5.5 eV) (Figure 6.8 & Figure 6.9) it can be seen that, whilst still being consistent with the data recorded at high repeller plate potential, two peaks in the exoergicity spectrum are now resolved at ~5.5 and ~7 eV, at both collision energies. The similarity between the exoergicity spectra indicates that predominantly the same final states are being populated in both the lower and higher energy collisions. The calibration of the exoergicity spectra has been confirmed by earlier studies of the electron transfer reactions in the Ar^{2+}-He collision system (see Chapter Five) where discrete reaction channels can be resolved [10].

6.3.2.2 Discussion

In trying to assign the transitions that are observed in the exoergicity spectrum it is necessary to bear in mind that several reactant states may be present in the Ne^{2+} beam and that there are potentially a large number of product (Ar^+ + Ne^+) states available. However, one might expect the observed transitions to be restricted to those that have a curve crossing in the "reaction window".

Previous studies of the reactions of Ne^{2+} have indicated that Ne^{2+} beams are principally composed of dications in the $2p^4$ (^3P, ^1D and ^1S) configuration and that the ^3P states are significantly the most abundant [14, 17, 27]. Energetic considerations show that the $Ne^{2+}(^3P)$ state can only populate the ground state of $Ne^+(2p^5, {}^2P)$. However, the

accompanying Ar^+ ions may be formed in electronic states ranging from the ground state to those corresponding to the $3s^2 3p^4 4d$ configuration. For example,

$$Ne^{2+}(2s^2 2p^4, {}^3P) + Ar \rightarrow Ne^+(2s^2 2p^5, {}^2P) + Ar^+(3s^2 3p^4[{}^3P]3d, {}^2D) \quad (6.2)$$

The energies of these available (spin-allowed) channels for the reaction of $Ne^{2+}({}^3P_2)$, each involving different degrees of excitation of the Ar^+ product, are indicated in Figure 6.8 and Figure 6.9.

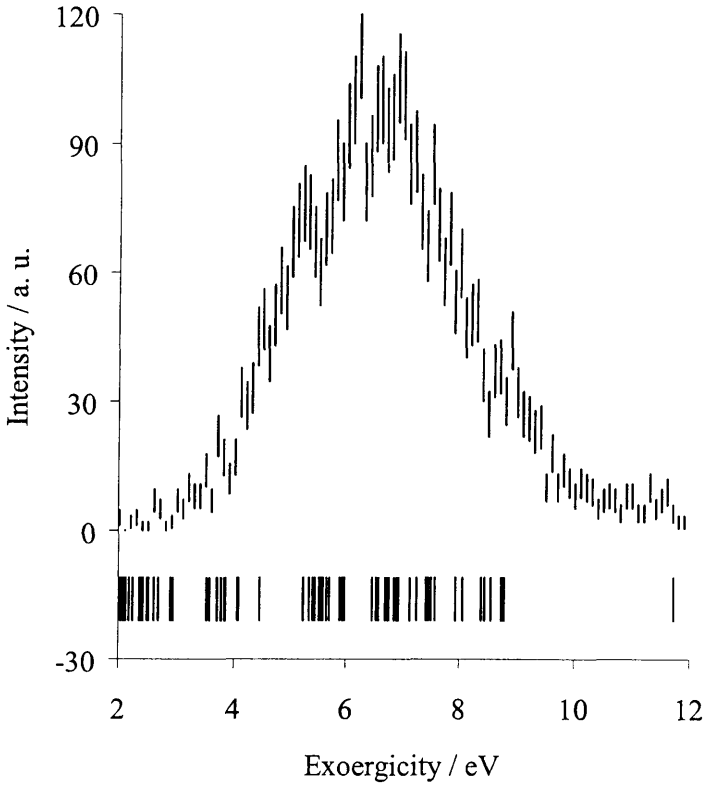

Figure 6.7 Distribution of reaction exoergicities following the reaction of Ne^{2+} with Ar at 9.3 eV in the COM frame. The data were recorded with a repeller plate potential of 300 V. The vertical lines above the energy axis indicate the exoergicity for forming the accessible states of Ar^+ together with Ne^+ in its ground electronic state from $Ne^{2+}({}^3P_2)$ see (Table 6.1).

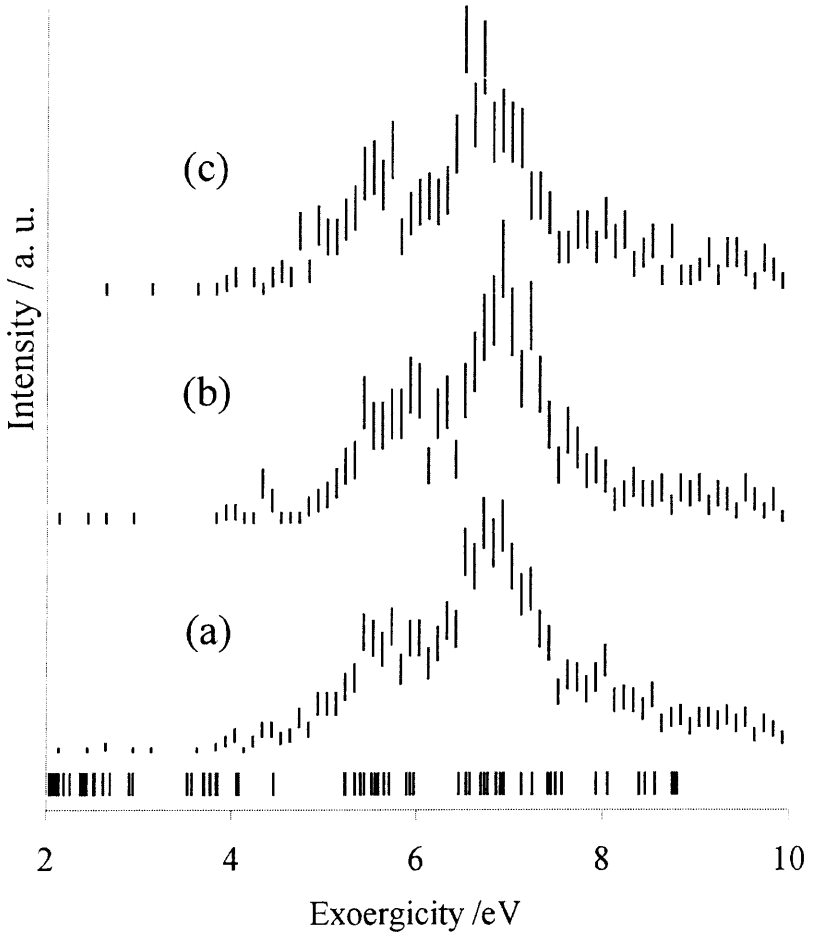

Figure 6.8 Reaction exoergicity following the reaction of Ne^{2+} with Ar at 2.9 eV in the COM frame recorded with a repeller plate potential of 50 V. Spectrum (a) displays the full data set, spectrum (b) the exoergicity distribution of the forward scattered peak and spectrum (c) the exoergicity distribution of the more angularly diverted peak. Spectra (b) and (c) are plotted on an expanded vertical scale with respect to the complete spectrum (a). The vertical lines above the energy axis indicate the exoergicity for forming the accessible states of Ar^+ together with Ne^+ in its ground electronic state from $Ne^{2+}(^3P_2)$ (see Table 6.1).

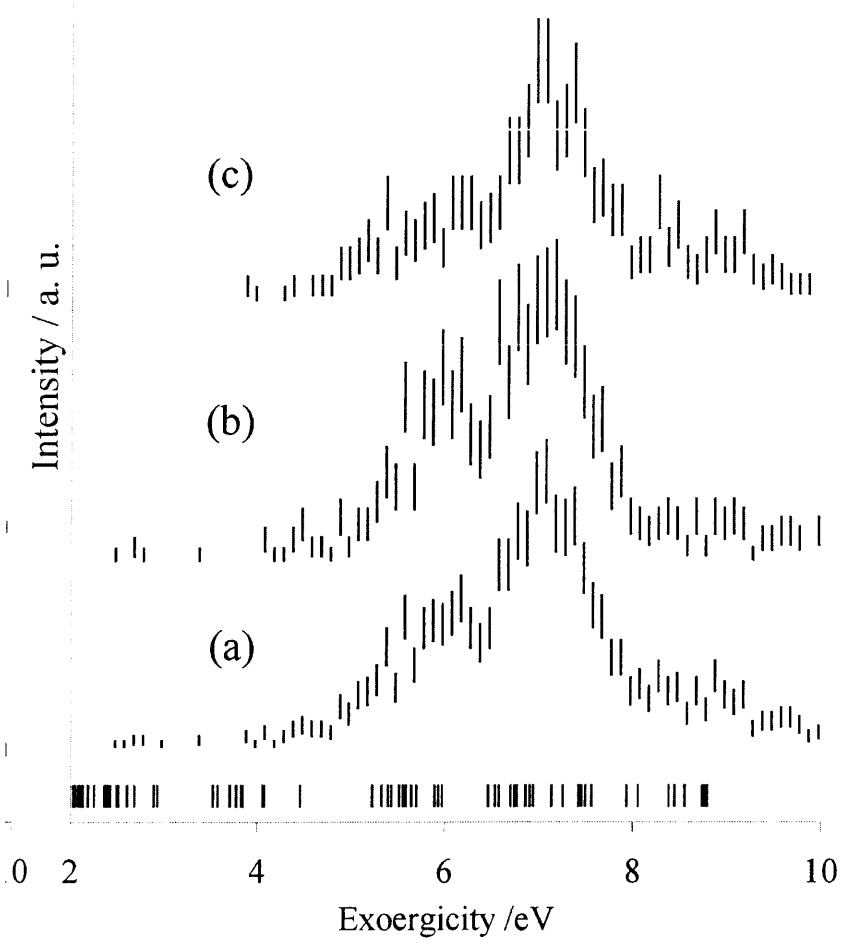

Figure 6.9 Reaction exoergicity following the reaction of Ne^{2+} with Ar at 5.5 eV in the COM frame recorded with a repeller plate potential of 50 V. Spectrum (a) displays the full data set, spectrum (b) the exoergicity distribution of the forward scattered peak and spectrum (c) the exoergicity distribution of the more angularly diverted peak. Spectra (b) and (c) are plotted on an expanded vertical scale with respect to the complete spectrum (a). The vertical lines above the energy axis indicate the exoergicity for forming the accessible states of Ar^+ together with Ne^+ in its ground electronic state from $Ne^{2+}(^3P_2)$ (see Table 6.1).

Table 6.1 Calculation of the exoergicity of the allowed electronic transitions from Ar to Ne^{2+} to form the ground state of Ne^{+} and the many available states of Ar^{+} at the low PSCO collision energy.

REACTANTS		PRODUCTS					ΔE (eV)
Ne^{2+}	Ar	Ne^{+}		J	Ar^{+}		J	
$^3P_2$	$^1S_0$	$2s^2\ 2p^5$	^2P	1 ½	$3s\ 3p^6$	^2S	½	11.72
				½	$3s^2\ 3p^4(^3P)3d$	^4D	3 ½	8.80
							2 ½	8.78
							1 ½	8.76
							½	8.74
					$3s^2\ 3p^4(^3P)4s$	^4P	2 ½	8.56
							1 ½	8.45
							½	8.39
					$3s^2\ 3p^4(^3P)4s$	^2P	1 ½	8.06
							½	7.94
					$3s^2\ 3p^4(^3P)3d$	^2P	1 ½	7.26
							½	7.14
					$3s^2\ 3p^4(^3P)3d$	^4P	2 ½	6.95
							1 ½	6.91
							½	6.87
					$3s^2\ 3p^4(^1D)4s$	^2D	1 ½	6.78
							½	6.75
					$3s^2\ 3p^4(^3P)3d$	^2D	1 ½	6.55
							½	6.47
					$3s^2\ 3p^4(^3P)3d$	^4P	2 ½	5.98
							1 ½	5.94
							½	5.90
					$3s^2\ 3p^4(^3P)3d$	^4P	3 ½	5.71
							2 ½	5.65
							1 ½	5.59
							½	5.56
					$3s^2\ 3p^4(^3P)3d$	^2D	1 ½	5.52
							½	5.44
					$3s^2\ 3p^4(^3P)3d$	^2P	1 ½	5.40
							½	5.33
					$3s^2\ 3p^4(^3P)3d$	^4S	½	5.23
					$3s^2\ 3p^4(^3P)3d$	^2S	½	5.23

(Cont...)

Table 6.1 continued from previous page...

REACTANTS		PRODUCTS					ΔE (eV)
Ne^{2+}	Ar	Ne^+		J	Ar^+		J	
$^3P_2$	$^1S_0$	$2s^2\ 2p^5$	^2P	1 ½	$3s^2\ 3p^4(^1S)4s$	^2S	½	4.46
				½	$3s^2\ 3p^4(^1D)4p$	^2P	1 ½	3.85
							½	3.77
					$3s^2\ 3p^4(^1D)4p$	^2P	1 ½	3.85
							½	3.77
					$3s^2\ 3p^4(^1D)4p$	^2D	1 ½	3.71
							½	3.70
					$3s^2\ 3p^4(^1D)3d$	^2P	1 ½	3.58
							½	3.53
						^2P	1 ½	2.93
							½	2.89
					$3s^2\ 3p^4(^3P)5s$	^4P	2 ½	2.69
							1 ½	2.61
							½	2.52
					$3s^2\ 3p^4(^3P)5s$	^2P	1 ½	2.50
							½	2.40
					$3s^2\ 3p^4(^3P)4d$	^4D	3 ½	2.43
							2 ½	2.41
							1 ½	2.39
							½	2.36
					$3s^2\ 3p^4(^1D)3d$	^2S	½	2.38
					$3s^2\ 3p^4(^3P)4d$	^4P	2 ½	2.12
							1 ½	2.08
							½	2.03
					$3s^2\ 3p^4(^1S)4s$	^2D	1 ½	2.05
							½	2.05

On inspection of Figure 6.8 and Figure 6.9 it is seen that the peaks in the exoergicity spectrum correspond well with two groups of final product states: one group with exoergicities from 5.5-6.0 eV and the other group with exoergicities from 6.5-7.5 eV. Both these groups of product channels correspond almost exclusively to the formation of Ar^+ in the $3s^23p^43d$ configuration.

The reactivity of Ne^{2+} with Ar has been investigated in flow tubes, where rate constants have been measured and rationalised using Landau-Zener theory [27, 28]. However, the only study of the final state selectivity in this collision system was carried out by translational energy spectroscopy in 1984 [22]. In this study, at a laboratory frame collision energy of 600 eV, the dominant signal was assigned to the reaction of $Ne^{2+}(^1S_0)$ forming excited Ne^+ states along with the ground state of $Ar^+(3s^23p^5, {}^2P)$:

$$Ne^{2+}(2s^22p^4, {}^1S_0) + Ar \rightarrow Ne^+(2s^12p^6, {}^2S_{1/2}) + Ar^+(3s^23p^5, {}^2P_{3/2}) \quad (6.3)$$

$$Ne^{2+}(2s^22p^4, {}^1S_0) + Ar \rightarrow Ne^+(2s^12p^6, {}^2S_{1/2}) + Ar^+(3s^23p^5, {}^2P_{1/2}) . \quad (6.4)$$

However, in this earlier study [22] signals assigned to the formation of excited Ar^+ states together with ground state Ne^+, for example (6.2), were also observed. Using the latest available data for the atomic state energies [29], reaction (6.3) has an exoergicity of 5.21, or 5.03 eV if the $^2P_{1/2}$ state of Ar^+ is formed (6.4). The intense signals in the exoergicity spectrum (Figure 6.8 & Figure 6.9) are at significantly higher values than the exoergicity of these two $Ne^{2+}(^1S_0)$ reactions (6.3 & 6.4), and other reactions of $Ne^{2+}(^1S_0)$, which populate excited states of Ar^+, will have even lower exoergicities. Hence, unlike the earlier experiments at 600 eV it seems that reaction (6.3) is not the dominant reactive pathway in the PSCO experiments where the collision energy is low, *i.e.* ~6eV. There are two obvious explanations for this difference in reactivity. Firstly, that the PSCO ion beam is composed overwhelmingly of Ne^{2+} in the ^3P, and possibly ^1D states. Secondly, that the reaction window is significantly different for reactions (6.2) and (6.3) at LAB collision energies of 600 and ~6 eV.

Previous experiments show that the ^3P states of Ne^{2+} are the most abundant when the ion beam is generated by electron impact [14]. By inspection of the detailed data recorded for the formation of Ar^{2+}, one would expect the $Ne^{2+}(^1S_0)$ fraction in the PSCO ion beam to increase with increasing ionising electron energy and not reach the statistical ratio until well above 200 eV [30]. However, as the PSCO ionising electron energy is 150 eV, the $Ne^{2+}(^1S_0)$ might be expected to be present in the PSCO ion beam

but with an abundance of approximately one third of the statistical ratio. However, if reaction (6.3) possesses a reasonable cross-section at the PSCO collision energy, some corresponding signals in the exoergicity spectrum would be expected (Figure 6.8 & Figure 6.9).

Table 6.2 Landau-Zener calculations of the cross-sections (units) for two Ne^{2+}-Ar reactive pathways at high and low collision energies.

Reaction	4.3 eV	600 eV
(6.2)	9	4.7
(6.3)	3	11.7

To assess the variation in the probability of reactions (6.2) and (6.3) with collision energy, Landau-Zener calculations [12, 13] (see Chapter Four) of the cross-section for these two processes at 4.3 eV, 8.3 eV and 600 eV laboratory frame collision energies were performed. Table 6.2 shows the cross-sections at 4.3 eV and 600 eV. Satisfyingly, these calculations show that the cross-section for reaction (6.3) is four times higher at 600 eV than at the "low" collision energies implemented in the PSCO apparatus. Conversely, the cross-section for reaction (6.2) is approximately twice as large at the "low" PSCO collision energies than for experiments at 600 eV. Given these cross-sections and the estimated relative abundance of the ^3P and ^1S reactants in the PSCO ion beam, the intensity of reaction (6.2) with respect to reaction (6.3) in the PSCO experiments can be estimated to be 24 times that observed at 600 eV. From the abundance of reactions (6.2) and (6.3) at 600 eV this estimation predicts an intensity ratio of ^3P to ^1S reactions in the exoergicity spectrum of approximately 5:1. This is in good accord with the PSCO data (Figure 6.8 & Figure 6.9) where reactions of the ^3P state appear to be dominant.

However, reactions of the $Ne^{2+}(^1S)$ state may well contribute to the weak signals at 5 eV in the exoergicity spectrum, since analogous reactions to reaction (6.2) involving

$Ne^{2+}(^1D_2)$ are possible. Such reactions would give exoergicities in the range of the PSCO experimental signals. However, the Landau-Zener calculations indicate that the cross-sections for such reactions are ten times smaller than for Ne^{2+} in the ^3P states. This fact, coupled with the fact that the PSCO ion beam is considered to be dominated by dications in the ^3P states, allows the conclusion that in the PCSO experiments the reactivity is dominated by the ^3P states of Ne^{2+} populating the ground state of Ne^+ and excited states of Ar^+ predominantly involving the $3s^23p^43d$ configuration.

Figure 6.8 and Figure 6.9 also show the exoergicity spectra for the strongly forward scattered events ($0 \leq \phi \leq 16^o$) in the angular distribution and for the more angularly diverted events ($\phi > 16^o$). From these spectra, it can be seen that, at the higher collision energy, reactive events with lower exoergicity seem to favour smaller scattering angles whilst more exoergic events result in larger scattering angles. For the more exoergic events, there will be a stronger coupling between the reactant and product potentials and these channels should predominantly follow "early" electron transfer pathways. Such pathways are predicted [26] to result in scattering to larger angles, as observed in the PSCO data. This preference for the more exoergic channels to scatter to larger angles is not as obvious in the data at the lower collision energy.

6.4 Conclusion

A new experiment employing position-sensitive detection coupled with TOF mass spectrometry has been used to investigate the single-electron transfer reaction between Ne^{2+} and Ar by detecting the resulting pairs of singly charged ions in coincidence. The experimental technique allows the determination of the velocity vectors of both of the products of the reaction in the COM frame for each reactive event detected. From these pairs of velocity vectors it is possible to derive the detailed dynamics and kinematics of the reaction. The experiments show that forward scattering dominates the reactivity, although a bimodal angular distribution is apparent. In addition, the spectra show that at laboratory kinetic energies between 4 and 14 eV the reactivity is dominated by the

reaction of $Ne^{2+}(2p^4, {}^3P)$ accepting an electron to generate the ground state of Ne^+ together with Ar^+ ions in excited electronic levels, predominantly arising from the $3s^23p^43d$ configuration. The form of this reactivity, and the differences between the reactivity observed in these experiments and those performed at higher collision energies, is well reproduced by Landau-Zener theory.

6.5 References

[1] Dolejsek, Z., Farnik, M., and Herman, Z., 1995, *Chem. Phys. Lett.* **235** (1-2) 99-104.

[2] Herman, Z., 1996, *Int. Rev. Phys. Chem.* **15** (1) 299-324.

[3] Price, S. D., 1997, *J. Chem. Soc.: Faraday Trans.* **93** (15) 2451-2460.

[4] Price, S. D., Manning, M., and Leone, S. R., 1994, *J. Am. Chem. Soc.* **116** (19) 8673-8680.

[5] Schroder, D., *et al.*, 1999, *J. Phys. Chem. A.* **103** (24) 4609-4620.

[6] Tosi, P., *et al.*, 1999, *Phys. Rev. Lett.* **82** (2) 450-452.

[7] Davies, J. A., LeClaire, J. E., Continetti, R. E., and Hayden, C. C., 1999, *J. Chem. Phys.* **111** (1) 1-4.

[8] Hsieh, S. and Eland, J. H. D., 1996, *J. Phys. B: At. Mol. Opt. Phys.* **29** (23) 5795-5809.

[9] Hsieh, S. and Eland, J. H. D., 1997, *J. Phys. B: At. Mol. Opt. Phys.* **30** (20) 4515-4534.

[10] Hu, W. P., Harper, S. M., and Price, S. D., 2002, *Meas. Sci. Technol.* **13** (10) 1512-1522.

[11] Saito, N., *et al.*, 1996, *Phys. Rev. A.* **54** (3) 2004-2010.

[12] Champkin, P., Kaltsoyannis, N., and Price, S. D., 1998, *Int. J. Mass Spectrom.* **172** (1-2) 57-69.

[13] Rogers, S. A., Price, S. D., and Leone, S. R., 1993, *J. Chem. Phys.* **98** (1) 280-289.

[14] Huber, B. A. and Kahlert, H. J., 1984, *J. Phys. B: At. Mol. Opt. Phys.* **17** (3) L69-L74.

[15] Schweinzer, J. and Winter, H., 1989, *J. Phys. B: At. Mol. Opt. Phys.* **22** (6) 893-905.

[16] Schweinzer, J., *et al.*, 1988, *J. Phys. B-At. Mol. Opt. Phys.* **21** (2) 315-328.

[17] Brazuk, A. and Winter, H., 1982, *J. Phys. B: At. Mol. Opt. Phys.* **15** (14) 2233-2244.

[18] Fukuroda, A., Kobayashi, N., and Kaneko, Y., 1989, *J. Phys. B-At. Mol. Opt. Phys.* **22** (21) 3457-3469.

[19] Manning, M., Price, S. D., and Leone, S. R., 1993, *J. Chem. Phys.* **99** (11) 8695-8704.

[20] Price, S. D., Manning, M., and Leone, S. R., 1993, *Chem. Phys. Lett.* **214** (6) 553-558.

[21] Winter, H., 1983, *Phys. Scr.* **T3** 159-162.

[22] Kahlert, H. J. and Huber, B. A., 1984, *Z. Phys. A: Hadrons and Nuclei.* **317** (2) 139-143.

[23] Herman, Z., Zabka, J., Dolejsek, Z., and Farnik, M., 1999, *Int. J. Mass Spectrom.* **192** 191-203.

[24] Mrazek, L., *et al.*, 2000, *J. Phys. Chem. A.* **104** (31) 7294-7303.

[25] Friedrich, B. and Herman, Z., 1984, *Chem. Phys. Lett.* **107** (4-5) 375-380.

[26] Friedrich, B., *et al.*, 1986, *J. Chem. Phys.* **84** (2) 807-812.

[27] Viggiano, A. A., *et al.*, 1981, *Int. J. Mass Spectrom. Ion Proc.* **39** (1) 1-8.

[28] Smith, D., Adams, N G, Alge E, and Lindinger W, 1980, *J. Phys. B: At. Mol. Phys.* **13** 2787-99.

[29] Martin, W. C., 2002, *NIST Atomic Spectra Database 2.0*, (Gaithersburg, MD: National Institute of Standards and Technology) webpage http://physics.nist.gov/asd.

[30] Jellenwutte, U., Schweinzer, J., Vanek, W., and Winter, H., 1985, *J. Phys. B: At. Mol. Opt. Phys.* **18** (22) L779-L785.

Chapter 7

The electron transfer reactions of Ne^{2+}-N_2

7.1 Introduction

The interactions of doubly charged atoms and molecules with neutral molecules at low collision energies exhibit many properties of fundamental interest [1-3]. At collision energies below 10 eV the significant interaction time between the reactants allows processes which form chemical bonds to occur [1, 4-7]. Further, the presence of two charges in the dication-neutral collision system means that electron transfer, and many bond-forming reactions, result in the formation of a pair of singly charged products which possess considerable translational energy [1]. Recent studies also show that dicationic species may contribute significantly to the ion density in planetary ionospheres [8] and the high internal energy of molecular dications has also made them a candidate for energy storage media [9]. In order to evaluate the importance of dications in these roles, an understanding of dication-neutral interactions is required.

The electron transfer processes of atomic dications have been extensively investigated at high collision energies (>100 eV) [2, 3]. However, significantly less attention has been paid to the dissociative electron transfer reactions of atomic dications with neutral molecules especially at collision energies below 10 eV [1]. This lack of attention arises as the dissociation of the monocation derived from the neutral molecule significantly complicates the interpretation of translational energy spectra when only the fast monocation derived from the incident dication is detected [1, 2]. However, the accepted mechanism of a dissociative dication electron transfer reaction in the low energy regime is a sequential process where the initial electron transfer, from the neutral to the dication, generates an excited electronic state of one (or both) of the primary product

monocations which subsequently dissociate to yield the observed daughter monocation [1, 4]. Studies of the angular distribution of CO^+ formed in collisions of CO_2^{2+} with D_2 show that the above sequential mechanism is operating, *via* population of the $C\ ^2\Sigma_g^+$ state of CO_2^+ [10].

This chapter reports some of the results from an investigation of the kinematics of the dissociative electron transfer reactions of Ne^{2+} with N_2 at a centre-of-mass collision energy of 7.8 eV using the PSCO experiment [5, 11, 12].

$$Ne^{2+} + N_2 \rightarrow Ne^+ + N^+ + N \qquad (7.1)$$

These results clearly indicate that, in contrast to the accepted mechanism outlined above, one route to the products of this reaction ($Ne^+ + N^+ + N$) involves the dissociation of a triatomic transitory species formed by the temporary association of the reactants (Eq. 7.2).

$$[Ne - N_2]^{2+} \rightarrow Ne^+ + N^+ + N \qquad (7.2)$$

7.2 Experimental details

A detailed account of the experimental arrangement is given in Chapter Three. For the Ne^{2+}-N_2 collision system, PSCO spectra were recorded at one setting: a laboratory frame collision energy of 13.3 eV (E^c = 7.8 eV) with a repeller plate voltage of 300 V. The resulting data was processed as described in Chapter Four to extract the relevant energetic and angular information.

7.3 Results

Figure 7.1 shows the scattering diagram for the detected events that form Ne^+ and N^+. Clearly, the Ne^+ ions are predominantly forward scattered, whilst the N^+ ions exhibit three clear channels involving forward, sideways and backward scattering. The relative intensities of these channels are 100:223:197, respectively, signifying the branching ratio for formation of Ne^+ and N^+. From the data, it is possible to examine the dynamics for an individual reactive channel by, for example, selecting from the dataset just the reactive events, which involve sideways scattering of the N^+ ions (Channel A, Figure 7.1). This chapter will focus on the two more intense channels, A and B, involving the sideways and backward scattering of N^+.

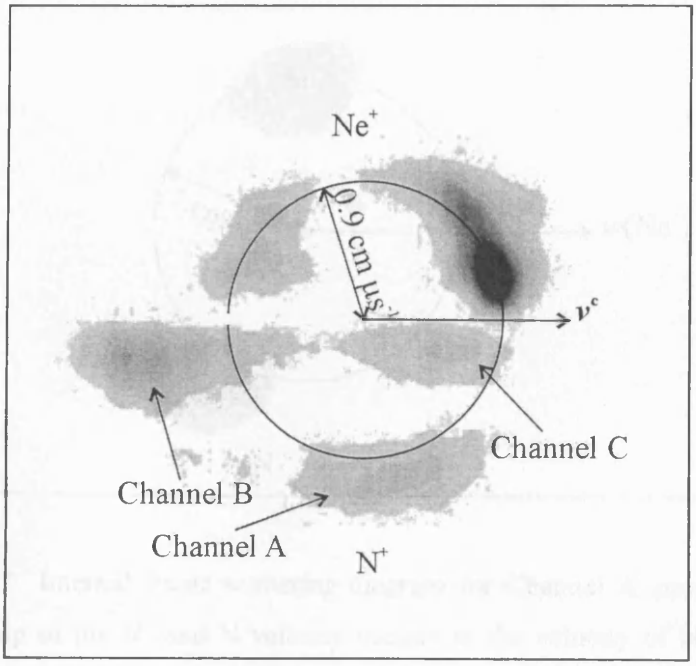

Figure 7.1 Scattering diagram for the formation of Ne^+ and N^+ following collisions of Ne^{2+} with N_2 at 7.8 eV in the COM frame. The speed of the product ions in the COM frame is the radial coordinate and their scattering angle (0-180°) is the angular coordinate. The data for Ne^+ is shown in the upper semicircle of the figure.

When the data for Channel A, coincidences between forward scattered Ne^+ and sideways scattered N^+, are selected and examined (Figure 7.2), it can be seen clearly that there is a fixed angular relationship between the initial velocities of all three products. Such a fixed angular relationship between product ions formed in a reactive process is that expected for the concerted decay of a $[Ne\text{-}N_2]^{2+}$ collision complex (Figure 7.3). Indeed, similar distributions have been observed for the decay of the dissociative states of molecular dications such as SO_2^{2+}, CS_2^{2+}, OCS^{2+}, ICN^{2+}, N_2O^{2+}, CO_2^{2+} [13].

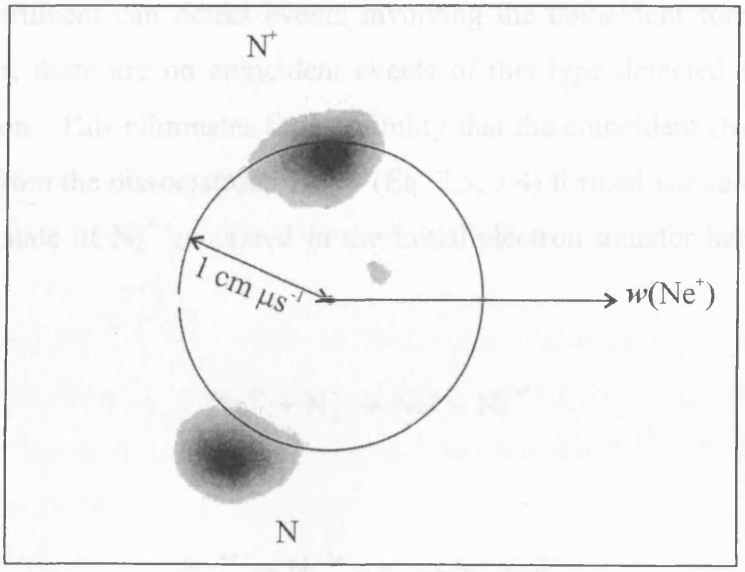

Figure 7.2 Internal frame scattering diagram for Channel A showing the relationship of the N^+ and N velocity vectors to the velocity of Ne^+. The speed in the COM frame of the product ions is the radial coordinate and their scattering angle with respect to the Ne^+ velocity is the angular coordinate.

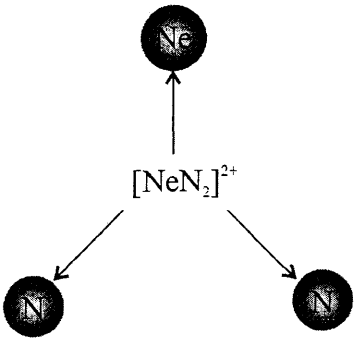

Figure 7.3 A schematic diagram of the concerted dissociation of a collision complex $[NeN_2]^{2+}$.

The PSCO instrument can detect events involving the coincident formation of three ions. However, there are no coincident events of this type detected for the reactive Ne^{2+}-N_2 collision. This eliminates the possibility that the coincident ($Ne^+ + N^+$) events detected arise from the dissociation of N_2^{2+} (Eq. 7.3, 7.4) formed *via* autoionisation of a highly excited state of N_2^+ generated in the initial electron transfer between Ne^{2+} and N_2.

$$Ne^{2+} + N_2 \rightarrow Ne^+ + N_2^{+*} \qquad (7.3)$$

$$N_2^{+*} \rightarrow N_2^{2+} + e^- \rightarrow N^+ + N^+ \qquad (7.4)$$

However, before being able to unambiguously attribute the scattering in channel A to the formation of a transitory collision complex (7.2), it is necessary to show that the scattering that would be detected for a sequential dissociative electron transfer is readily distinguishable from the experimentally observed scattering.

7.3.1 Sequential dissociative electron transfer

The general form of a sequential dissociation is described in Chapter Two. A sequential pathway for the dissociative electron transfer reaction described in this chapter would involve the decay of an excited electronic state of the N_2 monocation (N_2^{+*}) to $N^+ + N$. This decay could be *fast*, within the field of the Ne^+ ion, or *slow*, when the N_2^{+*} and Ne^+ are well separated. This section will discuss the scattering characteristics of slow and fast dissociation of a molecular product ion and present some Monte Carlo (MC) classical trajectory simulations of the Ne^{2+}-N_2 collision system for comparison with the experimental data. Only a brief description of the Monte Carlo classical trajectory simulation method is given in this chapter since the calculations described below were not carried out by the author of this thesis, but by contributing authors to reference [14] (Harper *et al*). See Appendix D for a detailed description of the MC code.

7.3.1.1 Scattering characteristics of N_2^{+*} dissociation – slow and fast

Slow dissociation of the N_2^{+*} will result in $w(N^+)$ and $w(N)$ being isotropically distributed about $w(N_2^{+*})$, the limiting velocity of the N_2^{+*} ion (0.56 cm μs^{-1}). Conservation of momentum in the separation of the Ne^+ and N_2^{+*} will result in $w(N_2^{+*})$ being directed antiparallel to $w(Ne^+)$ (Figure 7.4).

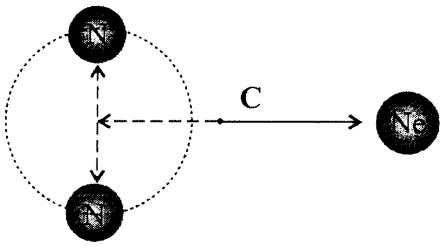

Figure 7.4 A schematic diagram for of the internal frame product scattering resulting from the slow dissociation of N_2^{+*} where the dotted circle indicates the possible scattering angles of N^+ and N, and **C** indicates the centre-of-mass of the system.

For fast dissociation of N_2^{+*}, the Coulomb repulsion is predominantly between the Ne^+ and N^+. This repulsion will result in $w(N^+)$ and $w(Ne^+)$ being significantly larger than $w(N)$, and being directed effectively at 180° to each other (Figure 7.5).

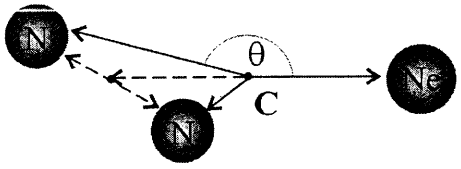

Figure 7.5 A schematic diagram for of the internal frame product scattering resulting from the fast dissociation of N_2^{+*} where **C** indicates the centre-of-mass of the system.

The angular scattering characteristics of the slow and fast dissociation of N_2^{+*}, as described above, may also be generated by a Monte Carlo classical trajectory simulation of this mechanism. As previously mentioned, only a brief description of the Monte Carlo classical trajectory simulation method is given in this chapter since the calculations described below were not carried out by the author of this thesis, but by contributing authors to reference [14] (Harper *et al*). However, a detailed description of how the Monte Carlo code works is given in Appendix D along with a flow diagram and the annotated Monte Carlo code.

7.3.1.2 Monte Carlo Classical Trajectory simulations

In principle, the product ion scattering resulting from a dication-neutral reaction may be modelled by a variety of simulation techniques. One method which is reasonably straightforward to implement is a Classical Trajectory simulation incorporating a Monte Carlo algorithm. The Monte Carlo methodology involves "randomly" selecting initial starting conditions for the reactants to reproduce the expected distributions of the relevant variables, in the experimental situation. That is, the configurations (*e.g.* relative velocity, impact parameter) of the reactants are "randomly" chosen by the

program in such a way that a large number of these initial configurations will reproduce the pre-selected "real life" distributions set up by the user. Following the selection of these initial parameters, the reactants are allowed to evolve on a classical potential energy surface by solving the relevant equations of motion. When the reactants reach the crossing radius, an electron is transferred and the potential energy surface is switched to that of the products. The product velocities are then similarly allowed to evolve on this surface until the products are well separated and the final product velocities recorded. This procedure is repeated many thousands of times and the correlations between the theoretical product velocities are examined, in exactly the same way as for a PSCO experiment. Thus, it is possible to derive a "theoretical" scattering diagram from the simulation to compare with experiment.

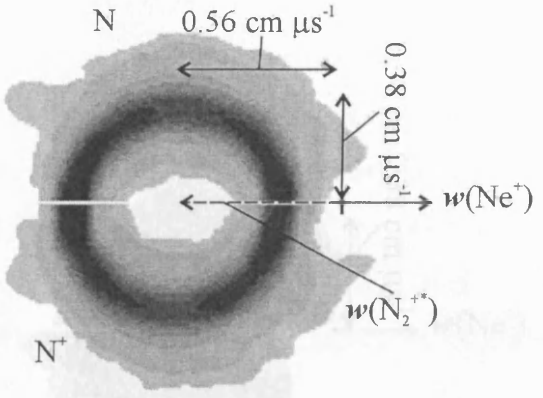

Figure 7.6 A Monte Carlo classical trajectory simulation showing the internal frame scattering diagram that results from a slow (τ = 1 ps) sequential dissociative electron transfer pathway with a N_2^+ dissociative kinetic energy release of 2 eV.

A Monte Carlo classical trajectory simulation of the slow mechanism results in the scattering diagram shown in (Figure 7.6) [14]. This general style of scattering diagram has been observed experimentally for the slow dissociation of both the dicationic collision complex (Eq. 7.5) and the primary product monocation (Eq. 7.6) in bond-forming chemical reactions of CF_2^{2+} with H_2O (Chapter Nine) [5].

$$CF_2^{2+} + H_2O \rightarrow [H_2O - CF_2]^{2+} \rightarrow [HOCF_2]^+ + H^+ \qquad (7.5)$$

$$[HOCF_2]^+ \rightarrow OCF^+ + HF \qquad (7.6)$$

A Monte Carlo classical trajectory simulation of the fast mechanism is shown in (Figure 7.7) [14]. Scattering diagrams of this form, following the sequential dissociation of a monocation in the field of the other charged product, have been observed before for the dissociation of CF_3^{+*} to CF_2^+ [5]. Comparing Figure 7.6 and Figure 7.7, it can be seen that the isotropic distribution of N^+ and N velocities about the velocity of N_2^{+*} as observed in Figure 7.6 for the slow mechanism, has been distorted in the fast dissociation, as indicated in Figure 7.5, due to the influence of the Coulomb field of the Ne^+ ion.

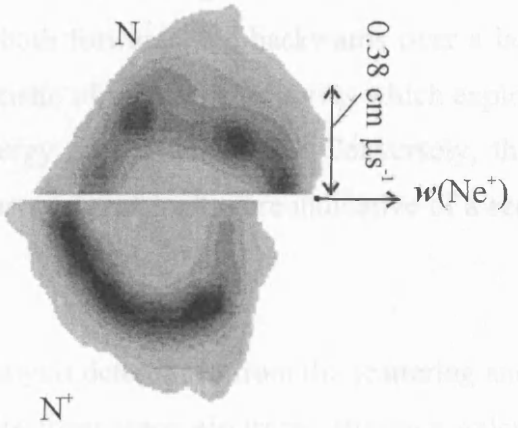

Figure 7.7 A Monte Carlo classical trajectory simulation showing the internal frame scattering diagram that results from a fast (τ = 10 fs) sequential dissociative electron transfer pathway with a N_2^+ dissociative kinetic energy release of 2 eV.

7.3.2 Complex or direct mechanism

By inspection of Figure 7.2, Figure 7.6 and Figure 7.7, it is clear there are fundamental differences between the form of the experimental data (Figure 7.2) and the form of the scattering diagrams (Figure 7.6, Figure 7.7) expected, and observed, for the sequential electron transfer mechanism. The key difference is the fixed angular relationship between all three product vectors in the experimental data (Figure 7.2) which is not present for the sequential pathways. Hence, it may be construed that the sideways scattered N^+ ions in this dissociative electron transfer channel arise *via* the formation of a transitory $[Ne\text{-}N_2]^{2+}$ intermediate. Indeed, the sharp angular relationship between the velocity vectors of the three product ions is very similar to that observed in the three-body unimolecular dissociation of the doubly charged ions formed by photoionisation of neutral molecules [13]. Further evidence for the formation of a collision complex in this channel comes from inspection of the Ne^+ scattering angle, which can be extracted from the experimental data. These angular distributions show that the Ne^+ ions in Channel A are scattered both forwards and backwards over a large range of angles in the COM frame, characteristic of *snarled trajectories* which explore a local minimum in the reactive potential energy surface [10, 15]. Conversely, the Ne^+ ions formed in Channel B are strongly forward scattered, more indicative of a sequential mechanism as discussed below.

In order to confirm the analysis determined from the scattering and calculated energetics in this channel, the results from some electronic structure calculations and geometry optimisations will be described briefly below. These calculations were not carried out by the author of this thesis, but by contributing authors to reference [14] (Harper *et al*) and are included as an additional aid to understanding the dynamics in this channel.

7.3.2.1 Channel A

The internal frame scattering (Figure 7.2) indicates that the $[Ne\text{-}N_2]^{2+}$ intermediate is distinctly nonlinear when it dissociates. By analogy with the isoelectronic N_2O

molecule, a strongly bound linear minimum should exist on the singlet $[Ne\text{-}N_2]^{2+}$ potential energy surface. This expectation is confirmed by electronic structure calculations (MP2, aug-ccpVTZ), performed by collaborating authors in reference [14] using GAUSSIAN 98 [16], which reveal a linear minimum 21.9 eV below the lowest triplet reactant asymptote. However, the majority of the Ne^+ ions in the PSCO beam are in the ground ^3P state [17, 18]. Hence, the majority of encounters may be expected to occur on a triplet surface. To explore the feasibility of nonlinear minima existing on a triplet surface an attempt has been made to locate such stationary points theoretically [16]. Geometry optimisations of triplet states using an aug-cc-pVTZ basis set and a CIS algorithm [16] have identified two minima of C_{2v} symmetry lying 17.4 and 12.6 eV below the lowest reactant asymptote.

Considering the potential uncertainties in *ab initio* calculations, in 1997, Feller and Peterson carried out an examination of the intrinsic errors in electronic structure methods using GAUSSIAN [16]. They compared the calculated energies, and other properties, for a large "benchmark set" of molecules (ranging from diatomics to at least hexatomics) with experimental data and values determined for the complete basis set limit. The investigation of Feller and Peterson showed a mean deviation for the MP2 methodology, using a cc-pVTZ basis set, of ± 5 kcal mol^{-1} (0.2 eV) and a maximal deviation of ± 20 kcal mol^{-1} (0.9 eV). This estimate of the error should apply to the calculation of the energy of the linear singlet geometry of $[NeN_2]^{2+}$ reported in reference [14]. Such energetic uncertainties are small in comparison to the differences in energy being considered. In addition, however, the MP2 calculations in reference [14] were principally used to show qualitatively that a linear singlet minimum exists below the asymptotic energy of the reactants. This qualitative result is clearly valid given the relative energetics (21.9 eV) and their uncertainty (0.9 eV).

The CIS calculations reported in reference [14] were used to show, again qualitatively, that minima of C_{2v} geometry can exist on the $[N_2\text{-}Ne]^{2+}$ triplet surface linking the reactants and products, to provide computational support for the experimental conclusions. In general, again as shown by Feller and Peterson, many lower-level computational methodologies converge readily to geometries close to the "true"

geometry, even though the uncertainties in the calculated energies are more significant. This justifies the use of the CIS procedure, which has an accuracy likened by its developers to that of Hartree-Fock (HF) theory in searching for the geometries of these intermediates on the triplet surface [19], which strictly is an excited state of the $[N_2\text{-}Ne]^{2+}$ system, lying above the $N_2^+ + Ne^+$ surface. Typical HF "errors" in bond lengths and angles are 0.1 Å and 2 degrees, respectively. Again, such uncertainties do not detract from the conclusions in reference [14] that the minima on the triplet surface are non-linear. With regard to the energies of these minima, the principal conclusion of reference [14] was that they lie below the reactant asymptote. Given the maximal uncertainties in the energetics of HF-ccVTZ calculations derived by Feller and Peterson of ± 50 kcal mol^{-1} (2.1 eV), the conclusion of reference [14], that energetically accessible C_{2v} minima may exist at 17.4 and 12.6 eV below the reaction asymptote on the triplet surface of the reaction of Ne^{2+} with N_2, seems reasonable.

Given the discussion above it seems clearer that the calculations in reference [14], whilst not a complete exploration of the accessible $[Ne\text{-}N_2]^{2+}$ potential energy surfaces, support the conclusion from the experimental data that non-linear potential energy minima of triplet spin symmetry are energetically available. Indeed, in one of these minima a significant percentage of the dipositive charge is carried by the nitrogen atoms. In the dissociation of such a transitory complex, all three atoms should receive a significant impulse before the two positive charges finally localise to form Ne^+ and N^+. Such a model of continuous electron transfer between the fragments of dicationic fragmentation, until the fragments separate sufficiently for the charges to localise, has been successfully used to model the fragmentation of small molecular dications [20].

7.3.2.1.1 Energetics

The centre-of-mass kinetic energy release in Channel A, which may be calculated from the magnitudes of the product velocity vectors as described in Chapter Four is centred at 25.7 eV with a FWHM of 8.6 eV. This kinetic energy release distribution corresponds to a range of reaction exoergicities, the energy separation of product and reactant states,

of between 13.6 and 22.2 eV (Figure 7.8). This range of reaction exoergicities correlates well with the formation of N^+, N, and Ne^+ in their ground electronic configurations from the $2p^4$ configuration of Ne^{2+}. However, the significant number of electronic states within these electronic configurations cannot be energetically resolved.

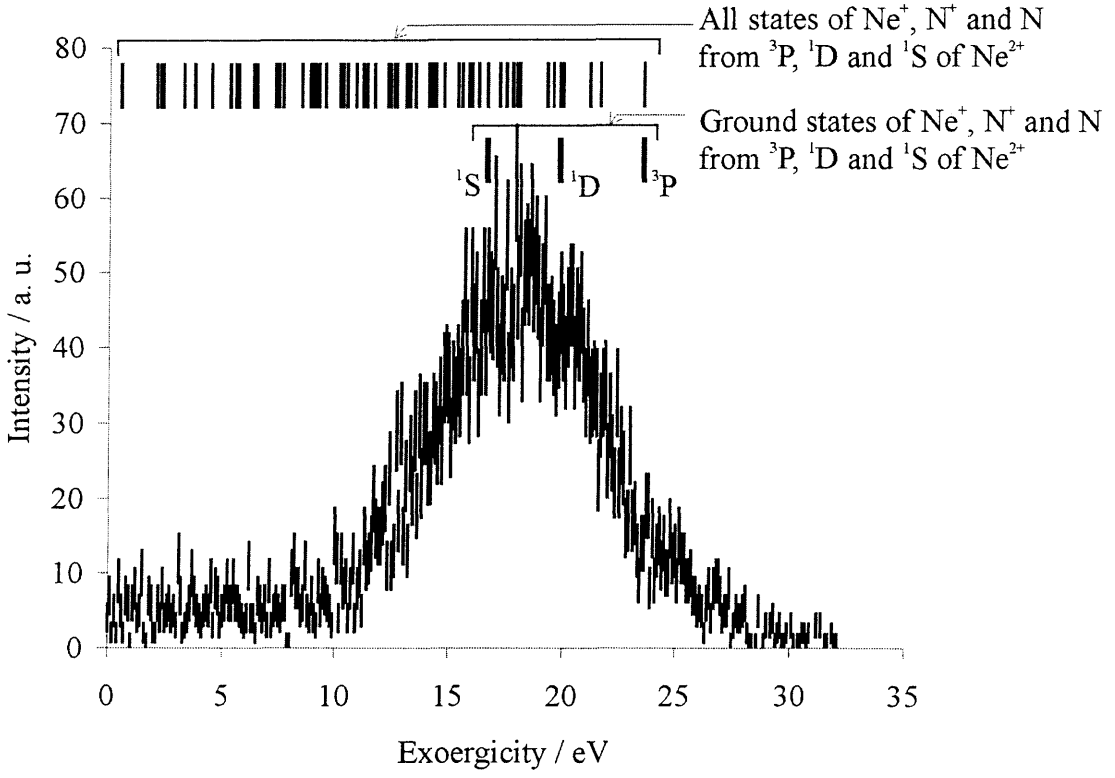

Figure 7.8 An exoergicity spectrum for Channel A indicating the exoergicities for forming all possible product states from all reactant states in the PSCO beam.

7.3.2.2 Channel B

Having established that Channel A involves a collision complex, Channel B (Figure 7.1), which produces backward scattered N^+ ions in coincidence with forward scattered Ne^+ ions, will now be examined. In Channel B Figure 7.9 (a) it can clearly be seen that the N^+ and Ne^+ separate at an angle closer to 180° with the neutral N atom having a much lower centre-of-mass velocity than the charged products. This internal frame

scattering (Figure 7.9 (a)) bears little immediate similarity to the prototypical scattering expected for a conventional sequential electron transfer reaction (Figure 7.6) and could be explained as the dissociation of a linear collision complex, perhaps involving the deep minimum on the singlet potential surface. However, the strong forward scattering of Ne^+ in this system and the associated backward scattering of the N^+ ion is indicative of a conventional electron transfer reaction and not of complexation [1, 10, 11, 15]. In addition, as indicated in Figure 7.9, $w(N^+)$ and $w(N)$ seem to be partially distributed about a circle centred at a precursor velocity displaced from the centre-of-mass.

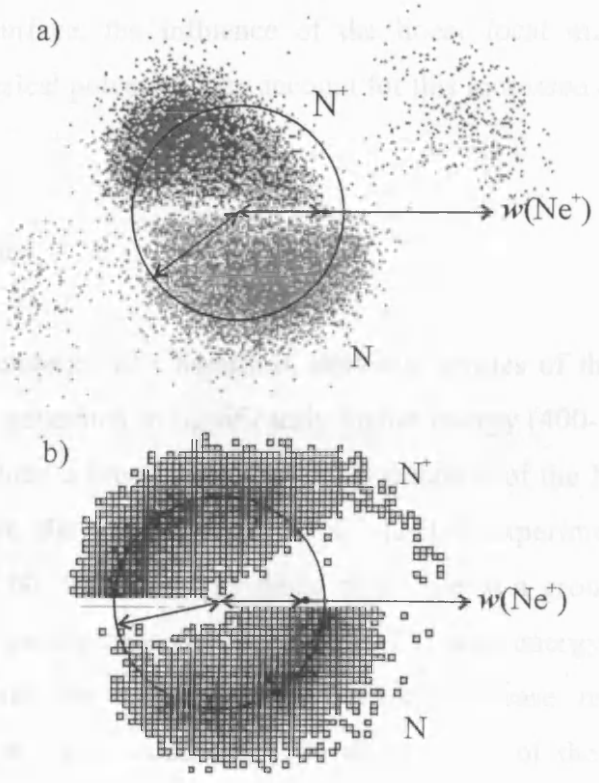

Figure 7.9 Internal frame scattering diagrams for Channel B; (a) is the experimental data, (b) is a simulation. The circle in the figure is of radius 0.8 cm μs^{-1}, displaced 0.6 cm μs^{-1} from the COM.

Simulating a sequential dissociative electron transfer process, using a Monte Carlo classical trajectory algorithm, gives qualitative agreement with the form of the experimental data (Figure 7.9) that is obtained when the following factors are included:

(i) the interaction between the quadrupole of the N_2 molecule and the Ne^{2+} ion, (ii) a N_2^{+*} lifetime of 60 fs, and (iii) a Gaussian energy release when the N_2^{+*} ion dissociates centred at 8 eV with a half width of 6 eV, with the charge being carried by the atom furthest from the Ne^+ ion. It does not seem unreasonable that an N_2^+ ion dissociating in the field of a Ne^+ ion will be polarised such that the charge finally resides on the nitrogen furthest from the Ne^+. Certainly, such an asymmetry in the dissociation is required for the simulation to generate the general form of the experimental data.

Comparing the experimental (Figure 7.9 (a)) and simulated (Figure 7.9 (b)) data, it can be seen that the experimental data displays an average angle between $w(N^+)$ and $w(Ne^+)$ closer to 180° than the simulation. Perhaps, if this channel proceeds on the singlet potential energy surface, the influence of the linear local minimum, which is not included in the classical potential, may account for this increased colinearity.

7.3.2.2.1 Energetics

Considering the energetics of Channel B, previous studies of the translational energy spectra of Ne^+ ions generated in significantly higher energy (400-1600 eV) collisions of Ne^{2+} with N_2 attributed a broad feature to the population of the $N_2^+(^2\sigma_g^{-1}, {}^2\Sigma_g^+)$ state at 20.6-22.6 eV above the ground state of N_2^+ [21]. Experiments have shown that electronic states of N_2^+ in this energy range dissociate to a ground state N^+ ion and a nitrogen atom in a variety of excited states [22, 23] with energy releases up to 12 eV [23], in accord with the significant 8 eV energy release required to model the experimental data in the simulations. The dissociation of the $N_2^+(^2\sigma_g^{-1}, {}^2\Sigma_g^+)$ state proceeds to a limit about 11.9 eV above the ground state of N_2^+, although it seems clear that a range of excited states are formed [22].

The kinetic energy release distribution determined experimentally for this channel corresponds to an exoergicity distribution centred at 14.2 eV with a FWHM of 8.0 eV (Figure 7.10). Adding this exoergicity to the dissociation asymptote for the $N_2^+(^2\sigma_g^{-1}, {}^2\Sigma_g^+)$ state indicates the products in this channel stem from a reactant asymptote 59-67

eV above the ground states of Ne and N_2, in good agreement with the electronic states arising from the $2p^4$ configuration of Ne^{2+} which make up the PSCO ion beam.

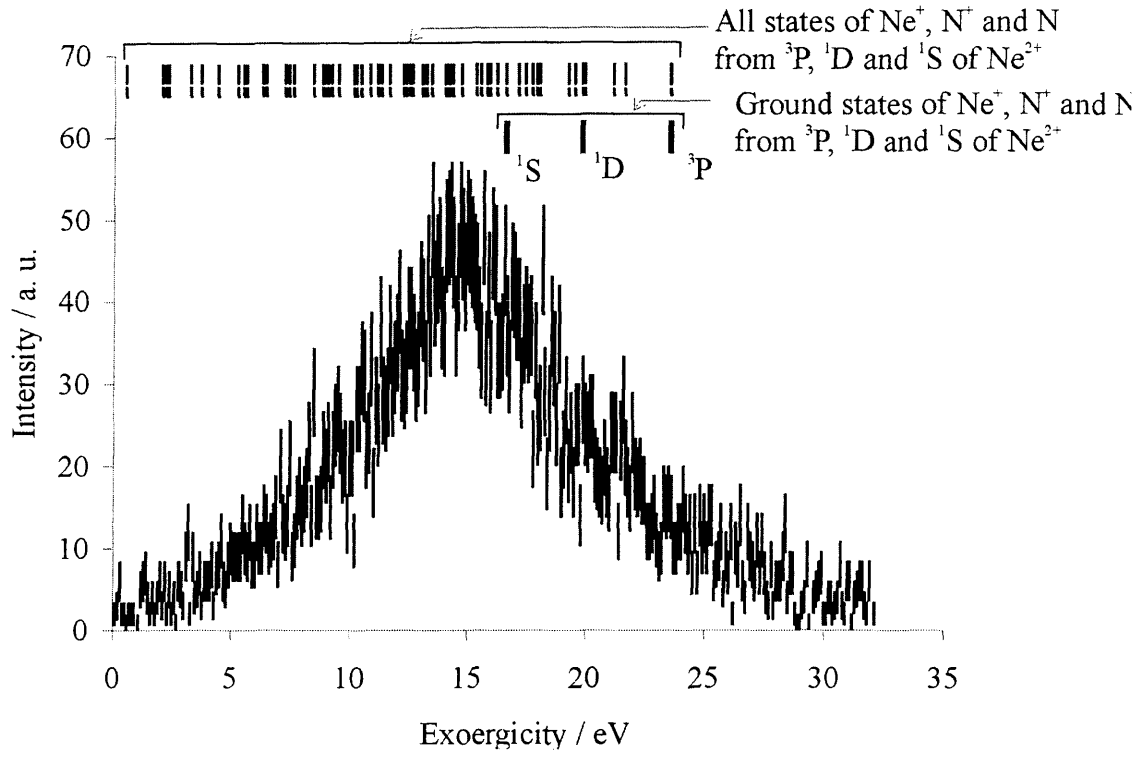

Figure 7.10 An exoergicity spectrum for Channel B indicating the exoergicities for forming all possible product states from all reactant states in the PSCO beam.

7.3.3 Channel C

From the relative intensities (branching ratios) of the three channels forming Ne^+ in coincidence with N^+, cited at the beginning of section 7.3, it is clear that Channel C is significantly weaker than Channels A and B described above. If a more detailed analysis of the dynamics and energetics in Channel C was desired, more experimental data would need to be recorded. A cursory examination of the observed scattering in Channel C (Figure 7.1) seems to indicate events analogous to Channel B are occurring,

i.e. sequential dissociation of N_2^+ subsequent to electron transfer between the reactants. However, in contrast to the forward scattering of Ne^+ and backward scattering of N_2^+ observed in Channel B, Ne^+ is backward scattered in Channel C and is accompanied by the forward scattering of N^+ when formed by the dissociation of N_2^+.

7.3.3.1 Energetics

From Figure 7.11, it seems that electronic transitions involving highly excited product states must give rise to the exoergicity signals observed for this channel. In order to make a definitive assignment of these signals, it will be necessary to investigate this channel in more detail.

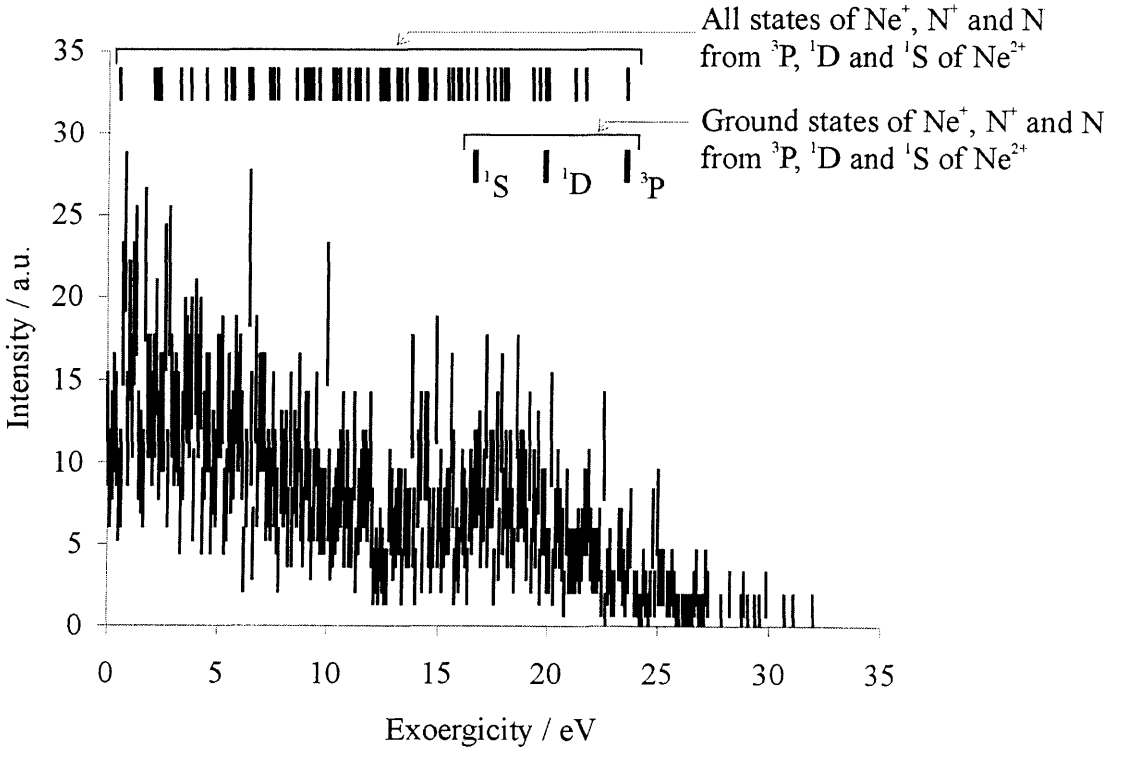

Figure 7.11 An exoergicity spectrum for Channel C indicating the exoergicities for forming all possible product states from all reactant states in the PSCO beam.

7.4 Conclusions

In conclusion, the PSCO experiments show that the formation of $Ne^+ + N + N^+$ from Ne^{2+} and N_2 in this low energy regime proceeds by two different pathways. One pathway, Channel A, involves the formation of a transitory collision complex. However, Channel B appears consistent with a sequential process involving the fast dissociation of N_2^{+*}.

7.5 References

[1] Herman, Z., 1996, *Int. Rev. Phys. Chem.* **15** (1) 299-324.

[2] Janev, R. K. and Winter, H., 1985, *Phys. Rep.: Rev. Section Phys. Lett.* **117** (5-6) 265-387.

[3] Mathur, D., 1993, *Phys. Rep.-Rev. Sec. Phys. Lett.* **225** (4) 193-272.

[4] Price, S. D., Manning, M., and Leone, S. R., 1994, *J. Am. Chem. Soc.* **116** (19) 8673-8680.

[5] Price, S. D., 2003, *Phys. Chem. Chem. Phys.* **5** (9) 1717-1729.

[6] Tosi, P., Lu, W. Y., Correale, R., and Bassi, D., 1999, *Chem. Phys. Lett.* **310** (1-2) 180-182.

[7] Price, S. D., 1997, *J. Chem. Soc.: Faraday Trans.* **93** (15) 2451-2460.

[8] Witasse, O., *et al.*, 2002, *Geophys. Res. Letts.* **29** (8) 1263.

[9] Nicolaides, C. A., 1989, *Chem. Phys. Lett.* **161** (6) 547-553.

[10] Mrazek, L., *et al.*, 2000, *J. Phys. Chem. A.* **104** (31) 7294-7303.

[11] Harper, S. M., Hu, W. P., and Price, S. D., 2002, *J. Phys. B: At. Mol. Opt. Phys.* **35** (21) 4409-4423.

[12] Hu, W. P., Harper, S. M., and Price, S. D., 2002, *Meas. Sci. Technol.* **13** (10) 1512-1522.

[13] Hsieh, S. and Eland, J. H. D., 1997, *J. Phys. B: At. Mol. Opt. Phys.* **30** (20) 4515-4534.

[14] Harper, S. M., Hu, S. W. P., and Price, S. D., 2004, *J. Chem. Phys.* **120** (16) 7245-7248.

[15] Herman, Z., Zabka, J., Dolejsek, Z., and Farnik, M., 1999, *Int. J. Mass Spectrom.* **192** 191-203.

[16] GAUSSIAN 98, Frisch, M. J., *et al.*, Revision A9, Gaussian Inc., Pittsburgh, PA, 1998.

[17] Huber, B. A. and Kahlert, H. J., 1984, *J. Phys. B: At. Mol. Opt. Phys.* **17** (3) L69-L74.

[18] Brazuk, A. and Winter, H., 1982, *J. Phys. B: At. Mol. Opt. Phys.* **15** (14) 2233-2244.

[19] Foresman, J. B. and Frisch, M. J., *Exploring chemistry with electronic structure methods*, 2nd ed. 1997, Pittsburgh, PA: Gaussian Inc.

[20] Hsieh, S. and Eland, J. H. D., 1995, *J. Chem. Phys.* **103** (3) 1006-1012.

[21] Okuno, K., Fukuroda, A., Kobayashi, N., and Kaneko, Y., 1989, *J. Phys. Soc. Jpn.* **58** (5) 1590-1594.

[22] Eland, J. H. D. and Duerr, E. J., 1998, *Chem. Phys.* **229** (1) 13-19.

[23] Samson, J. A. R., Chung, Y., and Lee, E. M., 1991, *J. Chem. Phys.* **95** (1) 717-719.

Chapter 8

The electron transfer reactions of CF_2^{2+}-H_2O

8.1 Introduction

The first investigation of the CF_2^{2+}-H_2O collision system was recently performed by Kearney *et al* using a crossed beam mass spectrometer [1]. Integral cross-sections were determined for the formation of the CF_2^+ (Eq. 8.1 & 8.3) and CF^+ (Eq. 8.2) product ions and for OCF^+, which is formed *via* a bond forming reaction (Eq. 8.4).

$$CF_2^{2+} + H_2O \rightarrow CF_2^+ + H_2O^+ \qquad (8.1)$$

$$CF_2^{2+} + H_2O \rightarrow CF^+ + H_2O^+ + F \qquad (8.2)$$

$$CF_2^{2+} + H_2O \rightarrow CF_2^+ + H^+ + OH \qquad (8.3)$$

$$CF_2^{2+} + H_2O \rightarrow OCF^+ + H^+ + HF \qquad (8.4)$$

Kearney *et al* employed a Landau-Zener model to account for the relative abundances of the product ions formed by electron transfer. This chapter presents results that are consistent with the reactivity seen by Kearney *et al*, and shows that by using the PSCO technique it is possible to make definitive product partner ion associations. Partner ion association allows the full dynamics of each reactive event, for both two and three-body collisions, to be calculated from the initial velocity vectors of the ionic products.

8.2 Experimental details

A detailed account of the experimental arrangement is given in Chapter Three. PSCO spectra were recorded at two settings for the collisions of CF_2^{2+} with H_2O: a laboratory frame collision energy of 21.28 eV (E^c = 5.63 eV) with a repeller plate voltage of 300 V, and at a laboratory frame collision energy of 16.28 eV (E^c = 4.31 eV) with a repeller plate voltage of 50 V. Using a high source field in the reaction source region of the TOF mass spectrometer allows collection of the full angular distribution of the scattered product ions, including those highly energetic ions with considerable energies perpendicular to the axis of the TOF mass spectrometer, but with lower energy resolution (Chapter Five). At low source field, better energy resolution is obtained in the TOF mass spectrum at the expense of ions with considerable x and y velocity components, which miss the detector. For this collision system, CF_2^{2+} was generated by ionising CF_4 with a beam of 200 eV electrons.

8.3 Results and discussion

This chapter and chapter nine present data on the collisions of CF_2^{2+} with H_2O. The four previously observed dication-neutral reaction channels mentioned in section 8.1 were detected along with the following channel:

$$CF_2^{2+} + H_2O \rightarrow HCF_2^+ + H^+ + O \qquad (8.5)$$

These five channels correspond to non-dissociative electron transfer (NDET) (Eq. 8.1), dissociative electron transfer (DET) (Eqs. 8.2, 8.3) and bond forming (BF) reactions (Eqs 8.4, 8.5). The BF reactions are discussed in Chapter Nine. The dynamics of each of these channels can be studied by selecting the events making up separate peaks in turn from the coincidence spectrum. The magnitudes of the product velocity vectors for each channel and the correlation between them are described below.

For all the reactive channels detected, the angular distribution, mutual angles of separation and the exoergicity were determined. In the same way that the mutual angle of separation between the products resulting from a two-body dissociation is determined, it is possible to derive the 'internal frame' relationship between the products resulting from a three-body dissociation. The velocity vector of each ion is calculated and, hence, the angle of one ion relative to another can be determined from the scalar product of the vectors. That is the mutual angle between $m(1)$ and $m(2)$, between $m(2)$ and $m(3)$ and $m(1)$ and $m(3)$. Such data analysis provides a critical insight into the mechanism of the reaction.

8.3.1 A comparison between PSCO and "crossed beam" (Kearney *et al*) ion intensities

The relative intensities of the six product ions detected for the collisions of CF_2^{2+} with H_2O are shown in Table 8.1. The intensities reported by Kearney *et al* [1] are also presented and are determined for all detected ions. The PSCO intensities are determined only from detected ion pair events, so it is possible that not all ion arrivals at the detector are counted if one ion out of the pair is missed. The intensities for the PSCO ion pair events were taken from data recorded at high source field and, hence, the intensities represent the full angular distribution for each ion detected in a pair event, so a comparison with Kearney *et al* may be made.

The lower intensity of OCF^+ when detected by the PSCO experiment is due to this particular 'pair events only' aspect of the PSCO data processing and is discussed in more detail in the Chapter Nine. Briefly, in the CF_2^{2+}-H_2O collision system OCF^+ is formed in coincidence with H^+ (Eq. 8.4). However, a significant proportion of these events where a highly energetic H^+ ion is formed will result in the sideways scattering of H^+, either to the extent that it never enters the TOF drift tube, or that it hits the walls of the drift tube. So, for this particular channel (Eq. 8.4), the PSCO intensity of OCF^+ is

slightly lower than the intensity reported by Kearney *et al* where all the 'single' arrivals of OCF^+ are counted.

Table 8.1 Relative intensities of the six product ions formed in the collisions of CF_2^{2+} with H_2O for the PSCO spectrometer at high TOF source field compared to intensities presented by Kearney *et al* [1].

Product ions	CF_2^+	H_2O^+	CF^+	OCF^+	H^+	HCF_2^+
PSCO	69	169	100	0.5	0.6	0.05
Kearney *et al*	58	62	100	5	0.4	-

Aside from this factor, the main difference between the two data sets is that the intensity of H_2O^+ is greater in the PSCO data. This discrepancy is due to the orthogonal alignment of the TOF mass spectrometer in Kearney *et al*'s experimental arrangement resulting in lower detection efficiency for H_2O^+ (Figure 8.1), as will be described below.

8.3.1.1 Detection efficiency of H_2O^+

Following dication-neutral collisions in the reaction source region of the apparatus used by Kearney *et al*, the majority of CF_2^+ (Eq. 8.1) and CF^+ (Eq. 8.2), formed by non-dissociative and dissociative electron transfer respectively, are forward scattered in the LAB frame (Figure 8.1 (b)). Correspondingly, the majority of H_2O^+ ions, from the same reactions that formed CF_2^+ and CF^+, are backward scattered in the LAB frame (Figure 8.1 (b)). Due to the orthogonal alignment of Kearney *et al*'s TOF mass spectrometer, with respect to the unreacted dication beam, the initial forward or backward scattering of the product ions is effectively translated to 'sideways' scattering with respect to the detector when the extracting field is applied to the repeller plate (Figure 8.1 (b) and (c)).

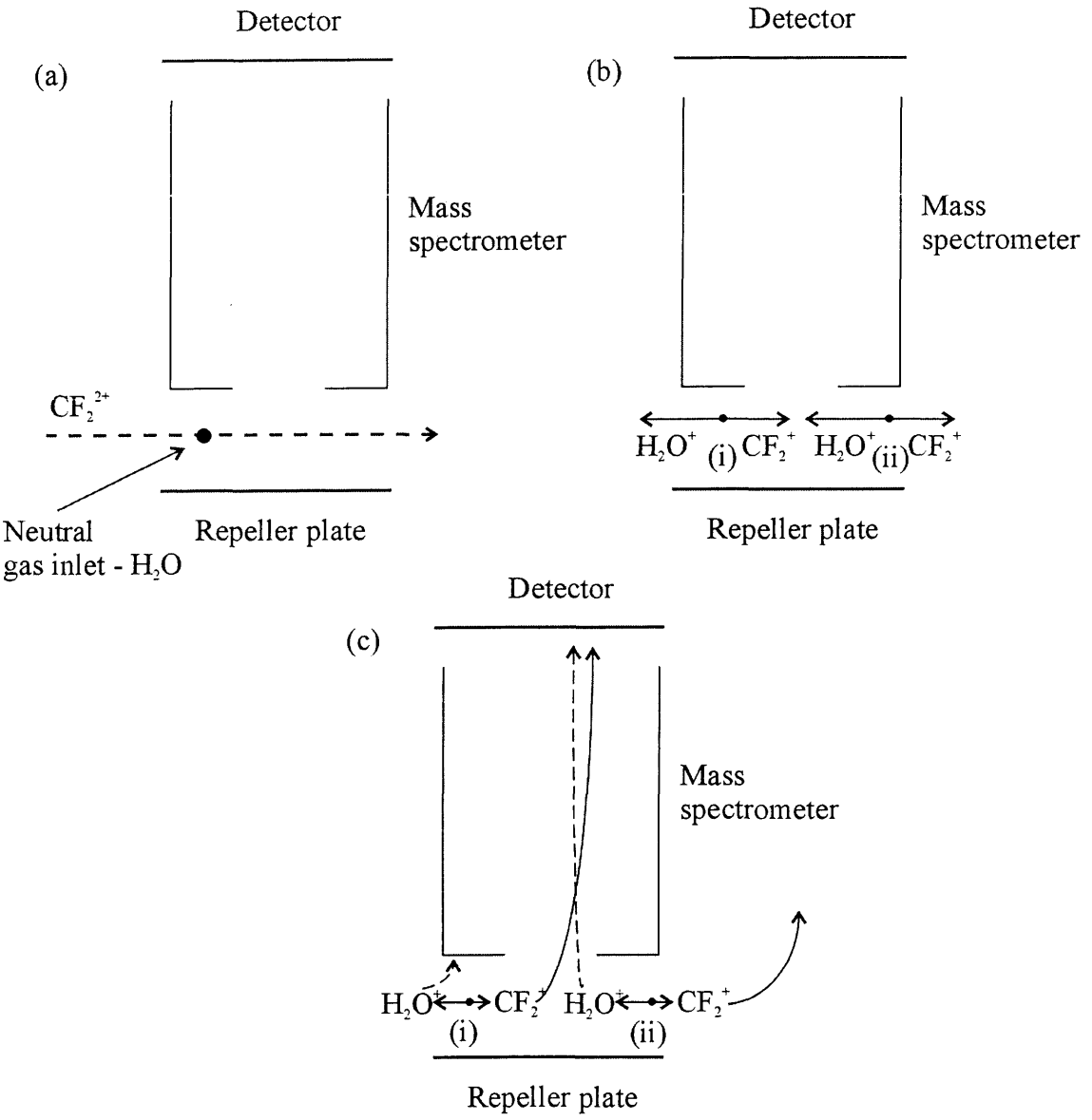

Figure 8.1 A schematic diagram demonstrating why some H_2O^+ ions are not detected by the crossed beam experiment [1], where (a) is before the collision, (b) immediately after the collision but before the repeller plate pulse and (c) after the repeller pulse. (i) and (ii) are two different dication-neutral reaction sites in the reaction source region, one of which (ii) will result in the detection of H_2O^+. However, the most likely point of dication-neutral interaction is (i) which is why the detection efficiency of H_2O^+ is low.

The detection efficiency of the product ions is therefore dependent on the actual position of dication-neutral interaction in the source region. From Figure 8.1 (b) (i) and (c) (i), it is clear that CF_2^+ will be detected and H_2O^+ will not reach the detector. In contrast, from Figure 8.1 (b) (ii) and (c) (ii), the opposite will be true where H_2O^+ is detected and CF_2^+ is lost. Only the detection efficiency of H_2O^+ is affected since the majority of dication-neutral collisions will occur at position (i) near the neutral gas inlet [1].

8.3.1.2 Detection efficiency of HCF_2^+

The data reported by Kearney *et al* do not resolve the HCF_2^+ peak as its intensity is too low to be distinguished from the spread of the very intense CF_2^+ signal that appears one mass unit lower than HCF_2^+ in the mass spectrum. The ability of the PSCO technique to separate the channel forming HCF_2^+ from the one forming CF_2^+ using the coincidence experiments is a distinct advantage over the conventional mass spectrometric crossed beam technique used by Kearney *et al.*

8.4 Non-dissociative electron transfer: $CF_2^{2+} + H_2O \rightarrow CF_2^+ + H_2O^+$

PSCO data was collected at both high and low TOF source fields for the NDET reaction channel (Eq. 8.1). As explained in Chapter Four, recording data for a collision system at two different source fields is beneficial since the high source field facilitates the collection of the full angular distribution of both ions in one experiment. The low source field setting, at the expense of the full angular distribution, then provides better resolution in the angular and energy distribution spectra.

8.4.1 Angular distribution

Two products, CF_2^+ and H_2O^+, are formed in the NDET channel (Eq. 8.1). The angular distribution of these products in the COM frame, derived from the data at high TOF source field, shows strong forward scattering of CF_2^+ and strong backward scattering of H_2O^+ (Figure 8.2).

Strong forward scattering is commonly observed for the NDET reactions of dications [2-5] and arises as the electron hops from the neutral to the dication at significant interspecies separations (3-6 Å). Hence, most of the reactive events involve the dications approaching the neutral at a significant impact parameter, picking up the electron and flying on in approximately the same direction as their initial velocity.

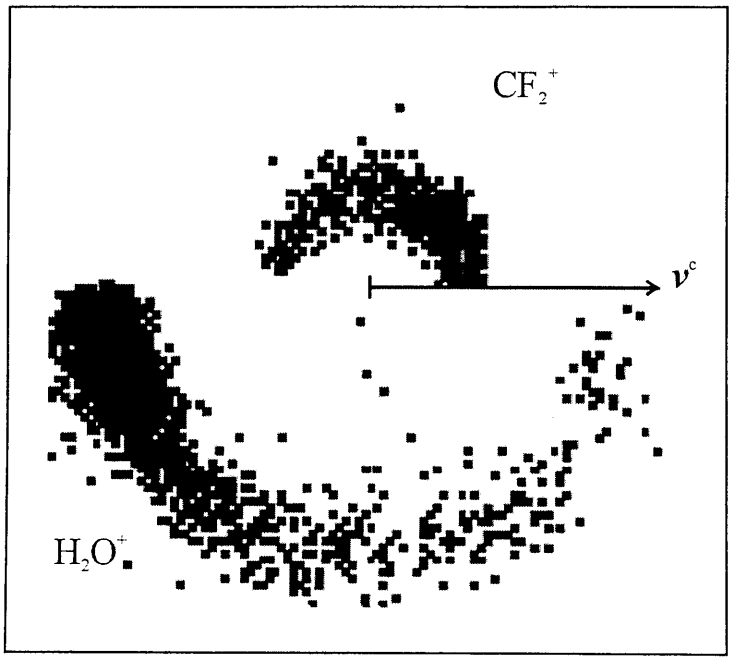

Figure 8.2 Scattering diagram for CF_2^+ and H_2O^+ with respect to v^c (scale: length of the arrow = 1 cm μs^{-1}).

Previous investigations of other dicationic NDET reaction channels have reported similar angular distributions to those observed here in the formation of CF_2^+ and H_2O^+

(Eq. 8.1). However, it has been noted that the PSCO ionic angular distributions for the product ions show some evidence for a bimodal COM angular distribution (Figure 8.3). Bimodal distributions have been detected in electron transfer reactions of atomic dications (Chapter Six). Such distributions are thought to arise from the different potential energy surfaces that are explored by reactive trajectories when electron transfer occurs as the reactants approach each other ('early' electron transfer) compared with when electron transfer occurs as the reactants are separating ('late' electron transfer) [2, 6].

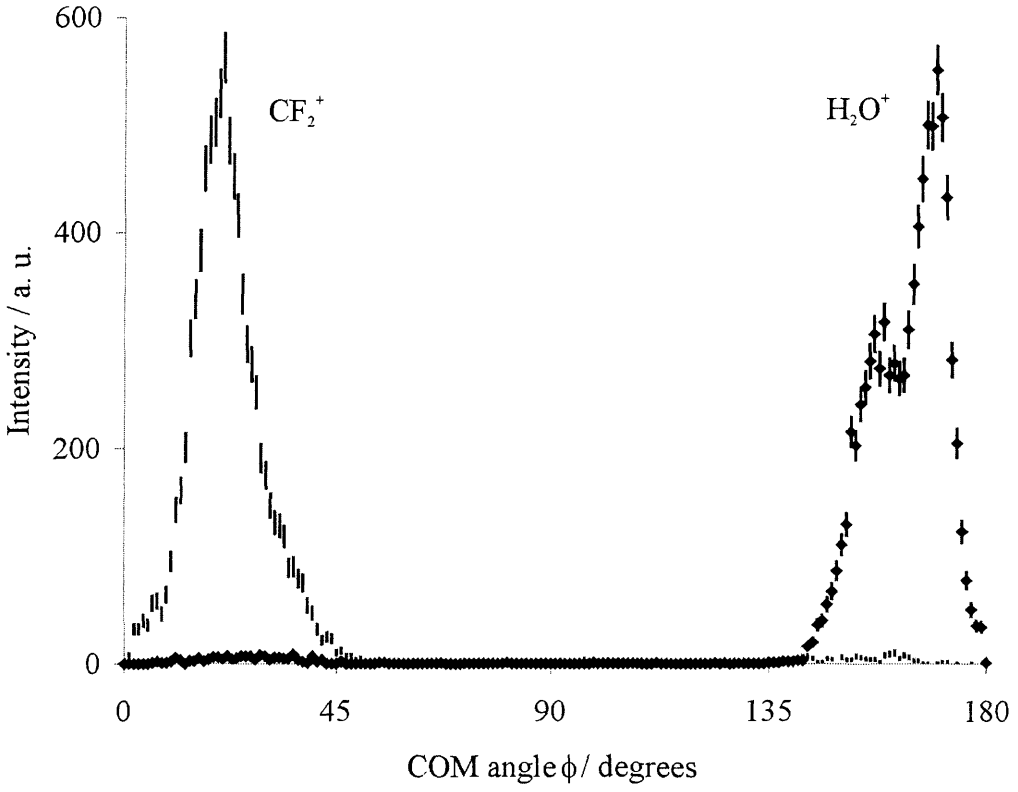

Figure 8.3 COM angular distribution of the products, CF_2^+ and H_2O^+, formed from non-dissociative electron transfer at low source field.

Reactive events associated with 'early' electron transfer result in larger scattering angles than 'late' electron transfer. In the Ne^{2+}-Ar collision system described in Chapter Six, there are a large number of accessible Ar^+ states, with different energies, at the low

PSCO collision energies and therefore there are incidences of both 'early' and 'late' electron transfer.

From Figure 8.3 it is clear that a bimodal distribution is only observed for H_2O^+ and not CF_2^+. At first glance, this might seem to be an anomaly since, in a two-body dissociation where the mutual angle between two species is always 180°, both ions should exhibit mirrored angular features in their scattering which is not what is observed in Figure 8.3. However, the bimodal scattering of H_2O^+ may be rationalised by considering the effect of the forward and backward scattering of CF_2^+ and H_2O^+, respectively, in COM frame on the product ion velocities in the LAB frame, and, hence, how well 'resolved' the angular distribution is for each of these ions. The quality of angular resolution is determined by the LAB velocity of ions towards the detector, as described in Chapter Four. H_2O^+ is backward scattered in the COM frame with most of the kinetic energy from the dication-neutral collision (Figure 8.2) resulting in a slow velocity in the LAB frame and, hence, better angular resolution.

8.4.1.1 Mutual angle

For a reaction forming two products, such as this channel, conservation of momentum in the centre-of-mass frame restricts the angle between $w(H_2O^+)$ and $w(CF_2^+)$ to 180°. When this angle is independently determined from the PSCO scattering data, a distribution centred at 180° with a FWHM of 1° is determined (Figure 8.4), as has previously been seen for two-body reactions with the PSCO apparatus. The agreement between the predicted angle and the experimentally determined angular distribution shows the validity of the PSCO data reduction algorithm and the angular resolution that the PSCO spectrometer is able to achieve.

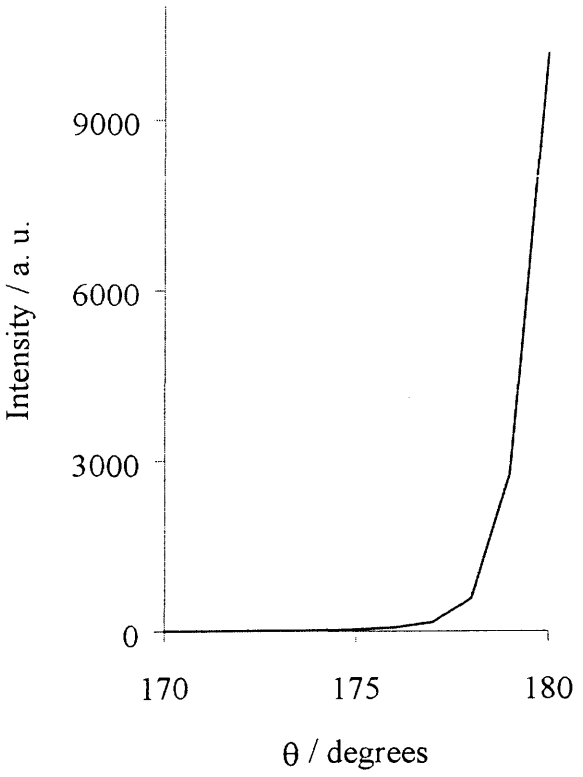

Figure 8.4 A mutual angle of 180° between CF_2^+ and H_2O^+, recorded at low source field.

8.4.2 Exoergicity

For this NDET channel (8.1), the data shows a single peak in the exoergicity spectrum centred at 4.8 eV with a full width half-maximum (FWHM) of 2.4 eV (Figure 8.5). The first step in determining which product ion states correspond to the experimentally determined exoergicity is to list those states of CF_2^+ and H_2O^+ which are non-dissociative, since the states of CF_2^+ and H_2O^+ detected in this reaction must be long-lived. Hence, CF_2^+ must be formed in its ground electronic state (X) since all its known excited electronic states are dissociative [7]. To form stable H_2O^+, the ground (X) or

first excited state (A) of H_2O^+ or vibrational levels of the (B) state within 1 eV of the v = 0 level must be populated (Table 8.2) [8].

Table 8.2 The vibrational envelopes determined by PES for the various stable electronic states of H_2O^+, together with the most intense transition within each envelope.

H_2O^+	X	A	B
Vibrational envelope (eV)	0.94	2.96	1
Probable vibrational excitation / eV	0	0.8	1

Table 8.3 Expected exoergicities of product ion formation in different combinations of electronic states, where (i) does not include any vibrational excitation of CF_2^+ or H_2O^+ and (ii) includes vibrational excitation for CF_2^+ (3 eV) and for H_2O^+ at the most intense transitions as described in Table 8.2.

ΔE of product ion formation (eV)		H_2O^+			
		X	A	B	
CF_2^+	X	7.7	6.03	3.14	←(i)
		4.70	2.23	-0.86	← (ii)

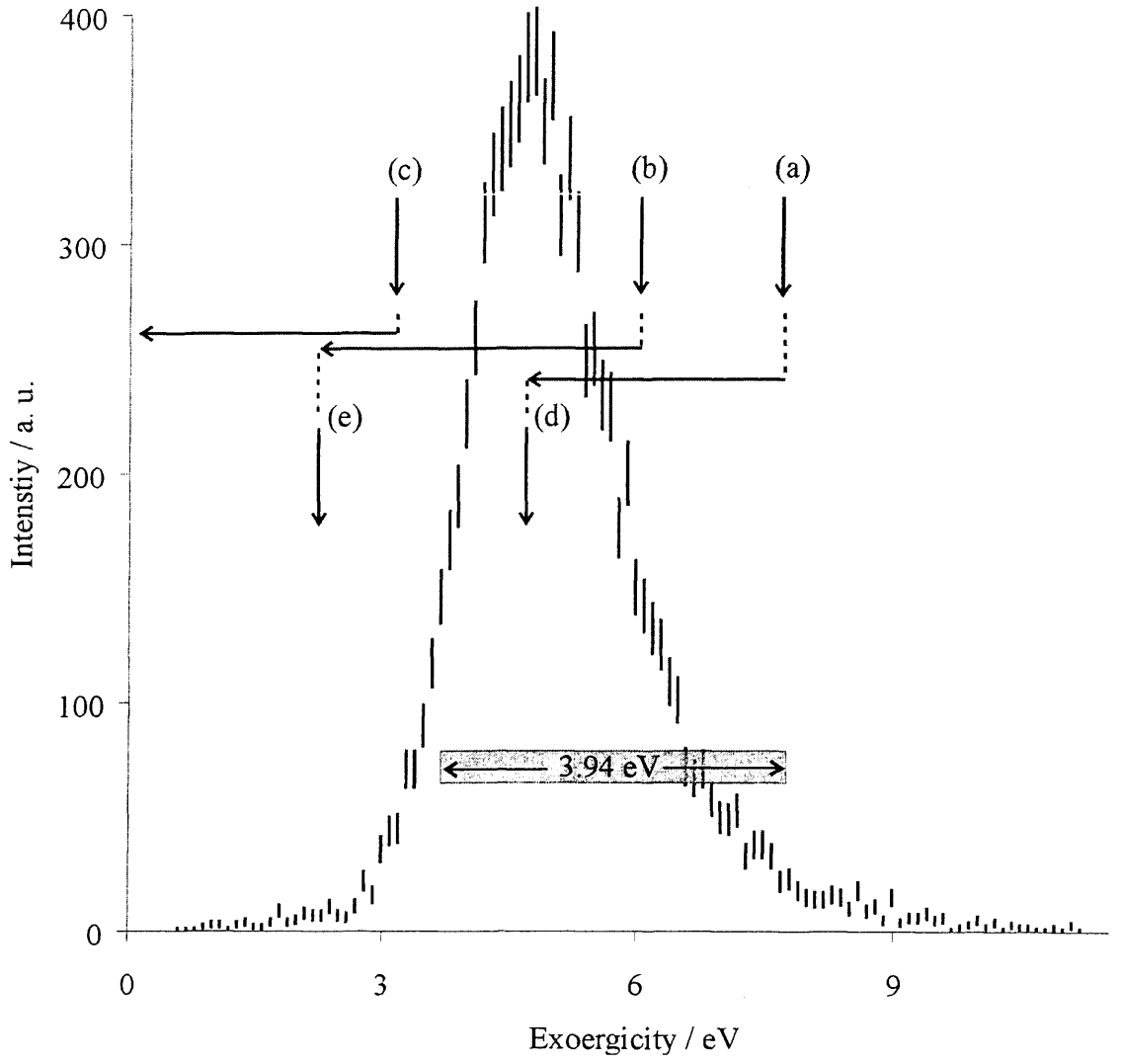

Figure 8.5 An exoergicity spectrum for NDET where the arrows indicate the exoergicities (from Table 8.3) for formation of CF_2^+ and H_2O^+, *via* the ground state of the dication, in the following states: (a) $CF_2^+(X)$, $H_2O^+(X)$, (b) $CF_2^+(X)$, $H_2O^+(A)$ and (c) $CF_2^+(X)$, $H_2O^+(B)$; (d) and (e) represent the exoergicities for formation of the product states taking into account vibrational excitation of the products (a) and (b), respectively. The shaded box indicates the possible range of exoergicities expected if the [$CF_2^+(X)$, $H_2O^+(X)$] states are populated with varying amounts of vibrational excitation (*i.e* 0-3.94 eV) of the products as discussed in the text.

The adiabatic exoergicities for forming [CF_2^+(X), H_2O^+(X)], [CF_2^+(X), H_2O^+(A)] and [CF_2^+(X), H_2O^+(B)] from the collisions of the ground state dication $CF_2^{2+}(^1\Sigma_g^+)$ [9] with H_2O(X) are 7.7, 6.0 and 3.1 eV respectively, using the adiabatic ionisation potentials of H_2O (Table 8.3). These product asymptotes are indicated in Figure 8.5 by the vertical arrows (a), (b) and (c). It can clearly be seen from Figure 8.5 that experimental exoergicity corresponds most closely to the [CF_2^+(X), H_2O^+(A)] asymptote.

However, the above preliminary assignment of the exoergicity spectrum is inadequate since it is assumed that the reactants and the products have no vibrational energy content (Table 8.3 (i)). Vibrational excitation of the reactants and products will of course affect the reaction exoergicity and the variation in this vibrational energy content can account for the position and width of the peak in the exoergicity spectrum (Table 8.3 (ii)). To interpret the exoergicity spectrum correctly, it is important to realise that the electron transfer process is usually well represented by a vertical transition at the dication geometry, and at this geometry, the exoergicity may markedly differ from that determined from adiabatic ionisation potentials.

Indeed, detailed experimental investigations of the formation of CO^+ from CO^{2+} have shown that the vibrational distribution of the CO^+ product is well modelled by a vertical transition from CO^{2+} [10]. Consequently, in evaluating the energetics of the formation of CF_2^+ and H_2O^+ from CF_2^{2+} and H_2O, it is necessary to note that CF_2^+ will be formed close to the equilibrium geometry of the dication $CF_2^{2+}(D_{\infty h})$. As discussed by Kearney *et al*, at the equilibrium geometry of CF_2^{2+}, CF_2^+ will be formed in highly excited vibrational levels, with approximately 3 eV of vibrational excitation [1].

The most probable vibrational energy deposition in the H_2O^+ product can be evaluated from the vibrational envelopes for the formation of H_2O^+(X), (A) and (B), in the photoelectron spectrum (PES) of water: 0, 0.8 and 1 eV respectively. Adjusting the above adiabatic exoergicities to allow for the expected vibrational energy content of both product ions results in predicted exoergicities of 4.7, 2.2 and -0.9 eV for forming the CF_2^+(X) together with the (X), (A) and (B) states of H_2O^+ (Table 8.3). These revised exoergicities are also indicated (Figure 8.5). From inspection of Figure 8.5, it

can be seen that the peak in the experimental exoergicity data corresponds excellently with that predicted for the formation of $CF_2^+(X)$ and $H_2O^+(X)$. Furthermore, it is clear from a comparison of the predicted exoergicities for the formation of $CF_2^+(X)$ together with excited electronic states of H_2O^+ (A, B) that there is no contribution to the experimental exoergicity from these channels.

In summary, by consideration of the available stable states (at the low PSCO collision energies) of the detected product ions, CF_2^+ and H_2O^+, together with the likelihood of vibrational excitation of either products, it has been possible to eliminate any contribution to the experimentally observed exoergicity spectrum (Figure 8.5) from the formation of $CF_2^+(X)$ together with excited electronic states of H_2O^+ (A or B). However, the experimental exoergicity signal does correspond well with the predicted exoergicity for the formation of $CF_2^+(X)$ with $H_2O^+(X)$.

It is clear from Figure 8.5 that the experimental exoergicity is not single valued. Indeed, a deviation in the experimental exoergicity from the predicted value of 4.7 eV, for the formation of $CF_2^+(X)$ with $H_2O^+(X)$, would be expected due to variations in the vibrational energy content of the product ions and any vibrational excitation of the dication. To estimate the possible spread in the expected reaction exoergicities, it must be noted that any vibrational excitation of the reactant CF_2^{2+} ion may well allow the population of a large number of vibrational states of $CF_2^+(X)$ in vertical transitions. Indeed, if it is assumed that $CF_2^+(X)$ may be formed at geometries from its equilibrium geometry to its dissociation limit (E_{vib} = 3.04 eV), and that $H_2O^+(X)$ may be formed in v = 0-2 (as is observed in the PES [8]), then the range of expected exoergicities is indicated in Figure 8.5 by the shaded box. As shown in Figure 8.5, the width of the experimental peak is in excellent agreement with the expected spread of predicted exoergicities. Indeed, it seems that the spread of exoergicities is well reproduced by just considering excitation of the product monocations. However, it is certainly possible that vibrationally excited states of the dication contribute to the higher energy tail in the experimental exoergicity spectrum.

The "Reaction Window" model based on the Landau-Zener (L-Z) theory has been used by Kearney *et al* to rationalise the relative abundance of the products resulting from the electron transfer reactions in this collision system. Kearney *et al*'s product state calculations for this channel predicted that NDET results in the formation of CF_2^+ in the (X) state and H_2O^+ in both the (X) and (A) states. The new PSCO experiments reported here clearly show that formation of $CF_2^+(X)$ and $H_2O^+(X)$ is the dominant pathway. The reaction window calculations for this NDET channel have also been carried out by the author of this thesis. The calculated cross-sections are given in section 8.5.2 along with a description of the program used for the calculations.

8.4.3 Summary

The PSCO experiments clearly show that the NDET formation of CF_2^+ and H_2O^+ from CF_2^{2+} and H_2O results principally in the formation of $CF_2^+(X)$ and $H_2O^+(X)$. The spread in the reaction exoergicity distribution can be qualitatively rationalised by allowing for vibrational excitation in the reactants and products.

8.5 Discussion: Dissociative electron transfer (DET)

There are two pathways leading to DET in this collision system. The channel forming CF^+ in coincidence with H_2O^+ and F (Eq. 8.2) is the dominant product channel following collisions of CF_2^{2+} with H_2O, and the channel forming CF_2^+ with H^+ and OH is the weakest detected in this collision system (Eq. 8.3).

8.5.1 $CF_2^{2+} + H_2O \rightarrow CF^+ + H_2O^+ + F$

8.5.1.1 Angular distribution

Three products are formed in this DET channel (Eq. 8.2): CF^+, H_2O^+ and F. It is observed that the ionic products CF^+ and H_2O^+ are strongly forward and backward scattered, respectively (Figure 8.6); F is also clearly forward scattered (Figure 8.7).

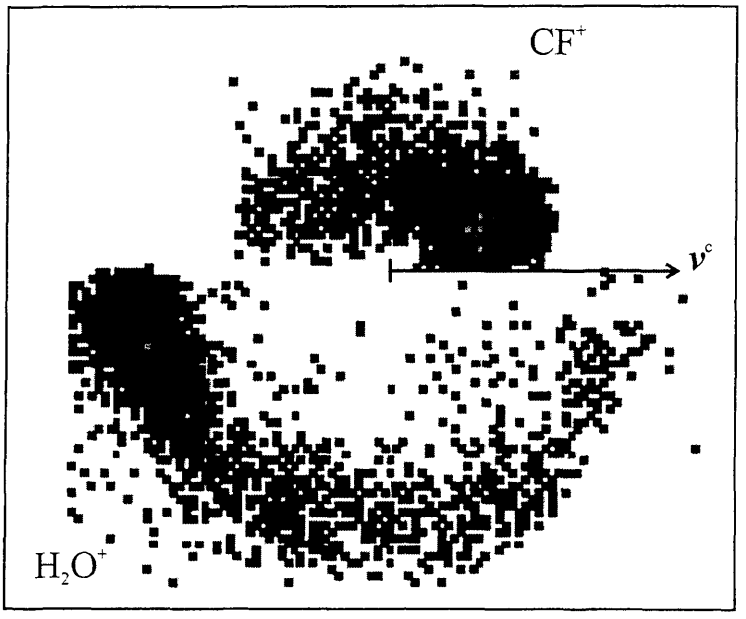

Figure 8.6 Scattering diagram for CF^+ with H_2O^+ with respect to v^c (scale = 1 cm μs^{-1}).

The strong forward and backward scattering of the ionic products in the COM frame and in the internal frame (Figure 8.6, Figure 8.7) is very similar to that observed for NDET reactions (Figure 8.2) [2-5], suggesting that product formation occurs *via* initial electron transfer followed by the subsequent dissociation of CF_2^+ to give CF^+ (Eq. 8.6, 8.7).

$$CF_2^{2+} + H_2O \rightarrow CF_2^{+*} + H_2O^+ \qquad (8.6)$$

$$CF_2^{+*} \rightarrow CF^+ + F \qquad (8.7)$$

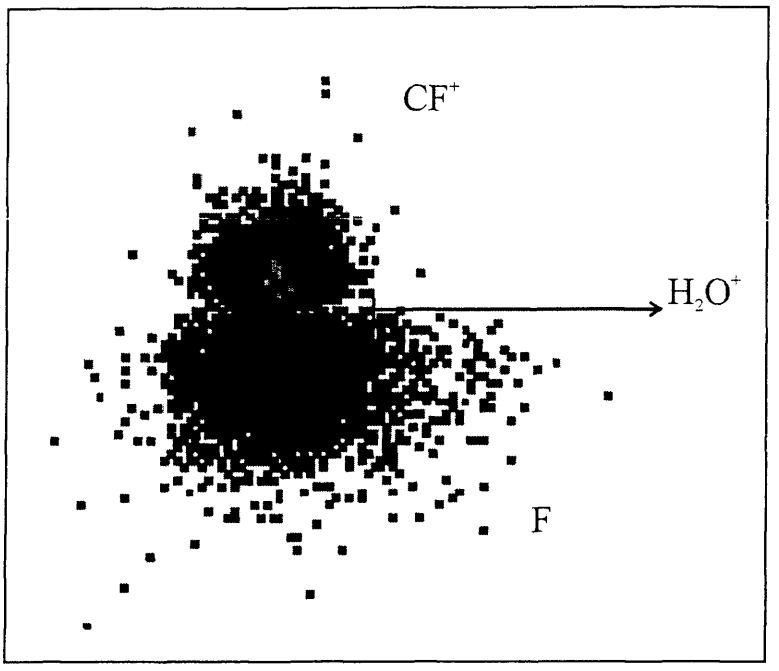

Figure 8.7 Internal frame scattering of CF^+ and F with respect to H_2O^+ (scale = 1 cm μs^{-1}).

Indeed, previous dynamical investigations have shown that the NDET reaction in the CO_2^{2+} + D_2 collision system has been shown to proceed by an analogous sequential mechanism [4]. The alternative mechanisms for this reaction involve the dissociation of a short or long-lived complex:

$$CF_2^{2+} + H_2O \rightarrow [H_2O - CF_2]^{2+} \rightarrow CF^+ + H_2O^+ + F. \qquad (8.8)$$

The decay of a long-lived complex would result in more isotropic scattering of at least two of the products in the COM frame, as will be seen in Chapter Nine for the chemical reactions in this collision system. Conversely, the concerted decay of a short-lived complex would result in a fixed angular relationship between the three products [11]. Neither of these experimental signatures of complexation is observed in the dynamical data for this channel.

8.5.1.1.1 Is the dissociation of CF_2^{+*} fast or slow?

All the data for this channel is consistent with the sequential mechanism. For example, the average velocities of CF^+ (w_{CF+} = 0.36 cm μs^{-1}) and F (w_F = 0.4 cm μs^{-1}) are of similar magnitude to each other and to the undissociated CF_2^+ ion velocity (w_{CF2+} = 0.34 cm μs^{-1}) in the NDET channel. This relationship between the velocities is expected if the Coulomb repulsion in the product channel occurs principally between CF_2^{+*} and H_2O^+, rather than between CF^+ and H_2O^+. Thus, the dissociation of CF_2^{+*} is clearly "slow", that is it takes place largely out of the field of H_2O^+ ion. Monte Carlo simulations have been performed involving classical trajectory code (see Chapter Seven), and indicate the lifetime of the CF_2^{+*} ion must be over 100 fs to result in the experimental scattering observed [12].

However, if the dissociation of CF_2^{+*} was "fast", within the field of H_2O^+, then the CF^+ would be accelerated with respect to F, and the CF_2^+ product of the NDET reaction, in contrast to what is observed in the PSCO data. The precise form of the relative scattering of the F and CF^+ (Figure 8.7) is easily understood when one considers that the dissociation of CF_2^{+*} to CF^+ and F involves a non-zero kinetic energy release as shown in the schematic diagram presented in Figure 8.8.

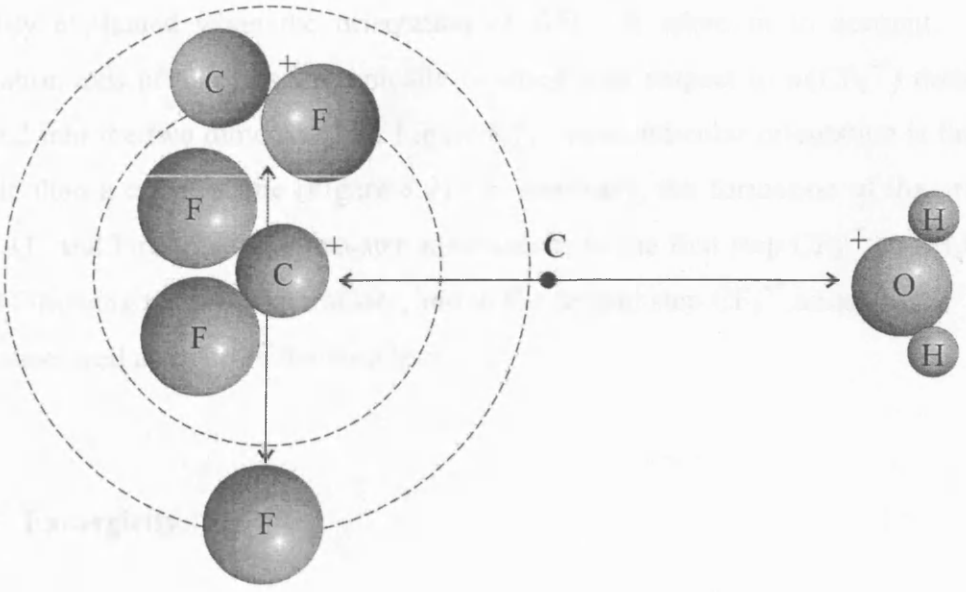

Figure 8.8 A schematic diagram showing the form of the product ion scattering for the dissociation of CF_2^{+*} away from the centre-of-mass of CF_2^{2+}-H_2O collision system, **C**.

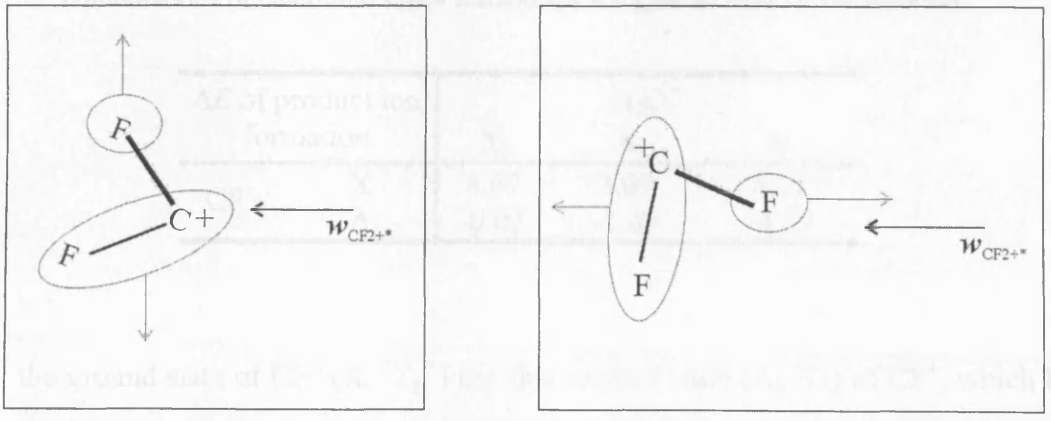

Figure 8.9 A schematic representation demonstrating why the experimentally observed intensity distribution of the scattering of CF^+ and F (Figure 8.7) appears to indicate a perpendicular orientation of CF_2^{+*} in contrast to a colinear one.

The intensity distribution of the CF^+ and F scattering described in Figure 8.7, which clearly shows the majority of CF_2^{+*} dissociations are perpendicular to its initial velocity, is readily explained when the orientation of CF_2^{+*} is taken in to account. If the dissociation axis of CF_2^{+*} is isotropically oriented with respect to $w(CF_2^{+*})$ then when projected into the two dimensions of Figure 8.7, a perpendicular orientation is far more probable than a colinear one (Figure 8.9). In summary, the formation of the products CF^+, H_2O^+ and F occurs *via* a two-step mechanism; in the first step CF_2^{+*} and H_2O^+ are formed following the electron transfer, and in the second step CF_2^{+*} undergoes a "slow" dissociation well away from the H_2O^+ ion.

8.5.1.2 Exoergicity

The exoergicity spectrum (Figure 8.10) for the DET channel (Eq. 8.2) shows a single peak at approximately 5.3 eV with a half width of 3 eV. To account for this exoergicity distribution it is necessary to consider the various accessible electronic states of the products.

Table 8.4 Expected exoergicities of product ion formation in different combinations of electronic states formed *via* the ground state of the dication.

ΔE of product ion formation		H_2O^+		
		X	A	B
CF^+	X	4.67	3.01	0.11
	A	-0.03	-1.69	-4.59

Both the ground state of CF^+ (X, $^1\Sigma_g^+$) the first excited state (A, $^3\Pi$) of CF^+, which lies 4.7 eV above the ground state, are stable [9]. The relevant states of H_2O^+ are as discussed for the NDET channel above. As indicated in Figure 8.10 (a), the [CF^+(X), H_2O^+(X), F(^{2}P)] and [CF^+(X), H_2O^+(A), F(^{2}P)] product asymptotes lie at adiabatic exoergicities of 4.7 and 3.0 eV respectively with respect to the reactant asymptote.

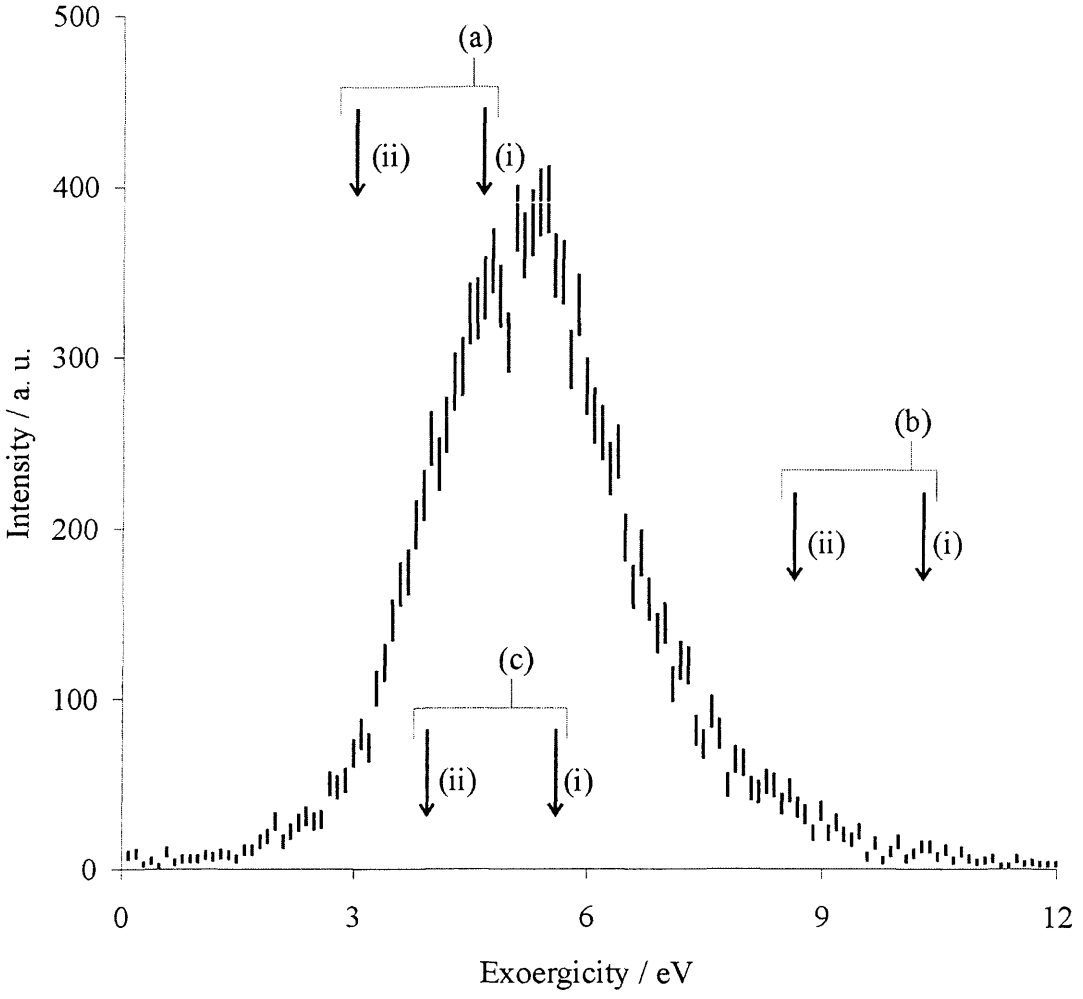

Figure 8.10 An exoergicity spectrum for formation of CF^+ with H_2O^+ with F in various different product ion state combinations: (a) *via* ground state dication to form (i) $CF^+(X)$, $H_2O^+(X)$, (ii) $CF^+(X)$, $H_2O^+(A)$ products; (b) *via* excited dication state to form (i) $CF^+(X)$, $H_2O^+(X)$, (ii) $CF^+(X)$, $H_2O^+(A)$; (c) excited dication to form (i) $CF^+(A)$, $H_2O^+(X)$, (ii) $CF^+(A)$, $H_2O^+(A)$ products.

Population of the (B) state of H_2O^+ in a vertical transition results in the formation of H_2O^+ or H^+ + OH or OH^+ + H as the $H_2O^+(B)$ potential energy surface only supports 1 eV of vibrational excitation [8]. Since no coincidences of CF^+ with H^+ or with OH^+ have been detected here it seems clear the (B) state of H_2O^+ is not being populated, therefore, the [$CF^+(X)$, $H_2O^+(B)$, F] asymptote has not been included in Figure 8.10. The product asymptotes for the formation of $CF^+(A)$ with H_2O^+(X and A) lie at

exoergicities 0 and -1.7 eV and so formation of $CF^+(A)$ in collisions of the ground state dication can therefore immediately be discounted as the relevant product asymptotes are well below the experimentally measured exoergicities (Figure 8.10).

In light of the above, an assignment of the experimental signals at low exoergicity (2-4.7 eV) to the formation of [$CF^+(X)$, $H_2O^+(X)$, F], with perhaps a small contribution from formation of [$CF^+(X)$, $H_2O^+(A)$, F], appears clear. Indeed the low exoergicity maximum in the experimental signal corresponds well with the [$CF^+(X)$, $H_2O^+(X)$, F] asymptote. From the excellent agreement between the most intense region of the experimental peak and the vibrationless [$CF^+(X)$, $H_2O^+(X)$, F] asymptote, which is the favoured vertical transition for H_2O, it may also inferred that CF^+ is formed with very little vibrational excitation in this process.

Having assigned the experimental signals below 4.7 eV in the exoergicity spectrum to the formation of principally $CF^+(X)$, $H_2O^+(X)$ and $F(^2P)$ from collisions of the ground state dication, the signals above 4.7 eV now need to be accounted for (Figure 8.10). These signals could be due to a the reaction of ground state dications with a significant amount of vibrational excitation (up to 4.5 eV) to form $CF^+(X)$, $H_2O^+(X)$ and $F(^2P)$. However, such a large range of excitation and the fact that such excitation was not readily apparent in the exoergicity spectrum of the NDET channel (Figure 8.5) makes such an explanation for the high exoergicity signals unlikely. Hence, the reactions involving long-lived excited electronic states of CF_2^{2+} must be considered.

The first long-lived excited electronic state of $CF_2^{2+}(^3B_1)$ has been calculated to lie 5.6 eV above the ground state of CF_2^{2+} [9]. For reactions of the $^3B_1$ state of CF_2^{2+} the [$CF^+(X)$, $H_2O^+(X)$, $F(^2P)$], [$CF^+(X)$, $H_2O^+(A)$, $F(^2P)$] product asymptotes lie at exoergicities of 10.3 and 8.7 eV (Table 8.5). The adiabatic exoergicities for forming $CF^+(A)$ with $H_2O^+(X)$ and $H_2O^+(A)$ from the $^3B_1$ state of CF_2^{2+} are 5.6 and 4.0 eV. All these asymptotes are marked on Figure 8.10. From Figure 8.10 it can be seen that the formation of $CF^+(X)$ + $H_2O^+(A)$ and $CF^+(A)$ + $H_2O^+(X)$, together with $F(^2P)$, from the $^3B_1$ state of CF_2^{2+} will give signals between 9 and 4.7 eV. Since, it is not possible to account for the observation of reactive events with this range of exoergicities by

reactions of the ground state of the reactant dications, it seems clear that excited states of the dication must be involved in forming CF^+ in this collision system.

Table 8.5 Expected exoergicities of product ion formation in different combinations of electronic states formed *via* the first excited state of the dication.

ΔE of product ion formation		H_2O^+		
		X	A	B
CF^+	X	10.31	8.65	5.75
	A	5.61	3.95	1.05

8.5.1.3 Summary

The exoergicity signal in Figure 8.10 corresponds well to the predicted exoergicity for the formation of CF^+(A) with H_2O^+(X). This is in good agreement with Kearney *et al*'s product state calculations for this channel using the Landau-Zener reaction window theory. Their method predicted that DET results in the formation of CF^+ in the (A) state and H_2O^+ in the (X) state. These L-Z calculations have also been carried out by the author of this thesis as described below in section 8.5.2.

8.5.2 Reaction window theory calculations

This section describes some Landau-Zener reaction window theory calculations carried out by the author of this thesis for the NDET and DET channels discussed above. The Landau-Zener and reaction window theories are described in detail in Chapter Two along with the algorithms used to calculate the cross sections given in Table 8.6 below. For the reaction window algorithm to be employed successfully, the exoergicities of the

transitions between the ground states of CF_2^{2+} and H_2O and the accessible electronic states of the product ions formed following an electron transfer reaction are required. These exoergicities are listed in Table 8.6 and have been principally obtained from thermodynamic tables [13, 14]. The heat of formation of CF_2^{2+} used in these calculations (29.88 eV) is a value recently calculated by Hrusak *et al* [15] and the relative energies of the excited states of the monocations used to calculate the exoergicities given in Table 8.6 have been determined from the relevant photoelectron spectra [7, 8].

Table 8.6 Exothermicities ΔE and calculated reaction cross-sections (σ in arbitrary units) for forming the various possible combinations of electronic states of CF_2^+ and H_2O^+ product ions in the NDET and DET channels described above, at a LAB collision energy of 21 eV. The final row of the table gives the exothermicities and cross-section for populating a vibrationally excited level of the stable electronic ground state of CF_2^+ at the equilibrium geometry of the reactant dication.

Electronic state of CF_2^+ product	Electronic state of H_2O^+ product					
	X (H_2O^+)		A (H_2O^+)		B (H_2O^+, H^+, OH)	
	ΔE /eV	σ	ΔE /eV	σ	ΔE /eV	σ
CF_2^+(X)	7.7	0	6.03	0.3	3.15	14.8
CF_2^+(A)	3.6	23.6	1.05	0	-1.8	0
CF_2^+(B)	2.6	3.5	0.06	0	-2.8	0
CF_2^+(X)	4.7	6.3	2.23	0.4	-0.86	0

The A and B states of CF_2^+ are dissociative, so the cross-sections cited for channels containing those states may be considered to be for the formation of $CF^+ + F$. The bottom row of Table 8.6 takes into account the proposed 3 eV of vibrational energy imparted to CF_2^+ due to populating a vibrationally excited level of its stable electronic ground state at the equilibrium geometry of the reactant dication, as explained in section 8.4.2. The cross-sections in Table 8.6 indicate that the dissociative electron transfer

forming $CF^+ + F + H_2O^+$ is more dominant than the NDET reaction with is in accord with the experimentally observed intensities.

The L-Z calculations were also carried out for the DET channel for formation of monocation products from the excited state of the dication, since the PSCO experiments indicate some of the exoergicity signals arise from this reaction. The cross-sections given in Table 8.7 indicate that the most abundant channel for the excited state of CF_2^{2+} involving a non-dissociative state of H_2O^+ (*i.e.* X or A) is the channel forming the dissociative state CF_2^+(B) with H_2O^+(A) followed by a less intense channel forming CF_2^+(B) with H_2O^+(X). The B state of CF_2^+ is dissociative and would therefore form $CF^+ + F$, which is in agreement with the products that are detected experimentally in this DET channel.

Table 8.7 Exothermicities ΔE and calculated reaction cross-sections (σ in arbitrary units) for forming the various possible combinations of electronic states of CF_2^+ and H_2O^+ product ions from the first excited state of the dication in the NDET and DET channels described above, at a LAB collision energy of 21 eV.

Electronic state of CF_2^+ product	Electronic state of H_2O^+ product					
	X (H_2O^+)		A (H_2O^+)		B (H_2O^+, H^+, OH)	
	ΔE /eV	σ	ΔE /eV	σ	ΔE /eV	σ
CF_2^+(X)	13.3	0	9.2	0	7.4	0
CF_2^+(A)	11.7	0	7.6	0	5.7	0.6
CF_2^+(B)	8.8	3.5	4.7	6.34	2.8	7

In conclusion, both the L-Z calculations that were carried out for the NDET and DET channels indicate that the L-Z model is a good approximation for the reactivity in the CF_2^{2+}-H_2O collision system.

8.5.3 $CF_2^{2+} + H_2O \rightarrow CF_2^+ + H^+ + OH$

8.5.3.1 Angular distribution

The products detected in this weak DET channel (Eq. 8.3) are CF_2^+ and H^+. CF_2^+ exhibits strong forward scattering, as observed in the NDET channel (Figure 8.2), and H^+ is scattered backwards between 90-180° in the COM frame (Figure 8.11). The third body formed in this channel (OH) is strongly backward scattered with respect to both the velocity of the centre-of-mass of the system and the CF_2^+ ion (Figure 8.12).

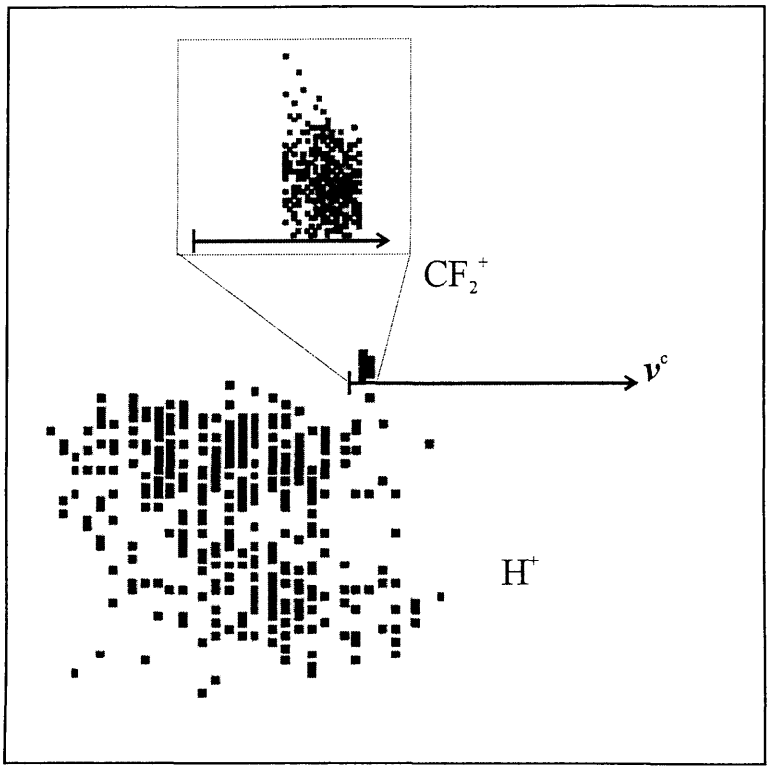

Figure 8.11 Scattering diagram of CF_2^+ and H^+ with respect to v^c (scale: horizontal arrow = 4 cm μs^{-1}, inset 0.4 cm μs^{-1}).

As described above, the determination of the velocity vector of the neutral species from the ion velocities will yield the nascent velocity of the initial neutral product. The PSCO experiment cannot detect if the primary neutral species subsequently fragments. However, as shown below the exoergicity of the reaction corresponds well with the

formation of bound states of OH. Again, the angular distributions show no signature of complexation and the strong forward-backward scattering is immediately indicative of a sequential electron transfer process:

$$CF_2^{2+} + H_2O \rightarrow CF_2^{+} + H_2O^{+*} \quad (8.9)$$

$$H_2O^{+*} \rightarrow H^{+} + OH \quad (8.10)$$

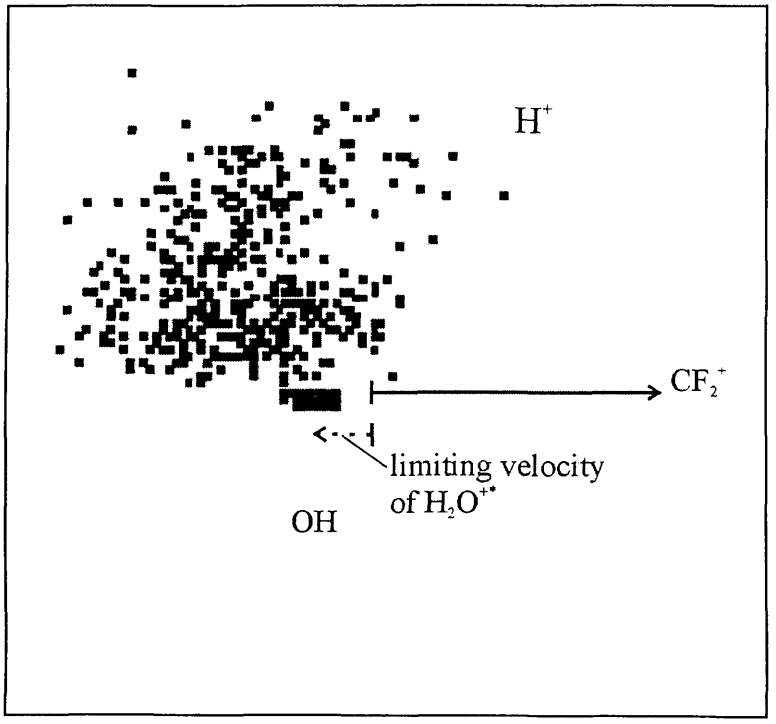

Figure 8.12 Internal frame angular scattering of H^+ and OH with respect to CF_2^+ (scale: horizontal arrow = 4 cm μs^{-1}).

However, in this reaction, in contrast to the other DET reaction (8.2), the product of the secondary dissociation, H^+ in this case, is markedly more widely scattered in both the COM and the internal frame (Figure 8.11, Figure 8.12) than the corresponding product, CF^+, in reaction (8.2). Also, comparing Figure 8.11 and Figure 8.12 it can be seen that $w(H^+)$ and $w(OH)$ are not symmetrically distributed about a precursor (H_2O^{+*}) velocity

vector, in contrast to $w(CF^+)$ and $w(F)$ in reaction (8.2). Figure 8.12 clearly shows that the H^+ distribution is skewed, tending towards backward scattering with respect to CF_2^+, rather than being isotropic about the limiting velocity of H_2O^{+*}. This is exactly the experimental signature one would expect if H_2O^+ was dissociating in the field of the CF_2^+ ion.

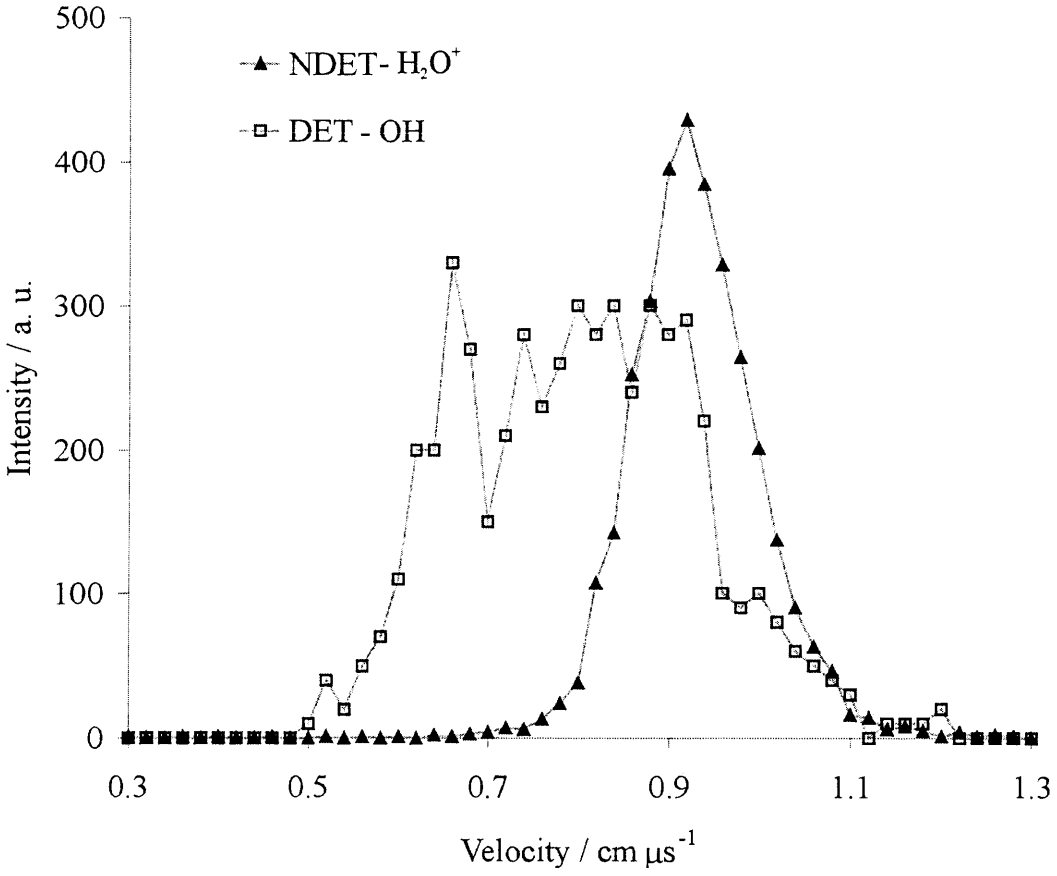

Figure 8.13 A comparison of the velocities of H_2O^+ (NDET) and OH (DET).

In this situation, the isotropic signature (Figure 8.12) of a secondary dissociation out of the field of the partner ion, as well as the isotropic distribution of the fragment velocities about the precursor ion velocity, as seen in reaction (8.2), will be skewed with the charged species (H^+ in this case) receiving an additional impulse due to its repulsion from the other charged fragment (in this case CF_2^+). This will result in the secondary

charged fragment being more strongly back-scattered than the neutral, exactly as observed.

Since the OH fragment will not experience a significant change in velocity from the dissociation of H_2O^{+*}, due to the light H^+ partner that is formed, the final velocity of OH would be expected to be close to that of the H_2O^{+*} species when it dissociated. Thus the velocity of the OH should be below that of the H_2O^+ ion in the NDET channel, since, at the time when the H_2O^{+*} ion dissociates, it has not received the full acceleration from the Coulomb repulsion with the CF_2^+. This is exactly what is observed in the plot of the product velocities in Figure 8.13. As described above, Monte-Carlo simulations with a classical trajectory simulation indicate that the asymmetry in the internal frame scattering (Figure 8.12) begins to arise when the lifetime of the dissociating monocation is of the order of 100 fs.

8.5.3.2 Exoergicity

The exoergicity spectrum (Figure 8.14) shows one very broad peak at approximately 6 eV. As discussed for the NDET channel, in this system CF_2^+ must be formed in its ground state (X, $^2A_1$) as its higher electronic states are dissociative. The product asymptote for formation of the products [CF_2^+(X), H^+, OH(X)] lies at an exoergicity of 1.6 eV with respect to the reactant ground states and at an exoergicity of 7.2 eV relative to the first stable excited dication state $CF_2^{2+}(^3B_1)$ and H_2O. Given that all the signals in the exoergicity spectrum (Figure 8.14) lie well above 1.6 eV, it seems clear that reactions of the ground state of CF_2^{2+} cannot be responsible for forming $CF_2^+ + H^+ + OH$ unless there is considerable vibrational excitation in the ground dication state. The depth of the potential well in the ground state of CF_2^{2+} has been calculated at 4.9 eV, so even the maximum possible vibrational excitation of this electronic state cannot account for exoergicity signals above 6.5 eV. Thus, it seems that again excited states of CF_2^{2+} must be at least in part, and probably almost exclusively, responsible for this reaction.

It can be seen in Figure 8.14 that the experimental exoergicity signal lies below the asymptotic exoergicity of 7.2 eV for the formation of CF_2^+, H^+ and OH from the $CF_2^{2+}(^3B_1)$ state. This lower experimental exoergicity is readily explained as arising from the population of vibrationally excited states of $CF_2^+(X)$, and perhaps OH. $CF_2^+(X)$ has a bond dissociation energy of approximately 3 eV and the population of vibrationally excited states of $CF_2^+(X)$ has already been observed from the ground state of CF_2^{2+}.

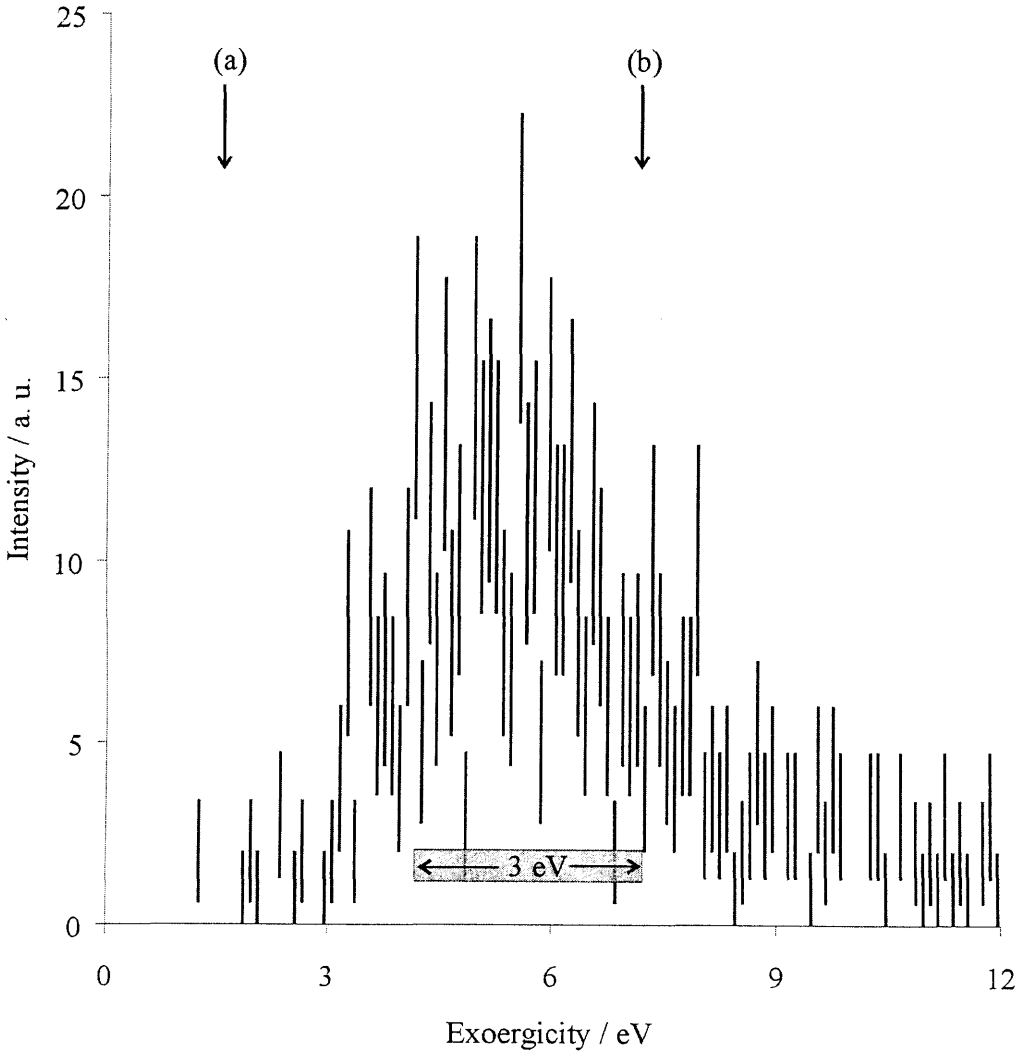

Figure 8.14 Exoergicity spectrum for CF_2^+ H^+ OH, where (a) indicates the exoergicity for forming the products in their ground states *via* the ground state of CF_2^{2+} and (b) indicates ground state product formation *via* excited CF_2^{2+}.

Indeed, the equilibrium geometry ($D_{\infty h}$) of the $CF_2^{2+}(^3B_1)$ state is markedly different to that of $CF_2^+(X)$ and, hence, vibrational excitation of the monocation is certain to occur in a vertical transition from the dication. In fact, as is clear in Figure 8.14 the vibrational envelope of $CF_2^+(X)$, extending 3 eV below the exoergicity for forming $CF_2^+ + H^+ + OH$ from $CF_2^{2+}(^3B_1)$, nicely encompasses the bulk of the experimental signals, supporting this assignment.

Given the excellent agreement of the experimental signals with the reaction of $CF_2^{2+}(^3B_1)$ with H_2O forming $CF_2^+(X)$ with a range of vibrational excitation together with H^+ and OH(X), it seems clear that the ground state of OH is formed in this reaction, as the first electronic excited state of OH (A) lies 4.1 eV above the ground state which moves the asymptotic product energy to 3.1 eV, well below the observed exoergicity signals. The precise electronic state of H_2O^+ involved in reaction (8.4) is not definitively determined from the data. Given the energetics of the PSCO collision system, it can be seen that the (B) state of H_2O^+ is the highest valence state accessible, although it is possible some satellite states of H_2O^+ are also energetically available. It is well established that higher vibrational levels of the $H_2O^+(B)$ state dissociate predominantly to yield $H^+ + OH$ (KER~5 eV). The population of such excited levels of the (B) state has an exoergicity lying in the Franck-Condon window for electron transfer. The formation of OH^+ from excited vibrational levels of the $H_2O^+(B)$ state decreases steadily with increasing vibrational excitation. Hence, if the (B) state is the intermediate H_2O^+ state involved in the formation of H^+, it must be postulated that highly excited levels of the (B) state are populated which dissociate almost exclusively to H^+ to account for the absence of any $CF_2^+ + OH^+$ signals in the PSCO coincidence spectra.

8.5.3.3 Summary

This minor channel clearly involves the formation $CF_2^+(X)$, H^+ and OH(X) formed *via* electron transfer from $H_2O(X)$ to $CF_2^{2+}(^3B_1)$. The mechanism involves initial electron

transfer, perhaps populating highly excited vibrational levels of the $H_2O^+(B)$ state, which then dissociate rapidly, within the field of the CF_2^+ ion, to form $H^+ + OH$.

8.6 Conclusions

The dynamics of the product channels forming $CF_2^+ + H_2O^+$, $CF^+ + H_2O^+ + F$ and $CF_2^+ + H^+ + OH$ following the collisions of CF_2^{2+} with H_2O have been investigated. The experimental results show that in the NDET channel the products are formed by direct electron transfer. Some atomic electron transfer collision systems have exhibited bimodal angular distributions of the ionic products in the NDET channel, but this has not been observed for the CF_2^{2+}-H_2O collision system, which is in agreement with scattering for other molecular systems. The kinetic energy release in this reaction indicates that this reaction involves the ground state of CF_2^{2+} and forms the ground electronic states of CF_2^+ and H_2O^+.

Formation of the ionic products in the two remaining electron transfer channels observed, proceeded *via* a two-step mechanism: electron transfer followed by the dissociation of one of the ionic products at some time after the initial electron transfer process. The scattering in the channel forming $CF^+ + H_2O^+ + F$ is very similar to the NDET channel and indicates a slow dissociation of CF_2^{+*} following electron transfer. The kinetic energy release for this channel shows that the ionic products CF^+ and H_2O^+ are formed in several different channels [$CF^+(X)$, $H_2O^+(X)$, $F(^2P)$], [$CF^+(X)$, $H_2O^+(A)$, $F(^2P)$] and [$CF^+(A)$, $H_2O^+(X)$, $F(^2P)$] *via* ground and excited dicationic states CF_2^{2+} ($^1\Sigma_g$) and $CF_2^{2+}(^3B_1)$, respectively.

In contrast to the major DET pathway described above, the angular scattering in this minor dissociative electron transfer channel forming $CF_2^+ + H^+ + OH$ indicates that the second step of the mechanism involving dissociation of an ionic product, in this case H_2O^{+*}, occurs rapidly following electron transfer. The exoergicity for this reaction

shows that the products are formed in their ground states solely *via* collisions of excited states of the dication.

8.7 References

[1] Kearney, D. and Price, S. D., 2003, *Phys. Chem. Chem. Phys.* **5** (8) 1575-1583.

[2] Friedrich, B. and Herman, Z., 1984, *Chem. Phys. Lett.* **107** (4-5) 375-380.

[3] Harper, S. M., Hu, W. P., and Price, S. D., 2002, *J. Phys. B: At. Mol. Opt. Phys.* **35** (21) 4409-4423.

[4] Mrazek, L., *et al.*, 2000, *J. Phys. Chem. A.* **104** (31) 7294-7303.

[5] Herman, Z., Zabka, J., Dolejsek, Z., and Farnik, M., 1999, *Int. J. Mass Spectrom.* **192** 191-203.

[6] Friedrich, B., *et al.*, 1986, *J. Chem. Phys.* **84** (2) 807-812.

[7] Dyke, J., *et al.*, 1974, *J. Chem. Soc.: Faraday Trans.* **70** 1828.

[8] Reutt, J. E., Wang, L. S., Lee, Y. T., and Shirley, D. A., 1986, *J. Chem. Phys.* **85** 6928.

[9] Hrusak, J., 2001, *Chem. Phys. Lett.* **338** (2-3) 189-194.

[10] Ehbrecht, A., Mustafa, N., Ottinger, C., and Herman, Z., 1996, *J. Chem. Phys.* **105** (22) 9833-9846.

[11] Hsieh, S. and Eland, J. H. D., 1997, *J. Phys. B: At. Mol. Opt. Phys.* **30** (20) 4515-4534.

[12] Harper, S. M., Hu, S. W. P., and Price, S. D., 2004, *J. Chem. Phys.*, In preparation.

[13] Lias, S. G., *et al.*, 1988, *J. Phys. Chem. Ref. Data.* **17 S1** 1-861.

[14] *NIST Chemistry WebBook, NIST Standard Reference Database Number 69*, 2003 (National Institute of Standards and Technology, Gaithersburg MD, 20899 (http://webbook.nist.gov)).

[15] Hrusak, J., Herman, Z., Sandig, N., and Koch, W., 2000, *Int. J. Mass Spectrom.* **201** (1-3) 269-275.

Chapter 9

The bond-forming reactions of CF_2^{2+}-H_2O

9.1 Introduction

Conventional mass spectrometric techniques have discovered that small molecular doubly-charged ions possess an extensive and unusual bimolecular chemistry involving the formation of new chemical bonds [1-15]. For example:

$$CF_2^{2+} + H_2 \rightarrow HCF_2^+ + H^+ \qquad (9.1)$$

$$CF_3^{2+} + H_2 \rightarrow HCF_2^+ + H^+ + F. \qquad (9.2)$$

The label "unusual" can be justified because these dicationic reactions commonly generate a pair of singly charged product ions and the mutual repulsion between these species gives each of them a considerable kinetic energy, in excess of 3 eV [2]. The formation of such highly translationally energetic product ions is in marked contrast to the dynamics of the chemical reactions of monocations [16, 17]. Over the last ten years, mass spectrometric experiments involving isotopic substitution, and experiments employing more advanced methodologies, both coupled with high-level quantum chemical investigations, have allowed significantly more insight into the dynamics and kinematics of the bond-forming processes of molecular dications.

The dynamics of the formation of HCF_2^+ following collisions of CF_2^{2+} with H_2 have been investigated by angularly resolved experimental studies [1, 2, 6, 9, 15] and studying the effect of isotopic substitution [9, 15]. These measurements showed that the

heavy chemical product XCF_2^+ (X = H, D) was predominantly forward scattered, although a significant amount of sideways and backward scattering is observed, indicative perhaps of a short-lived collision complex . The formation of HCF_2^+ from collisions with H_2 seems favoured relative to the formation of DCF_2^+ from the collisions of D_2, although in the COM collision frame, the ratio of XCF_2^+ to CF_2^+ seems similar for both collision systems.

Bond-forming (BF) reactions have also been observed for the CO_2^{2+}-X_2 (X = H, D) collision systems [3]. The angular scattering clearly showed that the major chemical product (XCO^+) was formed by dissociation of the energised XCO_2^+. As with CF_2^{2+}-X_2 [9, 15], the reaction of CO_2^{2+} with H_2 has a larger cross-section for both the electron transfer and chemical channels as a function of the LAB collision energy. A recent discussion of the application of the reaction window model to these systems [14] suggests that, at least for the electron transfer channels, this isotope effect may be a result of the differing radial velocities of the H_2 and D_2 collision systems at the same LAB or COM collision energies.

Recently a completely new class of bond-forming reactions of molecular dications, which produce dicationic products, has been observed. For example, the reaction of CO^{2+} with the rare gases [11]

$$CO^{2+} + Ar \rightarrow ArC^{2+} + O\,. \qquad (9.3)$$

These chemical reactions which form dicationic products have significantly smaller cross-sections than the competing electron transfer processes and are also observed for collisions of Ar^{2+} with CO, CO_2, O_2, N_2 and NH_3 [11, 18-22]. For example

$$Ar^{2+} + N_2 \rightarrow ArN^{2+} + N \qquad (9.4)$$

The recently developed PSCO TOF mass spectrometer [23-25] described in this thesis determines the kinematics and dynamics of dication-neutral reactions. As explained earlier, the experiment detects the two charged products from a dication chemical or

electron transfer reaction, in coincidence at a position sensitive detector. From such position sensitive data it is possible to extract the nascent velocities of the charged reaction products, providing considerable insight into the dynamics of these reactions. However, an additional advantage of this experimental methodology is apparent for the study of more complex reactions that produce three products (Eq. 9.2), in contrast to simpler two-body processes (Eq. 9.1). For a two-body reaction, conventional experimental approaches that detect just one product can determine the kinematics of the second product *via* conservation of momentum. However, this approach fails for a three-body reaction where two products are undetected. In contrast, the PSCO data on a three-body reaction, which determines the nascent velocities of the two ionic products, allows the velocity of the undetected neutral fragment to be determined by conservation of momentum, completely characterising the kinematics of the three-body process. Thus, the PSCO technique is in principle a powerful probe of the dynamics of complex reactions. For example, as discussed in Chapter Seven, the technique has shown that complexation appears important in the three-body dissociative electron transfer reaction of Ne^{2+} with N_2 [26].

Recent experiments by Kearney *et al* [27] have shown that CF_2^{2+} undergoes a chemical reaction with H_2O to form OCF^+ and these experiments imply, since no HF^+, H_2F^+ or F^+ is detected, that H^+ is the accompanying charged product in this reactive channel:

$$CF_2^{2+} + H_2O \rightarrow OCF^+ + H^+ + HF. \qquad (9.5)$$

Such an association between OCF^+ and H^+ from a particular bond-forming event may be inferred since the only other possible accompanying ions are H_2F^+, HF^+ or F^+ none of which are detected by Kearney *et al* [27]. Stimulated by this observation, a quantum chemical investigation determined several stationary points on the potential energy surface of this reactive channel [28]. This computational investigation indicated that the formation of OCF^+ proceeds *via* formation of a $[H_2O\text{-}CF_2]^{2+}$ collision complex which subsequently undergoes charge separation to form H^+ and $HO\text{-}CF_2^+$, with the molecular ion subsequently rearranging and dissociating to yield $OCF^+ + HF$.

Given the above information, the formation of OCF^+ following collisions of CF_2^{2+} with H_2O seems an ideal candidate for investigation by the PSCO technique. This chapter will focus on the dynamics of the bond-forming reactions, Eq. 9.5 and a new reaction

$$CF_2^{2+} + H_2O \rightarrow HCF_2^+ + H^+ + O \qquad (9.6)$$

detected in this collision system using the PSCO spectrometer (Eq. 9.6), which will be discussed in turn.

9.2 Experimental details

A detailed account of the experimental arrangement is given in Chapter Three. PSCO spectra were recorded at a LAB collision energy of 21.28 eV (E^c = 5.63 eV) with a repeller plate voltage of 300 V, giving a field of 202 V cm^{-1} in the source region of the TOF mass spectrometer. This high source field ensures the collection of the full angular distribution of the scattered product ions, including those highly energetic ions with considerable energies perpendicular to the axis of the TOF mass spectrometer.

Improved angular and energy resolution is obtained at a low source field (30.4 V cm^{-1}) compared to the high source field (202 V cm^{-1}), so initially an attempt was also made to record data at the low source field as for the other collision systems described in this thesis. However, at these low field settings, accumulation of coincidence data in these bond-forming channels proved to be very slow compared to usual acquisition times of a few hours or one day. As described in Chapter Three, any highly energetic ions that have significant x or y velocity components are 'lost' at low source fields. This occurs when these ions have moved out of the source region before the pulse of the repeller plate or hit the walls of the TOF drift tube before reaching the detector and is more likely to occur with small ions that have 'high' velocities (> 2 cm μs^{-1}).

Both of the bond-forming reactions discussed in this chapter form H^+ with isotropic scattering, and a significant proportion of these H^+ ions will therefore be lost at low source field. Therefore, only one ion from those reactive collisions will be detected and no pairs data would be recorded. Thus, recording PSCO spectra at low source field is not practical, so only high source field spectra have been recorded and analysed.

9.3 Results

The coincidence spectra recorded following collisions of CF_2^{2+} with H_2O clearly show the bond-forming channel (Eq. 9.5), and the non-dissociative (Eq. 9.7) and dissociative electron transfer (Eqs. 9.8, 9.9) channels that have been detected before in this collision system as described in Chapter Eight:

$$CF_2^{2+} + H_2O \rightarrow CF_2^{+} + H_2O^{+} \quad (9.7)$$

$$CF_2^{2+} + H_2O \rightarrow CF^{+} + H_2O^{+} + F \quad (9.8)$$

$$CF_2^{2+} + H_2O \rightarrow CF_2^{+} + H^{+} + OH. \quad (9.9)$$

In addition, the coincidence spectra clearly showed signals corresponding to a previously unobserved chemical reaction channel (Eq. 9.6) forming $HCF_2^{+} + H^{+} + O$.

The relative intensities of the full angular distribution of ions formed in these channels are listed in Table 9.1 for reactions 9.5 and 9.6-9.9 respectively. A comparison is made with data recorded previously for this collision system by Kearney *et al* using a crossed beam experiment to identify the ionic products of the electron transfer and bond-forming reactions that occur [27].

Table 9.1 Relative intensities of the six product ions formed in the collisions of CF_2^{2+} with H_2O for the PSCO spectrometer at high TOF source field compared to intensities presented by Kearney *et al* [27] .

Product ions	CF_2^+	H_2O^+	CF^+	OCF^+	H^+	HCF_2^+
PSCO	69	169	100	0.5	0.6	0.05
Kearney *et al*	58	62	100	5	0.4	-

The intensities reported by Kearney *et al* [27] are calculated for all detected ions. OCF^+ was the only product detected in this experiment that could be definitively linked to a bond-forming channel. The PSCO intensities are determined only from detected ion pair events, so it is possible that not all ion arrivals at the detector are counted if one ion out of the pair is missed. The relatively low intensity of OCF^+ detected by the PSCO experiment with respect to Kearney *et al* is due to this particular aspect of the PSCO data processing because its partner ion H^+ is hard to 'catch' as described earlier. The degree of chemical rearrangement required to form the OCF^+ certainly suggests that a collision complex must be involved. The data reported by Kearney *et al* cannot resolve the HCF_2^+ (Eq. 9.6) peak as its intensity is too weak to be distinguished from the spread of the very intense CF_2^+ signal that appears one mass unit lower than HCF_2^+ in the mass spectrum.

The low detection efficiency of H_2O^+ in the data presented by Kearney *et al* in comparison to the PSCO intensities has been discussed in Chapter Eight, and, since H_2O^+ is not formed in any of the bond-forming channels discussed in this chapter, the explanation for this low intensity will not be reiterated here.

Given the differences in detection efficiency between the two pieces of experimental apparatus compared in Table 9.1, it may be concluded that the intensities of the ions formed in the CF_2^{2+}-H_2O collision system, recorded by the two experiments, are in fact quite consistent.

9.3.1 $CF_2^{2+} + H_2O \rightarrow OCF^+ + H^+ + HF$

9.3.1.1 Angular distribution

The angular distribution of the ionic products in the COM frame is presented in Figure 9.1 which shows that the scattering of H^+ is fairly isotropic relative to v^c and OCF^+ is also scattered isotropically but with a much lower COM velocity (see inset in Figure 9.1).

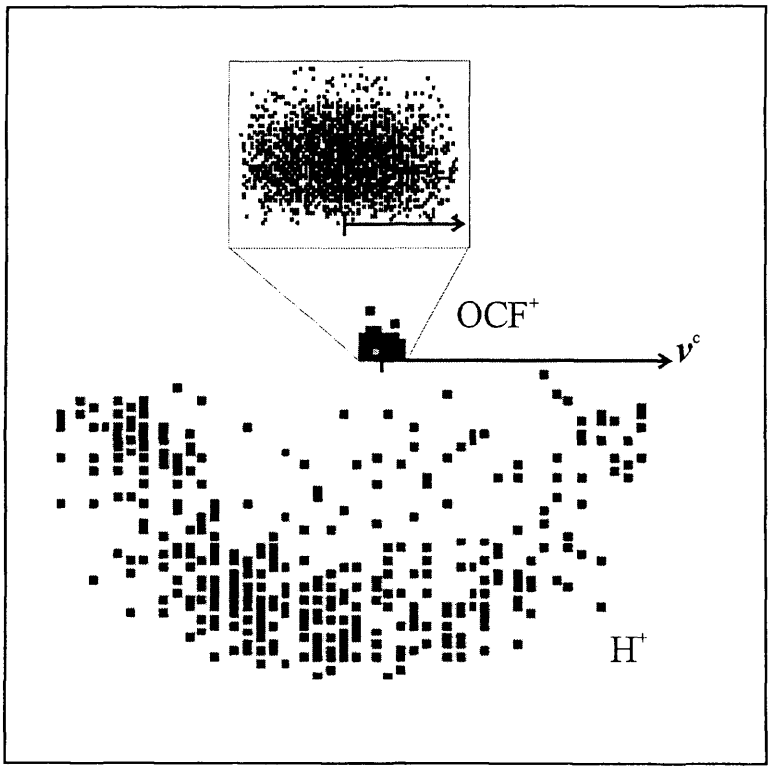

Figure 9.1 Isotropic scattering of H^+ relative to v^c in COM frame (scale: horizontal arrow = 4 cm μs^{-1}; inset scale: 0.4 cm μs^{-1}).

This close to isotropic scattering is the expected experimental signature of a reaction mechanism that involves the formation of a collision complex that has a lifetime at least comparable with its rotational period. The significant lifetime of the complex before its decay means that the products of its dissociation are scattered isotropically, their velocity vectors being uncorrelated with the centre-of-mass velocity v^c.

Satisfyingly, the earlier quantum chemical investigation of the potential energy surface of this reaction has proposed a mechanism involving the formation of a $[H_2O\text{-}CF_2]^{2+}$ adduct and such adducts have also been implicated in the mechanisms of other dication bond-forming reactions [28]. The velocity of the neutral species formed in this channel, which has been assigned to an HF molecule, as described below, is also distributed isotropically very close the COM velocity. From the internal frame scattering diagram (Figure 9.2) it can be seen that H^+ is approximately isotropically scattered with respect to OCF^+, which indicates that the formation of these two ions is separated in time, whereas the velocity of HF is sharply anti-correlated with that of OCF^+.

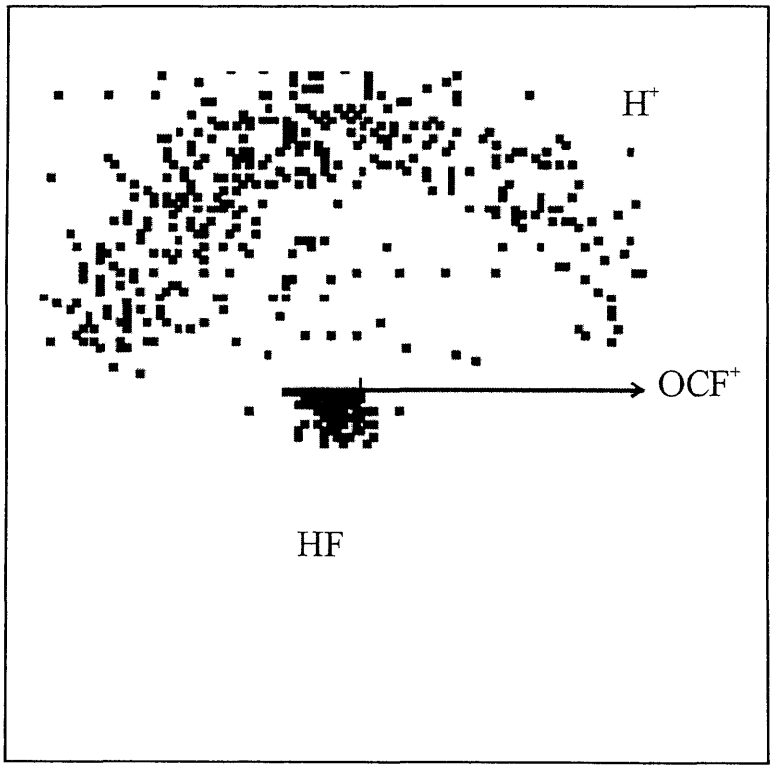

Figure 9.2 Scattering of H^+ and HF relative to OCF^+ in the internal frame (scale: horizontal arrow = 4 cm μs^{-1}).

9.3.1.2 Mechanistic pathway

Charge separation of the $[H_2O\text{-}CF_2]^{2+}$ adduct to form H^+ and $[HO\text{-}CF_2]^+$ results in the isotropic scattering of H^+ in the COM frame. Due to the mass difference between H^+ and $[HO\text{-}CF_2]^+$ the H^+ will take with it most of the kinetic energy of the dissociation. Hence the $[HO\text{-}CF_2]^+$ will be moving with a velocity close to the velocity of the centre-of-mass. If the $[HO\text{-}CF_2]^+$ then lives for a time scale comparable with its rotational period, before dissociating to HF and OCF^+, the H^+ velocity will be uncorrelated with that of OCF^+ as observed. However, considering the decay of $[HO\text{-}CF_2]^+$, the HF and OCF^+ species formed in this final dissociative process must have velocity vectors that are anti-correlated, as observed experimentally (Figure 9.2).

The above mechanism deduced from the PSCO data is precisely that predicted theoretically. The COM velocities of the OCF^+ and HF are low as the initial charge separation of the collision complex to form H^+ results in a fast H^+ ion and a slow molecular ion, with a velocity close to v^c, due to their difference in mass. The dissociation of the monocation $[HO\text{-}CF_2]^+$ should then not involve a large energy release, resulting in both the OCF^+ and HF velocities being close to that of the centre of mass and much smaller than that of the H^+ ion.

The scattering data indicates the energy release of the dissociation of $[HO\text{-}CF_2]^+$ is approximately 1-2 eV, perfectly consistent with the dissociation of a monocation. The average COM velocity of the H^+, when interpreted under the above mechanism indicates a total kinetic energy release of 7.3 eV perfectly consistent with a charge separating dicationic dissociation. As mentioned above, dication-neutral complexes have been implicated in other studies of the bond-forming reactivity of molecular dications, and the PSCO data presented above provides clear evidence for the existence of such species.

The rotational frequency ν_{rot} (Hz) of the collision complex, and hence its lifetime, may be calculated from

$$v_{rot} = 2B\sqrt{J(J+1)} \tag{9.10}$$

where B is the rotational constant. For the $[HO\text{-}CF_2]^{2+}$ complex, the rotational lifetime has been calculated to be approximately 100 ps for $J = 1$. Therefore, it is possible to conclude that the timescale of the mechanistic cycle, from the initial collision of the reactants to formation of the products, is greater than 100 ps.

9.3.1.2.1 Summary

Analysis of the angular scattering of the products in the COM frame, as described above, indicates the dissociation of a complex $[H_2O\text{-}CF_2]^{2+}$ by a stepwise mechanism (Figure 9.3) into $[OH\text{-}CF_2]^+ + H^+$, followed by dissociation of $[OH\text{-}CF_2]^+$ to form OCF^+ and HF.

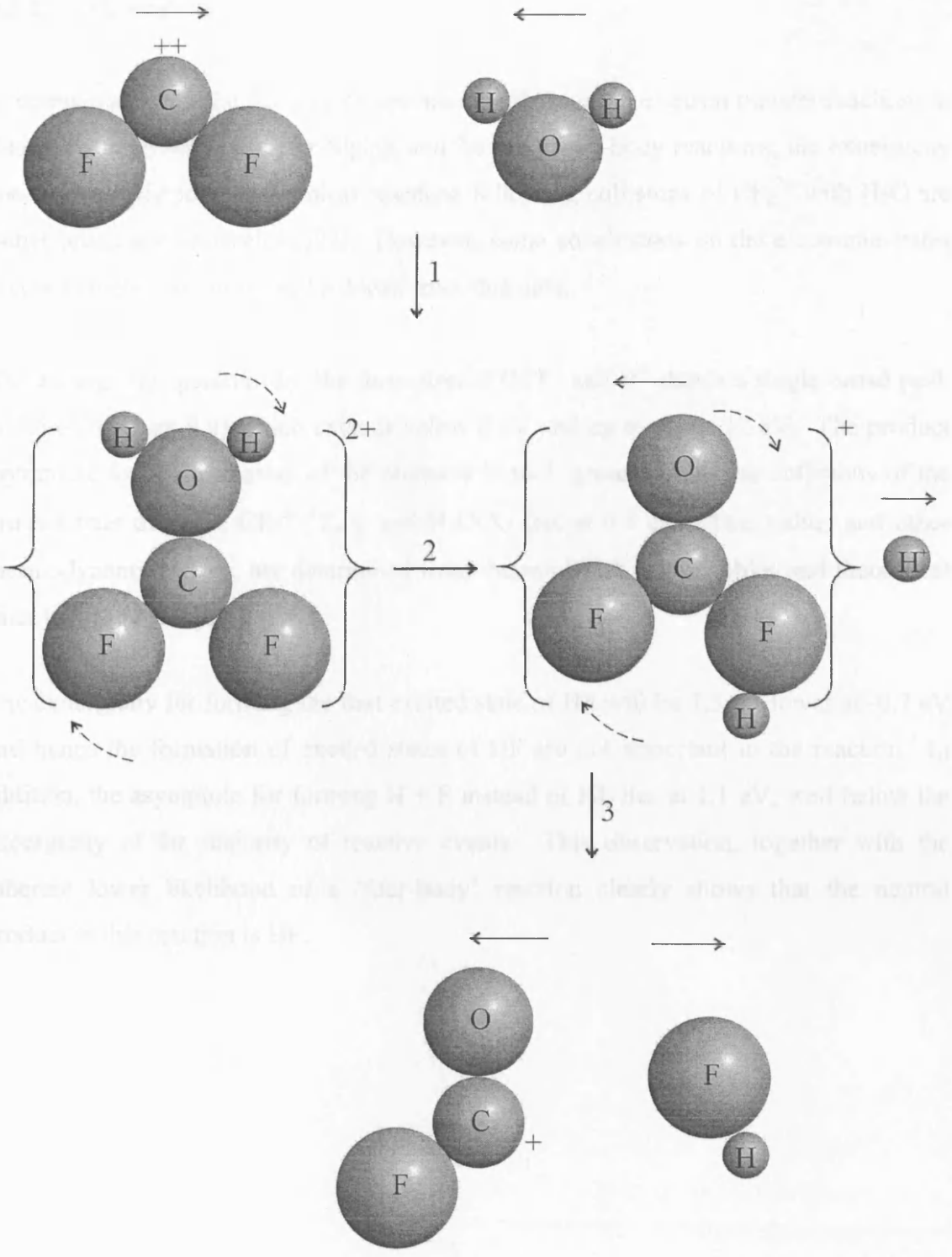

Figure 9.3 A schematic diagram of the bond-forming mechanism resulting in the formation of the $OCF^+ + H^+$ ion pair. The arrows above some of the species indicate the internal frame velocity direction (not to scale) for a step of the mechanism. The dotted arrows indicate rotation.

9.3.1.3 Exoergicity

In comparison with the exoergicity spectra recorded for the electron transfer reactions in this collision system (Chapter Eight), and for other two-body reactions, the exoergicity spectra recorded for the chemical reactions following collisions of CF_2^{2+} with H_2O are rather broad and featureless [23]. However, some conclusions on the electronic states involved in the reactions can be drawn from this data.

The exoergicity spectrum for the formation of OCF^+ and H^+ shows a single broad peak at 3.5 eV (Figure 9.4) which extends below 0 eV and up to about 12 eV. The product asymptote for the formation of the products in their ground states *via* collisions of the ground state dication, $CF_2^{2+}(^1\Sigma_g^+)$, and $H_2O(X)$ lies at 6.8 eV. This value, and other thermodynamic values, are determined from thermodynamic data tables and theoretical calculations [29-31].

The exoergicity for forming the first excited state of HF will lie 7.5 eV lower at -0.7 eV and hence the formation of excited states of HF are not important in the reaction. In addition, the asymptote for forming H + F instead of HF lies at 1.1 eV, well below the exoergicity of the majority of reactive events. This observation, together with the inherent lower likelihood of a 'four-body' reaction clearly shows that the neutral product in this reaction is HF.

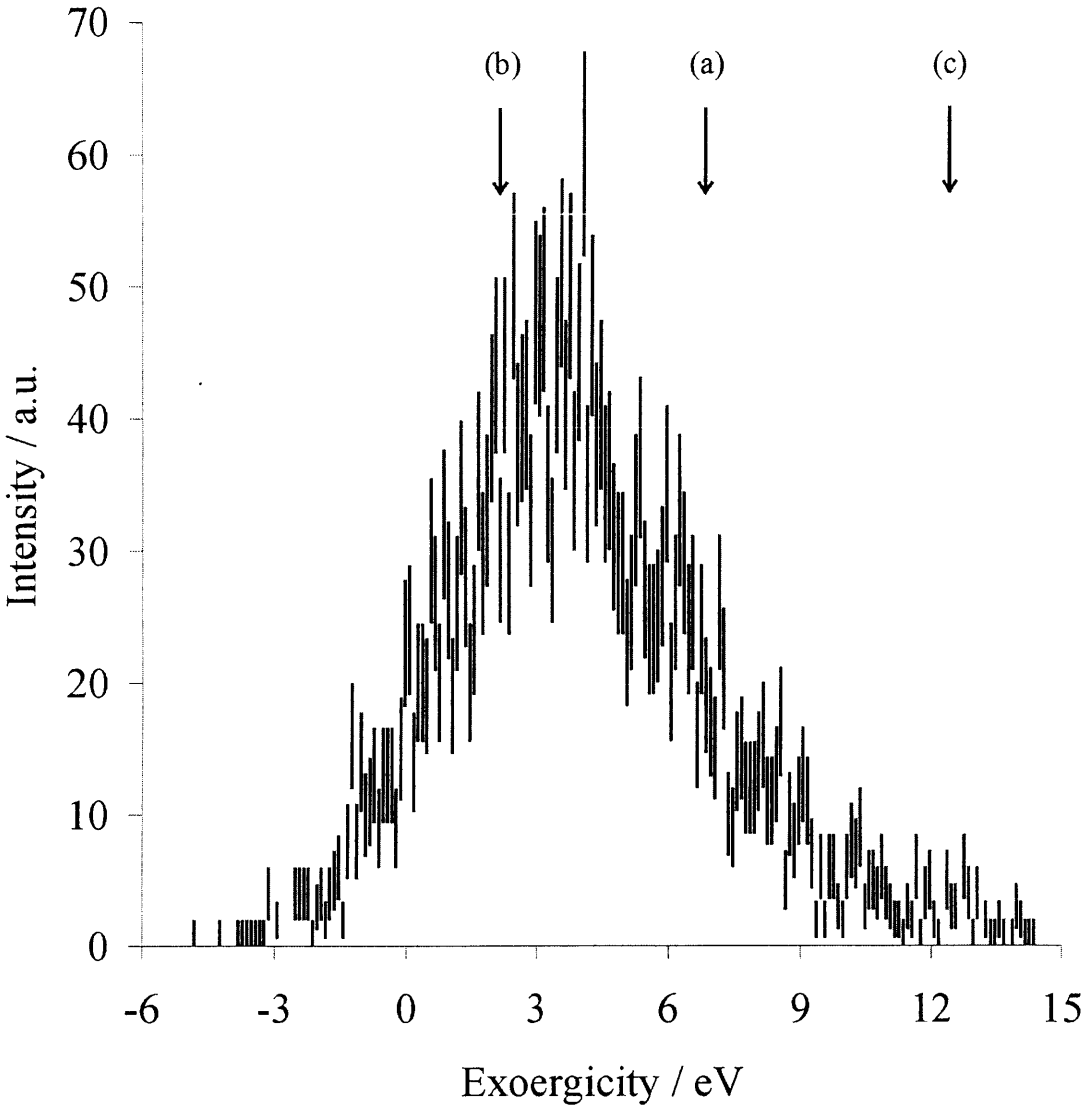

Figure 9.4 Exoergicity spectrum for the BF channel forming $OCF^+ + H^+ +$ HF at high TOF source field. The vertical lines above the spectrum indicate the calculated exoergicity for formation of (a) the products in their ground states from ground state reactants, (b) OCF^+ in its first excited electronic state from ground state reactants and (c) ground state products *via* reaction of the first excited electronic state of CF_2^{2+}.

The first electronic excited state of OCF^+ was calculated by Dyke *et al* to lie about 5.6±0.3 eV above the ($^1\Sigma_g^+$) ground state of OCF^+ [32]. Since these are rather old calculations the adiabatic excitation energy of the first excited ($^3A'$) state of OCF^+ were

re-determined computationally using GAUSSIAN98 implemented on a Linux workstation [33]. Optimised geometries of the ground electronic state of neutral OCF and single ionised OCF were determined using an MP2 algorithm with a CC-VTZ basis set. The relative energies of these minima were then evaluated using a coupled cluster [CCSD(T)] algorithm at the optimised geometries. These calculations gave results in excellent agreement with previous work [34].

The optimised geometry of the lowest lying triplet state of the monocation was then located using an MP2 optimisation, again with a cc-VTZ basis set, and the energy of this minimum determined by a coupled cluster calculation. The calculations indicate that the adiabatic excitation energy of the $^3A'$ state of OCF^+ from the ground ($^1\Sigma_g^+$) state of OCF^+ is 4.6 eV. Using this excitation energy, the exoergicity for forming the first excited state of OCF^+ in this reaction was calculated to be 2.1 eV, which again is indicated on Figure 9.4. The asymptote for the formation of OCF^+ in its first excited state lies below the exoergicity recorded for the majority of the reactive events (Figure 9.4). In addition, the formation of such a triplet state, from the ground electronic state of CF_2^{2+}, is spin forbidden if HF is formed in its ground state as has been deduced above. Hence, it is possible to conclude that the formation of OCF^+ in excited electronic states does not contribute significantly to the ion yield in this reaction. Such a conclusion is in accord with theoretical investigations of the potential energy surface for this reaction which found a reactive pathway which populated the ground electronic state of OCF^+ [28].

The asymptote for forming the ground state products (Figure 9.4) lies approximately 3.3 eV higher than the most intense signal in the PSCO experimental exoergicity spectrum. The events with exoergicities below this asymptote can be readily assigned to the formation of the molecular products with vibrational excitation. Since both molecular products (OCF^+ and HF) have deep potential wells in their ground electronic states, up to 6 eV of excitation could quite easily be distributed between the two molecular species. Above 6.7 eV in the exoergicity spectrum, the signals steadily decrease (Figure 9.4). The reactive events having exoergicities above 6.7 eV, which account for about 20% of the events detected, could either result from the reaction of dications possessing

significant vibrational excitation or a contribution to the product ion yield for the reactions of excited electronic states of CF_2^{2+}. Electronic structure calculations [35] indicate that a group of excited electronic states of CF_2^{2+} lie between 5.6-6.3 eV above the ground state. Hence, the asymptotic exoergicity for reactions of the excited state of the dication $CF_2^{2+}(^3B_1)$ with H_2O to form OCF^+, H^+ and HF in their ground states is 12.6 eV. As indicated in Figure 9.4, this asymptote is higher than almost all the recorded exoergicity signals.

In addition, there is no obvious sign of the bimodal exoergicity distribution one would expect if a second channel with a higher exoergicity was also contributing to the $OCF^+ + H^+$ signal. Hence, it seems unlikely that an excited state of the dication is responsible for exoergicity signals above 6.7 eV and therefore they must be assigned to the reaction of vibrationally excited states of the ground state of CF_2^{2+}. Indeed, theoretical calculations [35] show that this state can support up to 5 eV of vibrational energy. Thus, the assignment of the exoergicity signals above 6.7 eV to vibronic excitation in the reactant dication is supported by the fact that the upper limit of the exoergicity signals is 11.7 eV, 5 eV above the reaction asymptote.

9.3.1.3.1 Summary

Analysis of the exoergicity signals in Figure 9.11 indicate that the products are formed in their ground states with some vibrational excitation of OCF^+ and HF *via* collisions of the ground state of CF_2^{2+} with H_2O. The exoergicity signal also indicates that there is some vibrational excitation of the ground state dication.

9.3.2 $CF_2^{2+} + H_2O \rightarrow HCF_2^+ + H^+ + O$

9.3.2.1 Angular distribution

The scattering plots for this weak BF channel show that H^+ is isotropically scattered, with a large COM velocity, in the COM frame (Figure 9.5) with respect to v^c. In contrast, HCF_2^+ is forward scattered and O is backscattered (Figure 9.6) and both of these heavy species have markedly lower COM velocities than H^+. The isotropic scattering of H^+ again points to the presence of a collision complex in the reaction pathway.

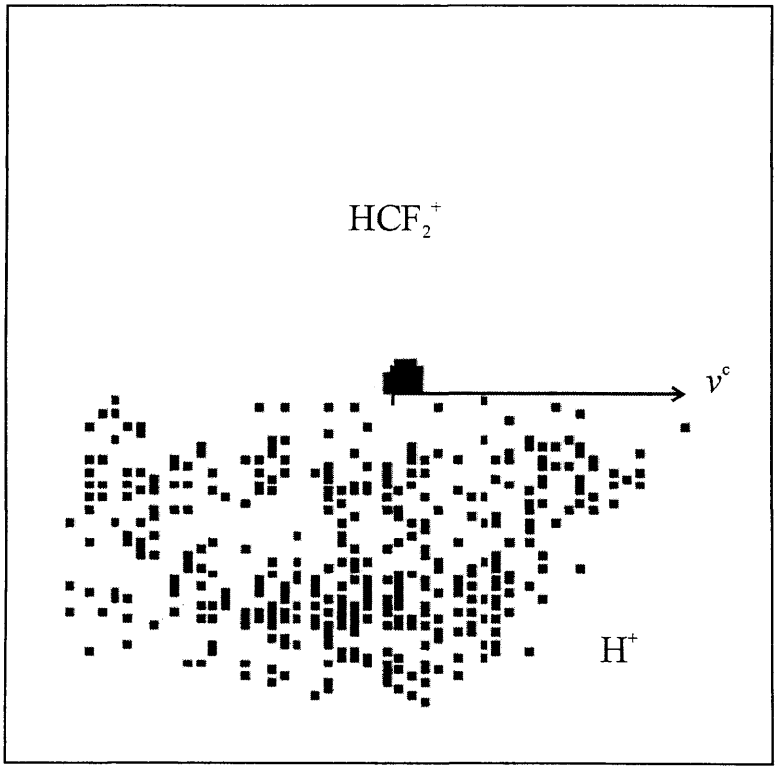

Figure 9.5 Scattering of HCF_2^+ and H^+ relative to v^c in the COM frame (scale: horizontal arrow = 4 cm μs^{-1}).

However, the scattering in this channel is significantly different to that involved in the formation of $OCF^+ + H^+ + HF$ in that molecular ionic product (HCF_2^+) and the neutral (O) are not isotropically scattered in the COM frame (Figure 9.6). This difference

indicates that a fundamentally different mechanism is operating in the formation of H^+ and HCF_2^+ in comparison with the formation of $OCF^+ + H^+$. The forward scattering of the HCF_2^+ with respect to the initial dication velocity is highly indicative of a "direct" reaction mechanism where the CF_2^{2+} "flies by" the H_2O molecule, grabbing an H atom and an electron as it passes, and leaving an OH^{+*} partner ion. Such strong forward scattering is also observed in dicationic electron transfer reactions where the reactant ion just flies past the neutral picking up an electron as it passes [2, 23].

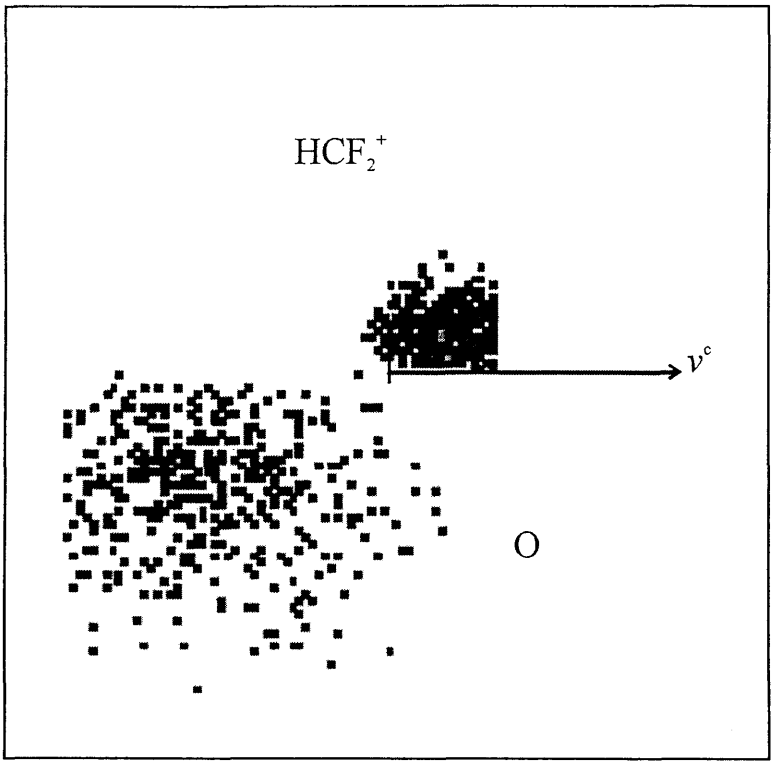

Figure 9.6 Scattering of HCF_2^+ and O relative to v^c in the COM frame (scale: horizontal arrow = 1 cm μs^{-1}).

If the OH^{+*} partner ion then lives long enough to rotate significantly before decaying to $H^+ + O$, the H atom will be isotropically scattered with respect to the initial dication velocity, as observed in Figure 9.5. If the OH^{+*} primary product decays when well separated from the HCF_2^+ ion, *i.e.* away from the centre-of-mass of the system (Figure 9.7), a symmetrical distribution of the H^+ and O atom velocities about the final OH^{+*} velocity might be anticipated. Such behaviour has been observed in PSCO data

from 'slow' dissociative electron transfer reactions as described for the Ne^{2+}-N_2 collision system [26] in Chapter Seven.

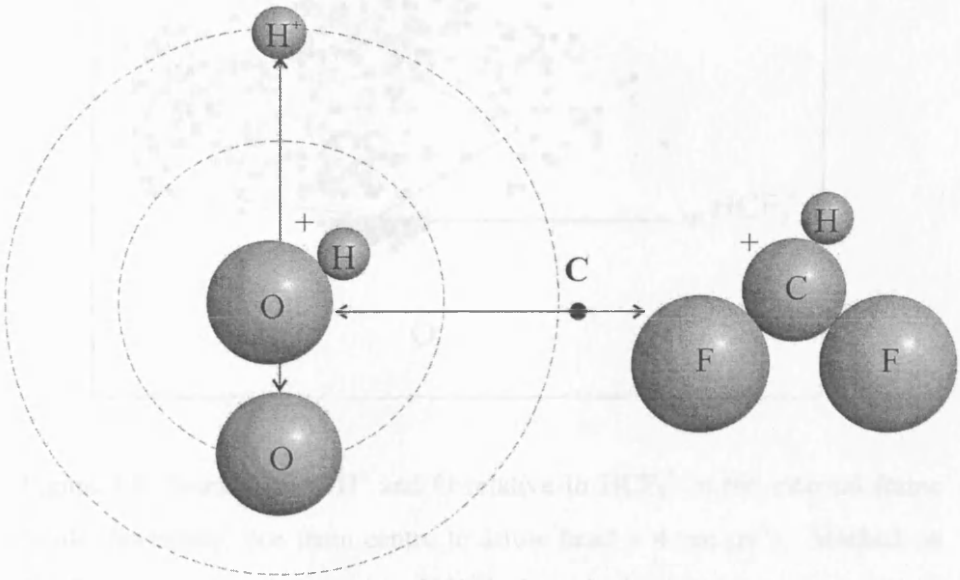

Figure 9.7 A schematic diagram representing the relative scattering of HCF_2^+, OH^{+*}, H^+ and O with respect to each other (not to scale) with respect to the centre-of-mass of the system **C**.

The expected final velocity of the OH^{+*} intermediate may be estimated, by conservation of momentum, from the velocity for the HCF_2^+ ion. The average velocity of HCF_2^+ is 0.25 cm μs^{-1}, which gives an average OH^{+*} velocity of 0.75 cm μs^{-1}. This initial velocity is apparent in the internal scattering diagram in Figure 9.8 where the COM velocity at which OH^{+*} dissociates lies away from the COM of the dissociating complex. Satisfyingly, it can be seen that the O and H^+ velocities are isotropically distributed about this vector, in excellent agreement with the proposed mechanism. Hence, it seems quite clear that the formation of HCF_2^+ and H^+ proceeds *via* a direct reaction to form HCF_2^+ and OH^{+*} with the OH^{+*} subsequently dissociating to H^+ and O.

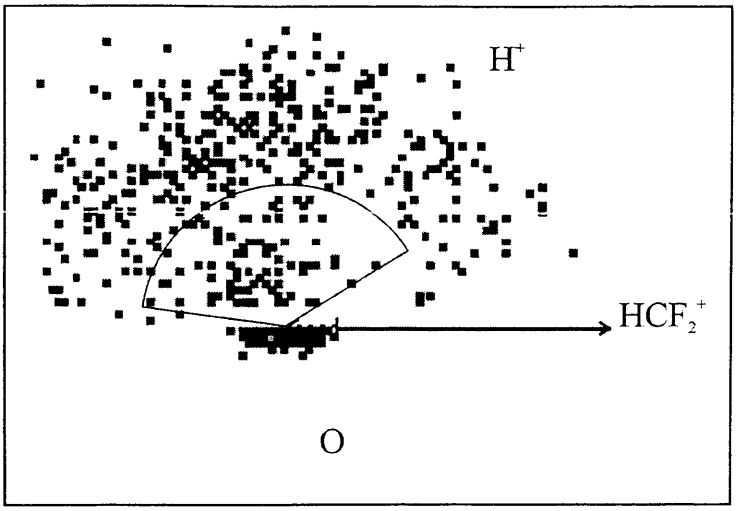

Figure 9.8 Scattering of H^+ and O relative to HCF_2^+ in the internal frame (scale: horizontal line from centre to arrow head = 4 cm μs^{-1}). Marked on the figure as a dotted arrow is $w(OH^{+*})$, the calculated precursor velocity of an OH^{+*} ion formed together with the HCF^{2+} ion. The arc represents the H^+ velocity formed from the fragmentation of such an ion with an energy release of 4.2 eV.

The energy release in the dissociation of OH^{+*} can be estimated from the distribution of $w(H^+)$ about $w(OH^{+*})$. This analysis indicates the energy release on forming $H^+ + O$ is approximately 3-5 eV. Such large kinetic energy releases in the dissociation of OH^{+*} perhaps arise from the population of the $c^1\Pi$ state [36], which is known to predissociate with a large energy release, or higher lying unbound levels [37].

9.3.2.1.1 Summary

Analysis of the angular scattering of the products in the COM frame, as described above, indicates the CF_2^{2+}-H_2O collision in this channel results in hydride transfer forming HCF^{2+} with OH^{+*}. OH^{+*} subsequently undergoes dissociation out of the field of HCF^{2+}, to form H^+ and O. Figure 9.9 shows a schematic summary of this mechanism.

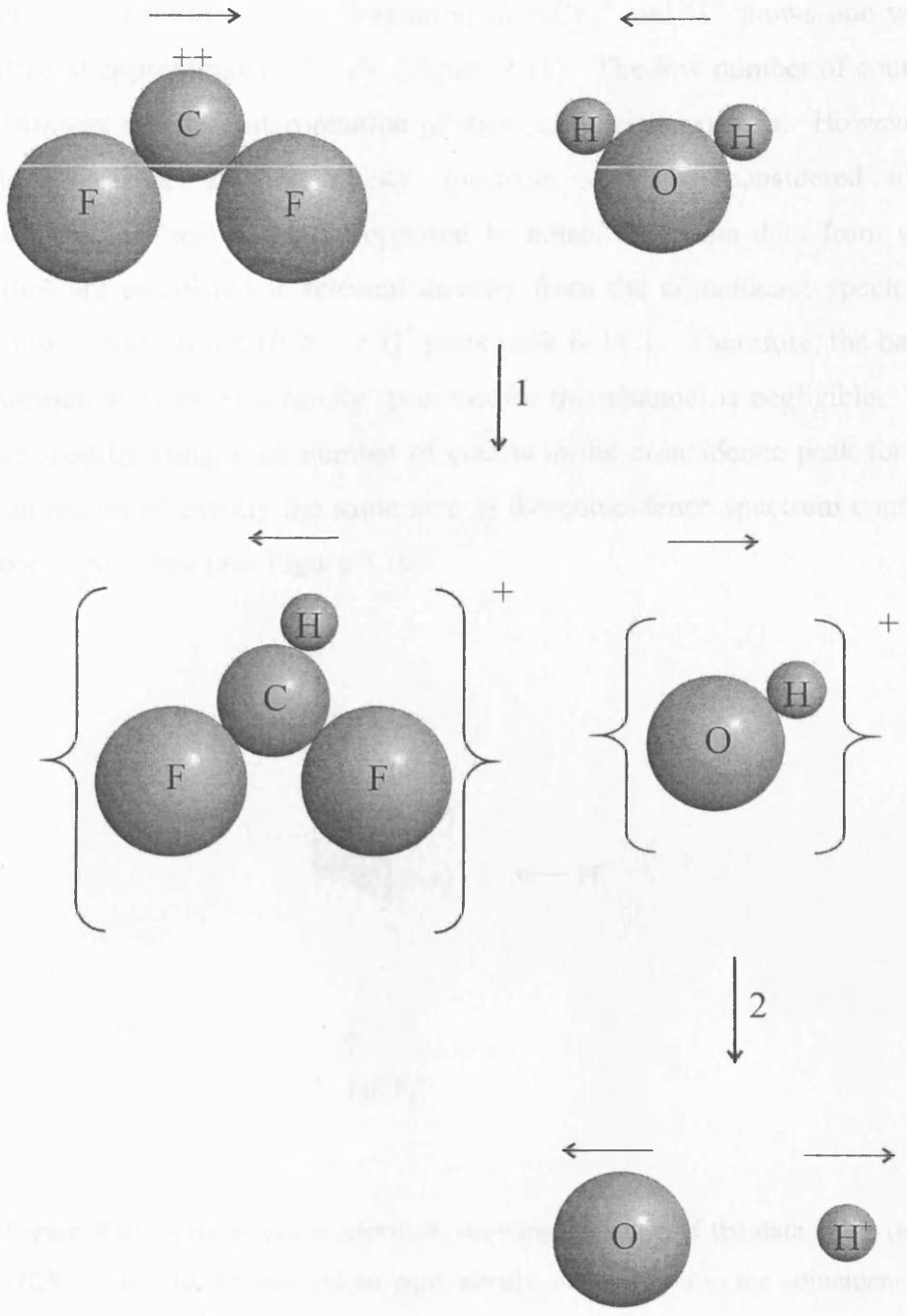

Figure 9.9 A schematic diagram of the bond-forming mechanism resulting in formation of the $HCF_2^+ + H^+$ ion pair. The arrows above some of the species indicate the internal frame velocity (not to scale) for a step of the mechanism.

9.3.2.2 Exoergicity

The exoergicity spectrum for the formation of HCF_2^+ and H^+ shows one very broad peak centred at approximately 7.4 eV (Figure 9.11). The low number of counts in this channel hampers detailed interpretation of these exoergicity signals. However, all the observed signals in the exoergicity spectrum may be considered to consist overwhelmingly of 'real' data, as opposed to noise, since the data from which the exoergicities are calculated is selected directly from the coincidence spectrum. The signal to noise ratio for the $HCF_2^+ + H^+$ pairs peak is 14:1. Therefore, the background noise contribution to the exoergicity spectrum for this channel is negligible. This ratio was determined by comparing number of counts in the coincidence peak for $HCF_2^+ + H^+$ with an region of exactly the same size in the coincidence spectrum containing no 'real' experimental data (see Figure 9.10).

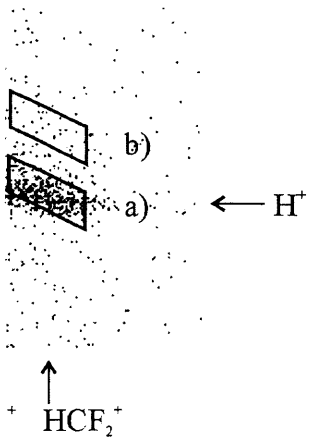

Figure 9.10 A coincidence spectrum showing selection of the data in the (a) $HCF_2^+ + H^+$ channel and (b) an equivalently sized region in the coincidence spectrum where there is no 'real' data.

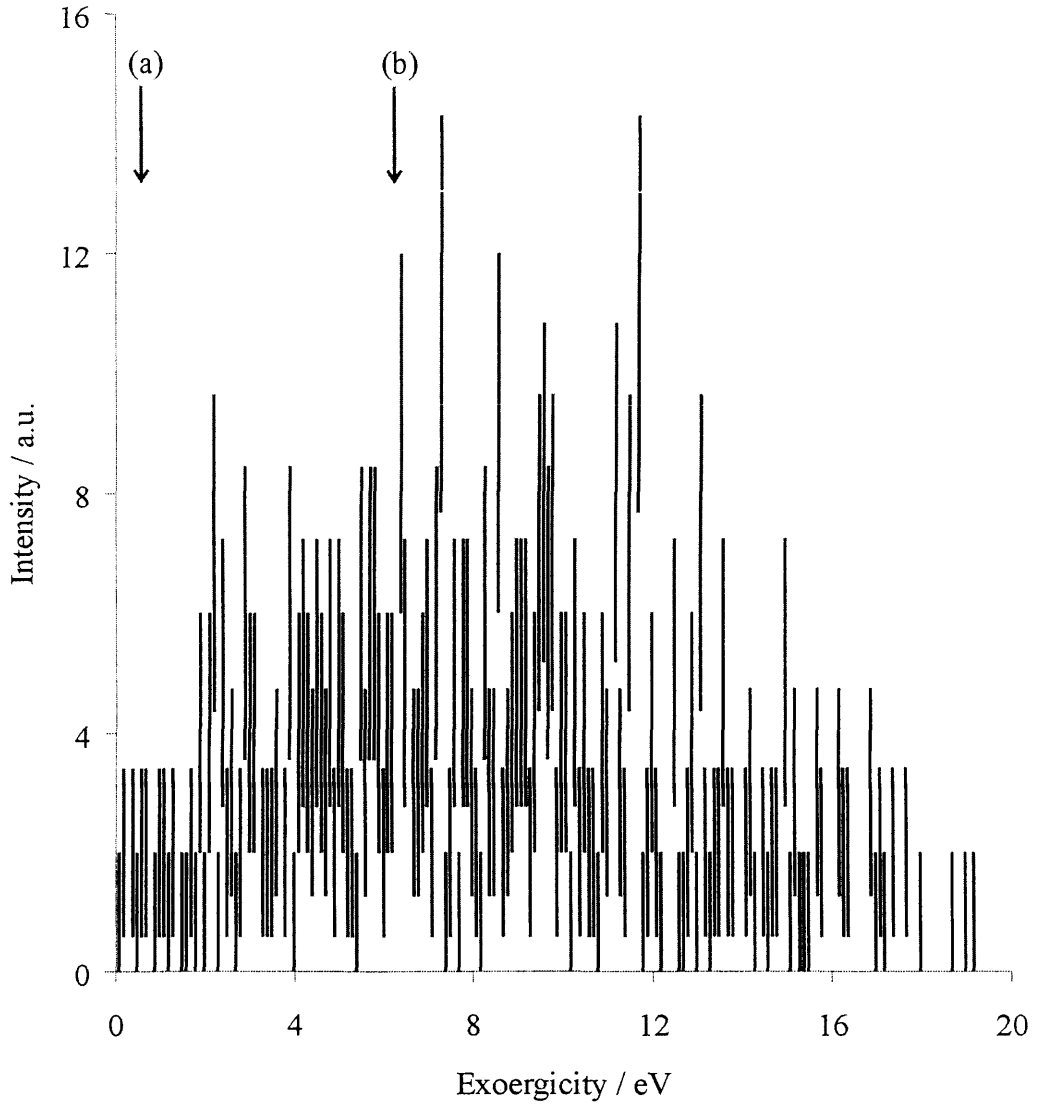

Figure 9.11 Exoergicity spectrum for the BF channel forming HCF_2^+ at high TOF source field. The vertical lines above the spectrum indicate the product asymptotes for formation of the products in their ground states *via* collisions of (a) the ground state of CF_2^{2+} and (b) the first excited state of CF_2^{2+} with H_2O.

The calculated exoergicity for formation of $HCF_2^+(X)$, H^+ and O *via* collisions of the ground state dication with H_2O lies at an exoergicity of 2.6 eV [29-31]. This asymptote clearly lies too low to account for all the experimentally observed exoergicity signals

even allowing for vibrational excitation of the dication. Hence, it seems clear that the reaction is from the excited state of the dication, the first of which, $CF_2^{2+}(^3B_1)$, has a nominal exoergicity of 8.2 eV (Figure 9.11) for forming the ground state products, which is much more in accord with the bulk of the exoergicity signals.

In summary, the exoergicity spectrum infers that the formation of $HCF_2^+ + H^+ + O$ is a result of the reaction of an excited state of CF_2^{2+} with H_2O. Indeed, the presence of such excited states in beams of CF_2^{2+} has been deduced from previous modelling of the electron transfer reactivity of this dication [10, 27, 38]. If an excited triplet state of CF_2^{2+} is indeed responsible for the formation of HCF^{2+}, as deduced above, then the formation of ground-state products would be a spin-allowed process, in contrast to a spin-forbidden process from the singlet ground state of CF_2^{2+}. This consideration of spin conservation provides further evidence in favour of the formation of HCF^{2+} by an excited triplet state of CF_2^{2+}.

9.3.3 General discussion

The results from the two bond-forming reactions discussed in this chapter agree well with previous indications in the literature. The possible formation of OCF^+ *via* a complex, suggested by Kearney *et al* [27], is clearly confirmed by the PSCO results with detailed evidence of the dissociation of a rotating complex to form OCF^+ paired with H^+.

The formation of HCF_2^+ in CF_2^{2+}-X_2 collision systems has been detected with strong forward scattering [2] as also observed with the PSCO experiment. The PSCO data clearly indicates a direct (H^-) transfer with detailed scattering information of the accompanying O and H^+ fragments thus ruling out product formation *via* a complex-forming mechanism.

9.4 Conclusions

The dynamics of the product channels forming $OCF^+ + H^+ + HF$ and $HCF_2^+ + H^+ + O$ following the collisions of CF_2^{2+} with H_2O have been investigated with a new position-sensitive coincidence (PSCO) experiment. The experimental results show the formation of OCF^+ occurs *via* the formation of a doubly-charged collision complex $[H_2O\text{-}CF_2]^{2+}$ that subsequently undergoes a charge separating dissociation to form H^+ and $HOCF_2^+$. The $HOCF_2^+$ monocation subsequently fragments to form HF and OCF^+. The lifetimes of the collision complex and the $HOCF_2^+$ ion are certainly at least of the order of their rotational period. This mechanism is in excellent agreement with earlier quantum chemical calculations. The kinetic energy release in this reaction indicates that this reaction involves the ground state of CF_2^{2+} and forms the ground electronic states of OCF^+ and HF.

In contrast to the formation of OCF^+, the mechanism for forming HCF_2^+ involves the direct and rapid abstraction of a hydrogen atom and an electron from H_2O by CF_2^{2+}. The resulting OH^{+*} ion subsequently fragments to $H^+ + O$. The PSCO data also gives some information on the electronic states of the reactants and products involved in these reactions.

9.5 References

[1] Herman, Z., Zabka, J., Dolejsek, Z., and Farnik, M., 1999, *Int. J. Mass Spectrom.* **192** 191-203.

[2] Herman, Z., 1996, *Int. Rev. Phys. Chem.* **15** (1) 299-324.

[3] Mrazek, L., *et al.*, 2000, *J. Phys. Chem. A.* **104** (31) 7294-7303.

[4] Price, S. D., Manning, M., and Leone, S. R., 1994, *J. Am. Chem. Soc.* **116** (19) 8673-8680.

[5] Chatterjee, B. K. and Johnsen, R., 1989, *J. Chem. Phys.* **91** (2) 1378-1379.

[6] Dolejsek, Z., Farnik, M., and Herman, Z., 1995, *Chem. Phys. Lett.* **235** (1-2) 99-104.

[7] Witasse, O., *et al.*, 2002, *Geophys. Res. Letts.* **29** (8) 1263.

[8] Hsieh, S. and Eland, J. H. D., 1996, *J. Phys. B: At. Mol. Opt. Phys.* **29** (23) 5795-5809.

[9] Newson, K. A. and Price, S. D., 1997, *Chem. Phys. Lett.* **269** (1-2) 93-98.

[10] Newson, K. A., Tafadar, N., and Price, S. D., 1998, *J. Chem. Soc.: Faraday Trans.* **94** (18) 2735-2740.

[11] Lu, W. Y., Tosi, P., and Bassi, D., 2000, *J. Chem. Phys.* **112** (10) 4648-4651.

[12] Hsieh, S. and Eland, J. H. D., 1997, *J. Phys. B: At. Mol. Opt. Phys.* **30** (20) 4515-4534.

[13] Tafadar, N., Kearney, D., and Price, S. D., 2001, *J. Chem. Phys.* **115** (19) 8819-8827.

[14] Tafadar, N. and Price, S. D., 2003, *Int. J. Mass Spectrom.* **223** (1-3) 547-560.

[15] Newson, K. A. and Price, S. D., 1998, *Chem. Phys. Lett.* **294** (1-3) 223-228.

[16] Larsson, M., 1993, *Comments At. Mol. Phys.* **29** 29-51.

[17] Mathur, D., 1993, *Phys. Rep.-Rev. Sec. Phys. Lett.* **225** (4) 193-272.

[18] Tosi, P., *et al.*, 1999, *Phys. Rev. Lett.* **82** (2) 450-452.

[19] Tosi, P., Lu, W. Y., Correale, R., and Bassi, D., 1999, *Chem. Phys. Lett.* **310** (1-2) 180-182.

[20] Tosi, P., Correale, R., Lu, W. Y., and Bassi, D., 1999, *J. Chem. Phys.* **110** (9) 4276-4279.

[21] Ascenzi, D., *et al.*, 2003, *J. Chem. Phys.* **118** (5) 2159-2163.

[22] Lambert, N., Kearney, D., Kaltsoyannis, N., and Price, S. D., 2004, *J. Am. Chem. Soc.* **126** (11) 3658-3663.

[23] Harper, S. M., Hu, W. P., and Price, S. D., 2002, *J. Phys. B: At. Mol. Opt. Phys.* **35** (21) 4409-4423.

[24] Hu, W. P., Harper, S. M., and Price, S. D., 2002, *Meas. Sci. Technol.* **13** (10) 1512-1522.

[25] Price, S. D., 2003, *Phys. Chem. Chem. Phys.* **5** (9) 1717-1729.

[26] Harper, S. M., Hu, S. W. P., and Price, S. D., 2004, *J. Chem. Phys.* **120** (16) 7245-7248.

[27] Kearney, D. and Price, S. D., 2003, *Phys. Chem. Chem. Phys.* **5** (8) 1575-1583.

[28] Lambert, N., Kaltsoyannis, N., and Price, S. D., 2003, *J. Chem. Phys.* **119** (3) 1421-1425.

[29] Hrusak, J., Herman, Z., Sandig, N., and Koch, W., 2000, *Int. J. Mass Spectrom.* **201** (1-3) 269-275.

[30] Lias, S. G., *et al.*, 1988, *J. Phys. Chem. Ref. Data.* **17 S1** 1-861.

[31] *NIST Chemistry WebBook, NIST Standard Reference Database Number 69*, 2003 (National Institute of Standards and Technology, Gaithersburg MD, 20899 (http://webbook.nist.gov)).

[32] Dyke, J. M., Jonathan, N., Morris, A., and Winter, M. J., 1981, *J. Chem. Soc.: Faraday Trans.* **66** 667-672.

[33] Harper, S. M., Hu, S. W. P., and Price, S. D., 2004, *J. Chem. Phys.* **121** (7) 3507-3514.

[34] Krossner, T., Peric, M., Vetter, R., and Zulicke, L., 1994, *J. Chem. Phys.* **101** (5) 3981-3988.

[35] Hrusak, J., 2001, *Chem. Phys. Lett.* **338** (2-3) 189-194.

[36] Levick, A. P., *et al.*, 1989, *Phys. Rev. Lett.* **63** (20) 2216-2219.

[37] Hirst, D. M. and Guest, M. F., 1983, *Mol. Phys.* **49** (6) 1461-1469.

[38] Manning, M., Price, S. D., and Leone, S. R., 1993, *J. Chem. Phys.* **99** (11) 8695-8704.

Chapter 10

Future work

The results presented in Chapter Five demonstrate that the position-sensitive coincidence experiment described in this thesis has been successfully commissioned. The experimental investigations described in Chapters Six to Nine reveal the power of the position-sensitive coincidence technique coupled with time-of-flight mass spectrometry. It has been possible, using these two techniques, to determine the dynamics and energetics of a given channel of reaction between dications and neutral collision partners. Such information provides a clear insight into dication-neutral reaction mechanisms and, hence, the lifetimes of the some of the species formed in these reactions.

The study of the chemical reactions of molecular dications is still developing. After more than a decade of experimental effort, there is now a generalised picture of the types of reactivity that occur in dication-neutral collisions and models to rationalise this behaviour. However, experimental investigations are far from complete and, undoubtedly, new classes of reactivity remain to be discovered. Thus, there is considerable scope for additional experimental efforts in this field. For example, guided ion beam techniques have recently been applied to measure total cross sections for dication chemical reactions [1]. To extend these experimental studies to state-selective experiments would be a logical step. However, for such experiments to be possible, methodologies for generating considerable numbers of dications in a given internal energy state will have to be developed.

Several factors may be improved to enhance the energy resolution of the PSCO experiment. These are the energy resolution of the reactant dication beam, further

localisation of the point of interaction between the dication and neutral beams and implementation of velocity imaging.

10.1 PSCO ion beam

At present, electron ionisation is used to generate the PSCO dication beam. This technique is not state-selective and, therefore, for some dications, there will be many states present in the beam at PSCO beam energies. As a result, there are numerous possibilities for electronic transitions forming products at different energies. The exoergicity spectra for such reactions are broad and featureless allowing very little information to be extracted about the energetics of specific reaction channels, as shown in Chapter Seven. In order for reactions of this type to become accessible using the PSCO instrument, it is necessary either to use a state-selective ionisation technique, or perhaps implement a method of quenching some of the more excited dicationic states that are formed by electron ionisation. The latter method could be instigated by introducing a secondary gas into the ionisation region with which these excited states would react.

Another factor that may currently contribute to degradation of the energy resolution of the PSCO ion beam is the 'free flying' region between the end of the decelerator and the repeller plate. Any spread in the beam that may occur at this point could be reduced or even eliminated by moving the end of the decelerator closer to the repeller plate.

10.2 Neutral collision gas

The dynamics of the products, formed in dication-neutral reactions within the PSCO instrument, are calculated from the initial LAB velocity vectors of the products which are determined from the ionic (x, y) positions at the detector and the initial point of

dication-neutral interaction (x_0, y_0) (as described in Chapter Four). (x_0, y_0) is calculated from the position of the unreacted dication beam at the detector. Although the dication beam is well collimated, it does have a finite diameter of ~3 mm.

At present, the neutral collision gas is introduced effusively into the reaction source region. Due to a combination of the dication beam diameter and the effusive neutral gas, it is not possible to confine the point of dication-neutral interaction exactly to the centre of the reaction source region. Therefore, there will be some uncertainty in the LAB velocity vectors and, hence, the energy resolution. The formation of a molecular beam of neutral gas to create much more specific dication-neutral interaction point would help to reduce this uncertainty in (x_0, y_0).

10.3 Velocity map imaging (VMI) [2, 3]

The current PSCO experimental arrangement allows the determination of x, y and z velocity vectors for each detected product ion. The ability to resolve the z velocity vectors of individual ions in mass spectrum is determined by the source field magnitude (Chapter Four). It is desirable to record mass spectra at high source field in order to detect the full angular distribution of the ionic products; however, this is at the expense of low energy resolution. This is a distinct disadvantage of the current PSCO arrangement, since, at low source field where the energy resolution is much improved, many of the more energetic ions, which may be collected at high source field, are lost.

A modification that may be made to overcome this problem is the use of velocity imaging of product ions. Velocity imaging uses an inhomogeneous field in the reaction source region to map ions of the same velocity onto the same part of the detector, irrespective of the z velocities of the ions. In the past, this method has required a much localised point of reactant interaction, however, there have been recent advances in this area of research that allow VMI to be used with crossed beam apparatus where the point of interaction between the reactants is not so localised.

10.4 Conclusion

This chapter has described some modifications that will improve the energy resolution of the PSCO instrument. Implementation of the above changes should allow the resolution of individual electronic states within 1 eV of each other with the potential to resolve vibrational levels within these electronic states.

10.5 References

[1] Tosi, P., Lu, W. Y., Correale, R., and Bassi, D., 1999, *Chem. Phys. Lett.* **310** (1-2) 180-182.

[2] Eppink, A. T. J. B. and Parker, D. H., 1997, *Rev. Sci. Instrum.* **68** (9) 3477-3484.

[3] Parker, D. H. and Eppink, A. T. J. B., 1997, *J. Chem. Phys.* **107** (7) 2357-2362.

Appendix A

Comparison of reactant velocities

This section compares the velocities of the reactant dication and its neutral collision partner in order to demonstrate that the velocity of the neutral in the PSCO apparatus may be considered as negligible in dynamical and energetic calculations. If this consideration is correct then the dication velocity may be considered equivalent to the centre-of-mass velocity of the collision system v^c.

A.1 Initial velocity of the dication beam

The LAB velocity of the dication beam s_d may be calculated from the energy of the beam using

$$s_d = 1.39\sqrt{\frac{E}{m}}. \qquad \text{(A.11)}$$

For a Ne^{2+} dication beam with E_d = 8.28 eV in the LAB frame, where m = 20, then s_d = 0.89 cm $\mu s^{-1} \equiv$ 8900 m s^{-1}.

A.2 Initial velocity of the neutral collision gas

The velocity of a neutral species, of mass m, may be calculated using the Maxwell-Boltzmann velocity distribution

$$v = \sqrt{\frac{3RT}{M}} \qquad \text{(A.12)}$$

where R is the gas constant (8.31 m^2 kg s^{-2} K^{-1} mol^{-1}), T = 300 K and the molar mass of the neutral collision gas, in this example argon, M = 0.04 kg mol^{-1}. Therefore, v_{Ar} = 432 m s^{-1}.

It can be seen from the above comparison that the velocity of the neutral collision partner is negligible and therefore the dication beam velocity v_d may be considered as equivalent to $\boldsymbol{v}^c$.

Appendix B

Calculation of the centre-of-mass velocity of the collision system v^c

This section shows examples of the calculation of v^c by both methods cited in Chapter Four to confirm the agreement between them. Data for a Ne^{2+} beam will be used to perform the calculations.

B.1 Method one

One method calculates v^c from the speed of the dication beam s_d. This approach may be used since the narrow and centrally aligned images of the PSCO ion beams at the detector is a good indication that the dication velocity is directed along the z-axis of the TOF mass spectrometer. The velocity of the neutral collision partner, of mass m_n, is negligible (Appendix A) in comparison to the dication velocity then $v_x^c = 0$ and $v_y^c = 0$, so

$$v_z^c = \frac{m_d s_d}{(m_d + m_n)}. \qquad \text{(B.1)}$$

Using this method, one distinct value of v^c is determined for an individual experiment and this value is used for transforming every reactive event from the LAB to the COM frame.

The energy of the dication beam, which is known from the voltages applied to the hemispherical energy analyser, may be used to calculate s_d

$$s_d = 1.39\sqrt{\frac{E}{m}}. \qquad \text{(B.2)}$$

Table B.1 shows the value of v^c calculated using this method for a Ne^{2+}-Ar collision system.

Table B.1 The value of v^c calculated using the velocity of the dication beam (method one).

m_d	m_n	E_d (eV)	s_d (cm μs^{-1})	$v^c = v_z^c$ (cm μs^{-1})
20	40	8.28	0.89	0.30

B.2 Method two

Alternatively, for a two-body reaction, v^c can be derived from the velocities $v(i)$ of both product ions for each reactive event and the data converted to the COM frame on an event-by-event basis:

$$v^c = \frac{m(1)v(1) + m(2)v(2)}{m(1) + m(2)}. \qquad \text{(B.3)}$$

where, for this example, Ar^+ is ion (1) and Ne^+ is ion (2). Table B.2 shows the values used to calculate v^c by this method.

Table B.2 The value of v^c calculated for one reactive event using the velocities of the products in the LAB frame (method two).

m_d	m_n	$v(1)$ (cm μs^{-1})	$v(2)$(cm μs^{-1})	v^c (cm μs^{-1})
20	40	0.44	0.9	0.33

B.3 Conclusion

It can be seen that the agreement between the calculations for methods one and two, shown above, is very good. This result reaffirms the assumption that the beam is well aligned along the z-axis of the TOF mass spectrometer.

Appendix C

Space focusing in a two-field TOF mass spectrometer

As discussed in Chapter Three, the mass resolution of a time-of-flight (TOF) mass spectrometer is affected by a condition known as space focusing. Space focusing is a procedure that attempts to overcome the problem that the ions to be analysed by the spectrometer are formed over a volume in the source region and not at a point in space.

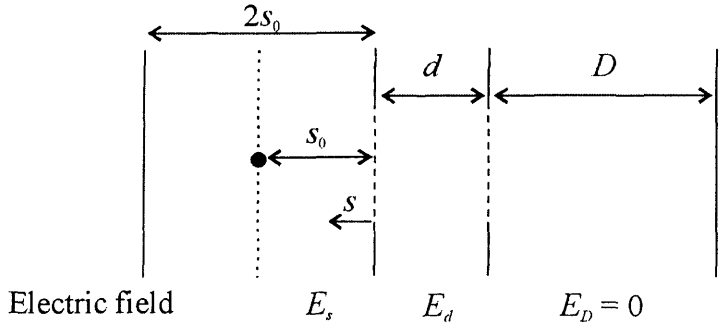

Figure C.1 A two-field space focusing mass spectrometer consisting of a source region, $2s_0$, acceleration region, d, and drift tube, D.

Let us consider a two-field spectrometer as illustrated in Figure C.1 with a source region of length $2s_0$, acceleration region of length d and drift tube of length D where E_s and E_d are defined as the electric fields in the source and acceleration regions, respectively. In an "ideal" situation, all of the ions would be formed with an initial energy, u_0, of zero at a single position in the source region. Let us define a variable s, which is the displacement of an individual ion's position in the source from the entrance of the acceleration region, as shown in Figure C.1. In the ideal situation, the ionic source position may be defined as the centre of the source region between the repeller plate and

the entrance to the acceleration region, a distance $s = s_0$ from the entrance of the acceleration region (Figure C.1). Under these ideal conditions, all the ions would be accelerated to the same kinetic energy as they are accelerated over the same distance from the same point, where $s = s_0$ in the source, towards the acceleration region. After flying out of the source region, ions pass through the acceleration region and into the drift tube, at the end of which they impact on the detector. Under these ideal conditions, all ions of the same mass, m, would have flight times of equal magnitude.

In a "real" spectrometer, ions are formed at a range of positions in the source region, rather than at a single point. When extracted from the source region, depending on the length of the drift tube, ions formed at a position $s \leq s_0$ (*i.e.* closer to the acceleration region) may eventually be overtaken by ions that were formed at a position $s > s_0$ (*i.e.* closer to the repeller plate). Ions with $s > s_0$ are accelerated for longer, and therefore have correspondingly higher kinetic energies on entering the acceleration region, than those formed closer to the acceleration region (*i.e.* $s \leq s_0$). For ions of the same mass, the ultimate effect of the variation in ionic source position results in a spread of kinetic energies in the drift tube that would cause a spread in flight times when the ions reach the detector if the ions are not focused. The spread in flight times would make it hard to separate ions of adjacent mass.

In order to overcome the effects of the variation in ionic source position, described above, an operating condition can be established where the spread in flight times due to the positional variation, for any ion of a given mass, is eliminated for a given apparatus geometry: a space focus. As will be described below, in a two-field instrument it is possible to achieve a space focus, where ions of any given mass arrive at the detector (the space focus plane) at the same time, by adjusting the extraction fields, E_s and E_d. The location of the space focus plane is independent of mass, but ions of different masses will arrive at the space focus plane at different times proportional to $m^{1/2}$.

To derive the position of the space focus plane in a two-field instrument, Wiley and McLaren proceeded as follows. Any ion moving through the source with initial energy,

u_0, will increase its energy to a value u after experiencing an electric field. u is independent of m, but dependent on u_0, s and q (ionic charge)

$$u = u_0 + qsE_s + qdE_d \tag{C.1}$$

where E_s and E_d are defined, as in Figure C.1, as the electric fields in the source and acceleration regions, respectively, s is the displacement of the ion in the source region from the entrance of the acceleration region, and d is the length of the acceleration region. Under these conditions, the total ionic time-of-flight T can be shown to be a function of the initial kinetic energy of the ion along the axis of the spectrometer, u_0, and the initial position, s:

$$T(u_0, s) = T_s + T_d + T_D \tag{C.2}$$

where T_s, T_d and T_D may be defined as

$$T_s = 1.02\frac{\sqrt{(2m)}}{qE_s}[\sqrt{(u_0 + qsE_s)} \pm \sqrt{(u_0)}], \tag{C.2a}$$

$$T_d = 1.02\frac{\sqrt{(2m)}}{qE_d}[\sqrt{(u) - \sqrt{(u_0 + qsE_s)}}] \tag{C.2b}$$

and

$$T_D = 1.02\frac{\sqrt{(2m)}D}{2\sqrt{u}}. \tag{C.2c}$$

where u is defined by Eq. (C.1). The "±" term in Eq. (C.2a) arises from the fact that the initial kinetic energy of the ion u_0 can be directed towards or away from the detector.

To provide a qualitative equation for the space focus in a two-field spectrometer, Wiley and McLaren [1] then investigated the behaviour of T assuming the initial energy, u_0, of

the ions was zero and that the ions are all formed at a point in the source region at $s = s_0$. Under these conditions, the energy of an ion in the drift tube, u_T, after passing through the source and the acceleration region is

$$u_T = qs_0E_s + qdE_d . \tag{C.3}$$

and we can define k_0, a constant determined by the parameters of the spectrometer,

$$k_0 = \frac{(s_0E_s + dE_d)}{s_0E_s} . \tag{C.4}$$

Substituting eqns (C.3) and (C.4) into equations (C.2) gives

$$T(0,s_0) = \left(\frac{m}{2u_T}\right)^{1/2}\left(2k_0^{1/2}s_0 + \frac{2k_0^{1/2}}{k_0^{1/2}+1}d + D\right). \tag{C.5}$$

The first order space focus of the spectrometer is then found by solving the equation

$$\left(\frac{dT}{ds}\right)_{s=s_0,u_0=0} = 0 , \tag{C.6}$$

i.e. there is no variation in ionic flight time, T, with respect to the ionic position in the source region, s, (under conditions where s = s_0 and $u_0 = 0$). The first differential of Eq. (C.5), under the conditions cited in Eq. (C.6), gives

$$D = 2s_0k_0^{3/2}\left(1 - \frac{d}{s_0(k_0 + \sqrt{k_0})}\right). \tag{C.7}$$

For a two-field spectrometer with first order focusing, where the physical dimensions, s, d and D are fixed, the space focusing condition depends entirely on the ratio of the electric fields, E_s and E_d.

The two-field TOF design of Wiley and McLaren [1], as described above, is still the basis of most TOF mass spectrometers. In summary, the focus condition given by Wiley and McLaren makes the arrival time of ions at a detector plane independent of their displacement about the centre of the source, to first order.

The design process for a two-field TOF mass spectrometer then usually involves constraining the total length of the instrument ($s + d + D$) and often stipulating the length of the source region to a practical value (*e.g.* 2 cm) and then solving equation (C.7) to find d and D for a given value of k_0. The value of k_0 determines the ratio of the voltages applied to the source and drift regions, so k_0 cannot be too large, otherwise the voltage on the drift tube becomes impractical. However, the resolution of the instrument, if determined solely by the quality of the space focus, is proportional to k_0 [1]. Thus, in the design phase one tries to achieve a practical set of dimensions with as large a value of k_0 as practically possible.

In 1993, Eland further developed Wiley and McLaren's first order focusing two-field spectrometer [2]. In the course of numerical simulations of TOF spectrometers, Eland found a sub-family of Wiley-McLaren designs for which, in addition to satisfying equation (C.6), the second derivative of the time-of-flight with respect to source position about the centre of the source could also be set to zero.

$$\left(\frac{d^2T}{ds^2}\right)_{s=s_0,u_0=0} = 0. \qquad \text{(C.8)}$$

The second order focus in these new designs gave ionic times-of-flight that were effectively constant over a significantly larger percentage of the source region (75%) than simple first order design (30%). This new family of second-order designs have significantly longer acceleration regions (d) than the commonly used first order designs. Subsequent experimental tests of second order space focusing in two-field time-of-flight mass spectrometers by Eland confirmed that, for diffuse sources, second order designs give superior resolution and, incidentally, an improved linearity of flight time deviation with initial ion velocity in comparison to first order designs (Figure C.2). Solving the

equations set up by equation (C.6) and (C.8), gives the key design equation for a second order focus

$$D = 2s_0 k_0^{3/2}\left(1 - \frac{\sqrt{k_0} - 1}{k_0 + \sqrt{k_0} - 2)}\right) \qquad \text{(C.9)}$$

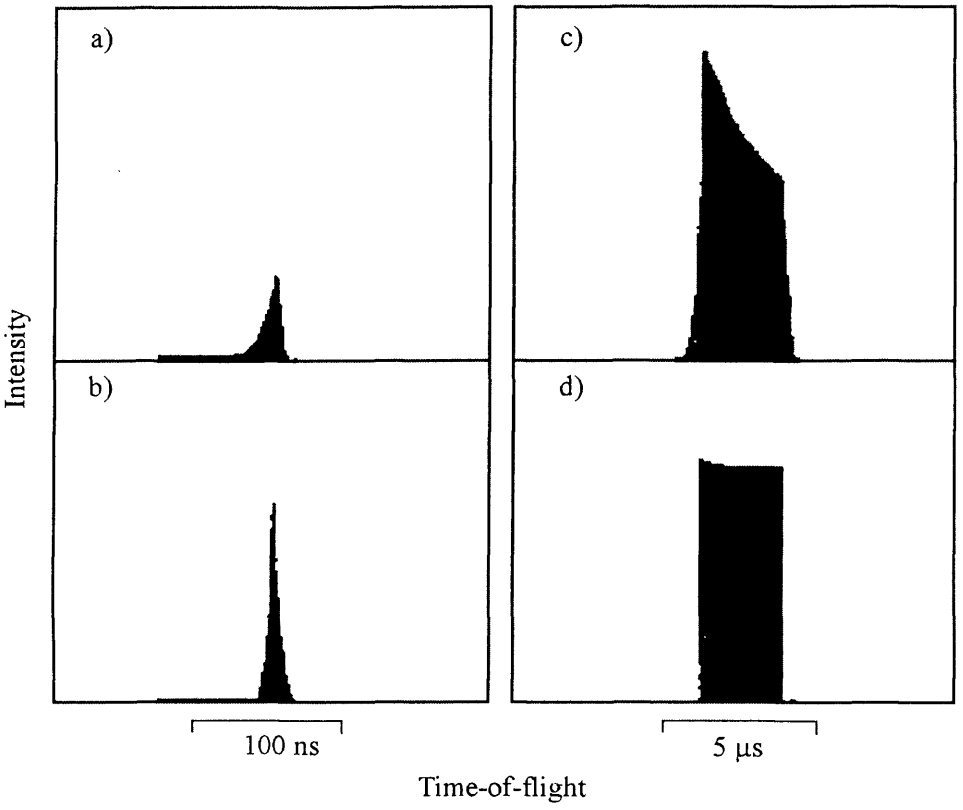

Figure C.2 Simulated peak shapes at first order focus, (a) and (c), and second order focus, (b) and (d), from Eland *et al* [2]. For (a) and (b) thermal (300 K) ions of relative mass 100 were spread throughout the source where a field of 1000 V cm^{-1} was applied. For (c) and (d) the ions were formed centrally with 5 eV initial energy in a field of 25 V cm^{-1}.

Note that in comparison to equation (C.7) we now have one fewer free parameter due to imposing the additional constraint of equation (C.8). Equation (C.9) then leads to a simple relationship between acceleration and drift lengths:

$$\frac{D}{d} = 2 + \frac{6}{(k_0 - 3)}. \qquad \text{(C.10)}$$

In this situation, the design procedure usually involves specifying the overall length of the instrument and a practical value of k_0. In the PSCO experiment described in this thesis k_0 = 15, as this gives a manageable drift tube voltage (-2800 V) for the largest voltage that can be driven by the pulser (400 V). In practice, adequate performance was given using 300 V across the source region and approximately -2100 V on the drift tube.

In order to demonstrate the improvement in the space focus for a second order design, Figure C.3 shows a plot of the time-of-flight, calculated using Eq. (C.2), of an ion of mass 40, as a function of source position, under comparable first order and second order designs. The first order design is that used in the first spectrometer developed at UCL to study the reactions of dications [3]. This mass spectrometer samples the reaction products from interactions of a dication beam with neutrals, as occurs in the PSCO spectrometer. The second order design is that used in the PSCO spectrometer.

Figure C.3 (b) clearly shows the improved and extended focus achieved in the second order design. This improved focus significantly improves the base mass spectral resolution when sampling from an ion beam which has a finite spread in the source region of the TOFMS. This improved resolution is also shown experimentally in the half widths of the dication peaks in both machines, which are 2 ns in the PSCO spectrometer and 14 ns in the first order instrument under similar conditions.

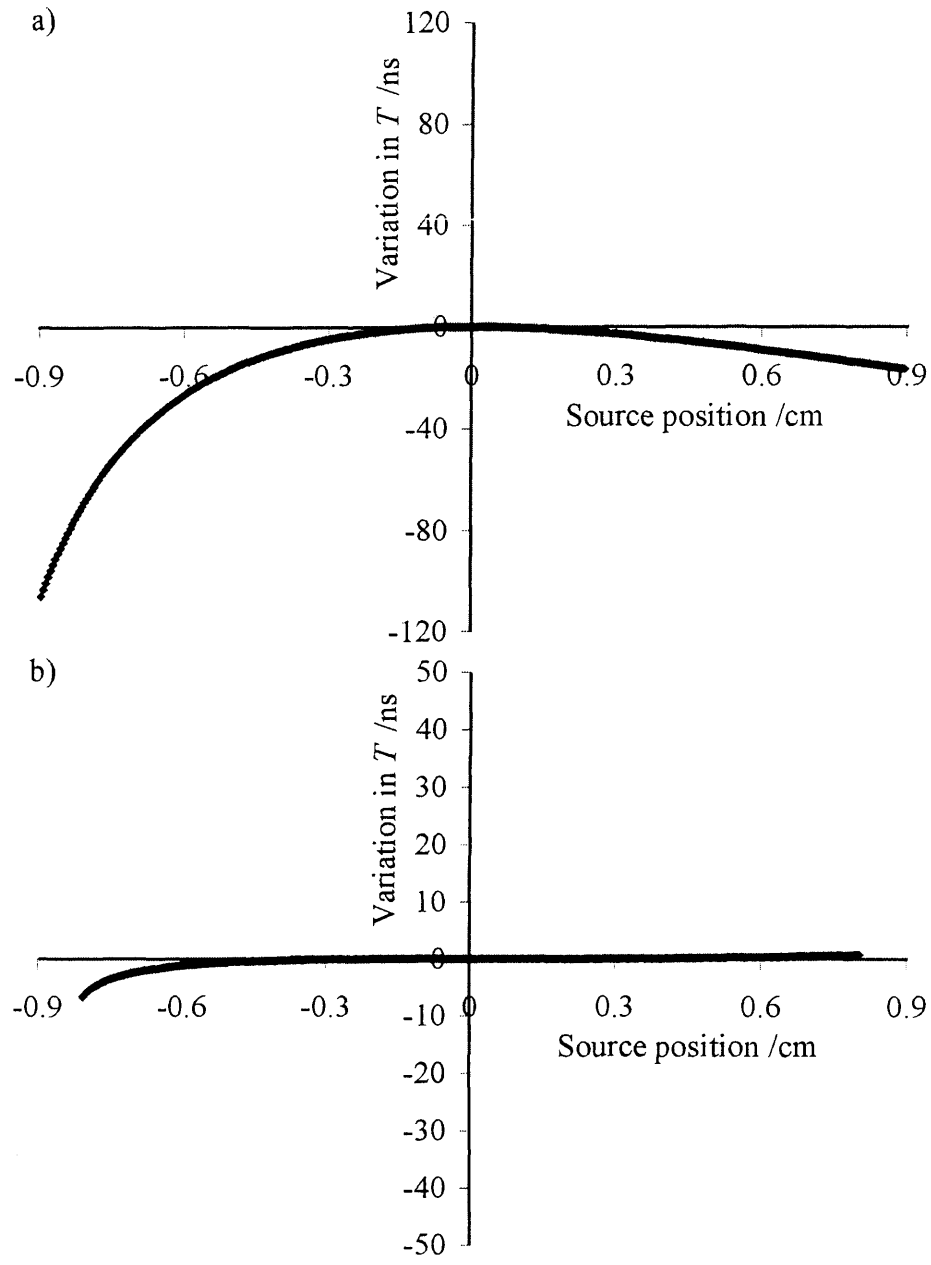

Figure C.3 Two plots showing the deviation from the expected TOF (ns) of an ion of mass 40, with respect to initial displacement from the centre of the source region (cm), under comparable (a) 1st order and (b) 2nd order designs. Parameters for first order machine: $k_0 = 6.5$, $2s_0 = 2$ cm, $d = 0.9$ cm, $D = 26$ cm; parameters for second order machine: $k_0 = 15$, $2s_0 = 1.6$ cm, $d = 11$ cm, $D = 27.5$ cm.

C.1 References

[1] Wiley, W. C. and McLaren, I. H., 1955, *Rev. Sci. Instrum.* **26** 1150-1157.

[2] Eland, J. H. D., 1993, *Meas. Sci. Technol.* **4** (12) 1522-1524.

[3] Kearney, D. and Price, S. D., 2003, *Phys. Chem. Chem. Phys.* **5** (8) 1575-1583.

Appendix D

Monte Carlo simulations of the Ne^{2+}-N_2 collision system

This section of the appendix gives a detailed explanation of the Monte Carlo program accompanied by a flow diagram and the annotated code. The code was used by authors contributing to reference [1] in order to carry out the Monte Carlo calculations cited in Chapter 7. It should be noted that the code included in this appendix was not written or run by the author of this thesis, but by a contributing author to reference [1]. However, the results from the Monte Carlo simulation were used to support the interpretation of the experimental data that was collected and analysed by the author of this thesis.

Abbreviations used in this section:
NDET: non-dissociative electron transfer
DET: dissociative electron transfer
MC: Monte Carlo
RK: Runge-Kutta

D.1 Discussion regarding the Monte Carlo code cited below

The Monte Carlo simulation program is written in Microsoft Visual Basic 6.0 and a schematic flow diagram of the program's operation is given in Figure D.1. After displaying a splash screen (see section D.5 below containing the annotated MC code), the program presents the user with four options, one of which is to exit. The remaining three options allow (1) a full Monte Carlo simulation of a series of Ne^{2+}-N_2 collisions, (2) the simulation of a single trajectory and (3) the display of the motions of the atoms from the simulation of a single trajectory. In effect, Option (1), the full simulation, repeatedly calls Option (2), the single trajectory simulation, with appropriate distributions of initial conditions, as will be discussed in detail below. Thus, it is appropriate to first discuss the basics of the single trajectory simulation and then to move on to discuss the choice of input parameters for the full Monte Carlo simulation.

D.2 Simulation of a single trajectory [Option (2)]

The input parameters required for the simulation of a single trajectory are as follows in Table D.1 and are defined by the user. The simulation operates in Cartesian co-ordinates where the x-axis is defined as the axis of the dication beam, with the COM of the neutral molecule at $x = 0$ and the centre of the dication beam at $y = 0$.

With the parameters defined (Table D.1), the execution of the classical trajectory simulation is begun. Under this single trajectory option, the positions and momenta of each atom are stored to a data file at each time step for subsequent examination using Option (3).

Table D.3 The input parameters required for the simulation of a single trajectory are as follows and are defined by the user.

Parameter	Typical Value	Comment
Initial x distance	50 Å	This value needs to be large enough so that the interactions between the reactants are negligible.
KER of dissociation	4 eV	The energy release when the N_2^+ dissociates
Dication beam energy	10 eV	The laboratory collision energy of the dication beam
Lifetime of N_2^+	200 fs	The precise lifetime of the N_2^+ ion for this particular trajectory
Angle of N_2^+	0-90°	The orientation of the N-N bond with respect to the x-axis
Angle of v_{Ne}	0-3°	Angle of the Ne^{2+} initial velocity with respect to the x-axis. This angle is small as the Ne^{2+} beam is well defined.
Time step	1 fs	The integration time step.
Reaction type	NDET or DET	Whether the N_2^+ is to dissociate or not. That is, whether to simulate a dissociative or non-dissociative reaction.
Impact parameter	0-20 Å	The initial y co-ordinate of the Ne^{2+}
Late/Early Crossing	Late/Early	Whether electron transfer is to occur at the first pass of the crossing radius, on approach of the reactants, or at the second pass as the reactants depart from each other
N^+ away	Yes/No	Whether the N^+ ion is going to be formed from the N atom furthest from the Ne^+ at the moment of N_2^+ dissociation, or whether which N atom forms the N^+ ion will be chosen at random.

The operation of the classical trajectory simulation is as follows. There are two different classical trajectory simulation sub-routines (`MC_diss_et` and

MC_non_diss_et), one for NDET one for DET. Which sub-routine is called depends on the value of the "reaction type" variable. The key initial parameters passed to the trajectory subroutines are the initial positions [q(n)] and momenta [p(n)] of all three atoms. The variables p(n) and q(n) are 9 element arrays (n = 1-9) where n = 1-3 refers to the position or momentum in the x, y, and z directions for the Ne atom. Similarly n = 4-6 refers to the position or momentum in the x, y, and z directions for one of the N atoms and n = 7-9 refers to the position or momentum in the x, y, and z directions for the other N atom.

The subroutine to simulate non-dissociative electron transfer (MC_non_diss_et) is also passed the time step (dt), whether the electron transfer occurs on approach or departure (etonapproach) and whether this call is for a single trajectory (singtraj). The sub-routine can pass back to the calling code whether a reaction occurred, that is if the trajectory reached the crossing radius (coulomb), the closest distance of approach (rmin). The heart of the classical trajectory simulation is numerical integration of Hamiltons' equations using a Runge-Kutta algorithm [2]. We will first describe how Hamiltons' equations are used and then how the numerical integration is carried out.

Firstly, we must set up the Hamiltonian of the system H. Classically H is the sum of the kinetic and potential energies. In principle, the procedure for using Hamiltons' equations is simple:

$$\left(\frac{dp_i}{dt}\right) = \left(\frac{\partial H}{\partial q_i}\right) \tag{D.1}$$

and

$$\left(\frac{dq_i}{dt}\right) = \left(\frac{\partial H}{\partial p_i}\right) \tag{D.2}$$

Thus one has just to write down the Hamiltonian in terms of the variables p_i and q_i and the differentiate the Hamiltonian with respect to the relevant p_i and q_i values to get differential equations which describe how the various p_i and q_i variables change. These differential equations can then be numerically integrated from a given set of initial values of p_i and q_i to give the values of p_i and q_i as a function of time: a trajectory. Thus, the procedure for calculating a trajectory can be broken down into three parts: firstly, constructing the Hamiltonian, secondly, differentiating the Hamiltonian appropriately to yield the key differential equations describing the trajectory, and thirdly, numerically integrating these differential equations to give p_i and q_i as a function of time. We will now describe briefly how each of these three steps is carried out.

D.2.1 Setting up the Hamiltonian

The kinetic energy part of the Hamiltonian simply involves a $p^2/2m$ term for each atom in each Cartesian degree of freedom. However, in addition to these kinetic energy terms there will be a different potential energy terms for the interaction of Ne^{2+} and N_2, the interaction of Ne^+ and N_2^+ following NDET and the interaction of Ne^+, N^+ and N after the N_2^+ has dissociated. For the interaction of Ne^{2+} and N_2, the classical Hamiltonian used incorporates the polarisation attraction of the dication and neutral and the interaction between the quadropole moment of the N_2 and the charge of the Ne^{2+}. In addition, a harmonic potential with a large force constant is established between the two N atoms so these two atoms move as an N_2 molecule. For the interaction of Ne^+ and N_2^+ following NDET, the Hamiltonian includes the coulombic repulsion between the two ions (which acts at the centre of mass of the N_2). For the interaction of Ne^+ and N^+ and N following DET, the Hamiltonian includes the coulombic repulsion between the two atomic ions whilst the N atom moves off with simple the velocity given to it by the dissociation of the N_2^+ as the kinetic energy of this dissociation dominates the polarisation attraction of the atomic ions with the neutral [3, 4].

D.2.2 Setting up Hamiltons' equations

The appropriate Hamiltonian is constructed using the relevant electrostatic equations, described in the previous section, for the interactions detailed above in terms of the q_i and p_i parameters. This involves using some trigonometry to determine the distances between the various species in terms of the q_i co-ordinates. Mathematica was then used to differentiate the different Hamiltonians for each of the above three cases ($Ne^{2+} + N_2$, $Ne^+ + N_2^+$, $Ne^+ + N^+ + N$) to yield the key differential equations (Hamiltons' Equations) which require numerical integration. These differential equations were then written as functions (`DHqn_polatt`, `DHpn` etc.) in the Visual Basic Program. Note that in the Hamiltonian, the momenta of the particles only contribute to the kinetic energy term, thus dH/dp_i (`DHpn`) will always be the same for each of the three above situations.

D.2.3 Numerically integrating Hamiltons' equations

The most straightforward way to integrate the differential equations (Hamiltons' Equations) generated by the above procedure is as follows:

$$q_i(t+\Delta t) = q_i(t) + \left(\frac{\partial H}{\partial p_i}\right)_t \Delta t \qquad \text{(D.3)}$$

and

$$p_i(t+\Delta t) = p_i(t) + \left(\frac{\partial H}{\partial q_i}\right)_t \Delta t \qquad \text{(D.4)}$$

However, more accurate methods of numerical integration are available, which mean that larger time steps can be used to achieve the same integration accuracy. A commonly used algorithm, and one that is employed in this program, is the Runge-Kutta (RK) procedure. The RK algorithm uses trial steps in the middle of the time interval Δt

to cancel out lower order error terms. The program implements the RK algorithm to fourth order [2].

In our situation, we have nine momenta variables, p_j, and nine position variables, q_i. For simplicity, in the equations below (D.5-D.16), two bold array variables are introduced, $\boldsymbol{p}_n$ and $\boldsymbol{q}_n$, which represent all nine values of the momenta and position coordinates, respectively. Using this notation, the propagation of each of the momenta variables (p_j) is given by the nine differential equations, where j = 1-9:

$$\frac{\partial H}{\partial q_j} = f_j(\boldsymbol{q}_n) = \frac{\mathrm{d}p_j}{\mathrm{d}t}. \tag{D.5}$$

Similarly, the propagation of each q_i variable is given by nine differential equations (i = 1-9):

$$\frac{\partial H}{\partial p_i} = g_i(\boldsymbol{p}_n) = \frac{\mathrm{d}q_i}{\mathrm{d}t}. \tag{D.6}$$

Then, using the 4th order Runge-Kutta algorithm, we have for the momentum (where j = 1-9),

$$k_{1,j} = \Delta t f_j(\boldsymbol{q}_n) \tag{D.7}$$

$$k_{2,j} = \Delta t f_j(\boldsymbol{q}_n + \frac{\boldsymbol{k}_{1,n}}{2}) \tag{D.8}$$

$$k_{3,j} = \Delta t f_j(\boldsymbol{q}_n + \frac{\boldsymbol{k}_{2,n}}{2}) \tag{D.9}$$

$$k_{4,j} = \Delta t f_j(\boldsymbol{q}_n + \boldsymbol{k}_{3,n}) \tag{D.10}$$

and

$$\boldsymbol{p}_{n+1} = \boldsymbol{p}_n + \frac{\boldsymbol{k}_{1,n}}{6} + \frac{\boldsymbol{k}_{2,n}}{3} + \frac{\boldsymbol{k}_{3,n}}{3} + \frac{\boldsymbol{k}_{4,n}}{6}. \quad \text{(D.11)}$$

Similarly, for the position, where i = 1-9,

$$k_{1,i} = \Delta t g_i(\boldsymbol{p}_n) \quad \text{(D.12)}$$

$$k_{2,i} = \Delta t f_i(\boldsymbol{p}_n + \frac{\boldsymbol{k}_{1,n}}{2}) \quad \text{(D.13)}$$

$$k_{3,i} = \Delta t g_i(\boldsymbol{p}_n + \frac{\boldsymbol{k}_{2,n}}{2}) \quad \text{(D.14)}$$

$$k_{4,i} = \Delta t g_i(\boldsymbol{p}_n + \boldsymbol{k}_{3,n}) \quad \text{(D.15)}$$

and

$$\boldsymbol{q}_{n+1} = \boldsymbol{q}_n + \frac{\boldsymbol{k}_{1,n}}{6} + \frac{\boldsymbol{k}_{2,n}}{3} + \frac{\boldsymbol{k}_{3,n}}{3} + \frac{\boldsymbol{k}_{4,n}}{6}. \quad \text{(D.16)}$$

In summary, the above Runge-Kutta algorithm is used to propagate values of the position and momenta for each atom involved in the simulation. As described below, the algorithm is called for many iterations until the products are well separated.

The program initiates the trajectory using the Hamiltonian described above to model the interactions of Ne^{2+} and N_2 and follows the trajectory, recording q_i and p_i at every point in the single trajectory mode, until the reactants reach the curve crossing. If the reactants never approach close enough to reach the curve crossing, they "miss" each other, the simulation continues until the reactants have separated to a distance of 50 Å

and the trajectory is aborted and flagged as a miss. If the reactants reach the curve crossing radius, which is set as a fundamental constant of 5 Å in the program, then the relevant differential equations being integrated are changed to those for Ne^+ and N_2^+. As described above, this "electron transfer" can be set to occur either on the approach of the reactants (early electron transfer) or on their separation (late electron transfer), or randomly at either curve crossing. If NDET is being simulated, the relevant differential equations for Ne^+ and N_2^+ continue to be integrated (with q_i and p_i being recorded at every point) until the products have separated to a distance of 50 Å and the trajectory then terminates. If DET is being simulated, a counter records the time since the formation of the N_2^+ ion and when this counter reaches the set lifetime the differential equations being integrated are switched to those for $Ne^+ + N^+ + N$ and the N and N^+ species are given an appropriate impulse (set by the KER for N_2^+ dissociation given by the user) along the direction of the N-N bond. As discussed above, the user can specify if the N atom which receives the positive charge is chosen at random or is the N atom furthest away from the Ne^+ when the N_2^+ dissociates. Again, the trajectory is followed until the N and N^+ have separated by 50 Å.

For the simulation of a single trajectory, which is what is being discussed here, the program then returns to the main menu and the user can select the "trajectory" option [Option (3)] to plot the trajectory from the data file created by option (2). The "trajectory" option allows the user to plot out the motions of the three atoms step by step or as a "movie" of the whole trajectory. The program displays the distances between the three atoms at every step and also the "status" of the system. The "status" being: if electron transfer has occurred, if the system has reached the crossing radius and if the N_2^+ has dissociated. The ability to visualise single trajectories has proven valuable in understanding from which initial conditions certain forms of scattering arise. For example, by examining individual trajectories it became clear that the orientation of the N_2, on the approach of Ne^{2+}, due to the molecular quadropole moment was an important influence on the scattering.

D.2.3.1 Full Monte Carlo simulations [Option (1)]

In summary, the algorithm for the full Monte Carlo simulation repeatedly calls the single trajectory algorithm (described above) with distributions of initial parameters designed to provide a realistic representation of a real collision experiment. After each reactive trajectory, the velocities of the product species are recorded, after they have separated to a significant distance (50 Å) to produce a dataset of nascent product velocities, exactly as is produced by the PSCO experiment. The correlations between these sets of product velocities for each individual reactive event simulates are then examined using the same code that is used in the analysis of the PSCO data.

Table D.2 A list of the variables defined by the user and given to the Monte-Carlo algorithm, together with the form of the distribution that is used for that variable where appropriate.

Variable	Distribution	Typical Value
Number of trajectories	-	10^6
Initial x distance	-	30 Å
Dication beam energy	Uniform, with user defined mean value and width	Mean value 6 eV, FWHM 0.5 eV
Energy release on N_2^+ fragmentation	Gaussian, with user defined mean value and width	Mean value 0.1 – 6 eV, FWHM = 0.5 eV
Initial angle ("cone angle") of Ne^{2+} velocity to x-axis	Uniform between given limits	0-3°, so within these limits the distribution is effectively uniform
N_2^+ lifetime in DET reactions	Exponential	0 – 100 ps
Integration time step	-	1 fs

The key point in generating a realistic Monte Carlo simulation is generating appropriate and realistic distributions of the initial parameters. We will now discuss how the

distribution of each of the parameters described in Table D.2 is chosen in the Monte Carlo simulation. It is important to realise that many of the initial parameters are not "randomly" distributed. For example, one would expect the KER upon dissociation of the N_2^+ ion to have some distribution (perhaps a Gaussian), of a given width, about a mean value. Thus, a key factor in a realistic Monte Carlo simulation is being able to select "randomly", values of the initial parameters that, over the several thousand trajectories of the simulation, reproduce the expected distributions.

We will now describe in detail how this selection procedure is achieved to produce a Gaussian distribution of KERs for the dissociation of the N_2^+ ion, and then explain how the same procedure is extended to other arbitrary functions. Let the probability of a KER k (in eV) be denoted p(k). If we assume, as is a common approximation, that the distribution p(k) is Gaussian with mean value k_m and FWHM of δk we have:

$$\mathrm{p}(k) = N \exp\left(-\frac{4\ln(2)(k-k_m)^2}{\delta k^2} \right) \qquad \text{(D.17a)}$$

where N is a normalisation constant and the 4 ln(2) term is required so that δk is the full width at half maximum. Practically, it is more efficient to work with a function, $f(k)$, which is proportional to the probability distribution:

$$f(k) = \frac{p(k)}{N} \qquad \text{(D.17b)}$$

Visual Basic, in common with many other computer programming languages, will generate a random number between 0 and 1, with the RND function. The objective then is to use this random number generator to give a Gaussian distribution of KERs given by equation (D.17a). In practice, the programme generates a Gaussian distribution, $g(k)$, of the appropriate width, $\delta(k)$, but centred at a mean value of $k = 0$, and then later shifts this distribution to be centred at the required average value of k to give $f(k)$ (Eq. (C.17b)). Using the simple RND function to give a variable with a distribution of $g(k)$, is achieved by dividing the area under the distribution that one wishes to replicate into many strips of equal area (probability), as shown in Figure D.1. In this program, each

function is divided up into 5000 strips. When choosing the KER for a given trajectory a random number between 0 and 5000 is then chosen which selects a given strip, with limits k_n and k_{n+1} as shown in Figure D.1. The actual value of the KER used, k_{chosen}, is then chosen at random between k_n and k_{n+1}. This procedure approximates the distribution as a series of rectangular strips, but given 5000 strips the approximation to the smooth function is perfectly acceptable.

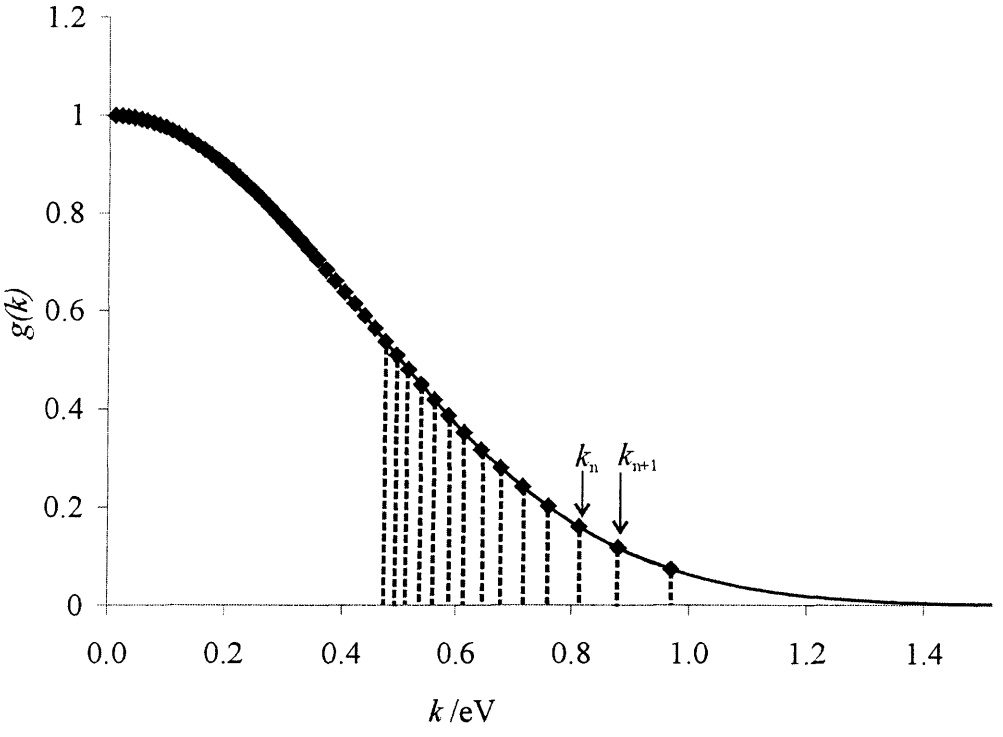

Figure D.1 This figure shows how a Gaussian distribution (FWHM = 1 eV is divided up into strips of equal area, 50 strips in this figure, but 5000 in the code. To choose a KER with a Gaussian distribution, a strip is chosen at random (0-4999) and then the KER is chosen at random within the limits (k_n, k_{n+1}) of the strip.

The program sets up the limits of the strips in an iterative manner in a subroutine (`setupker`) using the following algorithm. The area under the probability distribution, from $k = 0$ to $+\infty$ (Eq. D.18), can be determined from standard integrals. The area ΔA of one strip is hence $1/5000^{th}$ of this total area. The value of k for the lower

limit of the first strip is $k_0 = 0$. The value of k at the upper limit of the first strip, which is the lower limit of the second strip k_1, is then given by considering the rate of change of area under the distribution

$$k_{n+1} = k_n + \frac{\mathrm{d}k}{\mathrm{d}(area\,under\,function)}\Delta A \qquad \text{(D.18)}$$

However,

$$\mathrm{p}(k) = \frac{\mathrm{d}(area\,under\,function)}{\mathrm{d}k}. \qquad \text{(D.19)}$$

Thus

$$k_{n+1} = k_n + \frac{\Delta A}{\mathrm{p}(k_n)}. \qquad \text{(D.20)}$$

Thus if we know k_0, as described above, we can work out the limits of all the strips iteratively. The strip limits are stored in an array (`kerarr`) which is constructed by the (`setupker`) algorithm. When a kinetic energy release is required, a function (`getker`) is then called and also passed the required mean value of the distribution. This `getker` function then chooses a strip (0-4999) at random, and then randomly selects a value of k between the limits of that strip. Then, 50% of the time this value of k is multiplied by -1 to generate a distribution symmetrical about k = 0. Then this appropriately selected value of k is added to the required mean KER, the variable `ker` in the function `getker`, to produce the required distribution, $f(k)$. This algorithm has been extensively tested and can be adapted to generate a procedure to yield "random" variables which conform to any required distribution, as long as an analytic form for the required function can be written down (to enable equation D.18 to be propagated) and the function can be integrated so it can be appropriately normalised (equation D.20). This procedure for "randomly choosing variables with a prescribed distribution is employed in several situations in the programme. For example, the subroutines `setuplife` and `getlife` are used respectively to setup the "strip array" (`li()`) and

randomly choose a variable representing the lifetime of the N_2^+ ion which has the required exponential distribution. Similarly, the function `getangle`, and the associated initialisation code in `setupang`, are used to select the angle of the N_2 neutral with respect to the ion beam axis with an appropriate weighting. Such weightings for angular orientation variables are vital in satisfactory Monte Carlo simulations. Specifically in this example, it is clear that the probability of a reactant N_2 molecule lying along the ion beam x-axis is very small, whereas the probability of a molecule lying perpendicular to this axis is much larger. Consideration of the appropriate volume elements shows, in fact, that to reproduce the real life distribution in θ, where θ is the angle between the ion beam axis and the N-N bond, the angle θ must be chosen with a sine distribution.

Again, the impact parameter must be chosen so that collisions at large impact parameter are appropriately more likely than collisions at small impact parameter, as discussed for the N_2 orientation above. The program also estimates (`bmax`) the maximum value of the impact parameter for which the collision system will reach the crossing radius, and only allows a trajectory to proceed if the selected (weighted) value of the impact parameter for that trajectory is less than `bmax`. If the user does not stipulate whether the electron is to be transferred on approach of the reactant (early electron transfer) or on their separation (late electron transfer), early electron transfer occurs on 50% of trajectories and late electron transfer on 50% of trajectories. Similarly, if the user does not specify that the N atom furthest away from the Ne^+ should carry the positive charge one of the N atoms is selected at random to carry the positive charge when the N_2^+ dissociates.

If a reaction has occurred, the programme saves the final values of the positions and momenta for each trajectory calculated. With knowledge of the masses of each of the atoms, this dataset provides the lab frame velocity components for each of the atoms, the same data that is given by the experiment. Hence, the same data processing procedures, as defined in Chapter 4, can be applied to this simulated data set to display the scattering generated by the simulation (Chapter 7) for comparison with experiment.

D.3 Conclusion

Given above is a detailed explanation of how the Monte Carlo code, listed below, operates. The process of operation of the two key options presented to the user on running the Monte Carlo code – (1) a full Monte Carlo simulation of a series of Ne^{2+}-N_2 collisions and (2) the simulation of a single trajectory – are described, along with a detailed discussion on how all the relevant initial parameters are selected. In the sections that follow, an annotated listing of the code is produced with a more detailed explanation of the algorithmic structure. A summary of how the algorithm works is also given in a flow diagram in the next section.

D.4 Flow Diagram

The flow diagram below summarises how the Monte Carlo code (listed below) works. The section above gives detailed explanations of all variables, parameters and forms referred to in the flow diagram

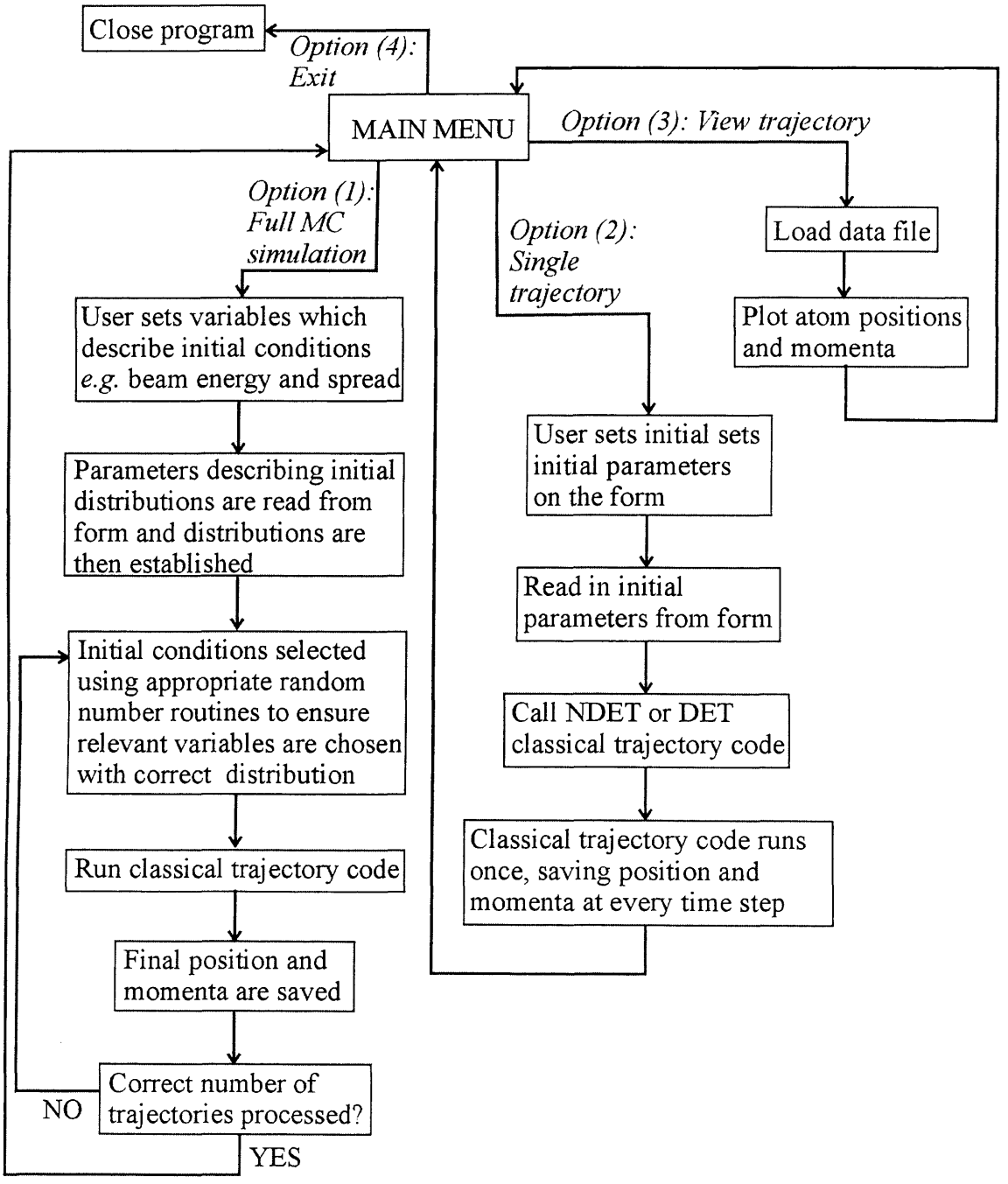

D.5 Annotated Monte Carlo Code

Form for *main menu*

The *main menu* is presented to the user on start-up of the programme. The user can choose to perform a full Monte Carlo simulation (Option (1)), to perform a simulation of a single trajectory (Option (2)), to display the motions of the atoms in that single trajectory (Option (3)), or to exit (Option (4))

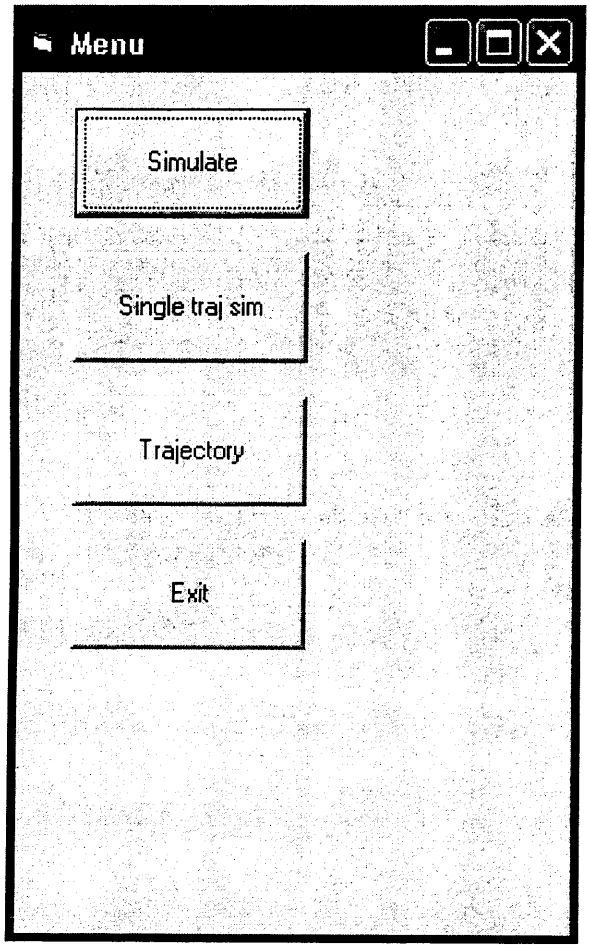

← Option (1)

← Option (2)

← Option (3)

← Option (4)

```
Option Explicit


Private Sub cmdsetup_Click()
frmmenu.Hide
frmsimulations.Show


 End Sub

Private Sub cmdsim_Click()
frmmenu.Hide
frmsim1traj.Show
End Sub

Private Sub cmdtraj_Click()
frmmenu.Hide
frmtraj.Show
End Sub

Private Sub Command1_Click()
End
End Sub
```

Start routine for full MC simulation

Start routine for single trajectory

Display motions of atoms from single trajectory run

Exit

Form for simulating *a single trajectory*

As described in section D.1, this routine allows the user to specify certain parameters of a single collision and then calls the classical trajectory simulation code to allow the collision to occur. This routine saves the positions of the atoms at each time step in a data file so the motions of the atoms can later be examined during the "trajectory" option

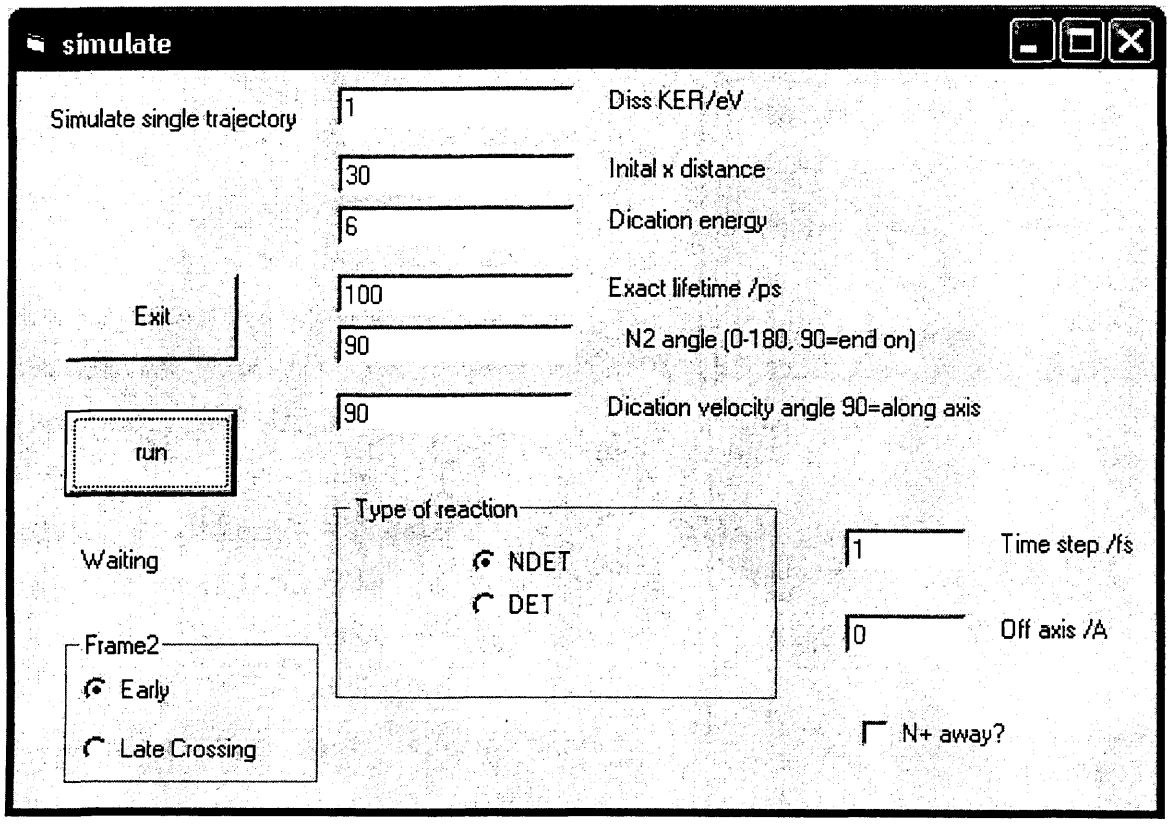

```
Option Explicit

Private Sub cmdexit_Click()
frmmenu.Show
Unload Me
End Sub

Private Sub cmdrun_Click()
Dim life As Double, energy As Double, jj%, j%, ang As
Double, ang1 As Double, offset As Double
Dim pold As Double
Dim crossing As Boolean
Dim react As Boolean
Dim rmin As Double, r12 As Double
Dim dissker As Double
Dim dt As Double
Dim naway As Boolean

Label1.Caption = "Running"
cmdexit.Enabled = False
Refresh

dt = Val(txtdt.Text) * 10 ^ -15

If Option2.Value = True Then

life = Val(txtlifetime.Text) * 10 ^ -12
dissker = Val(txtdissker.Text)
```

Exits this subroutine

This routine reads the user-entered parameters for this trajectory from the form and calls the classical trajectory simulation routines

Time step

Code below is executed when the user asks for a DET simulation

Reads lifetime and N_2^+ dissociation KER

```
energy = Val(txtenergy.Text)
```

Reads beam energy

```
Open "c:/temp/singtraj.dat" For Output As #1
```

Filename to save position and momenta at each time step

```
Refresh
For jj% = 1 To 9
p(jj%) = 0: q(jj%) = 0
Next jj%
```

Initialise position and momenta variables

```
ang = Val(txtn2angle.Text) / 180 * pi: ' 90 is co-linear
atom 2 towards dication

offset = 0.000000001

q(3) = 0
q(4) = offset - rbc / 2 * Sin(ang)
q(5) = -rbc / 2 * Cos(ang)
q(6) = 0
q(7) = offset + rbc / 2 * Sin(ang)
q(8) = rbc / 2 * Cos(ang)
q(9) = 0
```

Reads angle of N-N bond to beam axis

Position N_2 atoms appropriately given typical N-N bond length (`rbc`*)*

```
ang1 = Val(txtdicationang.Text)
ang1 = ang1 / 180 * pi
```

Read angle of dication velocity to x-axis

```
q(1) = -Val(txtinitdist.Text) * 10 ^ -10

pold = Sqr(energy * e * 2 * 20 / 1000 / Na)
p(1) = pold * Sin(ang1)
```

Set momenta of Ne^{2+} appropriately

```
p(2) = pold * Cos(ang1)
q(2) = Val(txtoffaxis.Text) * 10 ^ -10
```

Reads impact parameter and sets appropriate positional variable

```
crossing = optcross.Value
```

Boolean variable for early or late crossing

```
If chkaway.Value = 1 Then naway = True Else naway = False
```

Sets Boolean variable for whether N furthest from Ne^+ is to carry charge on N_2^+ dissociation

```
react = False
```

Boolean to record if reaction has occurred

```
Call MC_diss_et(react, crossing, rmin, life, dissker, True,
dt, naway)
```

Call main classical trajectory simulation routine for DET reaction

```
Print #1, "Reacted"; react
Print #1, "Rmin"; rmin
```

Add reactions status and minimum distance of approach to data file

```
Close #1
```

Close data file

```
Else
```

Code below is called if user selects NDET reaction to simulate, instead of DET. Essentially the same as above, but call NDET classical trajectory code

```
energy = Val(txtenergy.Text)
```

```
Open "c:/temp/singtraj.dat" For Output As #1

Refresh
For jj% = 1 To 9
p(jj%) = 0: q(jj%) = 0
Next jj%

ang = Val(txtn2angle.Text) / 180 * pi: ' 90 is co-linear
atom 2 towards dication

offset = 0.000000001

q(3) = 0
q(4) = offset - rbc / 2 * Sin(ang)
q(5) = -rbc / 2 * Cos(ang)
q(6) = 0
q(7) = offset + rbc / 2 * Sin(ang)
q(8) = rbc / 2 * Cos(ang)
q(9) = 0

ang1 = Val(txtdicationang.Text)
ang1 = ang1 / 180 * pi

q(1) = -Val(txtinitdist.Text) * 10 ^ -10

p(1) = pold * Sin(ang1)
p(2) = pold * Cos(ang1)

q(2) = Val(txtoffaxis.Text) * 10 ^ -10
```

Filename to save position and momenta at each time step

Initialise position and momenta variables

Reads angle of N-N bond to beam axis

Position N_2 atoms appropriately given typical N-N bond length (rbc)

Read angle of dication velocity to x-axis

Set momenta of Ne^{2+} appropriately

Reads impact parameter and sets appropriate positional variable

```
crossing = optcross.Value
```

Boolean variable for early or late crossing

```
react = False

Call MC_non_diss_et(react, crossing, rmin, True, dt)
```

Call main classical trajectory simulation routine for NDET reaction

```
Print #1, "Reacted"; react
Print #1, "Rmin"; rmin


Close #1


End If

Label1.Caption = "Waiting"
cmdexit.Enabled = True
End Sub
```

Update status display

```
Private Sub Form_Load()

Label1.Caption = "Waiting"
End Sub
```

Code execution on opening form. Just updates status display

Form for *full Monte Carlo simulation*

As described in section D.1, this routine repeatedly chooses the relevant parameters that describe the initial conditions of the collision (*e.g.* the collision energy), constrained by preset distributions and calls the appropriate classical trajectory simulation algorithm. The final velocities of the three atoms are stored and analysed using the same routines as used to process the PSCO data.

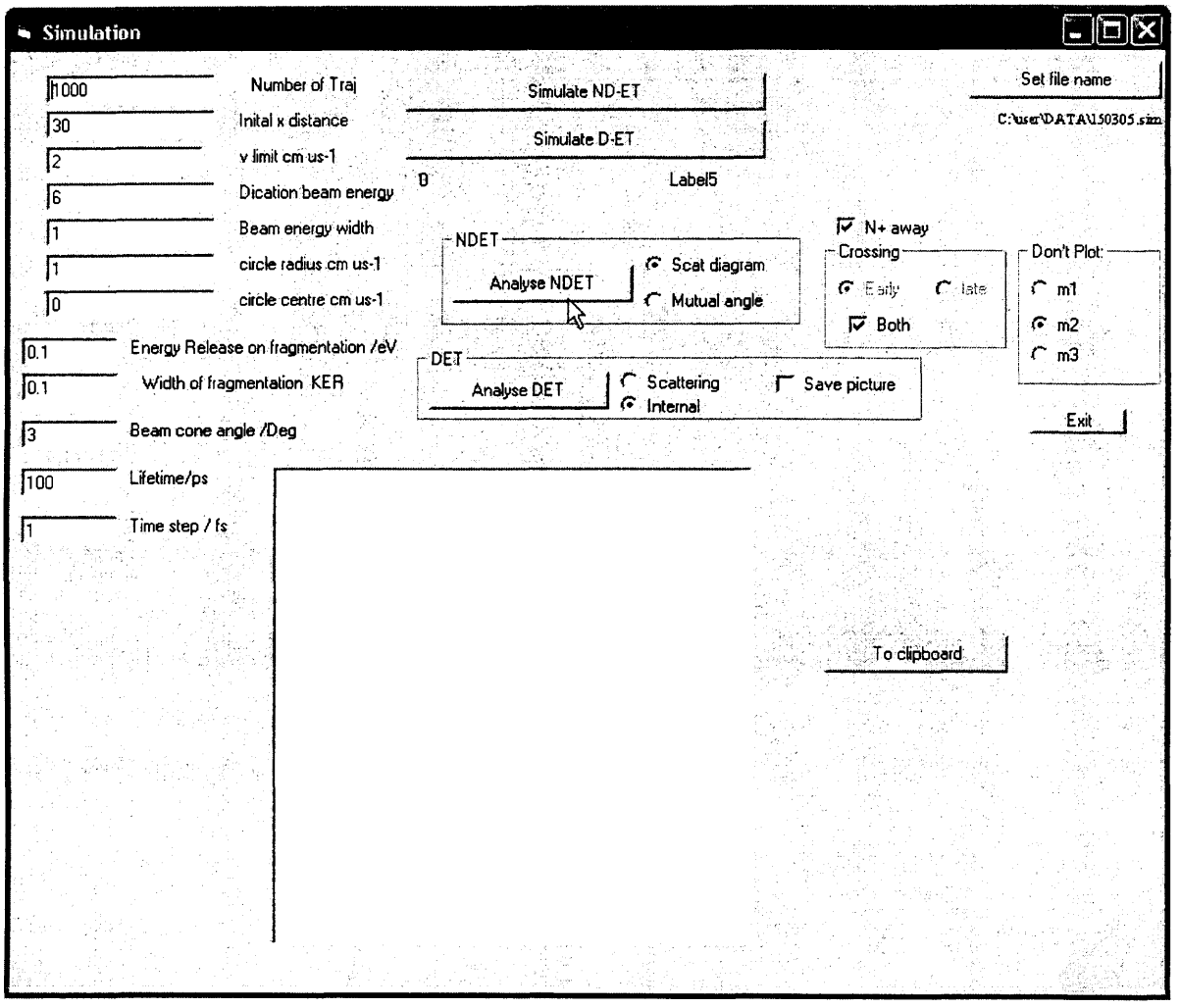

```
Option Explicit
Dim fn$
Dim kerarr(5000) As Double


Private Sub chkboth_Click()
If chkboth.Value = 1 Then
optearly.Enabled = False
optlate.Enabled = False
Else
optearly.Enabled = True
optlate.Enabled = True

End If

End Sub


Private Sub cmdanalyseNDET_Click()
Dim vcom(3) As Double
Dim v(9) As Double, energy As Double, vcomt As Double, jj%,
j%, v1 As Double, cost As Double
Dim ang As Double
Dim angdata(190) As Long
Dim vlimit As Double, pscale As Double
Dim theta As Double, jmax As Long
Dim a$
Dim v2 As Double
Dim dissker As Double
Dim xarr As Double, yarr As Double


energy = Val(txtenergy.Text)
```

Sets a variable to indicate if electron transfer happens at approach (early) or departure (late) or both (50:50)

This code processes the data file generated by a MC simulation of a NDET reaction to examine the velocity components. The algorithms are the same as used in the analysis of the PSCO data.

```
vcom(1) = Sqr(energy * e * 2 / m(1)) * m(1) / (m(1) + m(2)
+ m(3))
vcom(2) = 0
vcom(3) = 0
vcomt = Sqr(vcom(1) ^ 2 + vcom(2) ^ 2
+ vcom(3) ^ 2)
Picture1.Cls

jj = 0
Open fn$ For Input As #1
Do

Input #1, a$
jj = jj + 1
Loop While Not (EOF(1))
Close #1

vlimit = Val(txtvlimit.Text)

jmax = jj - 1

pscale = Picture1.ScaleHeight / 2 / (vlimit / 100 * 10 ^
6): 'conv cm us to ms-1

Picture1.Line (-vlimit / 100 * 10 ^ 6 * pscale, 0)-(vlimit
/ 100 * 10 ^ 6 * pscale, 0), QBColor(2)
Picture1.Line (0, -vlimit / 100 * 10 ^ 6 * pscale)-(0,
vlimit / 100 * 10 ^ 6 * pscale), QBColor(2)
```

Determines the length of the data file

Sets a variety of parameters concerned with the scaling of the scattering diagrams to be plotted.

Reads the final positions and velocities from each trajectory in turn

```
Open fn$ For Input As #1
For jj = 0 To jmax
Input #1, q(1), p(1), q(2), p(2), q(3), p(3), q(4), p(4),
q(5), p(5), q(6), p(6), q(7), p(7), q(8), p(8), q(9), p(9)

For j = 1 To 9
v(j) = p(j) / m(Int((j - 1) / 3) + 1) - vcom(((j - 1) Mod
3) + 1)
```

Converts momenta to velocities

```
Next j

v1 = Sqr(v(1) ^ 2 + v(2) ^ 2 + v(3) ^ 2)
```

Option1 determines the type of plot required: a simple scattering diagram (True) or a plot of mutual angle (False)

```
If Option1.Value = True Then
cost = (v(1) * vcom(1) + v(2) * vcom(2) + v(3) * vcom(3)) /
(v1 * vcomt)
Picture1.PSet (v(1) * pscale, -1 * Abs(v(2)) * pscale),
QBColor(1)
Picture1.PSet (v(4) * pscale, Abs(v(5)) * pscale),
QBColor(3)
Else
```

Calculates angles between products for mutual angle plot

```
v1 = Sqr(v(1) ^ 2 + v(2) ^ 2 + v(3) ^ 2)
v2 = Sqr(v(4) ^ 2 + v(5) ^ 2 + v(6) ^ 2)
```

```
cost = (v(1) * v(4) + v(2) * v(5) + v(3) * v(6)) / (v1 *
v2)

      If cost = 0 Then
      theta = pi / 2
      Else
        If cost <= -1 And cost >= -1.000001 Then

        theta = pi
        Else
            If cost = 1 Then
            theta = 0
            Else
            theta = Atn(Sqr(1 - cost ^ 2) / cost)
            End If
        End If
      End If
theta = theta / pi * 180
If theta < 0 Then theta = 180 + theta
theta = theta / 180 * pi
Picture1.PSet (v2 * pscale * Cos(theta), v2 * pscale *
Sin(theta)), QBColor(3)
```

Plots the angular data

```
End If

Next jj

Close #1



xarr = Val(txtcirccen.Text) * 10 ^ 4 * pscale
yarr = Val(txtcircrad.Text) * 10 ^ 4 * pscale
```

```
Picture1.Circle (xarr, 0), yarr, QBColor(7)
End Sub
```

Draws the circle of the required radius to provide scale

This routine processes the data file generated by a MC simulation of a DET reaction. The algorithms are the same as used in the analysis of the PSCO data.

Private Sub AnalyseDET_Click()

```
Dim vcom(3) As Double
Dim v(9) As Double, energy As Double, vcomt As Double, jj%,
j%, v1 As Double, cost As Double
Dim ang As Double
Dim sdp As Integer
Dim angdata(190) As Long
Dim vlimit As Double, pscale As Double
Dim theta As Double, jmax As Long
Dim aaa$, v3 As Double, v2 As Double
Dim a(3) As Double, b(3) As Double, d(3) As Double
Dim picarr(100, 100) As Integer
Dim xcord As Double, ycord As Double
Dim xarr As Integer, yarr As Integer
Dim dd$, aa$, ffn$

Erase picarr

energy = Val(txtenergy.Text)
```

Reads in the average collision energy and calculates the COM velocity

```
vcom(1) = Sqr(energy * e * 2 / m(1)) * m(1) / (m(1) + m(2)
+ m(3))
vcom(2) = 0
vcom(3) = 0
vcomt = Sqr(vcom(1) ^ 2 + vcom(2) ^ 2 + vcom(3) ^ 2)

Picture1.Cls

jj = 0
Open fn$ For Input As #1
Do

Input #1, aaa$
jj = jj + 1
Loop While Not (EOF(1))
Close #1

vlimit = Val(txtvlimit.Text)


jmax = jj - 1


pscale = Picture1.ScaleHeight / 2 / (vlimit / 100 * 10 ^
6): 'conv cm us to ms-1

Picture1.Line (-vlimit / 100 * 10 ^ 6 * pscale, 0)-(vlimit
/ 100 * 10 ^ 6 * pscale, 0), QBColor(2)
Picture1.Line (0, -vlimit / 100 * 10 ^ 6 * pscale)-(0,
vlimit / 100 * 10 ^ 6 * pscale), QBColor(2)


Open fn$ For Input As #1
```

Determines file length

Reads in final momenta and position from each trajectory and converts them to velocities

```
For jj = 0 To jmax
Input #1, q(1), p(1), q(2), p(2), q(3), p(3), q(4), p(4),
q(5), p(5), q(6), p(6), q(7), p(7), q(8), p(8), q(9), p(9)

For j = 1 To 9
v(j) = p(j) / m(Int((j - 1) / 3) + 1) - vcom(((j - 1) Mod
3) + 1)

Next j
```

Calculates product velocities from momenta

```
v1 = Sqr(v(1) ^ 2 + v(2) ^ 2 + v(3) ^ 2)
v2 = Sqr(v(4) ^ 2 + v(5) ^ 2 + v(6) ^ 2)
v3 = Sqr(v(7) ^ 2 + v(8) ^ 2 + v(9) ^ 2)
```

Plots scattering with respect to chosen product ion or in COM frame

```
If Optm1.Value = True Then
a(0) = v2: b(0) = v3: d(0) = v1
For j = 1 To 3
a(j) = v(j + 3): b(j) = v(j + 6): d(j) = v(j)
Next j
End If

If Optm2.Value = True Then
a(0) = v1: b(0) = v3: d(0) = v2

For j = 1 To 3
a(j) = v(j): b(j) = v(j + 6): d(j) = v(j + 3)
Next j
End If
```

Code assigns the relevant velocity components to the arrays a, b, d to allow a generic plotting routine to be used which uses a, b, d. This means a new plotting routine is not needed for each different type of plot.

```
If optm3.Value = True Then
a(0) = v1: b(0) = v2: d(0) = v3
For j = 1 To 3
a(j) = v(j): b(j) = v(j + 3): d(j) = v(j + 6)
Next j
End If



If optint.Value = True Then

cost = (a(1) * d(1) + a(2) * d(2) + a(3) * d(3)) / (a(0) *
d(0))
```

Calculates angles between velocities for internal scattering diagram

```
      If cost = 0 Then
      theta = pi / 2
      Else
        If cost <= -1 And cost >= -1.000001 Then
        theta = pi
        Else
            If cost = 1 Then
            theta = 0
            Else
            theta = Atn(Sqr(1 - cost ^ 2) / cost)
            End If
        End If
      End If
theta = theta / pi * 180
If theta < 0 Then theta = 180 + theta
theta = theta / 180 * pi
```

```
xcord = a(0) * pscale * Cos(theta): ycord = -1 * Abs(a(0) *
pscale * Sin(theta))
Picture1.PSet (xcord, ycord), QBColor(3)

xarr = CInt((xcord + Picture1.ScaleHeight / 2) /
Picture1.ScaleHeight * 100)
yarr = CInt((ycord + Picture1.ScaleHeight / 2) /
Picture1.ScaleHeight * 100)
picarr(xarr, yarr) = picarr(xarr, yarr) + 1

cost = (b(1) * d(1) + b(2) * d(2) + b(3) * d(3)) / (b(0) *
d(0))

      If cost = 0 Then
      theta = pi / 2
      Else
        If cost <= -1 And cost >= -1.000001 Then
        theta = pi
        Else
            If cost = 1 Then
            theta = 0
            Else
            theta = Atn(Sqr(1 - cost ^ 2) / cost)
            End If
        End If
      End If
theta = theta / pi * 180
If theta < 0 Then theta = 180 + theta
theta = theta / 180 * pi
```

Plots the ionic product angular scattering for the dissociative electron transfer data

```
xcord = b(0) * pscale * Cos(theta): ycord = Abs(b(0) *
pscale * Sin(theta))
Picture1.PSet (xcord, ycord), QBColor(1)

xarr = CInt((xcord + Picture1.ScaleHeight / 2) /
Picture1.ScaleHeight * 100)
yarr = CInt((ycord + Picture1.ScaleHeight / 2) /
Picture1.ScaleHeight * 100)
picarr(xarr, yarr) = picarr(xarr, yarr) + 1


Else
If optm3.Value = True Then
xcord = v(1) * pscale: ycord = -1 * Abs(v(2)) * pscale
Picture1.PSet (xcord, ycord), QBColor(1)

xarr = CInt((xcord + Picture1.ScaleHeight / 2) /
Picture1.ScaleHeight * 100)
yarr = CInt((ycord + Picture1.ScaleHeight / 2) /
Picture1.ScaleHeight * 100)
picarr(xarr, yarr) = picarr(xarr, yarr) + 1


xcord = v(4) * pscale: ycord = Abs(v(5)) * pscale
Picture1.PSet (xcord, ycord), QBColor(2)

xarr = CInt((xcord + Picture1.ScaleHeight / 2) /
Picture1.ScaleHeight * 100)
```

```
yarr = CInt((ycord + Picture1.ScaleHeight / 2) /
Picture1.ScaleHeight * 100)
picarr(xarr, yarr) = picarr(xarr, yarr) + 1


End If

If Optm2.Value = True Then

xcord = v(1) * pscale: ycord = -1 * Abs(v(2)) * pscale
Picture1.PSet (xcord, ycord), QBColor(1)

xarr = CInt((xcord + Picture1.ScaleHeight / 2) /
Picture1.ScaleHeight * 100)
yarr = CInt((ycord + Picture1.ScaleHeight / 2) /
Picture1.ScaleHeight * 100)
picarr(xarr, yarr) = picarr(xarr, yarr) + 1

xcord = v(7) * pscale: ycord = Abs(v(8)) * pscale
Picture1.PSet (xcord, ycord), QBColor(2)

xarr = CInt((xcord + Picture1.ScaleHeight / 2) /
Picture1.ScaleHeight * 100)
yarr = CInt((ycord + Picture1.ScaleHeight / 2) /
Picture1.ScaleHeight * 100)
picarr(xarr, yarr) = picarr(xarr, yarr) + 1

End If

If Optm1.Value = True Then

xcord = v(4) * pscale: ycord = -1 * Abs(v(5)) * pscale
Picture1.PSet (xcord, ycord), QBColor(1)
```

```
xarr = CInt((xcord + Picture1.ScaleHeight / 2) /
Picture1.ScaleHeight * 100)
yarr = CInt((ycord + Picture1.ScaleHeight / 2) /
Picture1.ScaleHeight * 100)
picarr(xarr, yarr) = picarr(xarr, yarr) + 1

xcord = v(7) * pscale: ycord = Abs(v(8)) * pscale
Picture1.PSet (xcord, ycord), QBColor(2)

xarr = CInt((xcord + Picture1.ScaleHeight / 2) /
Picture1.ScaleHeight * 100)
yarr = CInt((ycord + Picture1.ScaleHeight / 2) /
Picture1.ScaleHeight * 100)
picarr(xarr, yarr) = picarr(xarr, yarr) + 1

End If
End If

Next jj

Close #1

xarr = Val(txtcirccen.Text) * 10 ^ 4 * pscale
yarr = Val(txtcircrad.Text) * 10 ^ 4 * pscale
Picture1.Circle (xarr, 0), yarr, QBColor(7)
```

Saves plot if requested

```
If chkpicsave.Value = 1 Then

dlgcommon.CancelError = True
```

```
dlgcommon.Flags = cdlOFNOverwritePrompt +
cdlOFNHideReadOnly
dd$ = Str$(Day(Now)): If Len(dd$) = 2 Then dd$ = "0" +
Right(dd$, 1) Else dd$ = Right(dd$, 2)
aa$ = dd$
dd$ = Str$(Month(Now)): If Len(dd$) = 2 Then dd$ = "0" +
Right(dd$, 1) Else dd$ = Right(dd$, 2)
aa$ = aa$ + dd$
dd$ = Str$(Year(Now)): dd$ = Right$(dd$, 2)
aa$ = aa$ + dd$
dlgcommon.filename = "C:\user\data\" + aa$
dlgcommon.Filter = "Picture array files (*.pic)|*.pic"
dlgcommon.ShowSave
'MsgBox dlgCommon.filename

ffn$ = dlgcommon.filename
sdp = MsgBox("File name set to:" + ffn$, vbDefaultButton1)
```

Saves data to file

```
If ffn$ <> "" Then

Open ffn$ For Output As #1

Print #1, "0 0 0"
Print #1, "100 100 0"


    For j = 0 To 100
    For jj = 0 To 100
    If picarr(j, jj) > 0 Then Print #1, j; " "; jj; " ";
picarr(j, jj)
    Next jj, j

End If
```

```
Close #1
End If: ' chkpicsave

End Sub
```

```
Private Sub cmdclip_Click()
Clipboard.Clear
```

Puts picture onto clipboard

```
Clipboard.SetData Picture1.Image, 2
End Sub
```

```
Private Sub cmdexit_Click()
frmmenu.Show
Unload Me
End Sub
```

Exit simulation routine

```
Private Sub cmdfilename_Click()
Call filename(False)

End Sub
```

Calls routine to set the file name for the simulation data file

```
Private Sub filename(saver As Boolean)
Dim d$, a$, sdp As Integer

start:
dlgcommon.CancelError = True
On Error GoTo ErrHandler
dlgcommon.Flags = cdlOFNOverwritePrompt +
cdlOFNHideReadOnly
d$ = Str$(Day(Now)): If Len(d$) = 2 Then d$ = "0" +
Right(d$, 1) Else d$ = Right(d$, 2)
a$ = d$
d$ = Str$(Month(Now)): If Len(d$) = 2 Then d$ = "0" +
Right(d$, 1) Else d$ = Right(d$, 2)
a$ = a$ + d$
d$ = Str$(Year(Now)): d$ = Right$(d$, 2)
a$ = a$ + d$
dlgcommon.filename = "C:\user\data\" + a$
dlgcommon.Filter = "Simulation files (*.sim)|*.sim"
If saver = True Then dlgcommon.ShowSave Else
dlgcommon.ShowOpen
'MsgBox dlgCommon.filename

fn$ = dlgcommon.filename
sdp = MsgBox("File name set to:" + fn$, vbDefaultButton1)
GoTo Done

ErrHandler:

sdp = MsgBox("File load error", vbDefaultButton1)
fn$ = ""

Done:
If fn$ = "" Then GoTo start
```

Routine to set the file name for the simulation data file

Sets filename

```
lblfilename.Caption = fn$
End Sub
```

Private Sub cmdsimdet_Click()

The following code performs the MC simulations for dissociative electron transfer

```
Dim react As Boolean
Dim traj As Long, bmax As Double, energy As Double, jj As
Integer, j As Long
Dim factor As Double, ewidth As Double

Dim ang As Double, ang1 As Double
Dim cost As Double
Dim bpred As Double
Dim test(360) As Integer
Dim crossing As Boolean
Dim rmin As Double, misses As Long
Dim life As Single
Dim offset As Double
Dim chosenlt As Double
Dim dissker As Double, dt As Double
Dim spread As Double
Dim qold(9) As Double, pold(9) As Double, jjj As Integer
Dim vcom(3) As Double, v(9) As Double, actualker As Double
Dim away As Boolean
```

Defines variables

Reads if N^+ is to be formed from N atom furthest Ne^+

```
If chkaway.Value = 1 Then away = True Else away = False
```

```
fn$ = ""
Do
Call filename(True)
Loop While fn$ = ""
```

Check data file name is OK

```
Call setupker
```

Sets up an array to make KER distribution a Gaussian with user defined width and mean. (See section D.1)

```
frmsimulations.WindowState = 1
frmsimulations.Refresh
dissker = Val(txtdissker.Text)
```

Read mean value for the N_2^+ dissociation KER

```
dt = Val(txtdt.Text) * 10 ^ -15
```

Set time step

```
life = Val(txtlifetime.Text)
Call setuplife(life)
```

Read lifetime and set up array to allow random selection of a lifetime which reproduces user value (see Section D.1 for details)

```
misses = 0
cmdsimdet.Enabled = False
cmdsimulate.Enabled = False
traj = Val(txttraj.Text)
```

Read number of trajectories

```
energy = Val(txtenergy.Text)
```

Read collision energy

```
Open fn$ For Output As #1
```

Run the required number of trajectories

```
For j = 1 To traj
Label5.Caption = "Run: " + Str$(j)
frmsimulations.Refresh
For jj% = 1 To 9
p(jj%) = 0: q(jj%) = 0
Next jj%
```

Initialises p(momenta) and q(position) variables at start of trajectory.

```
frmsimulations.Caption = "Run: " + Str$(j) + "/" +
Str$(traj)

Do ' bmax loop

Do
ang = getangle
' tested give Cos dist 0-90 degrees
Loop While ang > pi / 2
If Rnd > 0.5 Then ang = pi - ang
'Gives a cos distribution between 0-180
' ie very rarely gives 90 degrees along beam axis


If Rnd > 0.5 Then ang = (2 * pi) - ang
' now should give a full 360 deg with 90 and 270
disfavoured:checked and this is true


offset = 0.000000001

chosenlt = getlife() * 10 ^ -12

'ang is angle to the perpendicular to the ion-mol
axis....so 90 and 270 are N-N in line with axis

q(3) = 0
q(4) = offset - rbc / 2 * Sin(ang)
q(5) = -rbc / 2 * Cos(ang)
q(6) = 0
q(7) = offset + rbc / 2 * Sin(ang)
q(8) = rbc / 2 * Cos(ang)
```

Chooses angle of N_2 relative to ion beam x-axis (appropriately weighted), see section D.1

x offset for N_2 COM position so not at origin to prevent some "zero errors"

Chooses a lifetime

Sets up position of COM of N_2 relative to origin

```
q(9) = 0
```

```
spread = Val(txtspread.Text) / 180 * pi / 2:
```

```
ang1 = Rnd * spread
If Rnd > 0.5 Then ang1 = -ang1
ang = ang1 + pi / 2
```

Chooses, with appropriate uniform weighting, within given cone angle, the angle of dication beam to x-axis.

```
q(1) = -Val(txtinitdist.Text) * 10 ^ -10
```

Set initial x position of Ne^{2+}

```
ewidth = Val(txtewidth) / 2 * Rnd
If Rnd > 0.5 Then ewidth = ewidth * -1
pold(0) = Sqr((energy + ewidth) * e * 2 * 20 / 1000 / Na)
```

Chooses a random amount of extra energy (from within specified beam energy spread) to add/subtract to the specified beam energy. Thus, the beam energy distribution is assumed to be uniform between the given limits. A conservative assumption.

```
p(1) = pold(0) * Sin(ang)
p(2) = pold(0) * Cos(ang)
```

```
factor = ((28 * 20) / (28 + 20) / 20): ' to turn collision
energy into com
```

Calculates maximum value of the impact parameter, b, which for a collision can reach the crossing radius

```
bmax = Sqr((energy * e * factor + Vpol / (5 * 10 ^ -10) ^
4) / (energy * e * factor) * (5 * 10 ^ -10) ^ 2)
```

```
q(2) = Sqr((Rnd * 20) ^ 2 + (Rnd * 20) ^ 2) * 10 ^ -10: '

If Rnd > 0.5 Then q(2) = -q(2)

cost = (q(4) - q(1)) * p(1) + (0 - q(2)) * p(2): ' zero as
centre of molecule at y=0
cost = cost / (Sqr(p(1) ^ 2 + p(2) ^ 2 + p(3) ^ 2) *
Sqr((q(4) - q(1)) ^ 2 + q(2) ^ 2))
bpred = Sqr((q(4) - q(1)) ^ 2 + q(2) ^ 2) * Sqr(1 - cost ^
2)

Loop While bpred > bmax


For jjj = 1 To 9
qold(jjj) = q(jjj): pold(jjj) = p(jjj)
Next jjj


If chkboth.Value = 0 Then
If optearly.Value = True Then crossing = True Else crossing
= False
Else
If Rnd > 0.5 Then crossing = True Else crossing = False
' true is for an early crossing
End If

Do
actualker = getker(dissker)
Loop While actualker < 0

react = False
```

Chooses the impact parameter with an appropriate distribution (see section D.1)

Works out the impact parameter for the given value of the y position of the Ne^{2+} and the angle of its velocity and checks that this collision will reach the crossing radius. If not choose again

Specifies when the electron transfer occurs (early or late)

Choose value for KER with appropriate Gaussian distribution

```
Call MC_diss_et(react, crossing, rmin, chosenlt, actualker,
False, dt, away)
```

Calculates product trajectories for the initial parameters chosen above dissociative electron transfer reaction

```
If react = True Then

For jj% = 1 To 9

Print #1, " "; q(jj%); " "; p(jj%); " ";
Next jj%
Print #1,
Else
misses = misses + 1
End If
lblmisses.Caption = "Misses: " + Str$(misses)
junk:
Refresh



Next j

Close #1
cmdsimulate.Enabled = True
cmdsimdet.Enabled = True

frmsimulations.WindowState = 0
frmsimulations.Refresh


End Sub
```

If the trajectory has reacted then save the final momenta and positions.

End of the main loop for each individual trajectory

Sub cmdsimulate_click()

Simulation routine for NDET reaction. Variable selection is the same as for the above routine and is documented there

```
Dim react As Boolean
Dim traj As Long, bmax As Double, energy As Double, jj As
Integer, j As Long
Dim factor As Double, ewidth As Double
Dim ang As Double, ang1 As Double
Dim cost As Double
Dim bpred As Double
Dim test(180) As Integer
Dim crossing As Boolean
Dim rmin As Double, misses As Long
Dim dt As Double, offset As Double, spread As Double
Dim pold(9) As Double, qold(9) As Double, jjj As Integer

'*********
```

Routine basically chooses initial conditions so that relevant parameters fit the required distributions and then calls the classical trajectory code for a NDET reaction

```
fn$ = ""
Do
Call filename(True)
Loop While fn$ = ""
```

Check data file name is OK

```
frmsimulations.WindowState = 1
frmsimulations.Refresh
```

Set time step

```
dt = Val(txtdt.Text) * 10 ^ -15
```

```
misses = 0
cmdsimdet.Enabled = False
cmdsimulate.Enabled = False
traj = Val(txttraj.Text)
```

Read number of trajectories

```
energy = Val(txtenergy.Text)
```

Read collision energy

```
Open fn$ For Output As #1
```

Run the required number of trajectories

```
For j = 1 To traj
Label5.Caption = "Run: " + Str$(j)
frmsimulations.Refresh
For jj% = 1 To 9
p(jj%) = 0: q(jj%) = 0
Next jj%
frmsimulations.Caption = "Run: " + Str$(j) + "/" +
Str$(traj)
```

Initialises p(momenta) and q(position) variables at start of trajectory.

```
Do ' bmax loop
```

Chooses angle of N_2 relative to ion beam x-axis (appropriately weighted), see section D.1

```
Do
ang = getangle
' tested give Cos dist 0-90 degrees
Loop While ang > pi / 2
If Rnd > 0.5 Then ang = pi - ang
'Gives a cos distribution between 0-180
' ie very rarely gives 90 degrees
```

```
If Rnd > 0.5 Then ang = (2 * pi) - ang
' now should give a full 360 deg with 90 and 270
disfavoured:checked and this is true

' for N+ to be going away from NE++ then angle needs to be
between 90-270 so cos is negative
```

```
offset = 0.000000001
```

x offset for N_2 COM position so not at origin to prevent some "zero errors"

```
'ang is angle to the perpendicular to the ion-mol
axis....so 90 and 270 are N-N in line with axis

q(3) = 0
q(4) = offset - rbc / 2 * Sin(ang)
q(5) = -rbc / 2 * Cos(ang)
q(6) = 0
q(7) = offset + rbc / 2 * Sin(ang)
q(8) = rbc / 2 * Cos(ang)
q(9) = 0
```

Sets up position of COM of N_2 relative to origin

```
spread = Val(txtspread.Text) / 180 * pi / 2: ' divided by
two ans input is full cone angle

ang1 = Rnd * spread
If Rnd > 0.5 Then ang1 = -ang1
ang = ang1 + pi / 2
```

Chooses, with appropriate uniform weighting, within given cone angle, the angle of dication beam to x-axis.

```
q(1) = -Val(txtinitdist.Text) * 10 ^ -10
```

Set initial x position of Ne^{2+}

```
ewidth = Val(txtewidth) / 2 * Rnd
If Rnd > 0.5 Then ewidth = ewidth * -1
pold(0) = Sqr((energy + ewidth) * e * 2 * 20 / 1000 / Na)
```

Chooses a random amount of extra energy (from within specified beam energy spread) to add/subtract to the specified beam energy. Thus, the beam energy distribution is assumed to be uniform between the given limits. A conservative assumption.

```
p(1) = pold(0) * Sin(ang)
p(2) = pold(0) * Cos(ang)
```

```
factor = ((28 * 20) / (28 + 20) / 20): ' to turn collision
energy into com
```

Calculates maximum value of the impact parameter, b, for a collision can reach the crossing radius reactive collision

```
bmax = Sqr((energy * e * factor + Vpol / (5 * 10 ^ -10) ^
4) / (energy * e * factor) * (5 * 10 ^ -10) ^ 2)
q(2) = Sqr((Rnd * 20) ^ 2 + (Rnd * 20) ^ 2) * 10 ^ -10: '
```

Chooses the impact parameter with an appropriate distribution (see section D.1)

```
If Rnd > 0.5 Then q(2) = -q(2)
```

```
cost = (q(4) - q(1)) * p(1) + (0 - q(2)) * p(2): ' zero as
centre of molecule at y=0
cost = cost / (Sqr(p(1) ^ 2 + p(2) ^ 2 + p(3) ^ 2) *
Sqr((q(4) - q(1)) ^ 2 + q(2) ^ 2))
```

```
bpred = Sqr((q(4) - q(1)) ^ 2 + q(2) ^ 2) * Sqr(1 - cost ^
2)

Loop While bpred > bmax

For jjj = 1 To 9
qold(jjj) = q(jjj): pold(jjj) = p(jjj)
Next jjj

If chkboth.Value = 0 Then
If optearly.Value = True Then crossing = True Else crossing
= False
Else
If Rnd > 0.5 Then crossing = True Else crossing = False
' true is for an early crossing
End If

react = False

Call MC_non_diss_et(react, crossing, rmin, False, dt)

If react = True Then

For jj% = 1 To 9

Print #1, " "; q(jj%); " "; p(jj%); " ";
Next jj%
Print #1,
```

Works out the impact parameter for the given value of the y position of the Ne^{2+} and the angle of its velocity and checks that this collision will reach the crossing radius. If not choose again

Specifies when the electron transfer occurs (early or late etc)

Calculates product trajectories for the initial parameters chosen above for non-dissociative electron transfer reaction

If the trajectory has reacted then save the final momenta and positions.

```
Else
misses = misses + 1
End If

lblmisses.Caption = "Misses: " + Str$(misses)
junk:
Refresh


Next j
```

End of the main loop for each individual trajectory

```
Close #1
cmdsimulate.Enabled = True
cmdsimdet.Enabled = True

frmsimulations.WindowState = 0
frmsimulations.Refresh

'***********

End Sub
```

Function getangle() As Double

```
Dim a As Integer

a = Int(Rnd * 5000)
getangle = xi(a) + ((xi(a + 1) - xi(a)) / 5000 * Int(Rnd *
5000))
End Function
```

Routine to choose angle with required sine distribution for correct angular distribution of N-N angle to x-axis. See section D.1.

Private Sub Form_Load()

Various initialisation routines when simulation is called.

```
Picture1.ScaleHeight = 4000
Picture1.ScaleWidth = 4000

chkboth.Value = 1
Do
Call filename(False)
Loop While fn$ = ""
Call chkboth_Click
End Sub
```

Function getker(ker#) As Double

```
Dim g!, a As Integer

a = Int(Rnd * 5000)
g = kerarr(a) + ((kerarr(a + 1) - kerarr(a)) / 5000 *
Int(Rnd * 5000))
If Rnd > 0.5 Then g = -g
getker = ker + g

End Function
```

Sub setupker()

```
Dim area As Double, k As Double, w As Double
Dim j As Integer
```

Routine to set up array which allows choosing of KER with appropriate Gaussian distribution. See section D.1.

```
w = Val(txtkerwid)

area = w / 2 * Sqr(3.141593 / (4 * Log(2)))
```

```
area = area / 4999.9
kerarr(0) = 0: k = -4 * Log(2) / w ^ 2
For j = 1 To 5000
kerarr(j) = kerarr(j - 1) + area / Exp(k * kerarr(j - 1) ^
2)
Next j

End Sub
```

Form for *Splash screen*

This splash screen displays when the program is started giving information on the version number and the revision date

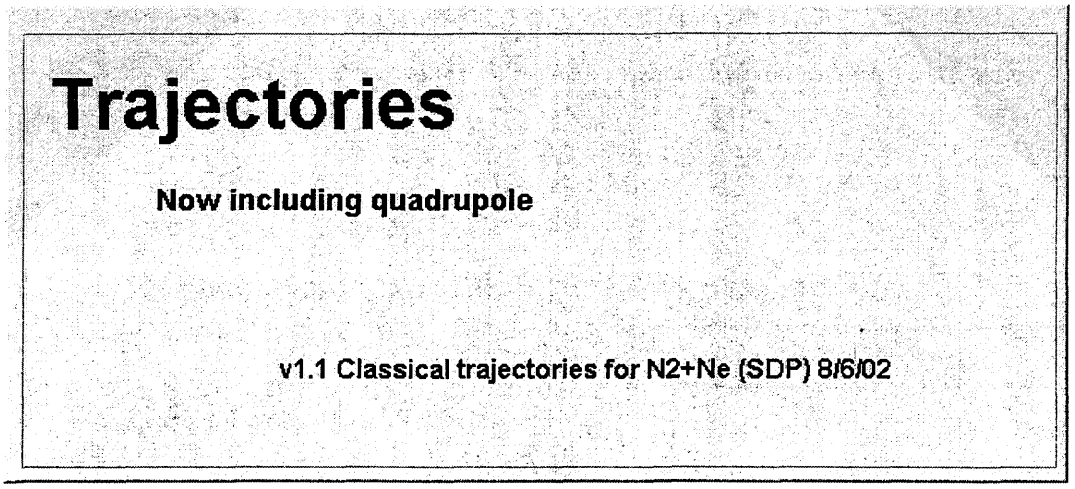

```
Option Explicit

Private Sub Form_KeyPress(KeyAscii As Integer)
    frmmenu.Show
    Unload Me
End Sub
```

Remove the splash screen and load the menu form if a key press.

```
Private Sub Form_Load()
    lblVersion.Caption = "v1.1 Classical trajectories for
N2+Ne (SDP) 8/6/02"
    lblchanges.Caption = "Now including quadrupole"

    lblProductName.Caption = "Trajectories"
End Sub
```

Display data for the splash screen

```
Private Sub Frame1_Click()
    frmmenu.Show
    Unload Me
End Sub
```

Remove the splash screen and load the menu form if a mouse click.

Form for *Trajectory* routines

These routines read data from the file created by a single trajectory simulation and plot the movements of the three atoms.

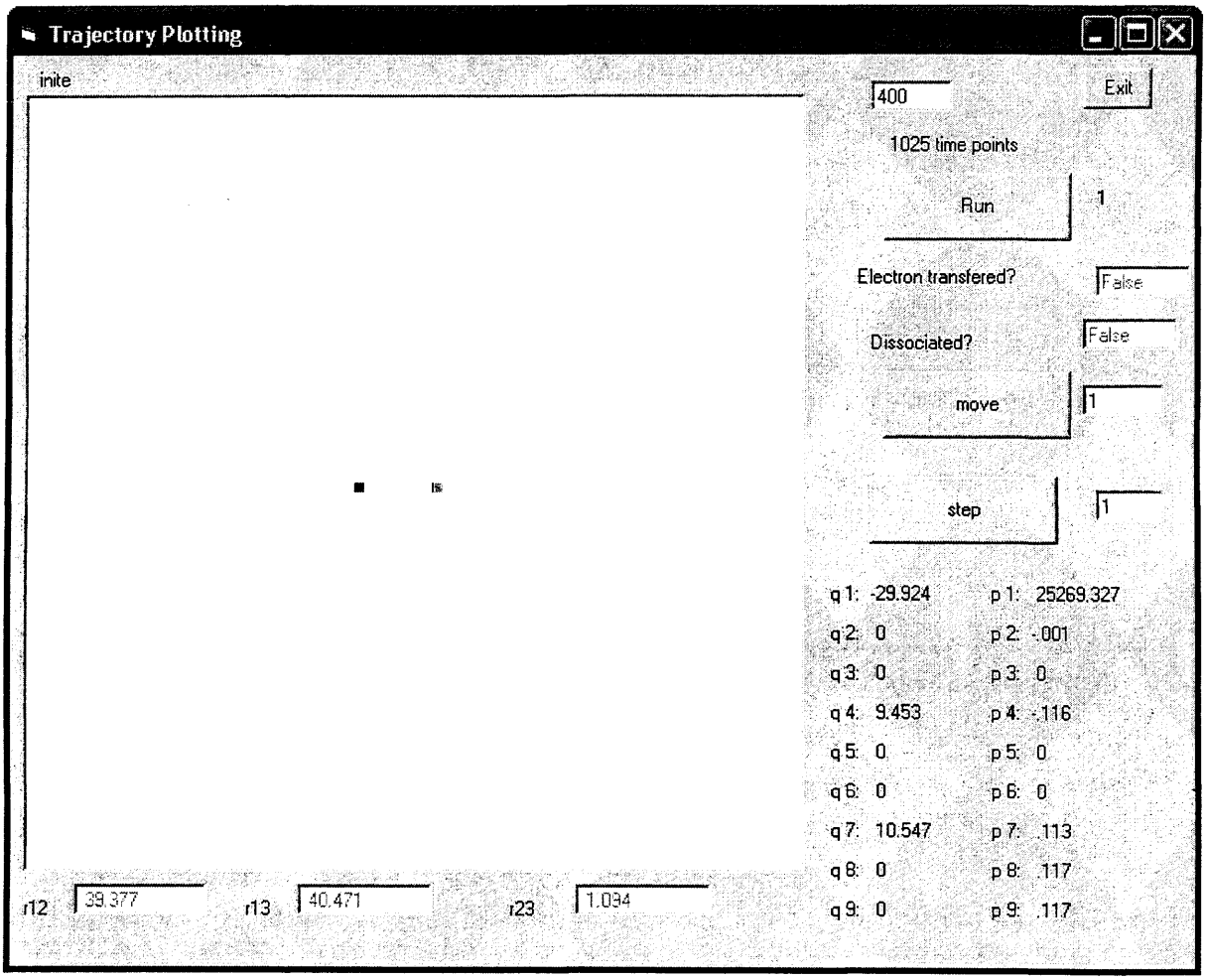

```
Option Explicit
Dim stat As Integer, diss As Integer

Dim pscale As Single
Dim lines As Long
Dim a$, j%
Dim ke As Double, pe As Double, tote As Double, inite As
Double
```

Private Sub cmdexit_Click()

Leave trajectory routine, return to main menu

```
frmmenu.Show
Unload Me
End Sub
```

Private Sub cmdmove_Click()

Move to a user specified point in the trajectory

```
Dim step&, j&
step = CLng(Val(Text2.Text))

Open "c:\temp\singtraj.dat" For Input As #1

For j = 1 To step - 1
Input #1, a$
Next j
```

Call routine to read in relevant data at the required time step

```
Call inp
Close #1
```

```
Label1.Caption = Str$(step)
Call Picture1_Paint

End Sub
```

Plot atoms' positions

```
Private Sub cmdrun_Click()
Dim j As Long

Open "c:\temp\singtraj.dat" For Input As #1

For j = 1 To lines - 3
Call inp
Label1.Caption = Str$(j)

Call Picture1_Paint

Refresh


Next j
Close #1
End Sub
```

Repeatedly plot atom positions from data file to give a "movie" of the motions

```
Private Sub cmdstep_Click()
Dim step%
step = CInt(Val(Label1.Caption))
step = step + CInt(Val(txtstep.Text))
Open "c:\temp\singtraj.dat" For Input As #1

For j = 1 To step% - 1
Input #1, a$
```

Move a given number of steps forward in the trajectory and display the atom positions

```
Next j

Call inp
Close #1

Label1.Caption = Str$(step)
Call Picture1_Paint
Refresh


End Sub
```

On load of the form read the first point in the data file and display the atomic positions

Private Sub Form_Load()

```
Open "c:\temp\singtraj.dat" For Input As #1

lines = 0
Do
Input #1, a$
lines = lines + 1
Loop While Not (EOF(1))

Close #1


Open "c:\temp\singtraj.dat" For Input As #1

Call inp
Label1.Caption = 1

Close #1
lbllines.Caption = Str$(lines - 1) + " time points"
```

```
End Sub
```

Private Sub Picture1_Paint()

Code to plot atom positions and display p and q data

```
Dim j%
Dim r12 As Double, r13 As Double, r23 As Double
pscale = Picture1.ScaleHeight / Val(Text1.Text)
Picture1.Cls
Picture1.Line (CLng(q(1) * pscale * 10 ^ 10), CLng(q(2) *
pscale * 10 ^ 10))-Step(100, 100), QBColor(12), BF
Picture1.Line (CLng(q(4) * pscale * 10 ^ 10), CLng(q(5) *
pscale * 10 ^ 10))-Step(100, 100), QBColor(2), BF
Picture1.Line (CLng(q(7) * pscale * 10 ^ 10), CLng(q(8) *
pscale * 10 ^ 10))-Step(100, 100), QBColor(7), BF



For j = 1 To 9
lblq(j - 1).Caption = "q" + Str$(j) + ":     " +
Str$(CLng(q(j) * 10 ^ 13) / 1000)
lblp(j - 1).Caption = "p" + Str$(j) + ":     " +
Str$(CLng(p(j) * 10 ^ 29) / 1000)
Next

r12 = Sqr((q(4) - q(1)) ^ 2 + (q(5) - q(2)) ^ 2 + (q(6) -
q(3)) ^ 2)
r13 = Sqr((q(7) - q(1)) ^ 2 + (q(8) - q(2)) ^ 2 + (q(9) -
q(3)) ^ 2)
r23 = Sqr((q(7) - q(4)) ^ 2 + (q(8) - q(5)) ^ 2 + (q(9) -
q(6)) ^ 2)
```

```
txtr12.Text = Str$(CLng(r12 * 10 ^ 10 * 1000) / 1000)
txtr13.Text = Str$(CLng(r13 * 10 ^ 10 * 1000) / 1000)
txtr23.Text = Str$(CLng(r23 * 10 ^ 10 * 1000) / 1000)
If stat = 1 Then txtcoulomb.Text = "True" Else
txtcoulomb.Text = "False"
If diss = 1 Then txtdiss.Text = "True" Else txtdiss.Text =
"False"
End Sub
Sub inp()
Input #1, q(1), p(1), q(2), p(2), q(3), p(3), q(4), p(4),
q(5), p(5), q(6), p(6), q(7), p(7), q(8), p(8), q(9), p(9),
stat, diss
End Sub
```

Subroutines

This section of code, which is not attached to any forms, sets up various global variables when the program is started. It also defines a number of functions and subroutines which are called by various of the forms. The code for integrating Hamiltons' equations is here and is called by the various routines in the other forms.

Various global variables

```
Public charge(3) As Integer
Public q(9) As Double
Public p(9) As Double
Public qnext(9) As Double
Public pnext(9) As Double
Public m(3) As Double
Public v12 As Double
Public v23 As Double
Public v13 As Double
Public c As Double
Public k As Double
Public v123 As Double
Public Vpol As Double
Public Vq As Double
Public pol As Double


Public rc As Double
Public xi(5000) As Double
Public li(5000) As Double

Dim coulomb As Boolean
```

```
Dim dissociation As Boolean
```

This is the first code executed when the program runs. Defines various global variables: crossing radius, electrostatic constants for polarisation attraction, masses of atoms

Sub Main()

```
Vpol = 1.74 * (10 ^ -10) ^ 3 * 4 * e ^ 2 / (2 * 4 * pi *
E0)
m(1) = 20 / (1000 * Na)
m(2) = 14 / (1000 * Na)
m(3) = 14 / (1000 * Na)
rc = 0.0000000005

frmSplash.Show
Call setupang(0, 90)
End Sub
```

Show the splash screen and pass control to that routine and set up the array to allow the selection of angles with the appropriate sin distribution from 0-90 degrees.

Sub setupang(a, b)

Routine to set up the array which allows the selection of sin distribution of angle variables for the orientation of N-N. See section D.1

```
Rem work in radians
Dim totalarea!, j As Integer
Dim aa, bb, bitarea As Double

aa = a / 180 * pi: bb = b / 180 * pi
totalarea = (Sin(bb) - Sin(aa))
bitarea = totalarea / 5000
xi(0) = aa
For j = 1 To 5000
xi(j) = xi(j - 1) + bitarea / (Cos(xi(j - 1)))
```

```
Next j
xi(5000) = bb

End Sub
```

Sub setuplife(lt!)

Routine to set up the array which allows the selection of a exponential distribution of N_2^+ lifetimes with the relevant half-life.

```
Dim totalarea!, bitarea!, j%

totalarea = lt * 0.999
bitarea = totalarea / 5000
li(0) = 0
For j% = 1 To 5000
li(j%) = li(j% - 1) + bitarea / (Exp(-li(j% - 1) / lt))

Next j%


End Sub
```

Sub MC_non_diss_et(coulomb, etonapproach As Boolean, rmin As Double, singtraj As Boolean, dt As Double)

```
Dim j%
```

Routine which takes the initial p and q variables set up by the calling routine and propagates them by solving Hamiltons' equations. This routine is for a NDET reaction

```
Dim tt As Double
Dim k1(9, 1) As Double
Dim k2(9, 1) As Double
Dim k3(9, 1) As Double
Dim k4(9, 1) As Double
Dim qlast(9) As Double
Dim plast(9) As Double
Dim jj%
```

```
Dim r1bc As Double
Dim ke As Double
Dim inite As Double, r1bcold As Double
Dim pe As Double
Dim erre As Double, approaching As Boolean, cou As Double


charge(1) = 1
charge(2) = 1
charge(3) = 1
m(1) = 20 / (1000 * Na)
m(2) = 14 / (1000 * Na)
m(3) = 14 / (1000 * Na)

v12 = -charge(1) * charge(2) * e ^ 2 / (4 * pi * E0)
v13 = -charge(1) * charge(3) * e ^ 2 / (4 * pi * E0)
v23 = -charge(2) * charge(3) * e ^ 2 / (4 * pi * E0): ' -ve
signs needed so like charges repel
v123 = -e ^ 2 / (4 * pi * E0):  ' -ve signs needed so like
charges repel
Vq = -2 * Qmoment * e / (4 * pi * E0)

k = 2295: 'force constant in relevant units, have large so
that bond doesn't break in Nm-1
c = -k / 2:

pol = 1.74: 'polarizability of N2 in A^3
Vpol = pol * (10 ^ -10) ^ 3 * 4 * e ^ 2 / (2 * 4 * pi *
E0): ' V= alpha Z^2 q^2/(2* 4 pi e0 r^4)


'  Origin is initial position of atom 1
```

Define masses.

Define various electrostatic constants for the Hamiltonian.

Force constant for N-N bond – so two N-N atoms stay together when bound

```
'  all co-ords go x,y,z for 1,2,3 etc
'  z is out of initial plane
```

Set various flags which record if ET has occurred and the N_2^+ has dissociated. Since this is NDET, dissociation = false, always

```
coulomb = False: dissociation = False
approaching = True: r1bcold = 0.0000003
ke = kenergy(pe)
inite = pe + ke
rmin = -1
Do
```

Evaluates kinetic and potential and total energy so can check energy is conserved through simulation

```
r1bc = (q(4) - q(1) + 0.5 * (q(7) - q(4))) ^ 2 + (q(5) -
q(2) + 0.5 * (q(8) - q(5))) ^ 2 + (q(6) - q(3) + 0.5 *
(q(9) - q(6))) ^ 2
r1bc = Sqr(r1bc)
```

Work out distance from Ne^{2+} to COM of N_2

```
If r1bcold > r1bc Then approaching = True Else approaching
= False
```

Determine if Ne^{2+} approaching or departing from N_2

Store distance of closest approach

```
If r1bc > r1bcold And rmin = -1 Then rmin = r1bcold

If r1bc <= 5 * 10 ^ -10 And coulomb = False And approaching
= True And etonapproach = True Then
     coulomb = True

     End If
```

If crossing radius has been reached and early electron transfer is selected, then transfer electron

```
If coulomb = False And r1bcold < 5 * 10 ^ -10 And r1bc >= 5
* 10 ^ -10 And etonapproach = False Then
```

```
      coulomb = True

      End If

r1bcold = r1bc
For j = 1 To 9
plast(j) = p(j): qlast(j) = q(j)
Next j

If coulomb = True Then

For j = 1 To 9
k1(j, 0) = DHqn_non_diss_et(j) * dt: k1(j, 1) = DHpn(j) *
dt:
Next j

For jj = 1 To 9
q(jj) = q(jj) + k1(jj, 1) / 2: p(jj) = p(jj) + k1(jj, 0) /
2:
Next jj

For j = 1 To 9
k2(j, 0) = DHqn_non_diss_et(j) * dt: k2(j, 1) = DHpn(j) *
dt
Next j

For jj = 1 To 9
q(jj) = qlast(jj) + k2(jj, 1) / 2: p(jj) = plast(jj) +
k2(jj, 0) / 2:
Next jj
```

If crossing radius has been reached and late electron transfer is selected, then transfer electron

Store last values for comparison with next time step

If electron has been transferred, use relevant Hamiltons' equations and Runge-Kutta algorithm to find new values of p and q

The function `DHqn_non_diss_et` *contains Hamiltons' equations for* Ne^+ *and* N_2^+

```
For j = 1 To 9
k3(j, 0) = DHqn_non_diss_et(j) * dt: k3(j, 1) = DHpn(j) *
dt
Next j

For jj = 1 To 9
q(jj) = qlast(jj) + k3(jj, 1): p(jj) = plast(jj) + k3(jj,
0)
Next jj


For j = 1 To 9
k4(j, 0) = DHqn_non_diss_et(j) * dt: k4(j, 1) = DHpn(j) *
dt
Next j


For j = 1 To 9
q(j) = qlast(j) + k1(j, 1) / 6 + k2(j, 1) / 3 + k3(j, 1) /
3 + k4(j, 1) / 6
p(j) = plast(j) + k1(j, 0) / 6 + k2(j, 0) / 3 + k3(j, 0) /
3 + k4(j, 0) / 6
Next j
```

Else

If electron has not been transferred, use relevant Hamiltons' equations and Runge-Kutta algorithm to find new values of p and q

If electron not yet transferred the function `DHqn_Polatt` *contains Hamiltons' equations for* Ne^{2+} *and* N_2

```
For j = 1 To 9
k1(j, 0) = DHqn_Polatt(j) * dt: k1(j, 1) = DHpn(j) * dt:
Next j
```

```
For jj = 1 To 9
q(jj) = q(jj) + k1(jj, 1) / 2: p(jj) = p(jj) + k1(jj, 0) /
2:
Next jj

For j = 1 To 9
k2(j, 0) = DHqn_Polatt(j) * dt: k2(j, 1) = DHpn(j) * dt
Next j

For jj = 1 To 9
q(jj) = qlast(jj) + k2(jj, 1) / 2: p(jj) = plast(jj) +
k2(jj, 0) / 2:
Next jj

For j = 1 To 9
k3(j, 0) = DHqn_Polatt(j) * dt: k3(j, 1) = DHpn(j) * dt
Next j

For jj = 1 To 9
q(jj) = qlast(jj) + k3(jj, 1): p(jj) = plast(jj) + k3(jj,
0)
Next jj

For j = 1 To 9
k4(j, 0) = DHqn_Polatt(j) * dt: k4(j, 1) = DHpn(j) * dt
Next j


For j = 1 To 9
q(j) = qlast(j) + k1(j, 1) / 6 + k2(j, 1) / 3 + k3(j, 1) /
3 + k4(j, 1) / 6
```

```
p(j) = plast(j) + k1(j, 0) / 6 + k2(j, 0) / 3 + k3(j, 0) /
3 + k4(j, 0) / 6
Next j

End If:  'coulomb


If coulomb = True Then cou = 1 Else cou = 0

If singtraj = True Then
    For jj% = 1 To 9
    Print #1, " "; q(jj%); " "; p(jj%); " ";
    Next jj%
    Print #1, cou; " 0"
End If

r1bc = (q(4) - q(1) + 0.5 * (q(7) - q(4))) ^ 2 + (q(5) -
q(2) + 0.5 * (q(8) - q(5))) ^ 2 + (q(6) - q(3) + 0.5 *
(q(9) - q(6))) ^ 2
r1bc = Sqr(r1bc)

Loop While r1bc < (50 * 10 ^ -10)

End Sub
```

If this is a single trajectory call, save values of p and q at every time step

Evaluate distance between Ne and N-N and if less than 50 Å keep going.

Sub MC_diss_et(coulomb, etonapproach As Boolean, rmin As Double, chosenlt As Double, dissker As Double, oneoff As Boolean, dt As Double, naway As Boolean)

Routine which takes the initial p and q variables set up by the calling routine and propagates them by solving Hamiltons' equations. This routine is for a DET reaction

```
Dim j%
Dim tt As Double
Dim k1(9, 1) As Double
Dim k2(9, 1) As Double
Dim k3(9, 1) As Double
Dim k4(9, 1) As Double
Dim qlast(9) As Double
Dim plast(9) As Double
Dim jj%
Dim r1bc As Double, r12 As Double, r23 As Double, looper As
Boolean
Dim ke As Double
Dim inite As Double, r1bcold As Double
Dim pe As Double
Dim erre As Double, approaching As Boolean
Dim dtime As Double
Dim vadded As Double
Dim cou As Integer


Dim diss As Integer



charge(1) = 1
charge(2) = 1
charge(3) = 0
m(1) = 20 / (1000 * Na)
m(2) = 14 / (1000 * Na)
m(3) = 14 / (1000 * Na)


v12 = -charge(1) * charge(2) * e ^ 2 / (4 * pi * E0)
```

Define masses.

```
v13 = -charge(1) * charge(3) * e ^ 2 / (4 * pi * E0)
v23 = -charge(2) * charge(3) * e ^ 2 / (4 * pi * E0): ' -ve
signs needed so like charges repel
v123 = -e ^ 2 / (4 * pi * E0):  ' -ve signs needed so like
charges repel
Vq = -2 * Qmoment * e / (4 * pi * E0)
```

Define various electrostatic constants for the Hamiltonian.

```
k = 2295: 'force constant in relevant units, have large so
that bond doesn't break in Nm-1
c = -k / 2: 'negative sign appears to be needed definitely
```

Force constant for N-N bond – so two N-N atoms stay together when bound

```
pol = 1.74: 'polarizability in A^3
Vpol = pol * (10 ^ -10) ^ 3 * 4 * e ^ 2 / (2 * 4 * pi *
E0): ' V= alpha Z^2 q^2/(2* 4 pi e0 r^4)


'  Origin is initial position of atom 1
'  all atoms stationary
'  all co-ords go x,y,z for 1,2,3 etc
'  z is out of initial plane
```

Set various flags which record if ET has occurred and the N_2^+ has dissociated.

```
coulomb = False: dissociation = False
approaching = True: r1bcold = 0.0000003

rmin = 1
Do
```

```
r1bc = (q(4) - q(1) + 0.5 * (q(7) - q(4))) ^ 2 + (q(5) -
q(2) + 0.5 * (q(8) - q(5))) ^ 2 + (q(6) - q(3) + 0.5 *
(q(9) - q(6))) ^ 2
r1bc = Sqr(r1bc)
```

Work out distance from Ne^{2+} to COM of N_2

```
If r1bcold > r1bc Then approaching = True Else approaching
= False
```

Determine if Ne^{2+} approaching or departing from N_2

```
If rmin > r1bc Then rmin = r1bc
```

Store distance of closest approach

```
If r1bc <= 5 * 10 ^ -10 And coulomb = False And approaching
= True And etonapproach = True Then
     coulomb = True

     End If
```

If crossing radius has been reached and early electron transfer is selected, then transfer electron

```
If coulomb = False And r1bcold < 5 * 10 ^ -10 And r1bc >= 5
* 10 ^ -10 And etonapproach = False Then
     coulomb = True

     End If
```

*If electron has transferred start counting the time (*dtime*) since N_2^+ formed and if greater than* chosenlt *then let N_2^+ dissociate*

```
r1bcold = r1bc

If coulomb = True Then dtime = dtime + dt
If dtime > chosenlt And dissociation = False Then

vadded = Sqr(2 * e * dissker / m(2) / (1 + m(2) / m(3))):

p(4) = p(4) + m(2) * vadded * (q(4) - q(7)) / (Sqr((q(7) -
q(4)) ^ 2 + (q(8) - q(5)) ^ 2))
```

```
p(5) = p(5) + m(2) * vadded * (q(5) - q(8)) / (Sqr((q(7) -
q(4)) ^ 2 + (q(8) - q(5)) ^ 2))

  vadded = Sqr(2 * e * dissker / m(3) / (1 + m(3) / m(2)))
```

Gives the N atoms the appropriate impulse from the dissociation of N_2^+

```
p(7) = p(7) + m(3) * vadded * (q(7) - q(4)) / (Sqr((q(7) -
q(4)) ^ 2 + (q(8) - q(5)) ^ 2))


p(8) = p(8) + m(3) * vadded * (q(8) - q(5)) / (Sqr((q(7) -
q(4)) ^ 2 + (q(8) - q(5)) ^ 2))

If naway = True Then Call which_n
dissociation = True
End If
```

If user has specified the N atoms furthest from the Ne^+ must take the positive charge then this routine (which_n) works out which atom that is and makes that N^+ atom2 q(4-6) and p(4-6) and the neutral q(7-9) p(7-9)

```
For j = 1 To 9
plast(j) = p(j): qlast(j) = q(j)
Next j

If coulomb = True Then

If dissociation = True Then
```

If electron transfer and dissociation have occurred, use the relevant set of Hamiltons' equations to propagate the motion of the atoms

```
For j = 1 To 9
k1(j, 0) = DHqn_Coulomb(j) * dt: k1(j, 1) = DHpn(j) * dt:
Next j
```

D_Hqn_Coulomb *is the function that contains the correct Hamiltons' equations for propagating p for three separated atoms*

```
For jj = 1 To 9
q(jj) = q(jj) + k1(jj, 1) / 2: p(jj) = p(jj) + k1(jj, 0) /
2:
Next jj

For j = 1 To 9
k2(j, 0) = DHqn_Coulomb(j) * dt: k2(j, 1) = DHpn(j) * dt
Next j

For jj = 1 To 9
q(jj) = qlast(jj) + k2(jj, 1) / 2: p(jj) = plast(jj) +
k2(jj, 0) / 2:
Next jj

For j = 1 To 9
k3(j, 0) = DHqn_Coulomb(j) * dt: k3(j, 1) = DHpn(j) * dt
Next j

For jj = 1 To 9
q(jj) = qlast(jj) + k3(jj, 1): p(jj) = plast(jj) + k3(jj,
0)
Next jj

For j = 1 To 9
k4(j, 0) = DHqn_Coulomb(j) * dt: k4(j, 1) = DHpn(j) * dt
Next j


For j = 1 To 9

q(j) = qlast(j) + k1(j, 1) / 6 + k2(j, 1) / 3 + k3(j, 1) /
3 + k4(j, 1) / 6
```

D_Hpn *is the function that contains the correct Hamiltons' equations for propagating q for three separated atoms*

```
p(j) = plast(j) + k1(j, 0) / 6 + k2(j, 0) / 3 + k3(j, 0) /
3 + k4(j, 0) / 6
Next j
Else

For j = 1 To 9
k1(j, 0) = DHqn_non_diss_et(j) * dt: k1(j, 1) = DHpn(j) *
dt:
Next j

For jj = 1 To 9
q(jj) = q(jj) + k1(jj, 1) / 2: p(jj) = p(jj) + k1(jj, 0) /
2:
Next jj

For j = 1 To 9
k2(j, 0) = DHqn_non_diss_et(j) * dt: k2(j, 1) = DHpn(j) *
dt
Next j

For jj = 1 To 9
q(jj) = qlast(jj) + k2(jj, 1) / 2: p(jj) = plast(jj) +
k2(jj, 0) / 2:
Next jj

For j = 1 To 9
k3(j, 0) = DHqn_non_diss_et(j) * dt: k3(j, 1) = DHpn(j) *
dt
Next j

For jj = 1 To 9
q(jj) = qlast(jj) + k3(jj, 1): p(jj) = plast(jj) + k3(jj,
0)
```

If electron transfer has occurred but with no dissociation of N_2^+, use the relevant set of Hamiltons' equations to propagate the motion of the atoms

D_Hqn_non_diss_et *is the function that contains the correct Hamiltons' equations for propagating p for three separated atoms*

D_Hpn *is the function that contains the correct Hamiltons' equations for propagating q for three separated atoms*

```
Next jj

For j = 1 To 9
k4(j, 0) = DHqn_non_diss_et(j) * dt: k4(j, 1) = DHpn(j) *
dt
Next j


For j = 1 To 9
q(j) = qlast(j) + k1(j, 1) / 6 + k2(j, 1) / 3 + k3(j, 1) /
3 + k4(j, 1) / 6
p(j) = plast(j) + k1(j, 0) / 6 + k2(j, 0) / 3 + k3(j, 0) /
3 + k4(j, 0) / 6
Next j


End If: ' dissociation =false
Else


For j = 1 To 9
k1(j, 0) = DHqn_Polatt(j) * dt: k1(j, 1) = DHpn(j) * dt:
Next j


For jj = 1 To 9
q(jj) = q(jj) + k1(jj, 1) / 2: p(jj) = p(jj) + k1(jj, 0) /
2:
Next jj

For j = 1 To 9
k2(j, 0) = DHqn_Polatt(j) * dt: k2(j, 1) = DHpn(j) * dt
Next j
```

If reaction has not occurred use the relevant set of Hamiltons' equations to propagate the motion of the atoms

D_Hqn_Polatt *is the function that contains the correct Hamiltons' equations for propagating p for three separated atoms*

D_Hpn *is the function that contains the correct Hamiltons' equations for propagating q for three separated atoms*

```
For jj = 1 To 9
q(jj) = qlast(jj) + k2(jj, 1) / 2: p(jj) = plast(jj) +
k2(jj, 0) / 2:
Next jj

For j = 1 To 9
k3(j, 0) = DHqn_Polatt(j) * dt: k3(j, 1) = DHpn(j) * dt
Next j

For jj = 1 To 9
q(jj) = qlast(jj) + k3(jj, 1): p(jj) = plast(jj) + k3(jj,
0)
Next jj

For j = 1 To 9
k4(j, 0) = DHqn_Polatt(j) * dt: k4(j, 1) = DHpn(j) * dt
Next j


For j = 1 To 9
q(j) = qlast(j) + k1(j, 1) / 6 + k2(j, 1) / 3 + k3(j, 1) /
3 + k4(j, 1) / 6
p(j) = plast(j) + k1(j, 0) / 6 + k2(j, 0) / 3 + k3(j, 0) /
3 + k4(j, 0) / 6
Next j

End If:  'coulomb

If coulomb = True Then cou = 1 Else cou = 0
If dissociation = True Then diss = 1 Else diss = 0

If oneoff = True Then
```

```
    For jj% = 1 To 9
    Print #1, " "; q(jj%); " "; p(jj%); " ";
    Next jj%
    Print #1, cou; " "; diss
End If

r12 = ((q(4) - q(1)) ^ 2 + (q(5) - q(2)) ^ 2 + (q(6) -
q(3)) ^ 2)
r12 = Sqr(r12)
r23 = ((q(4) - q(7)) ^ 2 + (q(5) - q(8)) ^ 2 + (q(6) -
q(9)) ^ 2)
r23 = Sqr(r23)

If coulomb = True Then
  If r23 < (50 * 10 ^ -10) Then looper = True Else looper =
False
 Else
If r12 < 50 * 10 ^ -10 Then looper = True Else looper =
False
End If

Loop While looper = True

End Sub
```

Continue iterations until there is more than 50 Å between all atoms

Function getlife() As Double

```
Dim a%

a% = Int(Rnd * 5000)
getlife = (li(a%) + ((li(a% + 1) - li(a%)) / 500 * Int(Rnd
* 500)))

End Function
```

Function to choose a lifetime using the previously created array, which allows an exponential distribution of lifetimes with the appropriate half life to be generated.

Function DHqn_Polatt(j%) As Double

```
Dim temp As Double
Dim temp2 As Double, temp3 As Double, rcom As Double, temp4
As Double, temp5 As Double, r12sq As Double
Dim rcomx As Double, rcomy As Double, rcomz As Double
Dim junk As Double
```

Hamiltons' equations for each of the momentum variables for a Hamiltonian for Ne^{2+} + N_2. Called by R_K code in the classical trajectory simulation routines above

```
rcomx = q(4) - q(1) + 0.5 * (-q(4) + q(7))
rcomy = q(5) - q(2) + 0.5 * (-q(5) + q(8))
rcomz = q(6) - q(3) + 0.5 * (-q(6) + q(9))
rcom = (rcomx) ^ 2 + (rcomy) ^ 2 + (rcomz) ^ 2
```

```
r12sq = (q(1) - q(4)) ^ 2 + (q(2) - q(5)) ^ 2 + (q(3) -
q(6)) ^ 2
junk = (-r12sq + rcom + rbc ^ 2 / 4) / (r12sq * rbc ^ 2)
```

J indicates which of the momenta p(1-9) we are working on

```
Select Case j
Case 1
temp = (rcomx) * 4 * Vpol
temp = temp / (rcom) ^ 3
temp3 = 12 * epsilon * Ro ^ 12 * rcomx
temp3 = temp3 / (rcom) ^ 7
temp4 = ((6 * (-2 * (q(1) - q(4)) - 2 * rcomx) * junk) - 6
* (q(1) - q(4)) * junk ^ 2 * rbc ^ 2) * Vq / (rcom ^ 1.5)
temp5 = 3 * Vq * rcomx / (rcom ^ 2.5) * (-1 + (3 * (junk ^
2) * r12sq * rbc ^ 2))
DHqn_Polatt = temp + temp3 + temp4 + temp5

Case 2
temp = (rcomy) * (4 * Vpol)
temp = temp / (rcom) ^ 3
temp3 = 12 * epsilon * Ro ^ 12 * (rcomy)
temp3 = temp3 / (rcom) ^ 7
temp4 = ((6 * (-2 * (q(2) - q(5)) - 2 * rcomy) * junk) - 6
* (q(2) - q(5)) * junk ^ 2 * rbc ^ 2) * Vq / (rcom ^ 1.5)
temp5 = 3 * Vq * rcomy / (rcom ^ 2.5) * (-1 + (3 * (junk ^
2) * r12sq * rbc ^ 2))
DHqn_Polatt = temp + temp3 + temp4 + temp5


Case 3
temp = (rcomz) * (4 * Vpol)
temp = temp / (rcom) ^ 3
temp3 = 12 * epsilon * Ro ^ 12 * (rcomz)
```

```
temp3 = temp3 / (rcom) ^ 7
temp4 = ((6 * (-2 * (q(3) - q(6)) - 2 * rcomz) * junk) - 6
* (q(3) - q(6)) * junk ^ 2 * rbc ^ 2) * Vq / (rcom ^ 1.5)
temp5 = 3 * Vq * rcomz / (rcom ^ 2.5) * (-1 + (3 * (junk ^
2) * r12sq * rbc ^ 2))
DHqn_Polatt = temp + temp3 + temp4 + temp5
```

```
Case 4
temp = 2 * c * (-q(4) + q(7)) * (Sqr((-q(4) + q(7)) ^ 2 +
(-q(5) + q(8)) ^ 2 + (-q(6) + q(9)) ^ 2) - rbc)
temp = temp / Sqr((-q(4) + q(7)) ^ 2 + (-q(5) + q(8)) ^ 2 +
(-q(6) + q(9)) ^ 2)
temp2 = 2 * Vpol * (rcomx)
temp2 = temp2 / (rcom) ^ 3
temp3 = 6 * epsilon * Ro ^ 12 * (rcomx)
temp3 = temp3 / (rcom) ^ 7
temp4 = ((6 * (2 * (q(1) - q(4)) + rcomx) * junk) + 6 *
(q(1) - q(4)) * junk ^ 2 * rbc ^ 2) * Vq / (rcom ^ 1.5)
temp5 = 1.5 * Vq * rcomx / (rcom ^ 2.5) * (-1 + (3 * (junk
^ 2) * r12sq * rbc ^ 2))
DHqn_Polatt = (-1 * temp) - temp2 - temp3 + temp4 - temp5
```

```
Case 5
temp = 2 * c * (-q(5) + q(8)) * (Sqr((-q(4) + q(7)) ^ 2 +
(-q(5) + q(8)) ^ 2 + (-q(6) + q(9)) ^ 2) - rbc)
temp = temp / Sqr((-q(4) + q(7)) ^ 2 + (-q(5) + q(8)) ^ 2 +
(-q(6) + q(9)) ^ 2)
temp2 = 2 * Vpol * (rcomy)
temp2 = temp2 / (rcom) ^ 3
temp3 = 6 * epsilon * Ro ^ 12 * (rcomy)
temp3 = temp3 / (rcom) ^ 7
```

```
temp4 = ((6 * (2 * (q(2) - q(5)) + rcomy) * junk) + 6 *
(q(2) - q(5)) * junk ^ 2 * rbc ^ 2) * Vq / (rcom ^ 1.5)
temp5 = 1.5 * Vq * rcomy / (rcom ^ 2.5) * (-1 + (3 * (junk
^ 2) * r12sq * rbc ^ 2))
DHqn_Polatt = (-1 * temp) - temp2 - temp3 + temp4 - temp5

Case 6
temp = 2 * c * (-q(6) + q(9)) * (Sqr((-q(4) + q(7)) ^ 2 +
(-q(5) + q(8)) ^ 2 + (-q(6) + q(9)) ^ 2) - rbc)
temp = temp / Sqr((-q(4) + q(7)) ^ 2 + (-q(5) + q(8)) ^ 2 +
(-q(6) + q(9)) ^ 2)
temp2 = 2 * Vpol * (rcomz)
temp2 = temp2 / (rcom) ^ 3
temp3 = 6 * epsilon * Ro ^ 12 * (rcomz)
temp3 = temp3 / (rcom) ^ 7
temp4 = ((6 * (2 * (q(3) - q(6)) + rcomz) * junk) + 6 *
(q(3) - q(6)) * junk ^ 2 * rbc ^ 2) * Vq / (rcom ^ 1.5)
temp5 = 1.5 * Vq * rcomz / (rcom ^ 2.5) * (-1 + (3 * (junk
^ 2) * r12sq * rbc ^ 2))
DHqn_Polatt = (-1 * temp) - temp2 - temp3 + temp4 - temp5

Case 7
temp = 2 * c * (-q(4) + q(7)) * (Sqr((-q(4) + q(7)) ^ 2 +
(-q(5) + q(8)) ^ 2 + (-q(6) + q(9)) ^ 2) - rbc)
temp = temp / Sqr((-q(4) + q(7)) ^ 2 + (-q(5) + q(8)) ^ 2 +
(-q(6) + q(9)) ^ 2)

temp2 = 2 * Vpol * (rcomx)
temp2 = temp2 / (rcom) ^ 3
temp3 = 6 * epsilon * Ro ^ 12 * (rcomx)
temp3 = temp3 / (rcom) ^ 7
temp4 = ((6 * rcomx) * junk) * Vq / (rcom ^ 1.5)
```

```
temp5 = 1.5 * Vq * rcomx / (rcom ^ 2.5) * (-1 + (3 * (junk
^ 2) * r12sq * rbc ^ 2))
DHqn_Polatt = temp - temp2 - temp3 + temp4 - temp5

Case 8
temp = 2 * c * (-q(5) + q(8)) * (Sqr((-q(4) + q(7)) ^ 2 +
(-q(5) + q(8)) ^ 2 + (-q(6) + q(9)) ^ 2) - rbc)
temp = temp / Sqr((-q(4) + q(7)) ^ 2 + (-q(5) + q(8)) ^ 2 +
(-q(6) + q(9)) ^ 2)
temp2 = 2 * Vpol * (rcomy)
temp2 = temp2 / (rcom) ^ 3
temp3 = 6 * epsilon * Ro ^ 12 * (rcomy)
temp3 = temp3 / (rcom) ^ 7
temp4 = ((6 * rcomx) * junk) * Vq / (rcom ^ 1.5)
temp5 = 1.5 * Vq * rcomx / (rcom ^ 2.5) * (-1 + (3 * (junk
^ 2) * r12sq * rbc ^ 2))
DHqn_Polatt = temp - temp2 - temp3 + temp4 - temp5

Case 9
temp = 2 * c * (-q(6) + q(9)) * (Sqr((-q(4) + q(7)) ^ 2 +
(-q(5) + q(8)) ^ 2 + (-q(6) + q(9)) ^ 2) - rbc)
temp = temp / Sqr((-q(4) + q(7)) ^ 2 + (-q(5) + q(8)) ^ 2 +
(-q(6) + q(9)) ^ 2)
temp2 = 2 * Vpol * (rcomz)
temp2 = temp2 / (rcom) ^ 3
temp3 = 6 * epsilon * Ro ^ 12 * (rcomz)
temp3 = temp3 / (rcom) ^ 7
temp4 = ((6 * rcomx) * junk) * Vq / (rcom ^ 1.5)
temp5 = 1.5 * Vq * rcomx / (rcom ^ 2.5) * (-1 + (3 * (junk
^ 2) * r12sq * rbc ^ 2))
DHqn_Polatt = temp - temp2 - temp3 + temp4 - temp5

Case Else
```

```
Stop

End Select
End Function
```

Function DHqn_Coulomb(j%) As Double

```
Dim temp As Double
```

Hamiltons' equations for each of the momentum variables for a Hamiltonian for $Ne^+ + N^+ + N$. Called by R_K code in the classical trajectory simulation routines above

```
Select Case j
Case 1
temp = (-(q(1) - q(4)) * v12) / ((q(1) - q(4)) ^ 2 + (q(2)
- q(5)) ^ 2 + (q(3) - q(6)) ^ 2) ^ 1.5


DHqn_Coulomb = temp - ((q(1) - q(7)) * v13) / ((q(1) -
q(7)) ^ 2 + (q(2) - q(8)) ^ 2 + (q(3) - q(9)) ^ 2) ^ 1.5

Case 2
temp = (-(q(2) - q(5)) * v12) / ((q(1) - q(4)) ^ 2 + (q(2)
- q(5)) ^ 2 + (q(3) - q(6)) ^ 2) ^ 1.5
DHqn_Coulomb = temp - ((q(2) - q(8)) * v13) / ((q(1) -
q(7)) ^ 2 + (q(2) - q(8)) ^ 2 + (q(3) - q(9)) ^ 2) ^ 1.5

Case 3
temp = (-(q(3) - q(6)) * v12) / ((q(1) - q(4)) ^ 2 + (q(2)
- q(5)) ^ 2 + (q(3) - q(6)) ^ 2) ^ 1.5
DHqn_Coulomb = temp - ((q(3) - q(9)) * v13) / ((q(1) -
q(7)) ^ 2 + (q(2) - q(8)) ^ 2 + (q(3) - q(9)) ^ 2) ^ 1.5

Case 4
temp = ((q(1) - q(4)) * v12) / ((q(1) - q(4)) ^ 2 + (q(2) -
q(5)) ^ 2 + (q(3) - q(6)) ^ 2) ^ 1.5
DHqn_Coulomb = temp + ((-q(4) + q(7)) * v23) / ((-q(4) +
q(7)) ^ 2 + (-q(5) + q(8)) ^ 2 + (-q(6) + q(9)) ^ 2) ^ 1.5

Case 5
temp = ((q(2) - q(5)) * v12) / ((q(1) - q(4)) ^ 2 + (q(2) -
q(5)) ^ 2 + (q(3) - q(6)) ^ 2) ^ 1.5
```

```
DHqn_Coulomb = temp + ((-q(5) + q(8)) * v23) / ((-q(4) +
q(7)) ^ 2 + (-q(5) + q(8)) ^ 2 + (-q(6) + q(9)) ^ 2) ^ 1.5

Case 6
temp = ((q(3) - q(6)) * v12) / ((q(1) - q(4)) ^ 2 + (q(2) -
q(5)) ^ 2 + (q(3) - q(6)) ^ 2) ^ 1.5
DHqn_Coulomb = temp + ((-q(6) + q(9)) * v23) / ((-q(4) +
q(7)) ^ 2 + (-q(5) + q(8)) ^ 2 + (-q(6) + q(9)) ^ 2) ^ 1.5

Case 7
temp = ((q(1) - q(7)) * v13) / ((q(1) - q(7)) ^ 2 + (q(2) -
q(8)) ^ 2 + (q(3) - q(9)) ^ 2) ^ 1.5
DHqn_Coulomb = temp - ((-q(4) + q(7)) * v23) / ((-q(4) +
q(7)) ^ 2 + (-q(5) + q(8)) ^ 2 + (-q(6) + q(9)) ^ 2) ^ 1.5

Case 8
temp = ((q(2) - q(8)) * v13) / ((q(1) - q(7)) ^ 2 + (q(2) -
q(8)) ^ 2 + (q(3) - q(9)) ^ 2) ^ 1.5
DHqn_Coulomb = temp - ((-q(5) + q(8)) * v23) / ((-q(4) +
q(7)) ^ 2 + (-q(5) + q(8)) ^ 2 + (-q(6) + q(9)) ^ 2) ^ 1.5

Case 9
temp = ((q(3) - q(9)) * v13) / ((q(1) - q(7)) ^ 2 + (q(2) -
q(8)) ^ 2 + (q(3) - q(9)) ^ 2) ^ 1.5
DHqn_Coulomb = temp - ((-q(6) + q(9)) * v23) / ((-q(4) +
q(7)) ^ 2 + (-q(5) + q(8)) ^ 2 + (-q(6) + q(9)) ^ 2) ^ 1.5

Case Else
Stop

End Select
End Function
```

Function DHqn_non_diss_et(j%) As Double

```
Dim temp As Double
Dim r23 As Double, r1bc_2 As Double, temp2 As Double
```

Hamiltons' equations for each of the momentum variables for a Hamiltonian for $Ne^+ + N_2^+$. Called by R_K code in the classical trajectory simulation routines above

```
r1bc_2 = (q(4) - q(1) + 0.5 * (q(7) - q(4))) ^ 2 + (q(5) -
q(2) + 0.5 * (q(8) - q(5))) ^ 2 + (q(6) - q(3) + 0.5 *
(q(9) - q(6))) ^ 2

r23 = Sqr((q(7) - q(4)) ^ 2 + (q(8) - q(5)) ^ 2 + (q(9) -
q(6)) ^ 2)
```

Evaluate key geometric parameters for Hamiltonian: distance between Ne^+ and COM of N-N^+ and distance between N and N

```
Select Case j
Case 1
temp = (-q(1) + q(4) + 0.5 * (-q(4) + q(7))) * v123
DHqn_non_diss_et = temp / r1bc_2 ^ 1.5

Case 2
temp = (-q(2) + q(5) + 0.5 * (-q(5) + q(8))) * v123
DHqn_non_diss_et = temp / r1bc_2 ^ 1.5

Case 3
temp = (-q(3) + q(6) + 0.5 * (-q(6) + q(9))) * v123
DHqn_non_diss_et = temp / r1bc_2 ^ 1.5

Case 4
temp = 2 * c * (q(7) - q(4)) * (r23 - rbc) / rbc
temp2 = 0.5 * (-q(1) + q(4) + 0.5 * (-q(4) + q(7))) * v123
/ r1bc_2 ^ 1.5
DHqn_non_diss_et = -temp - temp2
```

```
Case 5
temp = 2 * c * (q(8) - q(5)) * (r23 - rbc) / rbc
temp2 = 0.5 * (-q(2) + q(5) + 0.5 * (-q(5) + q(8))) * v123
/ r1bc_2 ^ 1.5
DHqn_non_diss_et = -temp - temp2

Case 6
temp = 2 * c * (q(9) - q(6)) * (r23 - rbc) / rbc
temp2 = 0.5 * (-q(3) + q(6) + 0.5 * (-q(6) + q(9))) * v123
/ r1bc_2 ^ 1.5
DHqn_non_diss_et = -temp - temp2

Case 7

temp = 2 * c * (q(7) - q(4)) * (r23 - rbc) / rbc
temp2 = 0.5 * (-q(1) + q(4) + 0.5 * (-q(4) + q(7))) * v123
/ r1bc_2 ^ 1.5
DHqn_non_diss_et = temp - temp2

Case 8
temp = 2 * c * (q(8) - q(5)) * (r23 - rbc) / rbc
temp2 = 0.5 * (-q(2) + q(5) + 0.5 * (-q(5) + q(8))) * v123
/ r1bc_2 ^ 1.5
DHqn_non_diss_et = temp - temp2

Case 9
temp = 2 * c * (q(9) - q(6)) * (r23 - rbc) / rbc
temp2 = 0.5 * (-q(3) + q(6) + 0.5 * (-q(6) + q(9))) * v123
/ r1bc_2 ^ 1.5
DHqn_non_diss_et = temp - temp2
```

```
Case Else
Stop
End Select
End Function
```

Function DHpn(j%)

```
DHpn = p(j%) / m(Int((j% - 1) / 3) + 1)
End Function
```

As discussed in section D.1, Hamiltons' equations for the propagation of changes in the q variables are always the same, since the values of the momenta do not affect the potential energy at a given point.

Function kenergy(potential As Double)

```
Dim kinetic As Double
Dim j%
Dim r1bc As Double, r23 As Double, r13 As Double, r12 As
Double
kinetic = 0
For j = 1 To 9
kinetic = kinetic + p(j) ^ 2 / (2 * m(Int((j - 1) / 3) +
1))
Next j
```

Function evaluates the total energy (kinetic plus potential) so we can monitor that energy is conserved and the simulation is working correctly.

```
If coulomb = True Then
r12 = Sqr((q(1) - q(4)) ^ 2 + (q(2) - q(5)) ^ 2 + (q(3) -
q(6)) ^ 2)
r23 = Sqr((q(4) - q(7)) ^ 2 + (q(5) - q(8)) ^ 2 + (q(6) -
q(9)) ^ 2)
r13 = Sqr((q(1) - q(7)) ^ 2 + (q(2) - q(8)) ^ 2 + (q(3) -
q(9)) ^ 2)
```

```
potential = -(v12 / r12 + v13 / r13 + v23 / r23)

Else

r1bc = (q(4) - q(1) + 0.5 * (q(7) - q(4))) ^ 2 + (q(5) -
q(2) + 0.5 * (q(8) - q(5))) ^ 2 + (q(6) - q(3) + 0.5 *
(q(9) - q(6))) ^ 2
r1bc = Sqr(r1bc)
r23 = Sqr((q(7) - q(4)) ^ 2 + (q(8) - q(5)) ^ 2 + (q(9) -
q(6)) ^ 2)
potential = -c * (r23 - rbc) ^ 2 - Vpol / r1bc ^ 4


End If
kenergy = kinetic
End Function
```

Sub which_n()

```
Dim dq(3) As Double, dp(3) As Double

Dim j As Integer, r12 As Double, r13 As Double

r12 = Sqr((q(4) - q(1)) ^ 2 + (q(5) - q(2)) ^ 2 + (q(6) -
q(3)) ^ 2)
r13 = Sqr((q(7) - q(1)) ^ 2 + (q(8) - q(2)) ^ 2 + (q(9) -
q(3)) ^ 2)
```

Works out which N atom is furthest from the Ne^+ then the N_2^+ dissociates and makes that the N^+ ion (atom2).

```
If r13 > r12 Then

For j = 1 To 3
```

```
dq(j) = q(j + 3)
dp(j) = p(j + 3)
Next j

For j = 1 To 3
q(j + 3) = q(j + 6)
p(j + 3) = p(j + 6)
Next j

For j = 1 To 3
q(j + 6) = dq(j)
p(j + 6) = dp(j)
Next j

End If
End Sub
```

D.6 References

[1] Harper, S. M., Hu, S. W. P., and Price, S. D., 2004, *J. Chem. Phys.*, 120 (16) 7245-7248.

[2] Press, W. H., Flannery, B. P., Teukolsky, and S. A., Vetterling, W. T., *Numerical Recipes in Fortran 77,* Vol 1, CUP (Cambridge), 1992.

[3] Atkins, P. W, *Physical Chemistry,* OUP (Oxford), 6th Ed. 1998.

[4] Duffin, W. J, *Electricity and Magnetism,* McGraw-Hill Book Company, 4th Ed.1990.